STRUCTURE AND STABILITY OF COMPRESSIBLE REACTING MIXING LAYERS

By

Mark J. Day, Nagi N. Mansour and William C. Reynolds

Report No. TF-75

Flow Physics and Computation Division
Department of Mechanical Engineering
Stanford University
Stanford, California 94305-3030

August, 1999

Structure and Stability of Compressible Reacting Mixing Layers

by

Mark J. Day, Nagi N. Mansour and William C. Reynolds

Report No. TF-75

Flow Physics and Computation Division
Department of Mechanical Engineering
Stanford University
Stanford, CA 94305-3030

August, 1999

Acknowledgments

Contents

List of Figures

Nomenclature

Acronyms

DNS   Direct Numerical Simulation

LST   Linear Stability Theory

PSE   Parabolized Stability Equations

PDF   Probability Density Function

Universal Notations

$()_1$ or $()_\infty$ Denotes a quantity of the fast fluid stream

$()_2$ or $()_{-\infty}$ Denotes a quantity of the slow fluid stream

$()_2$ Denotes, also, the cross-stream direction for a coordinate variable

$()_i$ Denotes the imaginary part of a complex number

$()_{ij}$ Denotes the i'th and j'th indices in tensor notation

$()_k$ Denotes a quantity of molecular species k

$()_{mn}$ Denotes a quantity of frequency mode m and spanwise mode n

$()_o$ Denotes a quantity at the inlet plane of the simulation

$()_r$ Denotes the real part of a complex number

$()_x$ Denotes a derivative with respect to x

$()^*$ Denotes a dimensional quantity

$\bar{()}$ Denotes a mean quantity

$\hat{()}$ Denotes an eigenfunction (LST) or shape function (PSE)

$\hat{()}^*$ Denotes an adjoint eigenfunction

$\hat{()}^\dagger$ Denotes a complex conjugate

$\hat{()}'$ Denotes an amplitude multiplied shape function, $A \cdot \hat{()}$

$\check{()}$ Denotes a transformed similarity solution

$\tilde{()}$ Denotes a fluctuating quantity

$\breve{()}$	Denotes a quantity modified by the thin-shear-layer assumption
$()'$	Denotes a derivative with respect to η or y

Roman Symbols

$\mathcal{A}$	Disturbance amplitude function
a	Sound speed
b_y	Grid stretching parameter
c	Complex disturbance phase speed, ω/α
c_+	Speed of a supersonic disturbance relative to the fast stream
c_-	Speed of a supersonic disturbance relative to the slow stream
c_p	Specific heat
c_r	Wave speed, the real part of the disturbance phase speed, c
D	Molecular diffusivity
E	Integrated energy of the shape function velocity vector
E'	Amplitude multiplied shape function velocity vector energy, $\mathcal{A} \cdot E$
F	Similarity variable
$\boldsymbol{F}, \boldsymbol{F}^r$	Nonlinear forcing vector in Fourier space, real space
g	Composite variable of eigenfunctions and flow variables
ΔH_c	Enthalpy of combustion per unit mass of fuel
$\Delta h^o_{f,k}$	Enthalpy of formation of species k
h_t	Total Enthalpy
h_k	Sensible enthalpy of species k
K	Total number of chemical species
L	Linear stability operator
$\mathcal{L}$	Linear PSE operator
L_y	Domain length in the cross-stream direction

Le	Lewis number
M	Mach number, or the number of frequency modes in a PSE simulation
$\mathcal{M}$	Molecular weight
M_c	Convective Mach number
M_x	Mach number in the streamwise direction at a given y position
N	Number of spanwise modes in a PSE simulation
n	Stoichiometric mass ratio of oxidizer to fuel
Pr	Prandtl number
p	Pressure
q	Coefficient of exponential decay for disturbances in the free stream
q_i	Heat conduction in the i direction
R	Universal gas constant
Re_o	Reynolds number based on δ_{ω_o} and fast stream properties
r	Velocity ratio, U_1/U_2
S_c	Schmidt number
s	Density ratio, ρ_2/ρ_1
T	Temperature
T_{ad}	Adiabatic flame temperature
T_f	Flame temperature
T_λ	Period of the fundamental disturbance
t	Time
u	Velocity component in the streamwise (x) direction
U	Free-stream velocity
U_c	Structure convection speed
v	Velocity component in the cross-stream (y) direction

$\hat{\boldsymbol{v}}$	Vector of velocity component shape functions, $(\hat{u}, \hat{v}, \hat{w})$
$\mathcal{W}$	Integrated amount of combustion product
w	Velocity component in the spanwise (z) direction
$\dot{w}_k$	Rate of production of species k on a mass basis
x	Streamwise direction
x_o	Distance from the virtual origin
y	Cross-stream direction
Y	Species mass fraction
Y_o	Oxidizer mass fraction
Y_f	Fuel mass fraction
z	Spanwise direction
Z	Passive scalar, $Y_f - Y_o/n$

Greek Symbols

α	Streamwise wavenumber
$-\alpha_i$	Spatial stability growth rate of a linear disturbance
β	Spanwise wavenumber
β_1	Base spanwise wavenumber in Fourier decomposition
χ	Composite eigenfunction in Gropengiesser formulation
δ_ω	Vorticity thickness, $(U_1 - U_2)/(d\bar{u}/dy_{\max})$
δ_{ω_o}	Initial vorticity thickness (reference length scale)
δ_{ij}	Kronecker delta
δ_{vis}	Visual thickness, based on 1% and 99 % values of ξ
δx	Streamwise step size
ϵ_o	Initial disturbance amplitude
η	Cross stream similarity variable

γ Ratio of specific heats, c_p/c_v

λ Velocity ratio parameter, $(U_1^* - U_2^*)/(U_1^* + U_2^*)$

λ_c Conductivity

μ Viscosity

ν Kinematic viscosity

Ω Coefficient on the streamwise pressure derivative term

ω Frequency

ω_1 Base frequency in the Fourier decomposition

ω_z Spanwise vorticity

ϕ Equivalence ratio, or the shape function vector

ϕ_s Phase angle shift applied to a PSE mode at input

$\hat{\Phi}$ The amplitude-adjusted shape function vector, $\mathcal{A}(x) \cdot \hat{\phi}$

ψ Stream function for compressible flow

Ψ Growth-rate normalized eigenfunction energy

ρ Density

ρ_m Density nondimensionalized by the mean of the free-stream values

σ Nonparallel, nonlinear disturbance growth rate

ς Streamwise similarity variable

$\check{\tau}_{ij}$ Viscous stress tensor carrying only cross-stream terms

θ Three-dimensional propagation angle of a wave disturbance

Θ Nondimensional heat release parameter, $T_{ad} - 1$

Υ Normalized accuracy for a velocity ratio scaling parameter

ξ Mixture fraction

ξ_{st} Stoichiometric mixture fraction value

ζ Stretched grid mapping variable

Chapter 1

Introduction

1.1 Motivation

Direct and efficient mixing of fuel and oxidizer streams is of primary interest in all combustion applications. This is particularly true in flows that combine significant heat release with compressible shear, where these two influences can cause a substantial change in the large-scale flow structure and hence in the mixing characteristics. This dissertation seeks to improve our understanding of how the structure of the compressible reacting mixing layer changes within its parameter space, and to lend insight on what implications this has for mixing and combustion performance.

There are a number of important technological applications where this understanding will be useful. Most notable among them is the supersonic combustion ram jet, or scramjet, where fuel must be mixed molecularly with a high-speed air stream to produce chemical reaction. The efficiency of this mixing will determine the size and ultimately the viability of these propulsion systems (Gutmark et al. 1995). The mixing and combustion of supersonic flow can also be found in some examples of chemical or gasdynamic lasers (see e.g. Dutton et al. 1982; Siegman 1986).

Other relevant applications can be found at the parameter space boundaries. In the absence of compressibility, for example, the interaction of velocity shear and heat release in buoyant diffusion flames produces the flow structure responsible for flame flicker (Chen et al. 1988). In nonreacting flows, an understanding of large-scale structure is critical to issues of jet noise abatement, and also has application to supersonic ejectors (Gutmark et al. 1995).

The present investigation studies the flow structure in a compressible reacting plane shear layer which, beyond its relevance to the applications discussed above, is of basic research interest because of its simple geometry; aspects of more complex flows can often be thought of in terms of a mixing layer model. This has lead to a considerable amount of previous study, both experimental and computational, and a review of this work is given in section 1.3. Our discussion starts here with an introduction to the types of flow structure

1

that are present in the compressible reacting mixing layer.

1.2 Flow Description and Structure

A schematic of the flow configuration is shown in figure 1.1. The high-speed stream on the upper side of the mixing layer (denoted with the subscript 1) carries a mass fraction of oxidizer, Y_o, while fuel, Y_f, enters in the slow-speed steam (subscript 2). The density, ρ, can vary between the two streams. This figure illustrates the type of two-dimensional flow structure that corresponds to the Kelvin-Helmholtz instability (Drazin and Reid 1981) and was first documented in the seminal work of Brown and Roshko (1974). This coherent structure, which dominates incompressible nonreacting mixing layers, will be used as a convenient reference point in this work, referred to as the 'central' mode based on its general location in the layer.

An intuitive understanding for the central mode can be developed by considering the density-weighted vorticity profile, $\rho \, du/dy$. The analytical basis for this comes from Lees and Lin's (1946) proof that the instability of a subsonic mixing layer requires one local extremum in the $\rho \, du/dy$ profile, and that the neutral-mode phase speed is given by the streamwise velocity at this extremum. This proof does not directly extend to compressible reacting situations, although intuitive arguments can be made for this and its applicability is seen in practice (Lessen *et al.* 1965; Gropengiesser 1969; Jackson and Grosch 1989; Shin and Ferziger 1991; Planché 1992).

The construction of the density-weighted vorticity profile in incompressible, constant-density conditions is shown in figure 1.2(a). The $\rho \, du/dy$ profile maintains the single peak of the vorticity profile and this corresponds to the central mode flow structure seen in figure 1.2(b). The same series of diagrams for compressible reacting conditions are shown in figure 1.3. The velocity and hence the vorticity profile remains the same, but the density profile develops a deficit due to the effect of both combustion (through heat release) and compressibility (through the coupling of kinetic and thermal energy). This results in a fundamental change in the $\rho \, du/dy$ profile from a single- to double-peak appearance (figure 1.3). This evolution suggests that the mixing layer will develop two additional instability modes—one associated with each of the fast and slow streams—that are distinct from the central mode and will be termed 'outer' modes in this work. The different location of these outer modes in the layer assures that they will convect at different speeds and, in practice,

they typically have different wavelengths.

The change in structure from central to outer mode dominance also implies a change in mixing mechanism. The implications of this are shown in figure 1.4, which offers a schematic comparison of the mixing processes in both configurations. In comparison to the direct entrainment of fuel and oxidizer provided in a central-mode-governed flow structure, a mixing layer with dominant outer modes will experience a two-step mixing process: the vortical structure of the fast mode mixes oxidizer into the reaction zone while the slow mode mixes in the fuel. The DNS simulations of Planché and Reynolds (1991, 1992) documented the adverse impact of this two-step process on the global reaction rate, implying a reduction in the mixing efficiency for the flow. Given this impact, there is significant interest in improving our understanding of how the structure of the mixing layer, and hence its mixing performance, changes as a function of flow conditions.

1.3 Literature Survey

Due to the fundamental nature of the mixing layer flow, there is a considerable body of literature attributed to its study in various combinations of incompressible, compressible, reacting, and nonreacting conditions. This section offers a selective review of articles relevant to the present investigation. The organization follows the general split seen in the literature between the study of incompressible and compressible flows, with the former coming first since it serves as a reference point of all discussion. Experimental and computational results will be addressed simultaneously to reinforce our view that both approaches offer complementary insight into flow physics.

1.3.1 Incompressible Mixing Layers

Coherent Structure

Investigations of the incompressible nonreacting mixing layer provide a well-studied foundation for the current work, particularly in terms of documenting the central mode structure and developing an understanding of its mixing characteristics. Ho and Huerre (1984) provide a comprehensive overview of early experimental and computational (stability) work that has been done in this area.

As mentioned in the previous section, the pivotal work of Brown and Roshko (1974)

identified the dominance of two-dimensional, large-scale structures in the flow. These structures were shown to grow downstream and provide the dominant mechanism for entrainment from the two streams. The prominence of these structure in high Reynolds number flow was also demonstrated (Brown and Roshko 1974; Dimotakis and Brown, 1976). The vortex-interaction mechanism of pairing was first discovered experimentally by Wille (1963) and later documented by Freymuth (1966). Theoretical work in support of these observations was done by Kelly (1967), who showed that the predominant features of the pairing process could be simulated by the resonant interaction of two stability modes with wavenumber ratio of 2:1 (fundamental:subharmonic). Winant and Browand (1974) were the first to identify successive pairing of neighboring vortices as the fundamental mechanism for mixing layer growth. Clemens and Mungal (1995) demonstrated that this remains a critical mechanism at high Reynolds number.

A secondary instability associated with these streamwise structures, which manifest themselves as streamwise streaks in plane view, have also been observed (Konrad 1976; Breidenthal 1981). These streaks were shown to be the result of streamwise vortices, organized in counter-rotating pairs, that occur simultaneously with the spanwise-oriented structures (Bernal and Roshko 1986). Similar observations have been made in studies at both significant Reynolds number and compressibility (Clemens and Mungal 1995; Messersmith and Dutton 1996).

An explanation for this behavior was developed in Pierrehumbert and Widnall's (1982) insightful stability work. This study built on the contribution of Kelly (1967) by adding a spanwise component to the analysis: both two-dimensional and oblique instabilities where introduced to a hyperbolic tangent mixing layer mean flow superimposed with spanwise-oriented Stuart (1967) vortices. Two-dimensional subharmonic waves were shown to cause the vortex pairing commonly observed in experiments, while a less-amplified, oblique version was shown to produce 'helical pairing', possibly corresponding to observations made in the experiments of Chandrsuda et al. (1978). Three-dimensional fundamental instabilities were categorized by their effect on the deformation of the vortex core: spanwise (z) symmetric forcing produced 'bulging', while its spanwise antisymmetric counterpart resulted in a 'translative' mode. The translative instability had the larger growth rate and its most-amplified mode had a spanwise wavelength that was in reasonable accord with the streamwise vortex spacing observed by Bernal and Roshko (1986). Sandham and Reynolds (1991) later confirmed the importance of each disturbance mechanism in the nonlinear

regime using direct numerical simulation at various levels of compressibility.

Monkewitz (1988) took a different approach from Pierrehumbert and Widnall's work by allowing both fundamental and subharmonic waves to be present at similar amplitudes, rather than assuming the subharmonic to be a secondary instability of initially-lower magnitude. Monkewitz's weakly-nonlinear analysis further supported the view that stability-wave interaction forms the basis of the pairing mechanism, as opposed to an explanation based on Biot-Savart interaction between vortices. Monkewitz (1988) also investigated the resonant interaction between the fundamental and oblique subharmonic waves. This analysis was later extended by Mallier and Maslowe (1994) in their analysis of resonant-triad interactions.

Scalar Measurements and Mixing

With the importance of large-scale structure established, Broadwell and Breidenthal (1982) incorporated this knowledge into a model for turbulent mixing and combustion. Based on experimental observations, their model defines three possible fluid states in the layer: (i) pure, unmixed fluid, (ii) homogeneous fluid inside the structures mixed at the entrainment ratio, and (iii) fluid in strained laminar diffusion layers (flame sheets) between free-streams (*i.e.* in the braid regions). This simplistic but useful model predicts a mixture fraction probability density function (PDF) with delta functions at the free stream values and at the entrainment ratio. In practice, experimental measurements of the PDF have shown considerable variation in shape. The main disagreement concerns whether the PDF shape should follow 'marching' or 'nonmarching' behavior. Marching implies that the most probable value of the mixture fraction, ξ, is nearly identical to the mean value at each cross-stream location, while a nonmarching PDF has a shape that is largely invariant to position. A 'tilted' profile describes an intermediate shape.

The studies of Konrad (1976), Koochesfahani and Dimotakis (1986), and Masutani and Bowman (1986) all found mixture fraction PDFs that were nonmarching with transverse position. These results indicate a preferred mixture fraction that is governed by the entrainment ratio, and imply the dominance of large-scale structure (Konrad, 1976). All three studies also found that entrainment favors high-speed fluid, and that free-stream fluid from both sides could be transported throughout the layer by large-scale structures without mixing, in accord with Broadwell and Breidenthal's model. However, the measurements of Frieler (1992) and Karasso and Mungal (1996) indicate marching or tilted PDF shapes,

respectively. Karasso and Mungal argue that the PDF profile changes from nonmarching to tilted behavior with downstream development and that the discrepancy in shape is caused by different measurement positions and resolution problems in some studies. Their conclusion receives some support from the DNS results of Rogers and Moser (1994), who were able to change the PDF shape from marching to nonmarching by applying forcing at the initial condition; this forcing led to large-scale rollers that engulfed pure fluid into the layer and resulted in a nonmarching profile. Freund (1997) also observed a nonmarching PDF in a low-compressibility DNS of a similarly-forced annular shear layer.

Heat Release

Experimental investigations of heat release effects on mixing layers have been performed by Wallace (1981) and at higher heat release levels by Hermanson and Dimotakis (1989). Despite the significant density decrease associated with combustion, these investigations measured a slight attenuation in growth rate as heat release was increased. These results, compiled by Hermanson and Dimotakis and normalized by the zero heat release growth rate, are presented in figure 1.5 using a heat release parameter, $\Theta = T_f - 1$, where T_f is the flame temperature normalized by the fast-steam temperature.

Hermanson and Dimotakis also inferred a decrease in entrainment relative to the zero heat release case to account for the difference between a 15% drop in growth rate and a 40% drop in mean density. They proposed that the growth rate attenuation was due to an observed drop in shear stress with heat release. A similar drop was seen in the DNS studies of McMurtry *et al.* (1989), who related a calculated reduction in turbulent kinetic energy to a drop in the production term. This investigation also looked at vorticity-altering mechanisms to describe a physical process for growth rate change. They found that thermal expansion and baroclinic torque effects resulted in suppression of both spanwise and streamwise vorticity. More diffuse vortex structures resulted in a decreased capacity to entrain fluid and grow the layer thickness.

The central mode growth rate attenuation has also been found in linear stability calculations, along with a prediction of central to outer mode transition when heat release addition exceeds the realm studied by Hermanson and Dimotakis (Shin and Ferziger 1991; Day *et al.* 1998 – see figure 1.5). Although discussed in different terms, the visualization of buoyant diffusion flames by Chen *et al.* (1988) and Katta *et al.* (1997) offer some compelling evidence of outer mode structure. Despite the different geometry, the physics of this flow are

identical to the shear layer: a flame-related deficit in the density profile occurs in a region of velocity shear, producing a $\rho \, du/dy$ profile with two extrema and hence supporting the development of outer modes.

Density Ratio Effects

Early studies of density ratio effect by Brown and Roshko (op cit) were motivated by the need to separate this influence from compressibility in experiments done with significant density variation. Their results at density ratios, $s = \rho_2/\rho_1$, of 1/7, 1, and 7 demonstrated that the growth of the layer is enhanced with increasing s. The well-resolved passive scalar measurements of Konrad (1976) indicated that the entrainment ratio is quite sensitive to density ratio variation, but otherwise noted little effect on the mixed region of fluid. The entrainment effect has been confirmed by Miller *et al.* (1998) at high Reynolds number and incorporated into the modeling effort of Dimotakis (1986). The most extensive experimental study of density ratio effects was undertaken by Frieler (1992). This study reported generally good agreement with the growth rate observations of Konrad and also Brown and Roshko, but noted a strong dependence on the velocity ratio that makes direct comparisons difficult. Frieler's mixed fluid measurements also confirmed Konrad's results in showing only a slight dependence on density ratio.

The movement in the vortical structure of the layer towards the stream with greater density has been observed in both experiment and computation (Dimotakis 1986; Soteriou and Ghoniem 1995; Day *et al.* 1998). As part of the development of semi-empirical formulas for spreading rate and entrainment ratio, Dimotakis (1986) proposed a pressure-based explanation for this effect. In a reference frame attached to moving eddies, matching the total pressure of streamlines terminating at stagnation points between structures requires a bias in position—and hence speed—toward the denser stream. An alternative, vorticity-based explanation for this movement and other effects of the density ratio appears in the work of Soteriou and Ghoniem (1995). Reasoning that a change in density ratio only affects the baroclinic vorticity generation, they considered this contribution in nonuniform density flows and developed a simple dipole model to explain structure movement toward the denser side.

1.3.2 Compressible Mixing Layers

Growth Rate Attenuation

The stabilizing effect of compressibility on the growth rate of the central mode was first observed in the linear stability studies of Dunn and Lin (1955), Lessen *et al.* (1965), and Gropengiesser (1970). Experimental evidence for the growth rate suppression built on the results of Brown and Roshko (1974), who were the first to separate density ratio and compressibility effects. For mixing layer flows, more definitive evidence came from the experiments of Chinzei *et al.* (1986). Papamoschou and Roshko (1988) followed this with a comprehensive study of the growth rate reduction across a large parameter space.

The concept of convective Mach number, M_c, was developed by Bogdanoff (1983) and further refined by Papamoschou and Roshko (1988) to parameterize the growth rate change. This approach suggests large-scale structures convect at a velocity, U_c, which is determined by equating the dynamic pressures in the two streams at stagnation points in a reference frame traveling at this speed. For flows with an equal ratio of specific heats, the definitions simplify to

$$U_c^* = \frac{a_2^* U_1^* + a_1^* U_2^*}{a_1^* + a_2^*} \qquad \text{and} \qquad M_c = \frac{U_1^* - U_2^*}{a_1^* + a_2^*}, \tag{1.1}$$

where U_1, a_1 and U_2, a_2 are the velocity and sound speed of the fast and slow free streams, and $(^*)$ denotes a dimensional quantity. The collapse of experimental measurements normalized by their incompressible growth rates (as compiled by Slessor 1998b), and plotted against M_c is shown in figure 1.6 along with the prediction from linear stability theory. The conventional explanation for the considerable scatter in this figure points to different definitions of thickness, initial conditions, flow development, and acoustic forcing (Island 1997). The use of scaling relations to obtain the incompressible growth rate is also known to lead to errors for large density ratios (Lu and Lele, 1994). Recently, however, Slessor *et al.* (1998b) have suggested that the problem is in fact with M_c and, as an alternative, have proposed a parameter that is inspired by the ratio of kinetic to thermal energy. This approach results in the parameter

$$\Pi_c = \max\left[\frac{\sqrt{\gamma_i - 1}}{a_i^*} \right] (U_1^* - U_2^*), \tag{1.2}$$

where i is the free-stream index, taking on a value of 1 or 2. This parameter yields the somewhat-improved collapse of experimental data seen in figure 1.7.

Direct numerical simulation databases have proven useful in determining the physical mechanism behind growth rate suppression. Simulations of homogeneously-sheared compressible turbulence by Sarkar *et al.* (1991) and Blaisdell *et al.* (1993) identified an increase in dissipation rate due to dilatation effects as the source of turbulent stress suppression and ultimately the growth rate reduction. However, the influence of dilatation was found to be negligible in mixing layer simulations of Vreman *et al.* (1995) and in Freund's (1997) simulation of an annular mixing layer. Further, as Vreman *et al.* point out, an intuitive inconsistency exists in dissipation models for mixing layers because linear stability predictions based on inviscid analysis offer an excellent prediction (see, for example, figures 1.6 and 1.7).

Building on this observation, Vreman *et al.* (1996) developed a model for the growth rate based on the integrated production of turbulent kinetic energy. Through the analysis of DNS databases at M_c=0.2, 0.6, 0.8, and 1.2, they demonstrated that suppression of the pressure-strain-rate redistribution term, caused by the reduction of pressure fluctuations, was responsible for growth rate attenuation with compressibility. This conclusion was supported by the development of a deterministic model for pressure fluctuations that provided good agreement to the DNS growth rate suppression. A similar pressure-strain-based mechanism was described by Freund (1997) in detailed simulations of a supersonic round turbulent shear layer. This explanation is also consistent with observations of reduced pressure 'communication' between large structures (Papamoschou and Lele 1993). The extrapolation of these ideas to the linear regime was also demonstrated by Vreman *et al.* (1996), who showed that these concepts, although developed in fully turbulent flow, apply equally in the linear stage of development and thereby explain the predictive success of linear stability calculations seen in figures 1.6 and 1.7.

Coherent Structure

In addition to predicting the growth rate attenuation caused by compressibility, the linear stability studies of Dunn and Lin (1955), Lessen *et al.* (1965), and Gropengiesser (1970) also demonstrated that three-dimensional disturbances have larger growth rates in compressible flow. The experiments of Clemens and Mungal (1995) used plane-view images to show that quasi-two-dimensional, spanwise-coherent flow structure at M_c=0.28 and 0.42 transforms into disorganized three dimensionality at M_c=0.62 and 0.72. This transformation is in good agreement with the linear stability prediction of Sandham and Reynolds

(1990) that showed the angle of the most-amplified disturbance follows

$$M_c \cos \theta \approx 0.6 \tag{1.3}$$

for $M_c \geq 0.6$. The cosine relation also suggests that there are a number of shallow obliquity angles where these waves are near-equally amplified for $0.6 \leq M_c \leq 0.8$ (Sandham and Reynolds 1990); this provides partial explanation for the chaotic structure viewed in Clemens and Mungal's high-compressibility results.

Side view images of Clemens and Mungal (1995) observed a change from Brown–Roshko type rollers at $M_c = 0.28$ to more elongated structure at $M_c = 0.62$ and $M_c = 0.79$. They also noted a kink that formed in the braid regions between structures as an effect of compressibility. Spatial correlations of scalar images used to evaluate the change in a phase-averaged picture of the structure shape (*e.g.* Messersmith and Dutton 1996) have provided similar conclusions.

Beyond the range of compressibility attainable by most experimental facilities, the generation of two additional instability modes, one associated with each of the fast and slow free streams, was first discovered by Lessen *et al.* (1966) and Gropengiesser (1970). A full characterization of the outer modes was provided in the spatial stability studies of Jackson and Grosch (1989). They characterized them as supersonic fast and slow modes, the former being supersonic relative to the low-speed stream and the latter relative to the high-speed stream. Disturbances that are supersonic with respect to a boundary were found to have purely oscillatory asymptotic solutions in that stream; this corresponds to outgoing waves in the far field. However, after taking account of three-dimensional instabilities, the central mode was found to have a significantly higher growth rate than the outer modes (Sandham and Reynolds 1991) and hence the latter modes were characterized as more of physical than practical interest.

Structure Velocimetry

Experimental estimates of the large-structure convection speed, U_c, have shown considerable differences between measured values and those predicted by equation 1.1 when compressibility is significant (Fourguette *et al.* 1991; Elliot *et al.* 1993; Hall *et al.* 1993; Papamoschou and Bunyajitradulya 1997). These results bring into question the symmetric assumption built into equation 1.1. This has lead some researchers to postulate that

local shocks generated near coherent structures are responsible for the discrepancy (Papamoschou 1989; Dimotakis 1991). Experimental evidence for eddy shocklets has been indirectly inferred from Mach-wave angles observed in the schlieren images of Hall *et al.* (1993). Papamoschou's (1995) investigation in a counter-flow mixing layer revealed more direct schlieren-image evidence of shocklets, although it is unclear if this absolutely unstable flow configuration has played a part in their creation.

Numerical simulations have provided some confirmation of shocklet presence, but only at significantly higher compressibility levels than the experiments. After discounting their premature appearance in two-dimensional simulations, shocklets have been observed in the three-dimensional direct simulations of Miller *et al.* (1994), Vreman *et al.* (1996), and Freund (1997) at $M_c = 1.2$, $M_c = 1.25$, and $M_c = 1.54$, respectively. It should be noted that Freund's number was obtained for a compressible jet, and also corresponds to a better-resolved simulation. These high M_c values suggest that shocklets—although they are physical—do not account for the U_c discrepancy seen experimentally at far lower compressibility.

Taking a different approach, Sandham (1989) theorized that structure convection speed could be estimated by the neutral mode (*i.e.* post saturation) phase speed calculated from linear stability theory. This perspective helps explain experimental measurements of convection speeds near the free streams because neutral mode phase speeds have been shown to correspond to outer mode solutions at significant Mach numbers (Jackson and Grosch 1989). Sandham's estimates, based on *asymmetric* velocity profiles calculated from the boundary-layer equations, showed considerably better agreement with Papamoschou's (1989) results than predictions from equation 1.1. Remaining discrepancies were attributed to differences in the mean profile, which can cause significant effect on linear stability predictions (Monkewitz and Huerre 1982; Jackson and Grosch 1991; Shin and Ferziger 1991).

Planned experiments of Rossmann *et al.* (1999) will hopefully resolve the shocklet issue by conducting experiments in a new shock tube that will access conditions up to $M_c < 4$, which is far beyond the $M_c < 1.5$ limit of current blowdown facilities. This regime was attained in the expansion tube experiments of Erdos *et al.* (1992) at $M_c = 2.8$, although their limited measurements and visualizations lacked the ability to resolve any outstanding questions.

Scalar Measurements and Mixing

In comparison to the incompressible case, relatively few scalar measurement of compressible mixing layers have been made. Island (1997) states that these results should be viewed cautiously because the high Reynolds number causes poor resolution in all compressible experiments done to date. All experiments agree on a marching mixture fraction PDF (Dutton *et al.* 1990; Messersmith and Dutton 1992; Clemens and Mungal 1995; Clemens and Paul 1995), which is notable in comparison to the considerable disagreement found in incompressible studies. Further evidence of a marching profile comes from Island (1997), who determined that the composition of mixed fluid near the layer edge became biased towards the free-stream composition as compressibility increased. Miller *et al.* (1998) provided an explanation for the change from nonmarching to marching PDF's based on the transition from two- to three-dimensional structure. Clemens and Mungal (1995) and Messersmith and Dutton (1992) both observe a narrowing of the PDF distribution at a given position with compressibility, implying a slight increase in the amount of mixed fluid.

Resolution-insensitive measurements of the mixing efficiency have predicted a small increase (Clemens and Paul 1995), negligible effect (Island 1997), and a decrease (Hall 1991) with compressibility, although follow-up work to Hall's in the same facility have suggested a weaker effect (Dimotakis and Leonard 1994). Hall also inferred a near unity volumetric entrainment ratio, which differs significantly from the fast-stream bias of incompressible flows. In well-resolved direct numerical simulations of an annular shear layer, Freund (1997) measured a mixing efficiency increase with compressibility. Freund's PDFs show a tilted distribution at compressibility levels beyond the experimental conditions.

Heat Release

When the effect of heat release is added to compressible flow, the importance and indeed dominance of the outer modes becomes clear. Heat release distorts the $\rho \, du/dy$ profile (see section 1.2) and consequently favors the outer mode instabilities (Planché 1992; Shin and Ferziger 1993). Planché introduced the flame convective Mach number to parameterize the effect of compressibility on outer modes according to the shear between the flame position and the appropriate free stream. Planché's numerical simulations also addressed the growth mechanism for outer mode structures and their transition to turbulence. Large baroclinic torques were found to prevent vortex pairing, causing the fast and slow mode

subharmonics to consume the saturated fundamental through a 'gulping' mechanism that occurs independently for the two modes.

Experimental work in this regime is relatively limited due to its considerable complexity. Significant work in compressible reacting mixing layers at $M_c > 0.4$ has been reported by Miller *et al.* (1998), although the combination of heat release and compressibility in this experiment was not sufficient to generate an outer mode structure (Planché 1992). In comparing two H_2 reacting cases at $M_c = 0.32$ and $M_c = 0.70$, Miller *et al.* observed two important effects of compressibility: first, in agreement with Hall (1991), acetone measurements indicated a near-equal entrainment from the two streams. Second, they note the surprising result that the high M_c case has an OH signal of larger width and significantly higher strength than observed at low M_c, suggesting that compressibility enhanced the combustion process. Both observations were attributed to the development of three-dimensional flow structure that produces a related change in entrainment and internal mixing.

1.4 Computational Techniques

The present work makes use of linear stability theory (LST) and the parabolized stability equations (PSE) to model the evolution of the compressible reacting mixing layer. We shall, therefore, limit our discussion to these two methods.

1.4.1 Linear Stability Theory

This analysis tool is based on quantifying the growth of a waves which are assumed as a model for disturbances in a laminar mean flow. This is a simple but extremely useful way to analyze the development of flow structure. Qualitative evidence for this comes from the early visualizations of Hama (1962) and Michalke (1965), who both demonstrated that simple patters of linear waves superimposed on a mixing layer base flow will produce vortical structure similar to that viewed in experiments. The underlying wave nature of the flow is also evident in the instantaneous views of the velocity field by Urban (1999) using PIV in a compressible mixing layer.

Quantitative evidence for the accuracy of linear stability predictions is available in studies that compare results to experimental (Lu and Lele 1994; Sandham and Reynolds 1990) or direct simulation results (Sandham and Reynolds 1991; Planché 1992; Planché and Reynolds 1992). These investigations have demonstrated the utility of using linear stability methods

to gain significant and accurate insight into the flow physics at negligible computational cost. Additional proof of this is seen in the good agreement between our linear stability predictions and experimental results for compressibility and heat release effects shown in figures 1.5 through 1.7. The slight disagreement at very high compressibility levels in these figures could be the result of acoustic modes becoming dominant for the confined-geometry experiments, although there is insufficient data to confirm this.

1.4.2 Parabolized Stability Equations

The parabolized stability equations proposed by Herbert and Bertolotti (1987) form a newly-developed simulation tool that has shown great promise for the study of convectively-unstable flows (see Huerre and Monkewitz [1995] for a complete discussion of convective and absolute instabilities in free shear layers). The PSE technique offers the accuracy of nonlinear analysis at the low computational cost of stability methods. In short, it can be thought of as a technique that adds nonparallel and nonlinear modeling to linear stability theory. Thus, it provides an extremely useful analysis tool to bridge the considerable gap between linear stability methods and more refined large eddy or direct simulation techniques.

Although the technical details of this method were first widely reported in Bertolotti et al. (1992), the technique has evolved significantly from this point and recent papers offer a more useful discussion of the PSE method and some helpful insights into its implementation. Foremost among these is Herbert's AGARD Report (1994), which offers technical detail and discussion at a level appropriate for developing a PSE code. This report also offers a demonstration of results from several different applications, including boundary-layer computations, and receptivity and transition studies. Another very useful—though less technical—overview of the PSE technique and its applications by Herbert appears in his recent Annual Review article (1997).

The extension of the PSE approach to compressible calculations was first addressed by Bertolotti and Herbert (1991) in a brief communication on the calculation of supersonic boundary layers. A more detailed discussion of this subject later appeared in the ICASE report of Chang et al. (1993), who discussed both subharmonic and fundamental types of breakdown in a compressible flat-plate boundary layer with excellent comparison to DNS results. Part of this work simulating the oblique-mode breakdown at $M = 1.6$ was reported in Chang and Malik (1994).

The study of transition on a cone in Mach 8 flow by Pruett and Chang (1995) used

a combination of PSE and DNS methods. This complementary approach employed PSE to compute the weakly- and moderately-nonlinear stages of transition, providing a harmonically diverse and quantitatively accurate input condition for the DNS calculation, and significantly lowering the cost of simulating the later stages of transition. The flexibility of the PSE technique also allowed variation of the inlet disturbance magnitudes until good agreement with experimental results was obtained. Overlap regions between the DNS and PSE calculations also served to validate PSE results. The two methods offered excellent agreement through the weakly and moderately nonlinear stages of the calculation, although PSE predicted a slightly earlier transition point. This discrepancy is likely due to the breakdown of PSE assumptions, particularly concerning the mean-flow correction, as nonlinear interactions began to dominate the flow.

The first application (to this author's knowledge) of the PSE technique to a free shear layer was done by Malik and Chang (1997) in their calculation of a $M = 2.5$ supersonic jet. They used a combination of linear and nonlinear simulations to study pressure wave creation and helical-mode interactions. Yen and Messersmith (1998) also applied the PSE method to jet instabilities, although this study was limited to linear analysis of Reynolds and Strouhal number effect on instability amplification.

The present investigation constitutes the first application of the PSE approach to the study of both mixing layer and chemical reacting flows. Detailed discussion of our method and validation of its results against direct numerical simulation will be provided in sections 2.3 through 2.5 before results from the technique are discussed in chapter 4. Finally, appendix C addresses the details of the actual code and includes directions for its public availability.

1.5 Overview and Objectives

The primary objective of this work is to develop an understanding for the different flow structure regimes in the compressible reacting mixing layer. This direction was motivated by the opportunity to interact closely with a complementary experimental effort at Stanford University. This collaboration identified a need to investigate flow physics in the extensive parameter space of a new shock tube facility (Rossmann *et al.* 1999). Our specific research objectives are as follows:

- To conduct a comprehensive parametric study to identify the effect of different flow

conditions on the structure of the compressible reacting mixing layer.

- To determine which parameters dominate the creation and change of flow structure.

- To develop a complete understanding of how these parameters combine to cause a change in flow structure in different regimes of the parameter space.

- To study, in detail, the properties of these different modes with a focus on determining how the mixing mechanism changes with flow structure, and what possibilities exist to enhance the combustion performance in different regimes.

- To provide support to the experimental investigation by answering questions that are well suited to computational analysis.

1.5.1 Parameter Space

Our parameter space is extensive but by no means exhaustive: the effects of compressibility, heat release and the flow-stream ratios of density, equivalence, and velocity have been analyzed to determine how these parameters change the flow structure and what implications this has for mixing and combustion performance.

The effect of compressibility is parameterized by the convective Mach number, M_c (equation 1.1). Given the experimental evidence (see section 1.3.2) that questions the validity of the symmetric assumption that leads to the M_c definition, this parameter should be only viewed as a generalized measure of compressibility. The expression for M_c can be further simplified for flows of uniform molecular weight, $\mathcal{M}$, to yield

$$M_c = \frac{M_1\sqrt{\rho_2}(1 - U_2)}{1 + \sqrt{\rho_2}}, \tag{1.4}$$

where ρ is the density, M is the Mach number, the subscripts (1) and (2) refer to the fast and slow streams, and the variables have been nondimensionalized by their fast-stream values. The present study assumes a uniform composition, implying constant molecular weight and specific heat ratios throughout the layer. The uniform molecular weight assumption, although acknowledged as a simplification of the parameter space, is justified for the compressible reacting mixing layer experimental cases of Miller *et al.* (1998) where N_2 was used as the fuel-stream diluent. It does not agree, however, with their third case that used He as the diluent, although this case appears to be less realistic in practical applications.

The presence of combustion is modeled through a single-step chemical reaction

$$F + nO \rightarrow (n+1)P, \tag{1.5}$$

where n indicates the number of unit-masses of oxidizer that stoichiometrically react with one unit-mass of fuel. The amount of heat release imparted to the layer is measured through a nondimensionalized enthalpy of combustion (heat release parameter)

$$\Theta = \frac{-\Delta H_c^* Y_{f,-\infty}}{c_{p_1}^* \bar{T}_1^* (1+\phi)}, \tag{1.6a}$$

$$= \frac{-\left[(n+1)\Delta h_{f,p}^{*,o} - n\Delta h_{f,o}^{*,o} - \Delta h_{f,f}^{*,o}\right] Y_{f,-\infty}}{c_{p_1}^* \bar{T}_1^* (1+\phi)}, \tag{1.6b}$$

$$= T_f - 1, \tag{1.6c}$$

where ΔH_c^* is the enthalpy of combustion per unit mass of fuel, $Y_{f,-\infty}$ is the fuel mass fraction on the slow side, $c_{p_1}^*$ is the specific heat, $\Delta h_{f,k}^{*,o}$ is the enthalpy of formation for species k, and T_1^* the temperature on the fast side of the mixing layer. Under this definition, the heat release parameter has the concise relation to the adiabatic flame temperature, T_f, given in equation (1.6c) (Williams 1985). The equivalence ratio is also included in the Θ equation, and its definition is

$$\phi = \frac{(Y_{f,-\infty}/Y_{o,+\infty})_{\text{real}}}{(Y_{f,-\infty}/Y_{o,+\infty})_{\text{stoich}}} = \frac{nY_{f,-\infty}}{Y_{o,+\infty}}. \tag{1.7}$$

The remaining parameters of the investigation are the density and velocity ratios $s = \rho_2^*/\rho_1^*$ and $r = U_2^*/U_1^*$.

1.5.2 Overview

In broad terms, this investigation employs three different techniques. First, the density-weighted vorticity profile is used to provide basic understanding and prediction of flow structure. Then linear stability methods are utilized to develop a full appreciation for how this structure changes as a function of a large parameter space. And finally, the parabolized stability equations are applied to the detailed study of different flow structures to address issues of mixing and interaction. The numerical aspects of these techniques and their validation are provided in Chapter 2.

Chapter 3 presents results from a parametric study of the compressible reacting mixing layer using linear stability analysis. Our study focuses on how these parameters affect

the dominant flow structure of the mixing layer; regime charts are presented to provide a complete view of the structure change. Issues surrounding velocity ratio scaling of the amplification rate in compressible reacting conditions are also investigated.

A more detailed view of the flow structure is presented in Chapter 4 using results from a nonlinear analysis method, the parabolized stability equations. Details on the evolution and mixing of the different flow structures will be discussed. An analysis of colayer flows, where two modes are equally amplified, is presented to identify what capabilities exist for enhancing mixing and to determine how prevalent these modes are in practical flow configurations. Finally, the strong correlation between linear stability growth rates and the nonlinear phenomenon of vortex pairing will be demonstrated. This correspondence helps to explain why linear stability theory offers such an accurate prediction for the measured growth rates of fully turbulent mixing layers.

The conclusions drawn from these results are summarized in Chapter 5. In addition, recommendations and areas of interest for future investigations are outlined here.
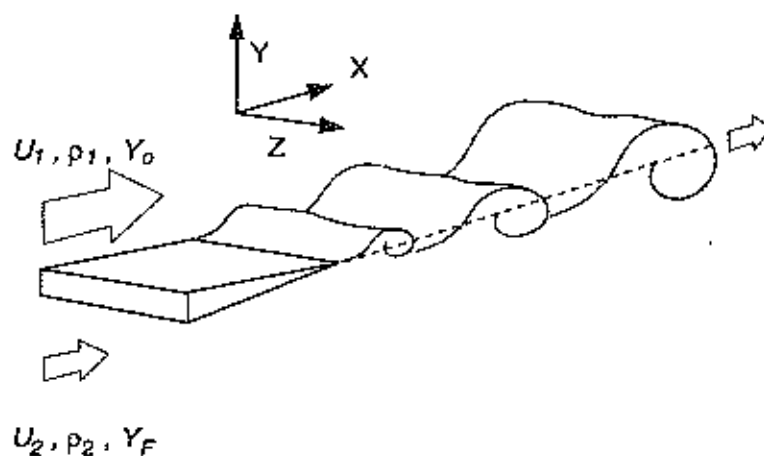
Figure 1.1: Schematic of the flow configuration with specified input conditions.

(a)

(b)
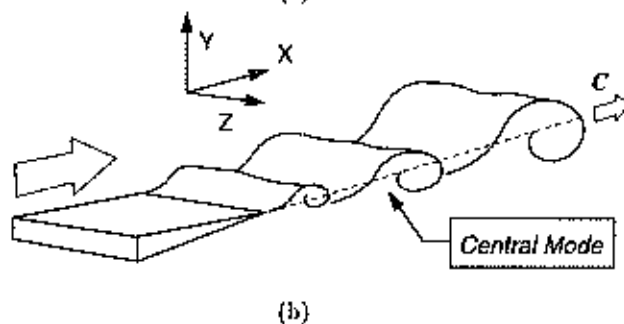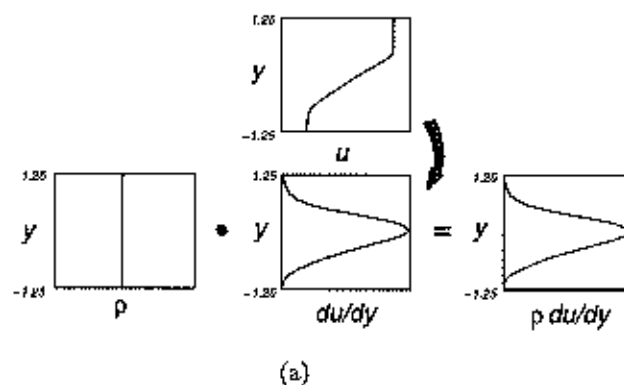
Figure 1.2: (a) Schematic of the incompressible nonreacting density-weighted vorticity profile that results in the central mode structure pictured in (b).

(a)

(b)
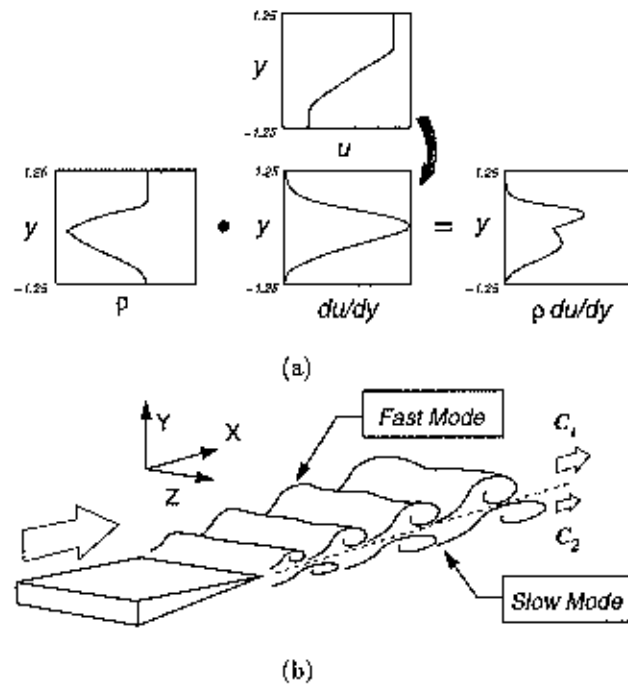
Figure 1.3: (a) Schematic of the compressible reacting density-weighted vorticity profile that results in the outer mode structure pictured in (b).

(a)

(b)
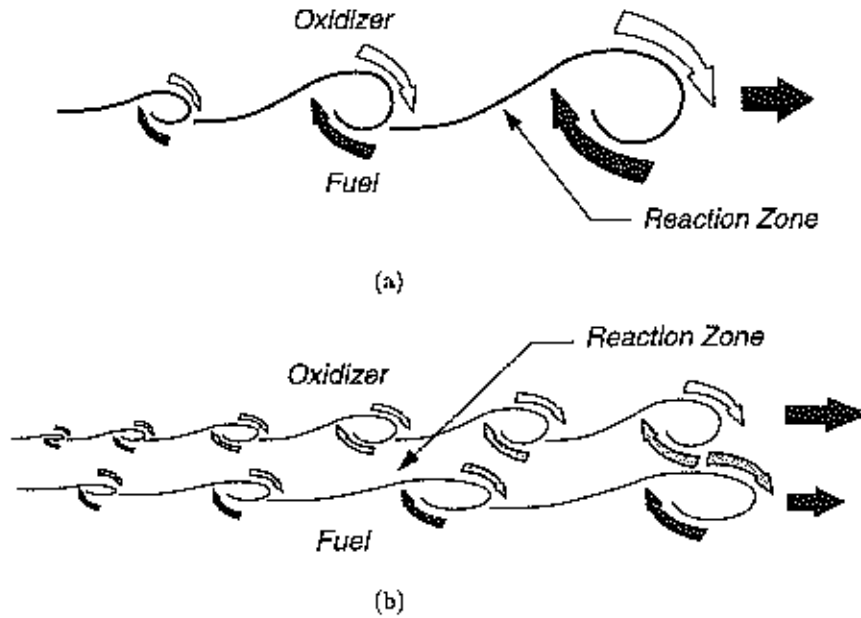
Figure 1.4: Schematic of the mixing mechanism in (a) central and (b) outer mode dominated flows.
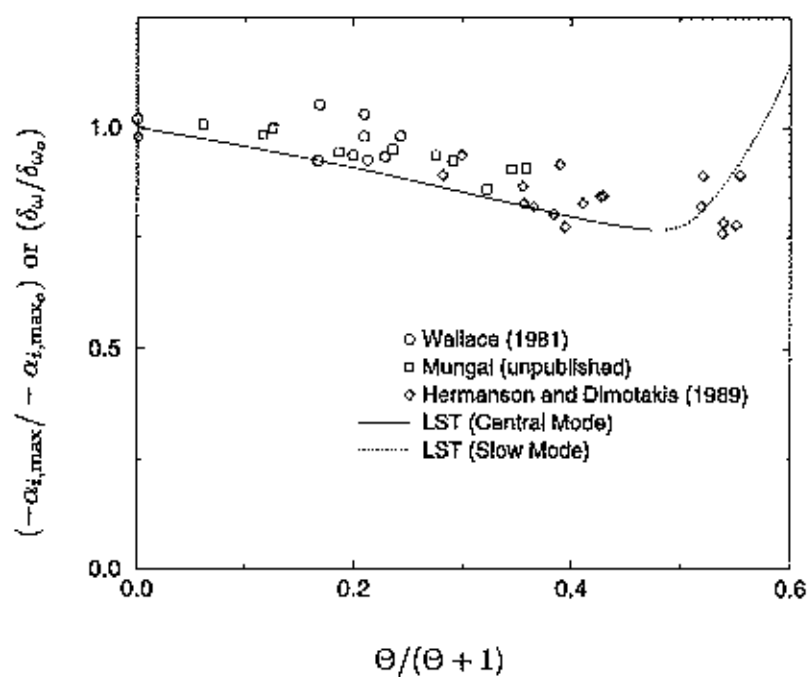
Figure 1.5: Comparison of the central mode linear stability prediction to experimental results for the effect of heat release on the normalized growth rate ($M_c = 0, s = 1, \phi = 1$). Experimental data assembled and described in Hermanson and Dimotakis (1989).
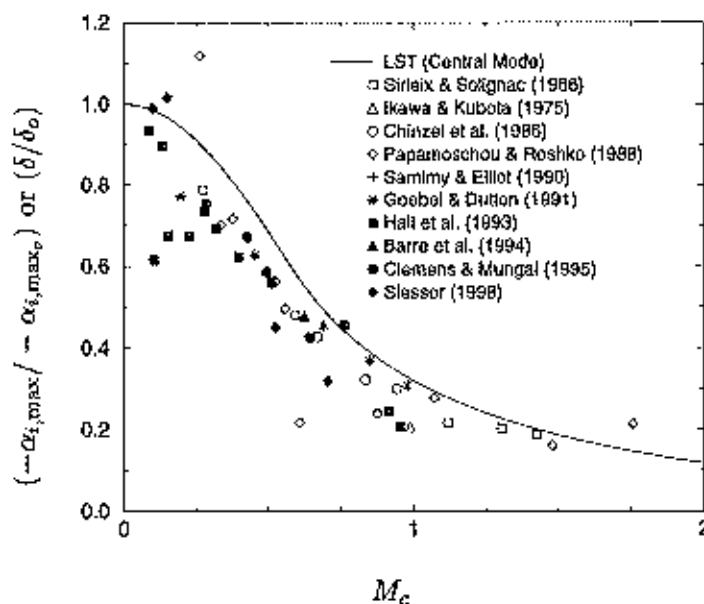
Figure 1.6: Comparison of the central mode linear stability prediction to experimental results for the effect of compressibility (parameterized by M_c) on the normalized growth rate ($\Theta = 0$). Experimental data assembled and presented in Slessor (1998).
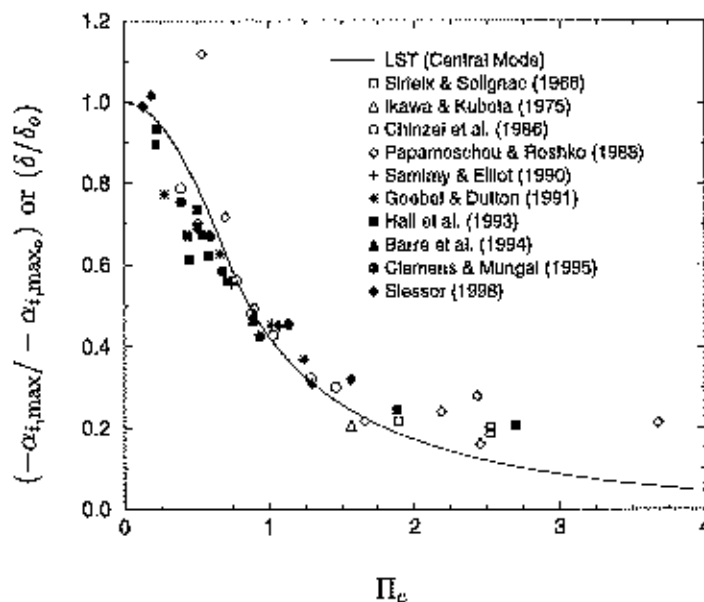
Figure 1.7: Comparison of the central mode linear stability prediction to experimental results for the effect of compressibility (parameterized by Π_c) on the normalized growth rate ($\Theta = 0$). Experimental data assembled and presented in Slessor (1998).

Chapter 2

Analytical Models and Solution Methods

This chapter offers a detailed discussion of the numerical methods that were applied to study compressible reacting mixing layers. The choice of numerical techniques was guided by this project's intent: to gain a broad understanding of the flow stability, structure, and mixing across a full parameter space. The first phase of this effort required an extensive parametric investigation, where the expanse of conditions to be studied demanded the use of the computationally cheap—although physically insightful—approach of linear stability theory (LST). This technique provides a fundamental understanding of the flow structure, but it understandably cannot predict the interaction of stability modes.

Building on the foundation of the LST parametric study, the second phase of the project required a nonlinear technique to study flow structure interaction and its implications on mixing. The parabolized stability equations (PSE) offer an excellent tool for this task by combining the low cost of a stability technique with the quantitative accuracy of a nonparallel, nonlinear method. This combination allows for a considerable advantage in flexibility over direct numerical or large eddy simulations within certain restrictions: the computations are limited to convectively unstable flows and can only be accurately carried to a moderately-nonlinear stage. A further advantage comes from the spatial nature of this stability method that, in comparison to temporal simulations, permits modeling velocity and density profile asymmetry.

This chapter will first consider the methodology for calculating solutions of the laminar mean flow which are required for both linear and parabolized stability methods. These solutions of the compressible boundary layer equations will be used in the development of linear stability theory in the next section. Finally, the chapter will close by addressing the evolution of the LST approach to incorporate both flow nonparallelism and nonlinearity in the PSE method.

2.1 Mean-Flow Development

This section outlines the governing equations for the mean flow and how they are manipulated to yield self-similar solutions for the mean velocity, density, temperature, and passive scalar profiles.

2.1.1 Mean-Flow Equations

Development of the mean-flow solution begins with the two-dimensional compressible boundary layer equations for laminar reacting flow. In dimensional form, the simplified equations for continuity, streamwise momentum, energy, species mass fraction, and the ideal gas equation of state are (Kuo, 1986)

$$\frac{\partial \rho^* u^*}{\partial x^*} + \frac{\partial \rho^* v^*}{\partial y^*} = 0, \tag{2.1a}$$

$$\rho^* \left(u^* \frac{\partial u^*}{\partial x^*} + v^* \frac{\partial u^*}{\partial y^*} \right) = -\frac{\partial p^*}{\partial x^*} + \frac{\partial}{\partial y^*} \left(\mu^* \frac{\partial u^*}{\partial y^*} \right), \tag{2.1b}$$

$$\rho^* \left(u^* \frac{\partial h_t^*}{\partial x^*} + v^* \frac{\partial h_t^*}{\partial y^*} \right) = \frac{\partial}{\partial y^*} \left\{ \frac{\mu^*}{Pr} \left[\frac{\partial h_t^*}{\partial y^*} + (Pr - 1) \frac{\partial (u^{*2}/2)}{\partial y^*} \right. \right.$$
$$\left. \left. + \frac{\partial}{\partial y^*} \sum_{k=1}^{K} (Le_k^{-1} - 1) h_k^* \frac{\partial Y_k}{\partial y^*} \right] \right\}, \tag{2.1c}$$

$$\rho^* \left(u^* \frac{\partial Y_k}{\partial x^*} + v^* \frac{\partial Y_k}{\partial y^*} \right) = \frac{\partial}{\partial y^*} \left(\frac{\mu^*}{Pr Le_k} \frac{\partial Y_k}{\partial y^*} \right) + \dot{w}_k^*, \tag{2.1d}$$

$$p^* = \rho^* R^* T^*, \tag{2.1e}$$

where * denotes a dimensional quantity; x^* and y^* are the streamwise and normal coordinate directions; u^* and v^* are the velocity components in those directions; ρ^*, p^* and T^* are the density, pressure, and temperature, respectively; μ^* is the viscosity; Y_k is the mass fraction of species k, where k is one of oxidizer, fuel or product, and the sum of k's is K; $\dot{w}_k$ is the time rate of production of species k; and R^* is the gas constant. Further, the Lewis and Prandtl numbers are defined as

$$Le_k = \frac{\lambda_c^*}{\rho^* D_k^* c_p^*} \quad \text{and} \quad Pr = \frac{c_p^* \mu^*}{\lambda_c^*}, \tag{2.2}$$

where D_k^* is the diffusivity of the species k, c_p^* the specific heat at constant pressure, and λ_c^* the conductivity. The energy equation (2.1c) is cast in terms of the total enthalpy h_t^*

that encompasses both internal and kinetic forms of energy with the definition

$$h_t^* = \sum_{k=1}^{K} Y_k h_k^* + u^{*2}/2, \tag{2.3}$$

where the internal contribution is further subdivided into sensible and chemical components

$$h_k^* = \int_{T_o^*}^{T^*} c_{p,k}^* dT^* + \Delta h_{f,k}^{*o}. \tag{2.4}$$

These equations were nondimensionalized with the respective fast-stream value (denoted by the subscript 1) for all flow variables. The length scale was chosen to be the initial vorticity thickness,

$$\delta_{\omega_o}^* = \frac{U_1^* - U_2^*}{d\bar{u}^*/dy_{max,o}^*}. \tag{2.5}$$

This normalization procedure gives

$$u = \frac{u^*}{U_1^*}, \quad \rho = \frac{\rho^*}{\rho_1^*}, \quad T = \frac{T^*}{T_1^*}, \quad p = \frac{p^*}{p_1^*}, \quad h_t = \frac{h_t^*}{U_1^{*2}}, \quad t = \frac{t*U_1^*}{\delta_{\omega_o}^*}. \tag{2.6}$$

These parameters result in a reference Reynolds number defined as

$$Re_o = \frac{\rho_1^* u_1^* \delta_{\omega_o}}{\mu_1^*}. \tag{2.7}$$

The equations are further simplified by assuming unity Prandtl and Lewis numbers, and negligible streamwise pressure gradient to yield the nondimensional system

$$\frac{\partial \rho u}{\partial x} + \frac{\partial \rho v}{\partial y} = 0, \tag{2.8a}$$

$$\rho u \frac{\partial u}{\partial x} + \rho v \frac{\partial u}{\partial y} = \frac{1}{Re_o} \frac{\partial}{\partial y} \left(\mu \frac{\partial u}{\partial y} \right), \tag{2.8b}$$

$$\rho u \frac{\partial h_t}{\partial x} + \rho v \frac{\partial h_t}{\partial y} = \frac{1}{Re_o} \frac{\partial}{\partial y} \left(\mu \frac{\partial h_t}{\partial y} \right), \tag{2.8c}$$

$$\rho u \frac{\partial Y_k}{\partial x} + \rho v \frac{\partial Y_k}{\partial y} = \frac{1}{Re_o} \frac{\partial}{\partial y} \left(\mu \frac{\partial Y_k}{\partial y} \right) + \dot{w}_k, \tag{2.8d}$$

$$\rho RT = 1. \tag{2.8e}$$

The derivation of the mean profiles in a similarity form requires the chemistry to be simplified down to a single step of the form

$$F + nO \rightarrow (n+1)P, \tag{2.9}$$
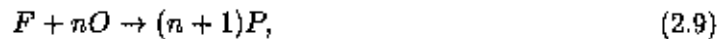
where n represents the mass of oxidizer that stoichiometrically reacts with one unit-mass of fuel to produce $n + 1$ unit masses of product. The passive scalar Z is defined as

$$Z = Y_f - Y_o/n. \tag{2.10}$$

Under the assumption of infinitely-fast chemistry, it follows that fuel and oxidizer cannot co-exist and that all chemical reaction is confined to a single point in a one-dimensional profile, and a line in two or a surface in three dimensions. With this assumption the species equation can be expressed in passive scalar form as

$$\rho u \frac{\partial Z}{\partial x} + \rho v \frac{\partial Z}{\partial y} = \frac{1}{Re_o} \frac{\partial}{\partial y}\left(\mu \frac{\partial Z}{\partial y}\right). \tag{2.11}$$

Finally, the stream function definition for compressible flow is

$$\rho u = \frac{\partial \psi}{\partial y} \quad \text{and} \quad \rho v = -\frac{\partial \psi}{\partial x}, \tag{2.12}$$

which implicitly satisfies continuity and eliminates equation (2.8a), and can be used to simplify the system. These definitions recast the equations for the conservation of momentum, species (passive scalar), and energy as

$$\frac{\partial \psi}{\partial y}\frac{\partial u}{\partial x} - \frac{\partial \psi}{\partial x}\frac{\partial u}{\partial y} = \frac{1}{Re_o}\frac{\partial}{\partial y}\left(\mu \frac{\partial u}{\partial y}\right), \tag{2.13a}$$

$$\frac{\partial \psi}{\partial y}\frac{\partial Z}{\partial x} - \frac{\partial \psi}{\partial x}\frac{\partial Z}{\partial y} = \frac{1}{Re_o}\frac{\partial}{\partial y}\left(\mu \frac{\partial Z}{\partial y}\right), \tag{2.13b}$$

$$\frac{\partial \psi}{\partial y}\frac{\partial h_t}{\partial x} - \frac{\partial \psi}{\partial x}\frac{\partial h_t}{\partial y} = \frac{1}{Re_o}\frac{\partial}{\partial y}\left(\mu \frac{\partial h_t}{\partial y}\right). \tag{2.13c}$$

2.1.2 Similarity Solutions

A similarity solution can be found by first introducing Howarth's coordinate transformations (Schlichting, 1979)

$$\varsigma = x \quad \text{and} \quad \eta = \sqrt{\frac{Re_o}{2x}} \int_0^y \rho \, dy. \tag{2.14}$$

Then, by assuming that the mixing layer is fully developed and that quantities are only dependent on η, the stream function, passive scalar, and total enthalpy have the form

$$\psi(x, y) = \sqrt{\frac{2x}{Re_o}} F(\eta), \quad Z(x, y) = Z(\eta), \quad \text{and} \quad h_t(x, y) = h_t(\eta). \tag{2.15}$$

In this form the streamwise evolution is contained only in the streamfunction, and its appearance in the energy and passive scalar equations then defines the evolution of these quantities explicitly. After substitution into equations (2.13a) to (2.13c) and simplification, the governing system takes the form

$$\left(\frac{\mu}{T}F''\right)' + FF'' = 0, \tag{2.16a}$$

$$\left(\frac{\mu}{T}Z'\right)' + FZ' = 0, \tag{2.16b}$$

$$\left(\frac{\mu}{T}h_t'\right)' + Fh_t' = 0, \tag{2.16c}$$

where $'$ denotes differentiation with respect to η. The additional, but not required, assumption that the nondimensional viscosity and temperature are linearly related yields the further-simplified form

$$F''' + FF'' = 0, \tag{2.17a}$$

$$Z'' + FZ' = 0, \tag{2.17b}$$

$$h_t'' + Fh_t' = 0. \tag{2.17c}$$

This system of equations was solved using the shooting method of Sandham (1989) with some refinements and additions that will be outlined here. Obtaining the solution for F is the first step, and it must satisfy the boundary conditions

$$F'(\infty) = U_1, \tag{2.18a}$$

$$F(0) = 0, \tag{2.18b}$$

$$F'(-\infty) = U_2, \tag{2.18c}$$

where the second condition comes from specifying $v = 0$ at the centerline, and U_1 and U_2 are the nondimensional velocities in the fast and slow streams. The shooting method is as follows.

- Guess $F'(0)$ and $F''(0)$. Setting $F'(0)$ equal to the mean velocity and $F''(0) = 0.1$ were found to be robust guesses.

- Integrate F to $\eta = \infty$ using a variable step, fifth-order Runge Kutta method from Press *et al.* (1992). The approximation $\infty = 15\delta_{\omega_o}$ was found to be more than sufficient.

- Exploit the invariance of equation (2.17a) to the transform $\check{F}(a\eta) = F(\eta)/a$ to make the three-point boundary value problem tractable. Set the constant a equal to $F(\infty)$ and recast equation (2.17a) in $\check{F}$ so that boundary conditions (2.18a) and (b) are directly satisfied.

- Integrate $\check{F}$ to $\eta = -\infty$ using $\check{F}(0) = 0$, $\check{F}'(0) = F'(0)/a$, and $\check{F}''(0) = F''(0)/a$.

- Compare $\check{F}(-\infty)$ to U_2 (the boundary condition 2.18c) and use a secant method to force agreement within a tolerance of 10^{-8} by adjusting $F''(0)$.

This procedure will drive a towards unity, but it will not reach this goal unless $F'(0)$ is also allowed to vary. And additional, outer iteration loop adds this capability.

- Repeat the secant iteration loop with $F'(0)$ set to the final value of $\check{F}'(0)$ in the previous iteration. Continue the outer iteration until $a = 1$ is satisfied within a 10^{-6} tolerance.

This dual-iteration procedure yields $F(\eta)$, which can then be used to obtain $h_t(\eta)$ and $Z(\eta)$ from equations (2.17b) and (2.17c) following the method of Planché (1992). These solutions can be arrived at in one shot because both equations are linear. For example, the invariance $\check{Z} = bZ + c$ can be used to satisfy the two boundary conditions

$$Z(\infty) = Y_f \quad \text{and} \quad Z(-\infty) = -Y_o/n. \tag{2.19}$$

The solution for h_t follows exactly the same procedure with the boundary conditions

$$h_t(\infty) = \frac{\gamma R T_1}{(\gamma - 1)M_1} + Y_{o,\infty}\Delta h_{f,o}^o + U_1^2/2, \tag{2.20a}$$

$$h_t(-\infty) = \frac{\gamma R T_2}{(\gamma - 1)M_1} + Y_{f,-\infty}\Delta h_{f,f}^o + U_2^2/2. \tag{2.20b}$$

These equations are nondimensionalized by u_1^2, and appear with the assumption of constant specific heats, $\gamma = \gamma_1 = \gamma_2 = 1.4$, and uniform molecular mass, $\mathcal{M}$, in the mixing layer. The latter assumption yields a uniform gas constant and, more importantly, a reciprocal relationship between ρ and T through the ideal gas equation and the thin-shear-layer assumption of uniform pressure.

After the solutions for $F(\eta)$, $h_t(\eta)$, and $Z(\eta)$ were obtained, the $Y_k(\eta)$ profiles were found from the passive scalar definition (equation 2.10). The mean velocity, passive scalar, and

temperature profiles were evaluated as

$$u(x,y) \;=\; F'(\eta), \tag{2.21a}$$

$$v(x,y) \;=\; \frac{1}{\rho(\eta)}\sqrt{\frac{2x}{Re_o}}\left[\eta F'(\eta) - F(\eta)\right], \tag{2.21b}$$

$$Z(x,y) \;=\; Z(\eta), \tag{2.21c}$$

$$T(x,y) \;=\; \left(h_t(\eta) - Y_f \Delta h^o_{ff} - Y_o, \Delta h^o_{fo} - u^2(\eta)/2\right)/c_p. \tag{2.21d}$$

The heats of formation were determined from equation (1.6c) for a prescribed value of Θ with the assumption that the chemical reference species included both the product and oxidizer, and hence $h^o_{f,f}$ is the only nonzero contribution to ΔH_c.

2.1.3 Streamwise Derivatives

The streamwise evolution of mean-flow quantities was obtained by taking the x derivative of the equations (2.21a) through (2.21d). Applying the chain rule to equation (2.21a), for example, yields

$$\frac{\partial u}{\partial x}(x,y) = \frac{\partial u}{\partial \eta}\frac{\partial \eta}{\partial x} + \frac{\partial u}{\partial \varsigma}\frac{\partial \varsigma}{\partial x}, \tag{2.22}$$

where the second term drops out because $u(x,y) = u(\eta)$. Applying this procedure to each equation yields

$$\frac{\partial u}{\partial x}(x,y) \;=\; F''\,\frac{\partial \eta}{\partial x}, \tag{2.23a}$$

$$\frac{\partial v}{\partial x}(x,y) \;=\; \sqrt{\frac{1}{2xRe_o}}\left[T'(\eta)\big(\eta F'(\eta) - F(\eta)\big) + \eta T(\eta)F''(\eta)\right]\frac{\partial \eta}{\partial x}, \tag{2.23b}$$

$$\frac{\partial Z}{\partial x}(x,y) \;=\; Z'\,\frac{\partial \eta}{\partial x} \tag{2.23c}$$

$$\frac{\partial T}{\partial x}(x,y) \;=\; \left[\frac{h'_t - Y'_f \Delta h^o_{ff} - Y'_o \Delta h^o_{fo} - F'F''}{c_p}\right]\frac{\partial \eta}{\partial x}, \tag{2.23d}$$

The evaluation of $\partial \eta/\partial x$ requires some development. Consider the coordinate transformation Jacobian and its inverse

$$\boldsymbol{J} = \begin{bmatrix} \varsigma_x & \varsigma_y \\ \eta_x & \eta_y \end{bmatrix} \quad \text{and} \quad \boldsymbol{J}^{-1} = \begin{bmatrix} x_\varsigma & x_\eta \\ y_\varsigma & y_\eta \end{bmatrix}. \tag{2.24}$$

Their product is defined by

$$JJ^{-1} = \begin{bmatrix} \varsigma_x x_\varsigma + \varsigma_y y_\varsigma & \varsigma_x x_\eta + \varsigma_y y_\eta \\ \eta_x x_\varsigma + \eta_y y_\varsigma & \eta_x x_\eta + \eta_y y_\eta \end{bmatrix} = \begin{bmatrix} 1 & 0 \\ 0 & 1 \end{bmatrix}, \tag{2.25}$$

and this yields the relation

$$\frac{\partial \eta}{\partial x}\frac{dx}{d\varsigma} + \frac{\partial \eta}{\partial y}\frac{\partial y}{\partial \varsigma} = 0. \tag{2.26}$$

Using the definitions of ς and η from equation (2.14), this can be expressed as

$$\frac{\partial \eta}{\partial x} = -\rho\sqrt{\frac{Re_o}{2x}}\,\frac{\partial y}{\partial \varsigma}. \tag{2.27}$$

Evaluation of $\partial y/\partial \varsigma$ can be determined from

$$\frac{\partial \eta}{\partial \varsigma} = 0 = \frac{\partial}{\partial \varsigma}\left(\sqrt{\frac{Re_o}{2x}}\int_0^y \rho\,dy\right), \tag{2.28}$$

or

$$\frac{\partial y}{\partial \varsigma} = \sqrt{\frac{2x}{Re_o}}\,\frac{\eta}{2\rho x}. \tag{2.29}$$

A combination of equations (2.27) and (2.29) then provides

$$\frac{\partial \eta}{\partial x} = -\frac{\eta}{2x}. \tag{2.30}$$

Using this expression in equations (2.23a) and (2.23d) provides the tractable form

$$\frac{\partial u}{\partial x}(x,y) = -\frac{\eta F''}{2x}, \tag{2.31a}$$

$$\frac{\partial v}{\partial x}(x,y) = -\eta\sqrt{\frac{1}{8x^3 Re_o}}\left[T'(\eta)\big(\eta F'(\eta) - F(\eta)\big) + \eta T(\eta)F''(\eta)\right], \tag{2.31b}$$

$$\frac{\partial Z}{\partial x}(x,y) = -\frac{\eta Z'}{2x} \tag{2.31c}$$

$$\frac{\partial T}{\partial x}(x,y) = -\frac{\eta\big(h'_t - Y'_f\Delta h^o_{ff} - Y'_o\Delta h^o_{fo} - F'F''\big)}{2x\,c_p}. \tag{2.31d}$$

Finally, to return to the original coordinate system, Howarth's transform was reversed by integrating

$$\frac{dy}{d\eta} = \sqrt{\frac{2x_o}{Re_o}}\,\frac{1}{\bar{\rho}(\eta)} \quad \text{with} \quad y(0) = 0 \tag{2.32}$$

where x_o, the distance from the virtual origin, is determined for a given Re_o by the condition that $\delta_{\omega_o} = 1$. Results will be presented in terms of $x = x' - x_o$, where x' originates at the virtual origin.

2.2 Linear Stability Theory

This section outlines the methodology for a linear stability analysis of the compressible reacting mixing layer. The analysis begins with the development of equations that govern the linear growth of flow-field disturbances. A general form for disturbances is then chosen—in this case a three-dimensional traveling wave—and the system of linearized equations is reduced to an eigenvalue problem. The solution of this problem yields eigenvalues and eigenfunctions that provide fundamental insight into the growth rate, length and time scales, velocity, and three dimensionality of flow disturbances. In summary, this method provides fundamental, qualitative insight into the flow structure at the negligible computational cost of solving an eigenvalue problem.

2.2.1 Linear Disturbance Equations

The simulation and analysis of compressible reacting flow requires solution of the continuity, momentum, energy, species, and state equations. In this investigation, these equations were simplified by assuming that the flow is inviscid. This simplification is physically justified by the inviscid nature of the Kelvin-Helmholtz instability and has been numerically validated in the viscous stability calculations of Ragab and Wu (1989), where results were shown to be independent of Reynolds number for $Re > 1000$.

It follows that the Euler equations, obtained by dropping the diffusion terms from the Navier-Stokes equations, can be used as the starting point for the linear stability analysis. The dimensional Euler equations for continuity, momentum, passive scalar (species), and total enthalpy are (Kuo, 1986)

$$\frac{\partial \rho^*}{\partial t^*} + \frac{\partial \rho^* u_i^*}{\partial x_i^*} = 0, \tag{2.33a}$$

$$\rho^* \left(\frac{\partial u_i^*}{\partial t^*} + u_j^* \frac{\partial u_i^*}{\partial x_j^*} \right) = -\frac{\partial p^*}{\partial x_i^*}, \tag{2.33b}$$

$$\rho^* \left(\frac{\partial Z}{\partial t^*} + u_j^* \frac{\partial Z}{\partial x_j^*} \right) = 0, \tag{2.33c}$$

$$\rho^* \left(\frac{\partial h_t^*}{\partial t^*} + u_j^* \frac{\partial h_t^*}{\partial x_j^*} \right) = \frac{\partial p^*}{\partial t^*}. \tag{2.33d}$$

And for ideal compressible fluids the perfect gas law

$$p^* = \rho^* R^* T^* \tag{2.34}$$

can be applied as the state relation to close the system of equations. Using the definition of h_t^*, the perfect gas law, and the continuity equation, the energy equation (2.33d) can be recast as

$$\rho^*(c_p^* - R^*)\left(\frac{\partial T^*}{\partial t^*} + u_j^*\frac{\partial T^*}{\partial x_j^*}\right) + \rho^* T^*\left(\frac{\partial c_p^*}{\partial t^*} + u_j^*\frac{\partial c_p^*}{\partial x_j^*}\right) = -p^*\frac{\partial u_i^*}{\partial x_i^*}. \qquad (2.35)$$

With the assumption of constant specific heats to this can be further simplified to

$$\rho^*\left(\frac{\partial T^*}{\partial t^*} + u_j^*\frac{\partial T^*}{\partial x_j^*}\right) = \frac{-p^*(\gamma - 1)}{R^*}\frac{\partial u_i^*}{\partial x_i^*}. \qquad (2.36)$$

Nondimensionalization was done with reference variables from the fast side of the layer and the initial vorticity thickness, which is consistent with the mean-flow derivation of section 2.1.1. The nondimensional system of governing equations then becomes

$$\frac{\partial \rho}{\partial t} + \frac{\partial \rho u_i}{\partial x_i} = 0, \qquad (2.37a)$$

$$\rho\left(\frac{\partial u_i}{\partial t} + u_j\frac{\partial u_i}{\partial x_j}\right) = -\frac{1}{\gamma_1 M_1^2}\frac{\partial p}{\partial x_i}, \qquad (2.37b)$$

$$\rho\left(\frac{\partial Z}{\partial t} + u_j\frac{\partial Z}{\partial x_j}\right) = 0, \qquad (2.37c)$$

$$\rho\left(\frac{\partial T}{\partial t} + u_j\frac{\partial T}{\partial x_j}\right) = -p(\gamma - 1)\frac{\partial u_i}{\partial x_i}, \qquad (2.37d)$$

$$p = \rho T, \qquad (2.37e)$$

where, similar to the development of the mean flow, the assumption of constant molecular weight has been made.

With the governing system established, the development of the linear disturbance equations can be addressed. This procedure begins with the decomposition of all physical variables into their mean and fluctuating parts, where the mean components correspond to the laminar solutions that were developed in the previous section. The flow is assumed to be quasi-parallel, i.e. mean velocities in the cross-stream and spanwise directions, $\bar{v}$ and $\bar{w}$, are neglected, leaving only a contribution in the streamwise direction. Consistent with the high Reynolds number assumption, the slow streamwise variation of mean-flow quantities is neglected and a one-dimensional solution in y results. Finally, the pressure is assumed to be uniform throughout the mixing layer and therefore it has a normalized mean value of

unity. With these restrictions, the decompositions become

$$
\begin{aligned}
\rho &= \bar{\rho} + \tilde{\rho}, & u &= \bar{u} + \hat{u}, \\
T &= \bar{T} + \tilde{T}, & v &= \tilde{v}, \\
p &= 1 + \tilde{p}, & w &= \tilde{w}, \\
Z &= \bar{Z} + \tilde{Z},
\end{aligned}
\tag{2.38}
$$

where $\bar{()}$ and $\tilde{()}$ denote mean and fluctuating quantities, respectively.

The process of substituting these decompositions into the governing equations, eliminating the terms that satisfy the averaged equations, and neglecting nonlinear terms yields the following system of linearized disturbance equations

$$
\frac{\partial \tilde{\rho}}{\partial t} + \tilde{\rho}\frac{\partial \bar{u}_i}{\partial x_i} + \tilde{u}_i\frac{\partial \bar{\rho}}{\partial x_i} + \bar{\rho}\frac{\partial \tilde{u}_i}{\partial x_i} + \bar{u}_i\frac{\partial \tilde{\rho}}{\partial x_i} = 0,
\tag{2.40a}
$$

$$
\bar{\rho}\frac{\partial \tilde{u}_i}{\partial t} + \tilde{\rho}\frac{\partial \bar{u}_i}{\partial t} + (\tilde{\rho}\bar{u}_j + \bar{\rho}\tilde{u}_j)\frac{\partial \bar{u}_i}{\partial x_j} + \bar{\rho}\bar{u}_j\frac{\partial \tilde{u}_i}{\partial x_j} = -\frac{\partial \tilde{p}}{\partial x_i},
\tag{2.40b}
$$

$$
\bar{\rho}\frac{\partial \tilde{Z}}{\partial t} + \tilde{\rho}\frac{\partial \bar{Z}}{\partial t} + (\tilde{\rho}\bar{u}_i + \bar{\rho}\tilde{u}_i)\frac{\partial \bar{Z}}{\partial x_i} + \bar{\rho}\bar{u}_i\frac{\partial \tilde{Z}}{\partial x_i} = 0,
\tag{2.40c}
$$

$$
\bar{\rho}\frac{\partial \tilde{T}}{\partial t} + \tilde{\rho}\frac{\partial \bar{T}}{\partial t} + (\bar{\rho}\tilde{u}_i + \tilde{\rho}\bar{u}_i)\frac{\partial \bar{T}}{\partial x_i} + \bar{\rho}\bar{u}_i\frac{\partial \tilde{T}}{\partial x_i} = -(\gamma-1)\left(\hat{p}\frac{\partial \bar{u}_i}{\partial x_i}, +\bar{p}\frac{\partial \tilde{u}_i}{\partial x_i}\right)
\tag{2.40d}
$$

$$
\tilde{p} = \bar{\rho}\tilde{T} + \bar{\rho}\tilde{T}.
\tag{2.40e}
$$

Note that there is no mechanism in these equations to account for density variations caused by chemical reaction and heat release. This is in keeping with the results of Shin and Ferziger (1991), who showed that it this coupling has a negligible effect on stability results.

2.2.2 Eigenvalue Problem Development

The fluctuating components are modeled with the general form of three-dimensional traveling waves,

$$
[\tilde{u}, \tilde{T}, \tilde{p}, \tilde{v}, \tilde{w}, \tilde{\rho}, \tilde{Z}](x,y,z,t) = \epsilon_o\,[\hat{u}, \hat{T}, \hat{p}, \hat{v}, \hat{w}, \hat{\rho}, \hat{Z}](y)\,e^{i(\alpha x + \beta z - \omega t)} + c.c.,
\tag{2.41}
$$

where ϵ_o is the initial amplitude of the disturbance; $\hat{u}, \hat{T}, \hat{p}, \hat{v}, \hat{w}, \hat{\rho}$, and $\hat{Z}$ are complex eigenfunctions dependent only on y; α and β are the complex wavenumbers in the streamwise and spanwise directions; ω is the disturbance frequency; and it *c.c.* denotes the complex conjugate which is included to make sure that the left hand side is real valued. For the spatial stability analysis conducted in this investigation, disturbances grow in space and

not in time and thus we considerer the case where ω is purely real and α complex. The converse is true for temporal analysis: disturbances are allowed to grow in time but not in space by requiring α to be purely real and ω complex. The spanwise wavenumber β is required to be real in order to prevent waves from amplifying as $z \to \pm\infty$. It is related to the streamwise wavenumber α through simple geometry,

$$\tan\theta = \frac{\beta}{\alpha_r}, \tag{2.42}$$

where θ is the oblique angle of the disturbance with respect to the streamwise direction. Three-dimensional disturbances are equally likely to travel at positive and negative values of θ.

Substituting the traveling wave model of equation (2.41) into the linearized disturbance equations yields the system

$$\hat{\rho}i(\alpha\overline{u} - \omega) + \hat{v}\overline{\rho}' + \overline{\rho}[i(\alpha\hat{u} + \beta\hat{w}) + \hat{v}'] = 0, \tag{2.43a}$$

$$\overline{\rho}[i(\alpha\overline{u} - \omega)\hat{u} + \hat{v}\overline{u}'] = \frac{-i\alpha\hat{p}}{\gamma_1 M_1^2}, \tag{2.43b}$$

$$\overline{\rho}i(\alpha\overline{u} - \omega)\hat{v} = \frac{-\hat{p}'}{\gamma_1 M_1^2}, \tag{2.43c}$$

$$\overline{\rho}i(\alpha\overline{u} - \omega)\hat{w} = \frac{-i\beta\hat{p}}{\gamma_1 M_1^2} \tag{2.43d}$$

$$\overline{\rho}[i(\alpha\overline{u} - \omega)\hat{Z} + \hat{v}\overline{Z}'] = 0, \tag{2.43e}$$

$$\overline{\rho}[i(\alpha\overline{u} - \omega)\hat{T} + \hat{v}\overline{T}'] = -(\gamma - 1)[i(\alpha\hat{u} + \beta\hat{w}) + \hat{v}'], \tag{2.43f}$$

$$\hat{p} = \overline{\rho}\hat{T} + \hat{\rho}\overline{T} \tag{2.43g}$$

where ()' denotes the operator d/dy. Algebraic reduction of this system begins by multiplying the linearized continuity equation (2.43a) by $\overline{T}$ before adding it to the energy equation (2.43f). The uniform pressure assumption gives $\partial\overline{p}/\partial y = 0$, i.e. $\overline{\rho}'\overline{T} + \overline{\rho}\overline{T}' = 0$, allowing the resulting expression to be written as

$$i(\alpha\overline{u} - \omega)[\hat{\rho}\overline{T} + \overline{\rho}\hat{T}] = -[i(\alpha\hat{u} + \beta\hat{w}) + \hat{v}']\gamma, \tag{2.44}$$

which can be further simplified with equation (2.43g) to give an equation in $\hat{p}$,

$$i(\alpha\overline{u} - \omega)\hat{p} = -[i(\alpha\hat{u} + \beta\hat{w}) + \hat{v}']\gamma. \tag{2.45}$$

Equations (2.43b) and (2.43d) are then used to eliminate $\hat{u}$ and $\hat{w}$ from equation (2.45). This result and the linearized v momentum equation (2.43c) together form a coupled set of

two ordinary differential equations in $\hat{v}$ and $\hat{p}$

$$(\overline{u} - c)\hat{v}' - \hat{v}\overline{u}' = \frac{i\alpha g \hat{p}}{\gamma_1 M_1^2}, \tag{2.46}$$

$$\overline{\rho}\alpha(\overline{u} - c)\hat{v} = \frac{i\hat{p}'}{\gamma_1 M_1^2}, \tag{2.47}$$

where g is defined as

$$g = \frac{1 + (\beta/\alpha)^2}{\overline{\rho}} - \frac{\gamma_1}{\gamma}M_1^2(\overline{u} - c)^2, \tag{2.48}$$

and c is the complex velocity (the real part of which is the phase speed)

$$c = \frac{\omega}{\alpha}. \tag{2.49}$$

For the purpose of recovering both the eigenvalue and eigenfunctions it is preferable (see section 2.2.4) to directly use this coupled set of equations. However, in the more common situation where interest lies in the growth rate, $-\alpha_i$, only the eigenvalue needs to be calculated. For this task it is computationally more efficient to reduce the coupled system to a single equation through the method of Gropengiesser (1970). This approach introduces the composite variable

$$\chi = \frac{i\alpha \hat{p}}{\gamma M_1^2 \hat{v}}, \tag{2.50}$$

which allows equations (2.46) and (2.47) to be combined into the following first order, nonlinear ODE

$$\chi' = \frac{\gamma_1}{\gamma}\,\overline{\rho}\alpha^2(\overline{u} - c) - \frac{\chi(\frac{\gamma}{\gamma_1}\chi g + \overline{u}')}{\overline{u} - c}. \tag{2.51}$$

The appropriate boundary conditions can be developed by evaluating the asymptotic behavior of equations (2.46) and (2.47) in the free stream, where $\overline{u}'$ is zero. With this simplification as $y \to \pm\infty$, the coupled set of equations become

$$\hat{v}'' = \overline{\rho}\alpha^2 g\hat{v} \tag{2.52}$$

$$\hat{p}'' = \overline{\rho}\alpha^2 g\hat{p} \tag{2.53}$$

It is clear from these equations that both $\hat{v}$ and $\hat{p}$ will decay with the same exponential form $e^{\mp\alpha\sqrt{\overline{\rho}g}y}$ in the two free streams. Therefore, the composite variable χ goes to a constant

as $y \to \pm\infty$. Setting χ' and $\bar{u}'$ equal to zero in equation (2.51) provides the appropriate free-stream boundary conditions

$$\chi(y = \pm\infty) = \mp\sqrt{\bar{\rho}/g}\,\alpha(\bar{u} - c), \tag{2.54}$$

where the signs are specified such that $q_r > 0$, where $q = q_r + iq_i = \alpha\sqrt{\bar{\rho}g}$ (Gropengiesser, 1970).

Note that equation (2.51) was derived without the assumption of a constant specific heat ratio. Consistent with the mean-flow derivation, this assumption was made and it results in equation (2.51) simplifying to the original Gropengiesser formulation

$$\chi' = \frac{\alpha^2(\bar{u} - c)}{\bar{T}} - \frac{\chi(\chi g + \bar{u}')}{\bar{u} - c}. \tag{2.55}$$

The iterative solution procedure for equation (2.51) is identical to that of (2.55), which is outlined below for the spatial stability problem that was studied in this investigation. The method is adapted, with enhancements, from Sandham and Reynolds (1989).

- A guess was made for the complex eigenvalue α for a given real-valued ω.

- Equation (2.55) was integrated from each free stream to the mixing layer centerline at $y = 0$. A variable step, fifth-order Runga Kutta integrator from Press *et. al.* (1992) was used with an error control of 10^{-8}. Integrations were started ten vorticity thicknesses away from the centerline, a sufficiently large distance to not affect the results.

- The integrations from each free stream yield two estimates for χ at the centerline. A complex-valued, Newton-Raphson procedure was used to iterate on the eigenvalue until the difference between $\chi^+(0)$ and $\chi^-(0)$ was driven below 10^{-7}.

It should be noted that all spatially amplifying eigenvalues ($\alpha_i < 0$) obtained in this manner are not necessarily valid. It is possible to encounter evanescent (nonphysical) modes; in this investigation they were found in conditions that combined large density ratios ($\rho_2/\rho_1 > 2$) with compressibility. These modes were characterized by growth rates which were an order of magnitude larger than the true instability modes, eigenfunction profiles that radiate energy into both free streams, and their tendency to have $\alpha_r \to 0$ at nonzero ω. Beyond these identifying characteristics, their status as evanescent modes can easily be verified with a computational test developed by Briggs (1964). Although the

mathematical development is intensive (see section 2.3.3 of this reference), the result is simple.

Consider an eigenvalue solution for what we suspect is a spatially amplifying mode: the imaginary part of the complex wavenumber α is negative and the frequency, ω_r is purely real and positive. For a mode to be truly spatially amplifying, the imaginary part of α must change sign (*i.e.* cross the axis) when the imaginary part of the frequency, ω_i, is increased from zero. Evanescent modes will typically start moving towards the axis and then deflect back into negative α_i territory when ω_i is further increased.

2.2.3 Growth Rate Calculation

The calculation of linear stability growth rates introduces two additional parameters of frequency and obliquity to the five-dimensional space of physical parameters outlined in section 1.5.1. This additional complexity in the parametric study can be removed by reporting only the maximum amplification rate, $-\alpha_{i_{max}}$, that was found for each specific mode by searching the (ω, θ) polar plane. This simplification is justified because this is the value that will grow with the largest exponential rate downstream, and therefore determines the developing flow structure. Further, this is also the value that correlates with experimental growth rates (see figures 1.5 through 1.7). The (ω, θ) search algorithm is outlined as follows.

- Converge on a complex eigenvalue α for specified ω_r and θ values according to the procedure of the previous section.

- Increment ω_r forward and backward from the converged starting point until $-\alpha_i$ is maximized. $\Delta\omega_r$ was monitored to constrain the change in $-\alpha_i$ to between 0.1 and 1% between steps.

- Index θ forward and backward from the original value, while searching ω_r at each value, until $-\alpha_i$ decreases in each direction. $\Delta\theta$ was initially set to 2° although this could be automatically reduced if eigenvalue convergence problems were encountered.

2.2.4 Eigenfunction Calculation

The approach adopted for the eigenfunction calculation follows a different method than that of Gropengiesser by retaining equations (2.46) and (2.47) as a system in a modified form rather than combining them into a single equation. While it is straightforward to

obtain the eigenfunctions with equation (2.55) (see, for example, Sandham and Reynolds 1989), retaining the coupled system was found to be a more robust approach. Specifically, in regions of the parameter space where evanescent modes were encountered, the Gropengiesser formulation occasionally resulted in nonphysical eigenfunction solutions that expanded as $y \rightarrow \pm\infty$; the alternate formulation did not share in this behavior. However, it does require the integration to two coupled equations, which has twice the cost of Gropengiesser's approach. Two new eigenfunctions are defined to simplify this formulation. The first holds a resemblance to the stream function definition and the second is a normalized version of the pressure eigenfunction

$$\hat{\psi} = \frac{\hat{v}}{i\alpha}, \tag{2.56}$$

$$\hat{\pi} = \frac{\hat{p}}{\gamma_1 M_1^2}. \tag{2.57}$$

With these variables the coupled set of equations (2.46) and (2.47) become

$$(\bar{u} - c)\hat{\psi}' - \bar{u}'\hat{\psi} = g\hat{\pi}, \tag{2.58}$$

$$\alpha^2 \bar{\rho}(\bar{u} - c)\hat{\psi} = \hat{\pi}'. \tag{2.59}$$

If $\bar{u}'$ is zero in the free stream, the solutions of these equations exhibit exponential decay of the form

$$\hat{\psi} = \begin{cases} a_1 e^{qy} & y \rightarrow -\infty \\ a_2 e^{-qy} & y \rightarrow \infty \end{cases} \quad \text{and} \quad \hat{\pi} = \begin{cases} b_1 e^{qy} & y \rightarrow -\infty \\ b_2 e^{-qy} & y \rightarrow \infty \end{cases}. \tag{2.60}$$

where $a_{1,2}$ and $b_{1,2}$ are complex constants and $q = \alpha\sqrt{\bar{\rho}g}$. Because the equations are invariant to multiplication by a constant, the value of both a_1 and a_2 can be set to $(1,0)$—although there is no requirement that they be equal—without loss of generality. The equations then determine the $b_{1,2}$ values as

$$b_1 = -\alpha\sqrt{\bar{\rho}/g}\,(\bar{u} - c)\,a_1 = -b_2. \tag{2.61}$$

The procedure for the integration and solution of the coupled eigenvalue problem of equations (2.58) and (2.59) is similar to that of the previous section, although now there are two eigenfunctions to match at the centerline. A one-dimensional Newton-Raphson method can still be used by exploiting the invariance of the equations to multiplication by the matching

factor

$$\zeta = \frac{\hat{\psi}^+(0)}{\hat{\psi}^-(0)}. \tag{2.62}$$

This constant was used to evaluate the convergence of $\hat{\pi}$ towards continuity at the matching point by evaluating

$$\mathcal{F}(\alpha, \omega) = \zeta \hat{\pi}^-(0) - \hat{\pi}^+(0). \tag{2.63}$$

Iterations were continued until $\mathcal{F}$ was driven below a tolerance of 10^{-8}.

With the completion of the iteration sequence, the eigenfunctions $\hat{v}$ and $\hat{p}$ that correspond to the specified ω and β values are directly available from the last integrations of $\hat{\psi}$ and $\hat{\pi}$. The corresponding eigenfunctions for $\hat{u}, \hat{v}, \hat{w}, \hat{T}, \hat{\rho}$ and $\hat{Z}$ are then easily obtained through algebraic manipulation of equations (2.43b) and (2.43d) through (2.43f). The result was normalized by setting the maximum eigenfunction magnitude to unity and the phase to a value that forced $\hat{v}$ to be purely real at the centerline. Finally, it is noted that the adjoint system provides an alternate set of equations to approach the same solution, and can serve as a helpful check during validation. A derivation of the adjoint system and the coupled set of stability equations that result is discussed in the appendix section B.2.3.

2.3 Development of the PSE Approach

The parabolized stability equation (PSE) approach was first conceived and developed by Herbert and Bertolotti (1987) as a tool that would, under limited conditions, provide the quantitative accuracy of a large eddy or direct simulation while maintaining the low computational cost and significant flexibility of the method it evolves from, linear stability analysis. The advantages of this technique, which were first widely demonstrated in Bertolotti *et al.* (1992), stem from the fact that it is nonparallel and nonlinear, implying better physical representation and greater quantitative accuracy than linear, parallel stability techniques.

As in linear stability theory, the computational benefit comes from the fact that fluctuations are modeled in the streamwise and spanwise directions as a time-dependent wave. This modeling is based on physics: it is well known that convectively-unstable disturbances take the form of growing waves and this is used to our computational advantage. The restriction to convectively-unstable problems defines the first assumption of the technique.

Absolutely-unstable flows, such as backward facing steps or any application with a recircula-tion region in which disturbance information can be communicated upstream, are excluded from this analysis. This assumption restricts analysis to the family of shear flows, which includes boundary and mixing layers, wakes, and jets.

The PSE method differs from the more commonly applied linear stability analysis by allowing for several very useful complexities. To begin with, both the eigenvalue and eigen-functions, which will be referred to as shape functions to differentiate from the LST ap-proach, are allowed to vary in the streamwise direction, and hence the equations become parabolic. This approach borrows from the more limited multiscale method (see, for ex-ample, Saric and Nayfeh 1975), where disturbances are decomposed into a rapidly-varying wave-like part and a slowly-varying shape function. The wave part of the expression retains the ellipticity while the parabolization can be applied to the shape function. This forms the second basic assumption of the PSE technique which appears in two parts

$$\frac{\partial^2 \hat{\phi}}{\partial x^2} = 0 \qquad \text{and} \qquad \frac{\partial^2 \hat{\alpha}}{\partial x^2} = 0, \tag{2.64}$$

where $\hat{\phi}$ represents the vector of all shape functions and α is the streamwise wavenumber. (Note that the first part *does not* imply that second derivatives in real space are zero; this will be made clear in section 2.3.3.) These assumptions allow the use of a spatial marching method to calculate $\hat{\phi}$ at successive streamwise positions. These marching steps can naturally be large because an assumption has been made about the shape of fluctuations in the streamwise direction. This allows the flow field to be accurately modeled between steps. The large-step, streamwise marching procedure yields significant savings over other computational approaches.

Perhaps the most significant advantage, however, is the ability to incorporate nonlinear effects in the PSE technique. Beyond simply extending the validity of this technique past the linear regime, nonlinear modeling also allows for the interaction of different structural modes in the flow. A low-cost technique with this capability was critical for the investigation of colayer conditions that will be presented in chapter 4.

2.3.1 Governing Equations

The parabolized stability approach begins with a set of governing equations that are similar to those employed for the linear stability analysis. For simplicity, the initial intention was to carry out an inviscid analysis, which has been shown to be valid at high Reynolds

number (see the discussion of section 2.2.1). However, it was found helpful to include a subset of viscous terms in the analysis to stabilize the technique. In section 2.4.5 of this chapter, the tendency of the PSE method to develop nonphysical jitter in the shape functions will be addressed. This development, which occurs when nonlinearities are large and effectively ends the PSE calculation, can be delayed by including viscous damping and heat conduction terms in the cross-stream (y) direction to counteract the formation of locally-sharp gradients. This amounts to nothing more than the commonly made thin-shear-layer approximation. However, unlike boundary layer flows, these terms are not critical to the physics of mixing layers and their effect was very small for the Reynolds numbers considered here (typically on order of 10^4).

With these additional refinements to the LST approach, the governing equations for the PSE technique are

$$\frac{\partial \rho^*}{\partial t^*} + \frac{\partial \rho^* u_i^*}{\partial x_i^*} = 0, \tag{2.65a}$$

$$\rho^* \left(\frac{\partial u_i^*}{\partial t^*} + u_j^* \frac{\partial u_i^*}{\partial x_j^*} \right) = -\frac{\partial p^*}{\partial x_i^*} + \frac{\partial \tau_{ij}^*}{\partial x_j^*}, \tag{2.65b}$$

$$\rho^* \left(\frac{\partial Y_f}{\partial t^*} + u_i^* \frac{\partial Y_f}{\partial x_i^*} \right) = \frac{\partial}{\partial x_i^*} \left(\mu^* \frac{\partial Y_f}{\partial x_i^*} \right) - \dot{w}_f^*, \tag{2.65c}$$

$$\rho^* \left(\frac{\partial Y_o}{\partial t^*} + u_i \frac{\partial Y_o}{\partial x_i^*} \right) = \frac{\partial}{\partial x_i^*} \left(\mu^* \frac{\partial Y_o}{\partial x_i^*} \right) - \dot{w}_o^*, \tag{2.65d}$$

$$\rho^* \left(\frac{\partial h_t^*}{\partial t^*} + u_i^* \frac{\partial h_t^*}{\partial x_i^*} \right) = \frac{\partial q_i^*}{\partial x_i^*} + \frac{\partial p^*}{\partial t^*}, \tag{2.65e}$$

$$p^* = \rho^* R^* T^*. \tag{2.65f}$$

The viscous terms are assumed to follow the Newtonian form

$$\tau_{ij}^* = \mu^* \left(\frac{\partial u_i^*}{\partial x_j^*} + \frac{\partial u_j^*}{\partial x_i^*} - \frac{2}{3} \frac{\partial u_k^*}{\partial x_k^*} \delta_{ij} \right), \tag{2.66}$$

although in practice this was truncated according to the thin-shear-layer approximation

$$\frac{\partial \tilde{\tau}_{ij}^*}{\partial x_j} = \begin{cases} \frac{\partial}{\partial y^*} \left(\mu^* \frac{\partial u^*}{\partial y^*} \right) & \text{if i=1, j=2,} \\[2mm] \frac{4}{3} \frac{\partial}{\partial y^*} \left(\mu^* \frac{\partial v^*}{\partial y^*} \right) & \text{if i=2, j=2,} \\[2mm] \frac{\partial}{\partial y^*} \left(\mu^* \frac{\partial w^*}{\partial y^*} \right) & \text{if i=3, j=2,} \\[2mm] 0 & \text{otherwise.} \end{cases} \tag{2.67}$$

And the heat conduction term, assuming a Fourier form, is similarly truncated

$$\ddot{q}_i^* = \begin{cases} -\lambda_c^* \frac{\partial T^*}{\partial y^*} & \text{if i=2,} \\ 0 & \text{otherwise.} \end{cases} \tag{2.68}$$

In a manner consistent with the mean-flow derivation of section 2.1, the viscosity was assumed to be a linear function of temperature, which yields $\mu = T$ when nondimensionalized.

Similar to the LST development, the PSE formulation applies an infinitely-fast chemistry assumption. (The complications noted with a finite-chemistry approach are discussed in section 5.2.3.) With this simplification, the production terms in equations (2.65c) and (2.65d) vanish and they can be coupled through the conserved scalar

$$Z = Y_f - Y_o/n. \tag{2.69}$$

This model and the assumption of constant specific heats allows the energy equation to be rewritten as

$$\rho^* \left(\frac{\partial T^*}{\partial t^*} + u_i^* \frac{\partial T^*}{\partial x_i^*} \right) = \frac{\gamma}{Pr} \frac{\partial}{\partial x_i^*} \left(\mu^* \frac{\partial T^*}{\partial x_i^*} \right) - \frac{p^*(\gamma - 1)}{r^*} \frac{\partial u_i^*}{\partial x_i^*} \tag{2.70}$$

by following the procedure outlined in section 2.2.

Nondimensionalized with fast-stream reference quantities $(U_1^*, T_1^*, p_1^*, \rho_1^*)$ and the vorticity thickness (δ_ω), the governing equations for fast chemistry in a uniform molecular mass flow are

$$\frac{\partial \rho}{\partial t} + \frac{\partial \rho u_i}{\partial x_i} = 0, \tag{2.71a}$$

$$\rho \left(\frac{\partial u_i}{\partial t} + u_j \frac{\partial u_i}{\partial x_j} \right) = -\frac{1}{\gamma_1 M_1^2} \frac{\partial p}{\partial x_i} + \frac{1}{Re_o} \frac{\partial \ddot{\tau}_{ij}}{\partial x_j}, \tag{2.71b}$$

$$\rho \left(\frac{\partial Z}{\partial t} + u_i \frac{\partial Z}{\partial x_i} \right) = \frac{\mu}{Re_o Sc} \frac{\partial}{\partial x_i} \left(\mu \frac{\partial Z}{\partial x_i} \right), \tag{2.71c}$$

$$\rho \left(\frac{\partial T}{\partial t} + u_i \frac{\partial T}{\partial x_i} \right) = \frac{\gamma}{Pr Re_o} \frac{\partial}{\partial x_i} \left(\mu \frac{\partial T}{\partial x_i} \right) - p(\gamma - 1) \frac{\partial u_i}{\partial x_i}, \tag{2.71d}$$

$$p = \rho T. \tag{2.71e}$$

The decomposition into mean and fluctuating components is identical to that of the linear stability theory (equation 2.38) with the exception that the mean v component is carried here to provide a nonparallel stability method. Substituting these decompositions into the governing equations and subtracting equations for the mean flow from the result, the

nonlinear disturbance equations for the disturbance vector $\tilde{\phi} = [\tilde{\rho}, \tilde{u}, \tilde{v}, \tilde{w}, \tilde{Z}, \tilde{T}, \tilde{p}]^T$ are obtained as

$$\Gamma \frac{\partial \tilde{\phi}}{\partial t} + A \frac{\partial \tilde{\phi}}{\partial x} + B \frac{\partial \tilde{\phi}}{\partial y} + C \frac{\partial^2 \tilde{\phi}}{\partial y^2} + D \frac{\partial \tilde{\phi}}{\partial z} + E \tilde{\phi} = F, \qquad (2.72)$$

where the right-hand-side term F represents the nonlinear terms. The expanded form of this equation appears in the appendix section A.1.

2.3.2 Linear PSE

Consider first the case where the nonlinear forcing vector F is assumed to be negligible. The PSE method assumes that disturbances are periodic in both time and the spanwise direction, and that they can be represented in the following form

$$\begin{aligned} \tilde{\phi}(x, y, z, t) &= \hat{\Phi}(x, y) \, e^{i(\beta z - \omega t)} + c.c., \\ &= \hat{\phi}(x, y) \, \mathcal{A}(x) \, e^{i(\beta z - \omega t)} + c.c., \end{aligned} \qquad (2.73)$$

where

$$\mathcal{A}(x) = \epsilon_o \exp\left(i \int_0^x \alpha(\xi) \, d\xi\right) \qquad (2.74)$$

is the amplification factor, ϵ_o is the initial disturbance magnitude, $\hat{\phi}$ is the vector of shape functions, and c.c. denotes the complex conjugate, used to obtain a real-valued expression on the right hand side. Substituting equation (2.73) into equation (2.72) allows the stability equations to be represented as

$$\mathcal{L}(\hat{\phi}) = 0, \qquad (2.75)$$

where

$$\mathcal{L} = -i\omega\Gamma + A\left(i\alpha + \frac{\partial}{\partial x}\right) + B \frac{\partial}{\partial y} + C \frac{\partial^2}{\partial y^2} + i\beta D + E.$$

The linear PSE operator $\mathcal{L}$ differs from the linear stability operator by the inclusion of streamwise derivative terms, diffusion terms in the cross-stream direction, and the mean velocity in the cross-stream direction, $\bar{v}$. The complete, expanded form of equation (2.75) is developed in the appendix section A.2.

2.3.3 Nonlinear PSE

The nonlinear formulation assumes disturbances are of the form

$$\tilde{\phi}(x,y,z,t) = \sum_{m=-\infty}^{\infty} \sum_{n=-\infty}^{\infty} \hat{\Phi}_{mn}(x,y) \, e^{i(\beta_n z - \omega_m t)}, \qquad (2.76)$$

where, for base frequency ω_1 and spanwise wavenumber β_1, $\omega_m = m\omega_1$ and $\beta_n = n\beta_1$. In practice, the modes are truncated to a finite number

$$\tilde{\phi}(x,y,z,t) = \sum_{m=-M}^{M} \sum_{n=-N}^{N} \hat{\Phi}_{mn}(x,y) \, e^{i(\beta_n z - \omega_m t)}. \qquad (2.77)$$

Note that the addition of a complex conjugate is already included here; because the fluctuations are real valued, $\hat{\Phi}_{-m,-n} = \hat{\Phi}_{mn}^{\dagger}$ and the conjugate (denoted by $\dagger$) that explicitly appears in equation (2.73) is included in the expansion. This also implies that the modes $m < 0$ are dependent and do not need to be evaluated. The computational cost may be further reduced by applying a symmetry condition about $z = 0$ in the spanwise direction. This is a good assumption for free-shear-layer flows, and it forces eigenfunctions to be even in z, with the exception of $\hat{w}$ which becomes odd, yielding

$$\hat{\phi}_{m-n} = \left[\hat{\rho}_{mn}, \hat{u}_{mn}, \hat{v}_{mn}, -\hat{w}_{mn}, \hat{Z}_{mn}, \hat{T}_{mn}, \hat{p}_{mn} \right]. \qquad (2.78)$$

A schematic of the modes that constitute the physical, computational, and symmetry fields is shown in figure (2.1).

Due to the nonlinear terms, the solution system now has a nonzero right hand side

$$\mathcal{L}_{mn}(\hat{\Phi}_{mn}) = F_{mn}, \qquad (2.79)$$

or, equivalently,

$$\mathcal{L}_{mn}(\hat{\phi}_{mn}) = \frac{F_{mn}}{A_{mn}}. \qquad (2.80)$$

(Note that the indices here imply a quantity of frequency mode m and spanwise mode n and not a tensor quantity – hence indices are not contracted. The operator $\mathcal{L}$ becomes mode dependent due to wavenumber terms.) The alternatives for evaluating the nonlinear terms include explicit accounting

$$\mathcal{L}_{mn}(\hat{\Phi}_{mn}) = \sum_{i=-M}^{M} \sum_{j=-N}^{N} \mathcal{F}(m,n,i-m,j-n,i+m,j+m), \qquad (2.81)$$

or, with the advantages of reduced complexity and significant computational savings, the nonlinear terms can be evaluated using a Fourier transform approach

$$F^r(x,y,z,t) = \sum_{m=-M}^{M} \sum_{n=-N}^{N} F_{mn}(x,y)e^{i(n\beta_1 z - m\omega_1 t)}, \qquad (2.82)$$

where F^r corresponds to the vector of nonlinear terms in *physical space*. The calculation procedure starts with an inverse fast Fourier transform (FFT) of the flow variables from Fourier to physical space to produce disturbance information at discrete space and time positions. Note that the mean-flow distortion component, $\hat{\phi}_{00}$, should not be included in this transform; it will be explicitly accounted for in the mean flow (see section 2.4.4). The nonlinear terms are then evaluated in real space to produce the **total** nonlinear forcing vector, F^r. A forward FFT was then used to determine F_{mn}, the forcing contribution to the different stability modes, in Fourier space. Two-dimensional FFT routines from the SGI/Cray math library were used in these calculations. Aliasing errors were avoided by performing all transforms with additional zero padding in each dimension according to the three-halves rule. From a physical perspective, this dealiasing region is required because the simulation needs an energy sink and viscous scales are not resolved in PSE calculations.

The expanded form of the real-space nonlinear terms are detailed in the section A.1 of the appendix. These terms contain real-space derivatives in the spanwise, streamwise, and temporal dimensions that were calculated by taking the analytical derivative of equation (2.77) and using an FFT routine to efficiently perform the addition. The streamwise derivative takes a special form within the PSE approximation,

$$\frac{\partial^k \tilde{\phi}}{\partial x^k} = \sum_{m=-M}^{M} \sum_{n=-N}^{N} i^k \left[\alpha^k \hat{\phi}_{m,n} - i\,k\,\alpha^{k-1} \frac{\partial \hat{\phi}_{m,n}}{\partial x} \right.$$
$$\left. - i\,\frac{k(k-1)}{2}\,\alpha^{k-2}\,\frac{\partial \alpha}{\partial x}\,\hat{\phi}_{m,n} \right] A_{mn}\,e^{i(\beta_n z - \omega_m t)}. \quad (2.83)$$

Derivatives in the cross-stream direction were evaluated using a fourth-order central difference method formula and grid stretching, which will be specifically addressed in section 2.4.3. This approach represents an evolution from an earlier version that used a fifth-order Padé technique but was found to cause instability in the PSE iteration (see section 2.4.5 for further details).

2.3.4 Norm-Based Closure Methods

An analysis of equation (2.73) reveals that the streamwise change of $\hat{\Phi}(x, y)$ can be absorbed into either the shape function, $\hat{\phi}(x, y)$, or the streamwise wavenumber, $\alpha(x)$, where the latter defines the value of the amplitude function, $A(x)$. This ambiguity must be resolved through the introduction of an additional constraint, although there is a lack of consensus on how this should be achieved. One commonly employed solution is to impose a constraint on the streamwise growth of $\hat{\phi}(x, y)$. An alternative and more robust approach is addressed in appendix B, although this adjoint-based technique lacks the ability to handle nonlinear simulations in its current form. As a result, the present investigation adopted the use of a streamwise norm.

With the lack of any formal basis in their derivation, there is understandably a wide range of norms in the literature. The ICASE report of Chang *et al.* (1993) demonstrated that the choice of norm produces a quantitative effect on the PSE results, but the variance is not significant. While a norm can most easily be applied at a single y position, for example, where the streamwise velocity has its largest fluctuation, it is preferable to base it on a more rigorous integral approach. The version proposed by Herbert (1994) has the benefit of having a mathematical basis, and it was employed in this investigation.

The development of this integral norm begins with a comparison between the streamwise logarithmic derivative of the linear stability formulation (equation 2.41)

$$-i \left(\ln \bar{\phi} \right)_x = -i \frac{\bar{\phi}_x}{\bar{\phi}} = \alpha, \tag{2.84}$$

and the result of the same derivative for the PSE formulation of equation (2.73)

$$-i \left(\ln \bar{\phi} \right)_x = \alpha - i \frac{\hat{\phi}_x}{\hat{\phi}}. \tag{2.85}$$

For consistency of growth rate definitions it is desirable to equate these expressions by removing the streamwise dependence term of equation (2.85). This can be realized by forcing $\partial \hat{\phi} / \partial x$ to zero in an integral sense. This approach is constructed by multiplying both sides of equation (2.85) by $|\hat{\phi}|^2$, integrating over the U domain in y, and dividing by the integral of $|\hat{\phi}|^2$. The procedure yields

$$-i \frac{\int_U |\hat{\phi}|^2 \left(\ln \hat{\phi} \right)_x dy}{\int_U |\hat{\phi}|^2 \, dy} = \alpha - i \frac{\int_U \hat{\phi}^\dagger \hat{\phi}_x dy}{\int_U |\hat{\phi}|^2 \, dy}, \tag{2.86}$$

where (†) denotes a conjugate. The second term can be eliminated by choosing

$$\int_{\mho} \hat{\phi}^{\dagger} \hat{\phi}_x dy = 0 \tag{2.87}$$

as the integral norm to provide closure to the PSE problem.

In practice, the norm definition takes on a more physical meaning if only the velocity contribution to the vector $\hat{\phi}$ is included. This formulation yields the kinetic energy integral in the denominator terms of equation (2.86) and presents the norm as

$$\int_{\mho} \hat{\upsilon}^{\dagger} \hat{\upsilon}_x dy = 0, \tag{2.88}$$

where $\hat{\upsilon} = (\hat{u}, \hat{v}, \hat{w})$. Equation (2.88) was used in all calculations of this investigation.

2.3.5 Ellipticity Issues

To this point in the analysis, the equation governing the evolution of the shape functions

$$\mathcal{L}_{mn}(\hat{\Phi}_{mn}) = \boldsymbol{F}_{mn}, \tag{2.89}$$

has been described as parabolic without further justification. However, the analyses of Haj-Hariri (1994) and, in greater detail, of Li and Malik (1996) and Andersson *et al.* (1998) have identified residual ellipticity in the parabolized equations that make them ill-posed for a streamwise marching solution. The majority of this ellipticity arises from the $\partial \hat{p}/\partial x$ term and can manifest itself by destabilizing the marching procedure in subsonic flows. One rather simplistic yet effective approach to this problem is to maintain a sufficiently large step size such that these effects are essentially lost due to their rapid decay. Unlike in DNS calculations, this is an acceptable strategy because the accuracy of the PSE solution is quite insensitive to large step sizes; the slowly-varying nature of the shape function solution ensures this.

In the presence of the $\partial \hat{p}/\partial x$ term, the step-size criterion for subsonic regions becomes (Haj-Hariri 1994; Li and Malik 1996)

$$\delta x > \frac{1}{|\alpha_{r_{mn}}|}, \tag{2.90}$$

where m and n are chosen such that $|\alpha_{r_{mn}}|$ is a minimum. The problem with a large step size approach appears in nonlinear cases where δx must be reduced below this limit in order to assure convergence of the nonlinear terms. This requirement necessitates a more complex

solution: introduce a damping function, Ω, to eliminate the primary source of upstream influence found in the streamwise pressure gradient

$$\frac{\partial p'}{\partial x} = \sum_{m=-M}^{M} \sum_{n=-N}^{N} \left(i\alpha_{mn}\hat{p}_{mn} + \Omega \frac{\partial \hat{p}_{mn}}{\partial x} \right) A_{mn}(x) \; e^{i(\beta_n z - \omega_m t)}. \tag{2.91}$$

Note that even the coarse assumption of setting $\Omega = 0$ eliminates, at worst, a secondary part of the streamwise derivative because $\hat{p}_{mn}$ is slowly varying in the streamwise direction. For boundary layer flows this has been shown to be an acceptably accurate procedure (Li and Malik 1996) that results in the stability criteria

$$\delta x > \frac{-\alpha_i}{4|\alpha|} \frac{1}{|\alpha_{r_{mn}}|}, \tag{2.92}$$

which is at least an order of magnitude less restrictive than the constraint of equation (2.90).

For this study, two different Ω models were investigated: $\Omega = 0$ and the slightly more refined approach of Malik and Chang (1997),

$$\Omega = \text{Min} \left(M_x^2, 1 \right), \tag{2.93}$$

where M_x is the local streamwise Mach number. For fully supersonic flows, where the left-running characteristic associated with the $\partial \hat{p}/\partial x$ term is absent, PSE results were invariant to the choice of Ω, as expected. For subsonic flows, however, the Malik and Chang model was found to introduce instabilities in the iteration procedure (see section 2.4.5) that would lead to early termination of the calculation. Up to the stage of termination, the results failed to differ from the $\Omega = 0$ calculation, and thus $\Omega = 0$ was adopted for this study. This choice will be further validated against DNS results for supersonic flow in section 2.5.3 and subsonic flow in section 4.4.

Finally, it is important to note that equation (2.91) must be treated differently for the mean-flow correction. In keeping with the $\partial \bar{p}/\partial x = 0$ assumption made in section 2.1.1, the entire streamwise pressure derivative must be set to zero. Failure to do this can cause the iteration to diverge in the first few steps for subsonic flows.

2.4 PSE Solution Procedure

With the governing equations and basic foundation of the PSE technique established, the more problem-specific aspects of initial and boundary conditions, and the numerical solution approach will now be addressed.

2.4.1 Initial Conditions

The ideal set of initial conditions for the PSE would come from a nonparallel, linear solution of the governing equations, provided that the input magnitude of these disturbances was well within the linear range. The multiscale approach addressed in appendix B for wavenumber advancement can provide such an input condition through a nonparallel correction to the quasi-parallel, linear stability eigenfunctions of section 2.2.4. The initial condition takes the form

$$\hat{\phi}_{mn_i} = \hat{\phi}_{mn_0} + \hat{\phi}_{mn_{10}}, \tag{2.94}$$

where $\hat{\phi}_{mn_{10}}$ represents the nonparallel correction to the linear stability eigenfunction vector, $\hat{\phi}_{mn_0}$, and $\hat{\phi}_{mn_i}$ is the input shape function for the stability mode (m, n). This formulation was found to slightly reduce the magnitude of adjustment required in the eigenfunctions at the start of the PSE calculation. However, a significant relaxation from the initial condition still remained in the first few steps of the calculation, mostly due to the introduction of viscous and heat diffusion terms and the inclusion of a mean v profile in the PSE calculation (see section 2.3.1). For this reason, the multiscale method was avoided in favor of parallel linear stability initial condition since it offered little benefit for its additional complexity. The initial magnitude, ϵ_a, of these disturbances was typically set to 0.001 for the fundamental modes, and 0.0002 for the other input modes.

For nonlinear PSE calculations, it was often necessary to introduce linearly-stable, high-frequency or high-β-wavenumber modes during the simulation, when the frequency spectrum broadens and energy reaches the shorter length scales by nonlinear interaction. Calculation of the linear stability solution for these stable modes is particularly difficult for supersonic conditions where a global solution based on the method of matched asymptotic expansions is required to solve the radiated sound field (Tam and Burton 1984). However, it is important to note that these modes will be unstable in a nonlinear PSE simulation due to the input of energy from lower, more energetic frequencies. There is little need therefore for the complex, though accurate, approach for generating these modes by asymptotic expansions. An approximate method was used instead to generate the shape functions for these modes.

This technique required an explicit solution for $\hat{\Phi}_{mn}$ according to the PSE governing

equation

$$\mathcal{L}^*(\hat{\Phi}_{mn}) = F_{mn},\tag{2.95}$$

where the streamwise derivative terms in $\mathcal{L}$ have been removed to yield $\mathcal{L}^*$. In order to generate a reasonable solution, the real part of α_{mn} was initially phase locked such that $\mathcal{R}\{\alpha_{mn}\} = m\mathcal{R}\{\alpha_{10}\}$, while the imaginary part of α_{mn} was set slightly negative (10^{-4}) to avoid numerical singularities. The frequency and spanwise wave number were fixed at their appropriate harmonic levels, $\omega_{mn} = m\omega_{10}$ and $\beta_{mn} = n\beta_{01}$. The result of this procedure was normalized according to the same method applied to the linear stability input functions: the maximum magnitude was set to unity and the phase was specified by requiring that $\hat{v}_{mn}$ was purely real along the centerline. For some cases, notably those studying the interaction of subharmonic and fundamental frequencies in pairing, the phase of a specific mode was shifted by an angle ϕ_s at the input condition by multiplying the shape function with an $e^{i\phi_s}$ factor.

The code was developed with the capability to dynamically add modes during the calculation. Similar to padding the grid in DNS calculations, this mode addition amounts to providing enhanced resolution of the high-wavenumber, high-frequency modes when they become significant. This was done not only to reduce the computational cost but also by necessity; input conditions calculated from equation (2.95) were found to cause instability in the iteration procedure if there was insufficient forcing of the newly-input Fourier mode (see section 2.4.5). Presumably, this was result of instabilities in the numerical procedure overwhelming the solution of physically insignificant modes. This required a delay in their introduction, and the addition was made when the nonlinear forcing on either of the streamwise momentum or energy equations for the mode of interest surpassed a magnitude of 10^{-8}. (For reference, forcing reached a maximum magnitude on the order of 10^{-4} in fully nonlinear flow.) Simulations were conducted by specifying a maximum M and N value (see figure 2.1) at input and adding modes within those bounds were appropriate. The status of modes—physical, transient, or unspecified—was accounted for in an array table.

It should also be noted that a large magnitude of forcing on a mode generated from equation (2.95) can cause numerical instability in its introduction. The iterative convergence of all modes is sensitive to the transients associated with mode introduction, where a new forcing influence is 'turned on' and all shape functions are required to adjust to its presence. This is typically only a problem for the steady modes ($m = 0$, $n > 0$) in the first several

steps of the simulation. It can be directly addressed by reducing the magnitude of the linear stability solutions inserted at $x = 0$. However, a more robust approach, found useful in the introduction of all modes, was to incorporate a transient period of five solution steps where the mode was introduced to the flow but not formally considered in the iteration convergence to be discussed in section 2.4.5. This introduction period allows initially large growth rate transients to attenuate before the mode is officially added to the flow.

2.4.2 Cross-Stream Boundary Conditions

Previous PSE studies have demonstrated that homogeneous Dirichlet boundary conditions in the free stream are adequate for accurate simulations (Herbert 1994). This approach, reasoned from the characteristic exponential decay of disturbances in the free stream, allows for the approximation

$$\hat{\phi} = 0 \quad \text{at} \quad y = -\infty \text{ and } \infty \tag{2.96}$$

to be applied without adverse effect, provided the boundary equation is applied far—at least $10\delta_\omega$—from the centerline. However, applying the PSE to supersonic shear layer calculations often requires the solution of cases where a disturbance travels supersonically relative to either, or both, free streams. An example of this is shown in figure 2.2 for a slow mode at $M_c = 1.0$. This mode is supersonic relative to the fast free stream and therefore displays as an oscillatory decay as $y \to \infty$. It is clear from this figure that equation (2.96) is only appropriate for non-oscillatory free-stream decay; applying it to both boundaries will cause stability problems in the PSE evolution.

In developing an alternative boundary condition for these supersonic modes, it is important to keep in mind that it is applied to the slowly-varying shape function. In real space these oscillatory perturbations are traveling waves that would require a non-reflecting boundary condition. However, the oscillations in the shape functions are essentially stationary: the phase variation in Fourier space is contained in the streamwise wavenumber. This provides considerable simplification to the boundary condition formulation. The complex coefficient of exponential decay, q, defined in section 2.2.4, is used to advantage in developing the implicit boundary condition

$$\frac{\hat{\phi}'}{\hat{\phi}} = \mp q \quad \text{for} \quad y \to \pm\infty. \tag{2.97}$$

The derivative term was evaluated with a first-order difference at the boundary.

Applying this boundary condition to all modes was found to generate instabilities in the PSE solution for disturbances that were not supersonic relative to a free stream. Therefore, a combination of equations (2.96) and (2.97) were used according to a disturbance's sub- or super-sonic status

$$y \to -\infty \quad : \quad \begin{cases} \hat{\phi} = 0 & \text{for } c_r < c_- \\ \dfrac{\hat{\phi}'}{\hat{\phi}} = q & \text{for } c_r > c_- \end{cases} \qquad (2.98)$$

$$y \to \infty \quad : \quad \begin{cases} \hat{\phi} = 0 & \text{for } c_r > c_+ \\ \dfrac{\hat{\phi}'}{\hat{\phi}} = -q & \text{for } c_r < c_+ \end{cases} \qquad (2.99)$$

where s is the density ratio, $\bar{\rho}_2/\bar{\rho}_1$, and c_+ and c_- are the speeds of sonic disturbance relative to the fast and slow stream, respectively (Jackson and Grosh 1989). For the general mixing layer with $U_2 \neq 0$ these criteria are

$$c_+ = 1 - \frac{1}{\tilde{M}} \qquad (2.100)$$

$$c_- = \frac{1}{\sqrt{s}\tilde{M}} + U_2, \qquad (2.101)$$

where $\tilde{M} = M_1 \cos(\theta)$, the fast stream Mach number in the direction of disturbance propagation. These boundary conditions were applied at $y = \pm L_y/2$, where the domain thickness, L_y was typically set to $30\delta_\omega$ (see Appendix C).

The mean-flow correction receives a different boundary condition treatment that will be addressed in section 2.4.4.

2.4.3 Discretization

The conflicting needs to offer high resolution of the flow in the shear region while still requiring the computational domain to extend far into each free stream demand the use of grid stretching. The selected mapping is based on a sinh function and takes the form

$$y = \frac{L_y}{2} \frac{\sinh(b_y \zeta)}{\sinh b_y}, \qquad (2.102)$$

where b_y and ζ are the stretching coefficient and mapping coordinate. Derivatives in this direction are then evaluated as

$$\frac{\partial \hat{\phi}}{\partial y} = \frac{1}{y'} \frac{\partial \hat{\phi}}{\partial \zeta} \qquad \text{and} \qquad \frac{\partial^2 \hat{\phi}}{\partial y^2} = \frac{1}{y'^2} \frac{\partial^2 \hat{\phi}}{\partial \zeta^2} + \frac{y''}{y'^3} \frac{\partial \hat{\phi}}{\partial \zeta} \qquad (2.103)$$

where

$$y' = \frac{L_y}{2} \frac{b_y \cosh(b_y \zeta)}{\sinh b_y} \qquad \text{and} \qquad y'' = \frac{L_y}{2} \frac{b_y^2 \sinh(b_y \zeta)}{\sinh b_y}. \tag{2.104}$$

The stretching coefficient was typically set to 2, although simulations of outer modes, which have oscillatory solutions in the free streams, often required tailoring this value in combination with increasing L_y to achieve stability in the PSE iteration procedure (see appendix C for specific numbers).

For derivatives of a particular shape function in the cross-stream direction, fourth-order central difference approximations of the form

$$\frac{\partial \hat{\phi}_j}{\partial \zeta} = \frac{-\hat{\phi}_{j+2} + 8\hat{\phi}_{j+1} - 8\hat{\phi}_{j-1} + \hat{\phi}_{j-2}}{12\Delta\zeta} \tag{2.105}$$

and

$$\frac{\partial^2 \hat{\phi}_j}{\partial \zeta^2} = \frac{-\hat{\phi}_{j+2} + 16\hat{\phi}_{j+1} - 30\hat{\phi}_j + 16\hat{\phi}_{j-1} - \hat{\phi}_{j-2}}{12\Delta\zeta^2} \tag{2.106}$$

are used while second-order central differences

$$\frac{\partial \hat{\phi}_j}{\partial \zeta} = \frac{\hat{\phi}_{j+1} - \hat{\phi}_{j-1}}{2\Delta\zeta} \qquad \text{and} \qquad \frac{\partial^2 \hat{\phi}_j}{\partial \zeta^2} = \frac{\hat{\phi}_{j+1} - 2\hat{\phi}_j + \hat{\phi}_{j-1}}{\Delta\zeta^2} \tag{2.107}$$

are applied at points adjacent to boundaries.

The choice of numerical scheme for evaluating streamwise derivatives was guided by the PSE approximation (equation 2.64),

$$\frac{\partial^2 \hat{\phi}}{\partial x^2} = 0.$$

Therefore, a first-order approximation will yield good accuracy since the leading error term of order $(\Delta x^2\, \partial^2\hat{\phi}/\partial x^2)$ will be very small where the PSE approximation is appropriate. Indeed, Herbert (1994) indicated that the second-order central difference provided no advantage over first-order methods. In its simplest, explicit form, the first-order difference is

$$\frac{\partial \hat{\phi}}{\partial x}\bigg|^i \approx \frac{1}{\Delta x}(\hat{\phi}^{i+1} - \hat{\phi}^i), \tag{2.108}$$

where i is the step index in the streamwise direction and $\hat{\phi}^i = \hat{\phi}^i(y) = \hat{\phi}(x_i, y)$. However, the use of explicit methods in the PSE evolution can be shown to lead to instability problems (Andersson 1998) and therefore the backward, implicit version,

$$\frac{\partial \hat{\phi}}{\partial x}\bigg|^{i+1} \approx \frac{1}{\Delta x}(\hat{\phi}^{i+1} - \hat{\phi}^i) \tag{2.109}$$

was used.

The basic form of the PSE solution (equation 2.75) can be written as

$$\mathcal{L}\hat{\phi} = L\hat{\phi} + M\frac{\partial \hat{\phi}}{\partial x} = 0, \tag{2.110}$$

where the decomposition into L and M is done to isolate the unknown streamwise shape function derivatives in the latter operator. Using the backward difference approximation of equation (2.109) in place of the derivative, the linear problem takes the form

$$\left[\Delta x L^{i+1} + M^{i+1}\right] \hat{\phi}^{i+1} = M^{i+1}\hat{\phi}^{i}, \tag{2.111}$$

where an iteration scheme is used with this equation to reduce the error in the norm to zero (see section 2.4.5). For the nonlinear problem, an additional forcing term appears on the right hand side

$$\left[\Delta x L_{mn}^{i+1} + M_{mn}^{i+1}\right] \hat{\phi}_{mn}^{i+1} = M_{mn}^{i+1}\hat{\phi}_{mn}^{i} + \frac{F_{mn}^{i+1}}{A_{mn}^{i+1}}\Delta x. \tag{2.112}$$

2.4.4 Mean-Flow Correction

Nonlinear interactions between modes will redistribute energy in the Fourier domain and will also result in a contribution at zero frequency and spanwise wavenumber, $\hat{\Phi}_{00}$, which is the nonlinear correction to the mean flow. At the calculation inlet, the real part of the wavenumber and frequency of this mode was set to zero, and the shape function was evaluated according to the procedure of section 2.4.1. The correction modes were evolved downstream in the same manner as other modes by solving

$$\left[\Delta x L_{00}^{i+1} + M_{00}^{i+1}\right] \hat{\phi}_{00}^{i+1} = M_{00}^{i+1}\hat{\phi}_{00}^{i} + \frac{F_{00}^{i+1}}{A_{00}^{i+1}}\Delta x. \tag{2.113}$$

and constraining the streamwise growth with equation (2.88). This approach was found to be more robust than the procedure proposed by Herbert (1994) where the imaginary part of α_{00} is also set to zero and the growth of the mean-flow correction in entirely contained in $\hat{\phi}_{00}$.

In order to satisfy mass balance constraints, the boundary conditions must allow for nonzero $\hat{v}_{00}$ at the cross-stream limits. In most PSE implementations, this is done by setting $\hat{\phi}_{00} = 0$ with the exception of $\hat{v}_{00}$, which is treated with

$$\frac{\partial \hat{v}_{00}}{\partial y} = 0 \quad \text{at} \quad y = -\infty \text{ and } \infty. \tag{2.114}$$

However, due to the coupling between $\hat{v}$ and $\hat{p}$ described in equations (2.52) and (2.53), setting one to zero and the other nonzero was found to cause convergence problems while iterating on the norm. A more consistent approach was adopted in this study by applying the wave-based boundary condition of equation (2.97) to the mean-flow correction.

The mean variables used in the PSE calculation were formed from the sum of the laminar and nonlinear contributions. For example, the mean streamwise velocity was evaluated as

$$\bar{u} = \bar{u}_{\text{laminar}} + \hat{u}_{00} \, \mathcal{A}_{00}(x), \tag{2.115}$$

where the laminar solution is the self-similar solution of the compressible boundary layer equations described in section 2.1. Derivatives of mean flow quantities were calculated using the first- and fourth-order methods of section 2.4.3 for the streamwise and cross-stream directions, respectively.

It should be noted that great care must be taken in the calculation of the mean flow distortion. This quantity exhibits a very strong dependence on history because it accumulates small changes during streamwise progression (Herbert 1994). The importance of this correction to the accuracy of the PSE will be demonstrated in section 2.5.3.

2.4.5 Iteration Method

With an implicit streamwise derivative used to form the PSE problem represented in equation (2.112), an iterative technique is necessary for its solution. A cost function approach based on the specified norm of equation (2.88) can be developed to yield the following iteration strategy for the wavenumber at the next step, α_{j+1},

$$\alpha_{j+1}^{n+1} = \alpha_{j+1}^{n} - \rho_j \frac{i}{\Delta x_j} \frac{\int_U (\hat{v}_{j+1}^n)^{\dagger} (\hat{v}_{j+1}^n - \hat{v}_j^n)}{\int_U |\hat{v}_{j+1}^n|^2 \, dy}, \tag{2.116}$$

where n indicates the iteration step number, $\hat{v}$ is the vector of velocity shape functions, $\dagger$ denotes a conjugate, and ρ_i is a convergence constant that was set to unity. In nonlinear problems this iteration sequence must be simultaneously conducted for all stability modes, including the mean-flow correction, and it was continued until each norm was satisfied within a tolerance of 10^{-6}. The integrals were evaluated using a variable-step Runge-Kutta integration routine from Press *et al.* (1992). The streamwise integral of the converged α_{mn} values, required for the calculation of the amplitude factor (equation 2.74), was done with Simpson's Rule due to its slow variation — in keeping with the PSE approximation of equation (2.64).

As this procedure is carried downstream in a stepwise fashion, the nonlinear interactions will continue to grow until the iteration eventually fails to converge. Typically, the convergence will stall and, in the subsequent iterations, the shape functions will develop jagged profiles that are nonphysical. This development, which the cross-stream viscous and heat conduction terms discussed in section 2.3.1 help to suppress, will cause the iteration to diverge and eventually overflow. It is the opinion of some PSE researchers (C. Hill, personal communication) that this convergence failure is related to the saturation of the mean-flow correction and, more precisely, the inability of the PSE technique to effectively redistribute energy leaving this mode. However, this failure is not too restrictive because it generally occurs just prior to the flow becoming highly nonlinear, at which point the parabolizing assumption (equation 2.64), and hence the PSE results, are clearly invalid.

2.4.6 Combustion Modeling

Conventional application of finite-chemistry methods is made impossible by the time-periodic nature of the PSE calculation. The present investigation used an infinitely-fast chemistry assumption to make the application of the PSE to reacting flow tractable. This assumption is in keeping with the fundamental limitation of studying combustion problems with the PSE; the lack of resolution at molecular-mixing levels only allows for qualitative—but still highly informative—observations. Most importantly with fast chemistry, the passive scalar $Z = Y_f - Y_o/n$ becomes conserved and only one equation needs to be carried for combustion modeling. The value of Z directly determines the fuel, oxidizer, and product mass fraction and temperature fields. However, the use of Z to uniquely determine the temperature distribution creates a problem in zero or low heat release supersonic flow conditions where viscous heating effects often outweigh the influence of combustion on the temperature profile. Because these cases constitute the majority of the conditions of our interest, the conflict was resolved by ignoring the influence of the passive scalar on temperature fluctuations. With this approximation, the effect of combustion on the stability modes is only through its modification of the mean flow, as described in section 2.1.

In keeping with convention, combustion results were presented in terms of the mixture fraction, ξ, which is defined as

$$\xi = \frac{Y_f - Y_o/n + Y_{o,\infty}/n}{Y_{f,-\infty} + Y_{o,-\infty}/n}, \tag{2.117}$$

and is easily derived from Z through

$$\xi = \frac{Z + Y_{o,\infty}/n}{Y_{f,-\infty} + Y_{o,-\infty}/n}. \tag{2.118}$$

The stoichiometric mixture fraction value defines the flame sheet position, and this occurs when Z is zero,

$$\xi_{st} = \frac{Y_{o,\infty}/n}{Y_{f,-\infty} + Y_{o,-\infty}/n}. \tag{2.119}$$

The mass fractions Y_o and Y_f are easily extracted from equation (2.117) because they cannot coexist under the fast-chemistry assumption. And finally, the mass fractions for the product and diluent species are given by

$$Y_p = \begin{cases} (1-\xi)/(1-\xi_{st}) & \text{if } \xi > \xi_{st}, \\ \xi/\xi_{st} & \text{if } \xi < \xi_{st}, \end{cases} \tag{2.120}$$

$$Y_d = 1 - Y_p - Y_o - Y_f. \tag{2.121}$$

It is important to note that the realizability condition $0 \leq \xi \leq 1$ is not directly built into the PSE formulation. This is a result of evolving the equations in Fourier space, where the real-space value of ξ is separated into component parts. Even if ξ was calculated at each step and a realizability violation detected, the question remains of how to allocate the correction to the different stability modes in Fourier space. Some exploration of these methods was made, but each was found to be unsatisfactory on the basis of introducing instabilities in the iteration convergence or arbitrary destruction of mass. In practice, however, violations were not found to be significant and a simple truncation was applied at the end of the calculation when transforming to real space. Further discussion on this topic in connection to the use of finite-rate chemistry methods with the PSE is made in section 5.2.3.

2.4.7 Statistics

The growth rate is determined from two components: the local streamwise wavenumber to capture the growth in the amplification factor, and the logarithmic derivative of the eigenfunction energy to account for its streamwise growth

$$\sigma_{mn} = -\text{Im}(\alpha_{mn}) + \frac{\partial}{\partial x}(\ln\sqrt{E_{mn}}), \tag{2.122}$$

where E_{mn} is the integral energy in the velocity shape functions defined as

$$E_{mn} = \int_{-\infty}^{\infty} \left(|\hat{u}_{mn}|^2 + |\hat{v}_{mn}|^2 + |\hat{w}_{mn}|^2 \right) dy. \tag{2.123}$$

2.5 PSE Validation

With the creation of any nonlinear model such as this implementation of the PSE technique, there is an obvious need for validation. The adopted approach was a statistical comparison of the nonlinear PSE output to a full DNS calculation for a spatially-developing mixing layer.

2.5.1 DNS Simulation

The DNS code used in this study was developed from a round jet version originally written by J. Freund for acoustic studies. To ready the code for the PSE validation, changes were made to, in essence, roll out the cylindrical geometry to form a rectangular box for plane mixing layer simulations. Details of the equations and general numerical approach are described in Freund (1997) in the context of a temporal simulation. The inflow, outflow, and cross-stream boundary conditions for the spatial simulation are detailed in Freund (1997b). In summary, a spectral method was used in the spanwise direction, while a fifth-order Padé method was used in streamwise and cross-stream direction to evaluate derivatives. Time advancement was done with a fourth-order Runge-Kutta method on a grid that was stretched in both the cross-stream and streamwise directions. The input flow condition was identical to the PSE calculation in its use of mean flow and linear stability solutions described in sections 2.1 and 2.2. The introduction of these modes to the inlet plane was moderated with a tanh function over time to limit initial transient effects.

Although the resultant DNS code was capable of three-dimensional simulations, it was not optimized for this purpose and the associated computational cost would have been prohibitive for a validation experiment. To avoid this situation, test conditions were selected to achieve a moderate compressibility that still maintained a dominant two-dimensional central mode instability: $M_c = 0.5$, $r = 0.6$, $s = 1$. A spatial simulation was done at $Re_o = 5000$ for these flow conditions in a computational box that spanned $160 \times 30 \ \delta_{\omega_o}$ and was resolved with a 1500×200 point grid.

The complementary PSE simulation was done with eight frequency modes. Two frequency modes, the fundamental and its first harmonic, were specified at the input condition

using their linear stability solutions normalized to a maximum real-space fluctuation magnitude of 0.001 and 0.0002, respectively. These two linear stability modes also constituted the DNS initial condition. The subharmonic of the fundamental was not forced in this validation case because there was some concern about the ability of the PSE to model pairing, and we preferred to eliminate this unknown while validating the basic nonlinear formulation. A separate discussion of simulating vortex airing with the PSE appears in section 4.4.

Input conditions for PSE frequency modes $m = 3$ through $m = 8$ were calculated by equation (2.95). As the results will demonstrate, all frequencies saturate in this simulation at moderate levels, and hence the PSE calculation was able to run through to $x = 160$ without iteration convergence problems.

2.5.2 Validation Statistics

For the purpose of validating the nonlinear PSE, it is desirable to extract the growth rate of the different modes, the fundamental and its higher harmonics, that were imposed at the input of the DNS calculation. The determination of growth rate information at different frequencies requires a Fourier-based method where different modal contributions can easily be separated from the whole. This type of growth rate calculation is based on the integrated disturbance kinetic energy

$$E'_m \equiv \int_{-\infty}^{\infty} \left(|\hat{u}'_m|^2 + |\hat{v}'_m|^2 + |\hat{w}'_m|^2 \right) dy, \tag{2.124}$$

where, for example, $\hat{u}'_m$ is the time Fourier transform coefficient of the u velocity component at the frequency $\omega_m = m\omega_1$. This is related to the PSE shape function through $\hat{u}'_m = \hat{u}_m \cdot A(x)$. The calculation of Fourier coefficients can be done directly from their definition

$$\hat{u}' = \frac{1}{N} \sum_{j=0}^{N-1} u \, e^{i\omega t_j}, \tag{2.125}$$

where the contribution is added at each step as the simulation runs through an extent that is just short of a complete period (*i.e.* $t_N - t_0 = T$). The computation of Fourier coefficients from a FFT approach is not practical because of the intensive memory requirements of saving flow field information at each step. Further, an FFT application is undesirable due to its additional complexity and the lack of any significant computational advantage since this is not a repetitive calculation.

With the energy E'_m available at each streamwise location, the frequency-dependent growth rate can be extracted though the logarithmic derivative

$$\sigma = \frac{1}{2}\frac{1}{E'_m}\frac{dE'_m}{dt},$$

(2.126)

where the 1/2 factor is required since E'_m is quadratic. Obtaining smooth growth rate results from this calculation requires two refinements: first, the streamwise derivative calculation must be done with an accuracy no higher than second order, which is quite sufficient since the energy is a smooth function. Second, the derivative calculation should be done inside the integral of equation (2.124) in order to reduce its sensitivity to numerical inaccuracies.

2.5.3 Validation Results

The first validation task is to look at the growth of individual modes from the initial condition through the linear and nonlinear stages. This is best done through an integrated measure like the modal energy, E'_m, and these results are shown in figure 2.3 for the first two modes of the DNS and PSE simulations, where the latter are shown for both linear and nonlinear calculations. Excellent agreement in the linear growth of the $m = 1, 2$ modes, who together defined the initial condition, confirms that the DNS and PSE simulations correctly model the linear domain. The departure of linear and nonlinear solutions for the fundamental mode ($m = 1$) marks the start of saturation at approximately $x = 80$. The linear solution, which lacks any such physical limit mechanism, continues its exponential growth to the end of the simulation. Figure 2.3 shows that the post-saturation result for the nonlinear PSE is indistinguishable from the DNS solution.

Equally impressive agreement is found in the first harmonic ($m = 2$) mode, where the nonlinear PSE solution closely follows the DNS in the addition of energy from the fundamental mode starting at $x = 25$. The saturation of this mode later in the simulation is also in excellent agreement. The difference between linear and nonlinear PSE solutions for the first harmonic is particularly striking. These solutions depart significantly earlier than those of the fundamental ($x = 20$ verses $x = 80$) because this mode becomes stable without the nonlinear addition of energy from the fundamental.

The energy growth of higher harmonics ($m = 3, 4$) of the PSE are shown in figure 2.4. The interest in these modes concerns their growth from the initial condition which was generated through equation (2.95) rather than with linear stability modes. The results demonstrate some disagreement early in the simulation when these modes are completely

insignificant, but the comparison becomes excellent when they start to play a role in the simulation by receiving energy via the turbulent cascade from lower, more dominant frequencies. These modes also saturate later in the simulation, with the PSE solution predicting a slightly lower energy level than the DNS in the post-saturation phase.

A more detailed comparison of the growth, saturation, and decay of the primary and first harmonic modes can be seen in the growth rate plots of figure 2.5. Linear and nonlinear PSE σ results are shown in comparison to the DNS solution for the fundamental and first harmonic modes. The onset of nonlinearity is again demonstrated in the departure of both the PSE and DNS solutions from the linear calculation. Both modes saturate (defined by $\sigma = 0$) near $x = 100$. The PSE method provides an excellent prediction for the saturation of both modes, and even correctly models the post-saturation recovery. This agreement is surprisingly good considering that the high level of nonlinearity in the flow past $x = 100$ brings the validity of the PSE assumptions into question.

The integrated energy result for all eight modes of the simulation are shown in figure 2.6. The trend of initial linear growth followed by saturation and slight decay is present in all modes because the layer has grown sufficiently large to render high frequencies stable. Normally, growth at this stage would come from the subharmonic mode that was explicitly neglected in these simulations. Note the addition of higher-frequency modes ($m > 4$) to the simulation as the nonlinear forcing becomes significant. Also, it is important to point out the lack of differentiation in the energy of high-frequency modes towards the end of the simulation, which clearly implies poor resolution of the fine-scale motion. This is not an aliasing effect because dealiasing was applied according to the three-halves rule to act as an energy sink in the simulation. Rather, it is a natural consequence of modeling the transition to turbulence with only eight frequency modes. The number of modes would need to be raised by at least an order of magnitude to achieve DNS-like resolution and an energy spectrum of appropriate shape. Fortunately, however, the focus of this investigation lies on evaluating mean measures of mixing and layer growth that are dominated by the accurately-modeled large scales. Results that are affected by fine-scale motion, like RMS calculations for example, will not be reported.

While the integrated energy and growth rate results are insightful for analyzing specific modes, it is the real-space flow field and the related statistics that ultimately hold greater interest. The first of these plots, showing the streamwise evolution of $\bar{u}_{max}$ and $\bar{v}_{max}$, appears in Figure 2.7. The figure shows a comparison between results from PSE simulations—both

with and without cross-stream diffusion terms—to the DNS solution. The kinks in the profiles are simply caused by a change in the location of the maximum fluctuation. In the $\tilde{u}_{max}$ results of figure 2.7(a) the viscous PSE and DNS results compare extremely well, with the peak value agreement within 0.6% and the difference between the solutions only discernible at the very late stages of the calculation. The viscous PSE solution offers better agreement with the DNS in the later streamwise stages of the calculation, which is not surprising considering the DNS-limited Reynolds number of 5000. The combination of excellent agreement with the DNS and only a slight variation from the inviscid solution, which lessens at the higher Reynolds number of interest, justifies the use of the thin-shear-layer approximation in the current calculations.

The $\tilde{v}_{max}$ results of figure 2.7(b) offers some insight into the breakdown of the PSE approximation. The agreement is still impressive—the estimates of the peak differ by only 2.2%—although the 14% peak fluctuation intensity seems to suggest a nonlinearity level where the PSE will start to encounter accuracy problems. The larger discrepancy could also be a legacy of linear stability input conditions that did not account for a mean v profile. In a similar manner to figure 2.7(a), the difference between inviscid and partially viscous PSE simulations is generally negligible.

A full-field appreciation for PSE calculation can be seen in the spanwise vorticity contour plots of figure 2.8. The streamwise range from $x = 60$ to 120 documents the development of the central mode flow structure in the nonlinear regime. The agreement between the non-linear PSE and DNS calculations in figures 2.8(a-c) for the large-scale structure is excellent. A plot of the linear PSE contours in figure 2.8(d) offers an additional perspective on the importance of nonlinear modeling past $x = 65$, and clearly shows why a nonlinear analysis is required to study the large-scale flow structure responsible for initiating mixing.

The effect of adding frequency modes to the PSE simulation is demonstrated in the comparison of figure 2.8(b) and (c). The higher spatial resolution of the $M = 8$ PSE simulation enables it to better resolve the braid structure between rollers, but it also generates a large amount of fine-scale noise that does not appear in the DNS. This disagreement between the DNS and PSE simulations on the small-scale structure is primarily due to the previously-described resolution problems for fine-scale energy when only eight modes are employed. An explicit demonstration of this is shown in figure 2.9. The contours of a test function are shown in figure 2.9(a); it has a high value in the center with a sharp-edged decay to a low value at the edges. The contour representation of this function with eight Fourier modes

in each of the x and y directions is shown in figure 2.9(b). This figure shows additional contours, the nature of which is explained in the cross-sectional view of figure 2.9(c). The truncated series simply lacks the spatial resolution to resolve the rapidly-changing features of the test function. Oscillations result when the energy of the highest-resolved mode is not canceled out by the absent higher-resolution modes.

A similar problem affects the vorticity field representation when a limited number of Fourier modes are used in a PSE simulation. This is clearly seen in figure 2.10, a plot of the spanwise vorticity along the centerline for DNS and PSE calculations, where the latter was done with $M = 8$. The resolution problems that exist when a mode-limited PSE simulation attempts to simulate the fine-scale structure of the braid region are evident. These oscillations are also likely enhanced by the lack of streamwise viscous dissipation in this implementation of the PSE. In summary, the reader is cautioned against attributing the fine-scale structure in contour plots to well-resolved, physical phenomenon.

To demonstrate the qualitative aspects of mixing in this flow, plots of the mixture fraction are shown in figure 2.11. The complete ξ field is shown along with detailed views of the oxidizer side ($0 \leq \xi \leq 0.5$) and reaction sheet ($\xi = 0.5$) for this stoichiometric, zero-heat-release case with infinitely-fast chemistry. These plots demonstrate that the PSE technique is fully capable of recreating the large scale structures responsible for dominant mixing processes, documenting the entrainment of species into the reaction zone, and profiling the convolution and straining of the flame sheet.

The DNS validation can also be used to gain insight into the effect of the mean flow on stability calculations. In figure 2.12, PSE growth rate predictions with and without the nonlinear correction to the mean flow are compared to the DNS solution. In the absence of the correction, the PSE misses the majority of the moderately nonlinear section of the flow ($x \geq 60$). The sensitivity of stability methods to the accuracy of the mean flow is well known (Monkewitz and Huerre 1982; Jackson and Grosch 1991; Shin and Ferziger 1991), and these results further reinforce this by demonstrating the importance of profile corrections to the accurate modeling of nonlinear behavior. Additional evidence that the mean profile was accurately calculated appears in figure 2.13, a plot of the vorticity thickness, $\delta_\omega = (U_1 - U_2)/(d\bar{u}/dy_{max})$. The DNS and PSE predictions offer near-identical agreement for this $\bar{u}$-sensitive quantity, and the PSE even manages to capture the secondary growth in the thickness at the end of the calculation.

2.5.4 Run Time Comparison

With the accuracy of the PSE now verified, the run time comparison becomes the critical result. To fill the same domain as the DNS, the PSE calculation ran for fifteen minutes on a conventional workstation, which was roughly 350 times faster than the DNS calculation. Based on experience, it seems reasonable to characterize the speed up as $O(10^3)$ and $O(10^4)$ for two- and three-dimensional simulations, respectively. It should be noted that these numbers will reduce slightly when temporal rather than spatial DNS are used in the comparison. However, temporal simulations, while statistically very useful, do not allow certain aspects like acoustics or asymmetry in the velocity profile to be studied.

The other worthy measure of comparison is memory usage. The streamwise stepping procedure is extremely memory efficient in comparison to the global-domain-update nature of the DNS. This efficiency and the low computational cost make the PSE technique an ideal candidate for desktop workstation solutions of practical flow phenomenon.
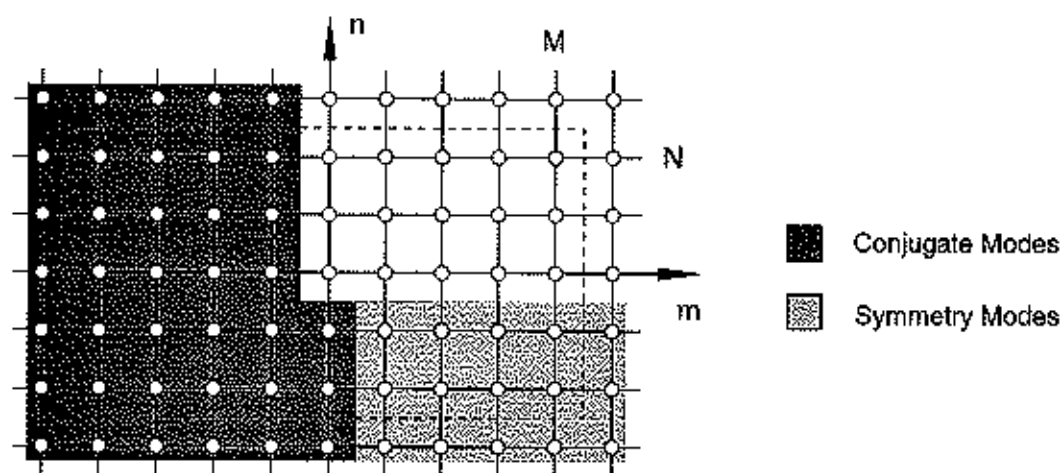
Figure 2.1: Schematic representing modes in the physical field (enclosed in the dashed line) and the modes that are excluded from the computation based on either conjugate (dark shading) or spanwise symmetry (light shading) arguments. Adapted from Herbert, 1993.
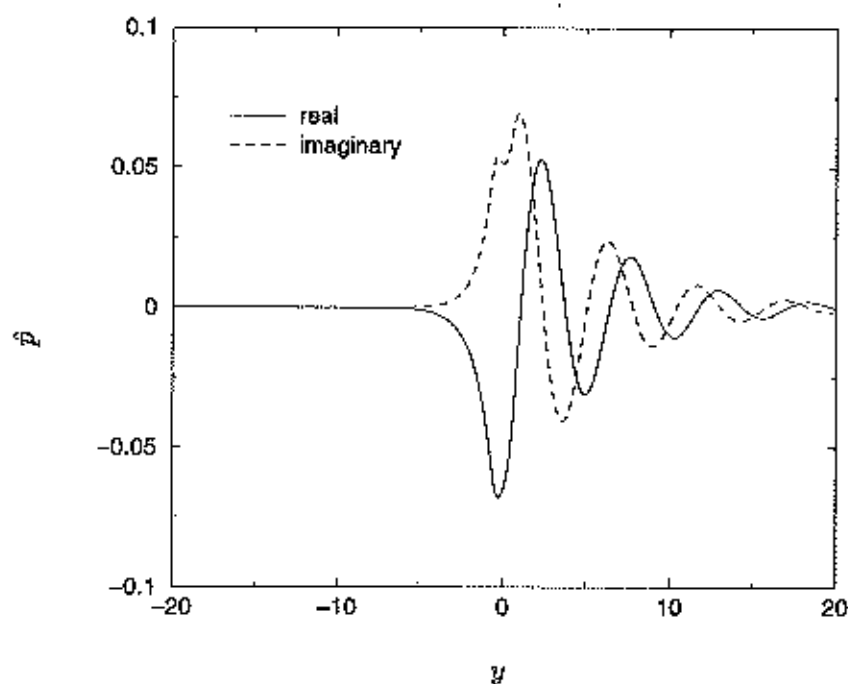
Figure 2.2: Decay of the pressure eigenfunction for a most-amplified supersonic slow mode in the two free streams ($M_c = 1.0$, $\Theta = 0.75$, $\phi = 1$, $s = 1.5$, $r = 0.5$). Note the different nature of the boundary conditions as $y \to \pm\infty$.
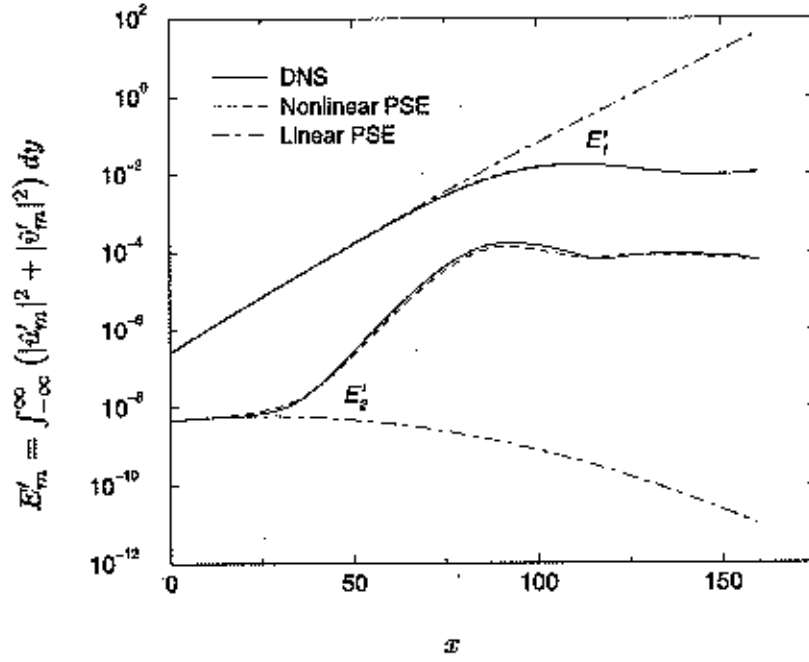
Figure 2.3: Comparison of DNS to linear and nonlinear PSE integrated energy results for the fundamental and first harmonic modes (M_c=0.5, r=0.6, s=1, $\Theta = 0$, M=8).
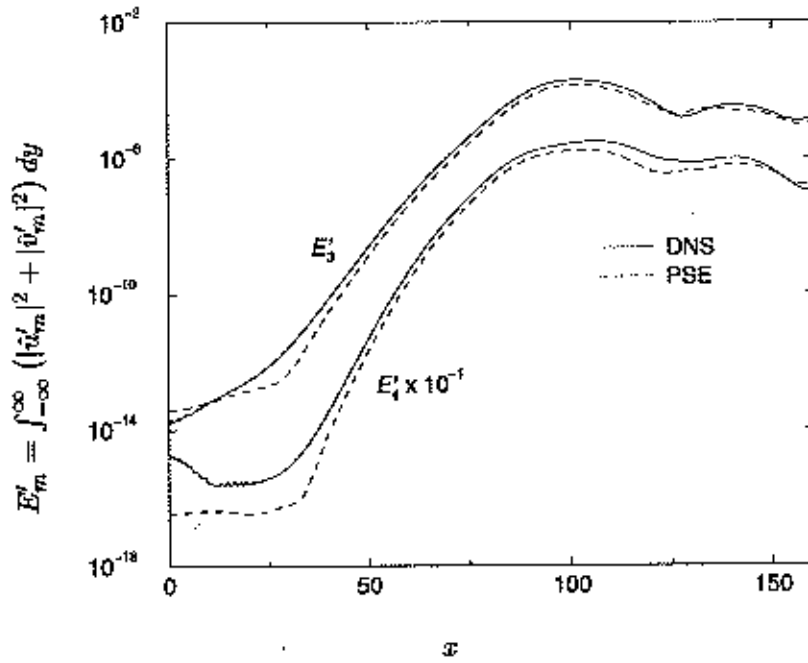
Figure 2.4: Comparison of DNS and PSE integrated energy results for two of the higher harmonics (M_c=0.5, r=0.6, s=1, $\Theta = 0$, M=8). Note that E_4' results are shifted for readability.
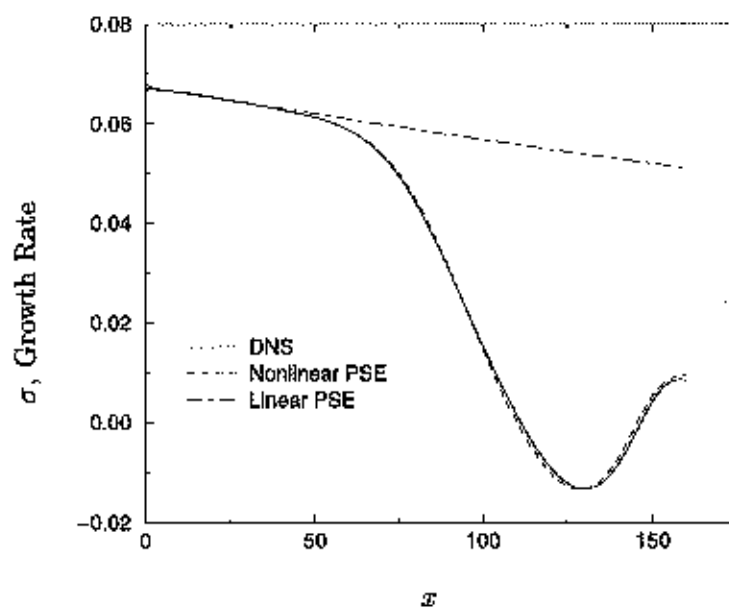
(a)
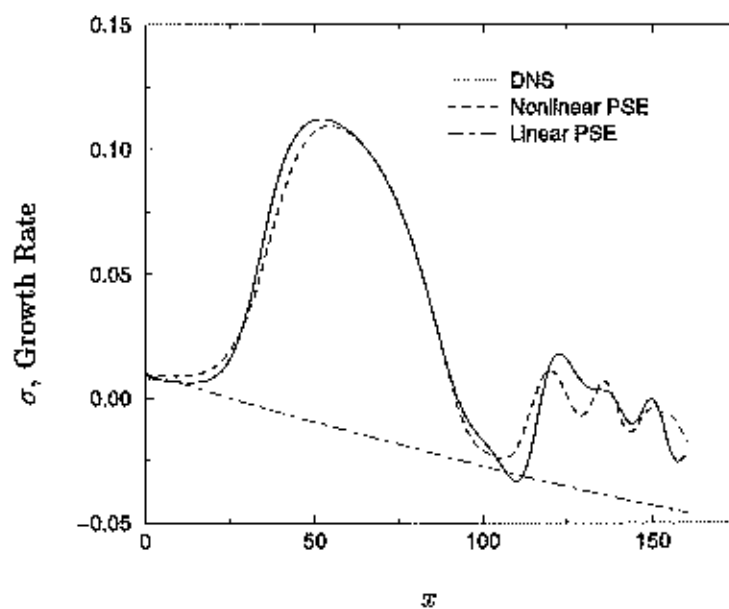
(b)

Figure 2.5: Comparison of both linear and nonlinear PSE growth rate predictions to the DNS results for the (a) fundamental and (b) first harmonic mode (M_c=0.5, r=0.6, s=1, $\Theta = 0$, M=8).
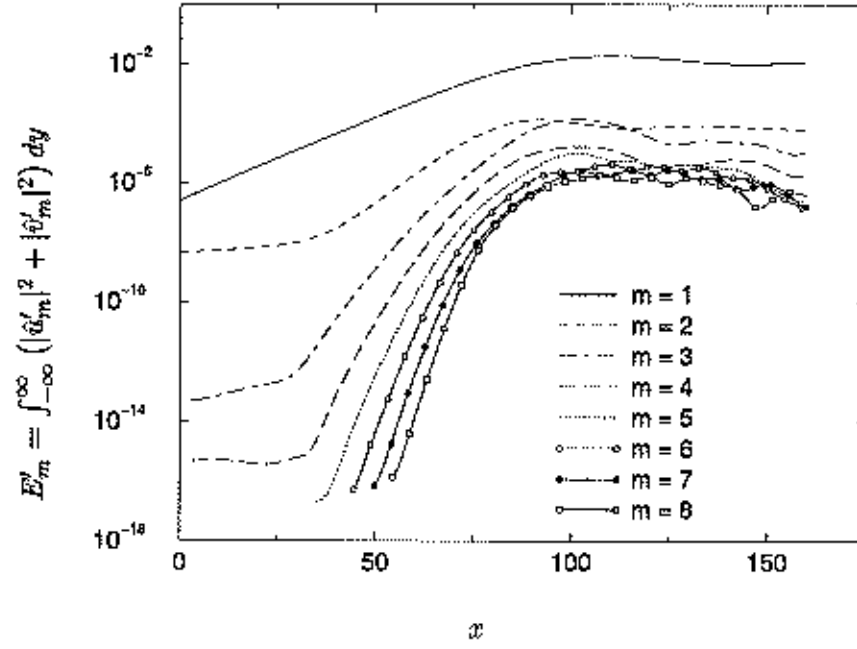
Figure 2.6: PSE Modal contributions to the integrated energy (M_c=0.5, r=0.6, s=1, $\Theta = 0$, M=8).
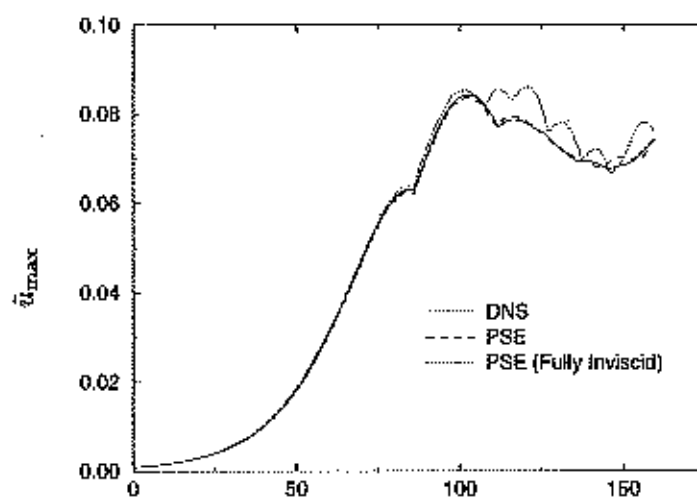
(a)
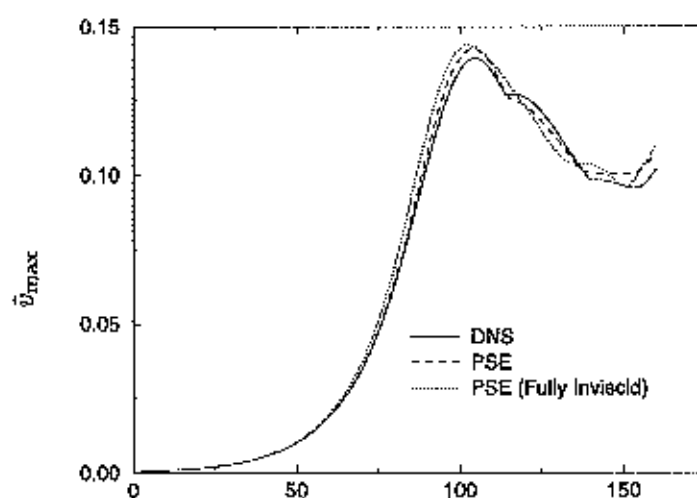
(b)

Figure 2.7: Comparison of inviscid and thin-shear-layer PSE predictions to DNS results for the maximum (a) u and (b) v fluctuation at a given streamwise position (M_c=0.5, r=0.6, s=1, $\Theta = 0$, M=8). Note that the kinks · present in both DNS and PSE calculations—are caused by the change in location of the maximum fluctuation.
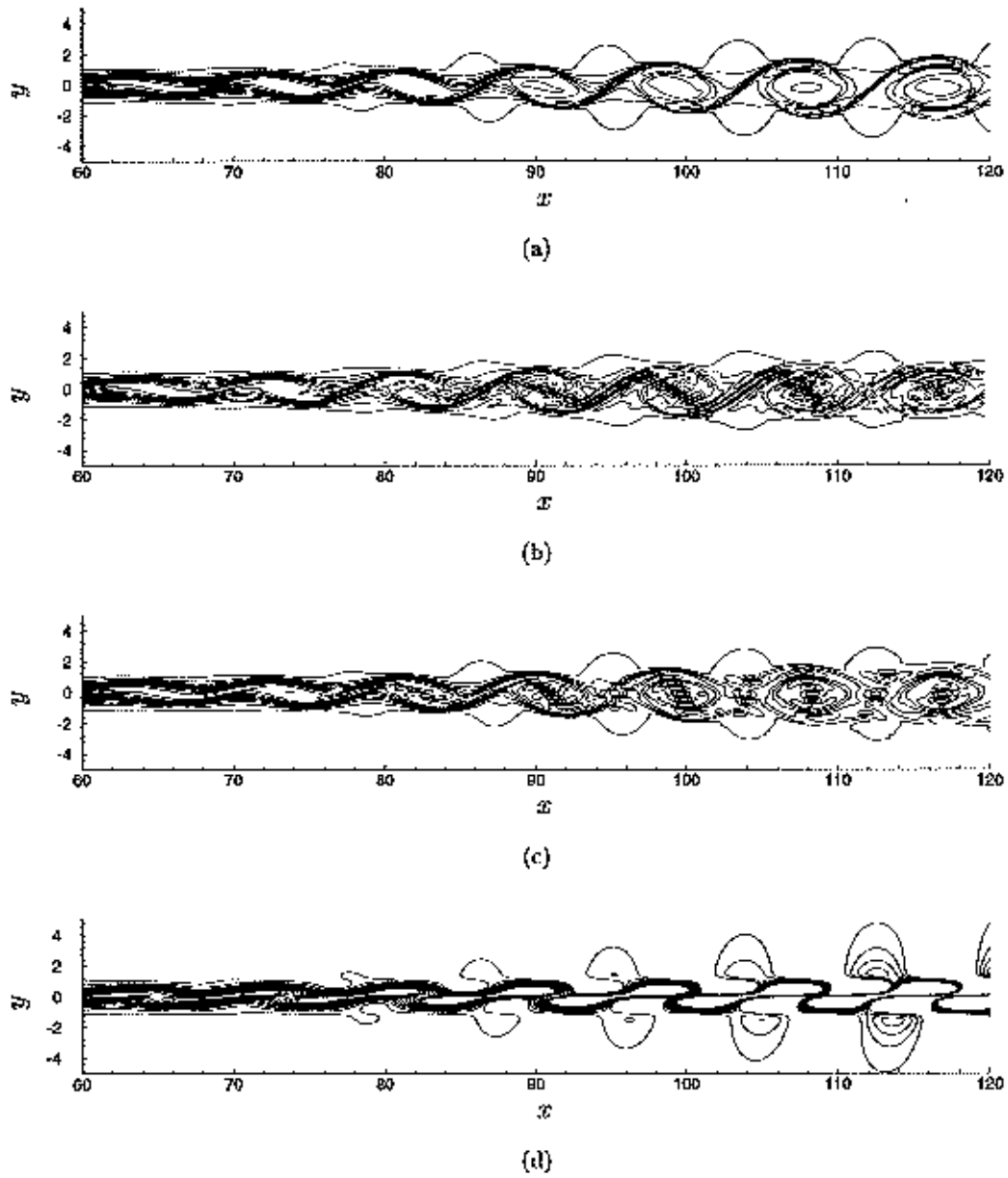
Figure 2.8: Comparison of spanwise vorticity contours for the test case (M_c=0.5, r=0.6, s=1, Θ=0) with the contour max and min set to -0.42 and -0.02 and $\Delta\omega_z = 0.04$. Results are plotted for (a) DNS, (b) nonlinear PSE with M=8, (c) nonlinear PSE with M=4, and (d) linear PSE.

(a)   (b)

(c)
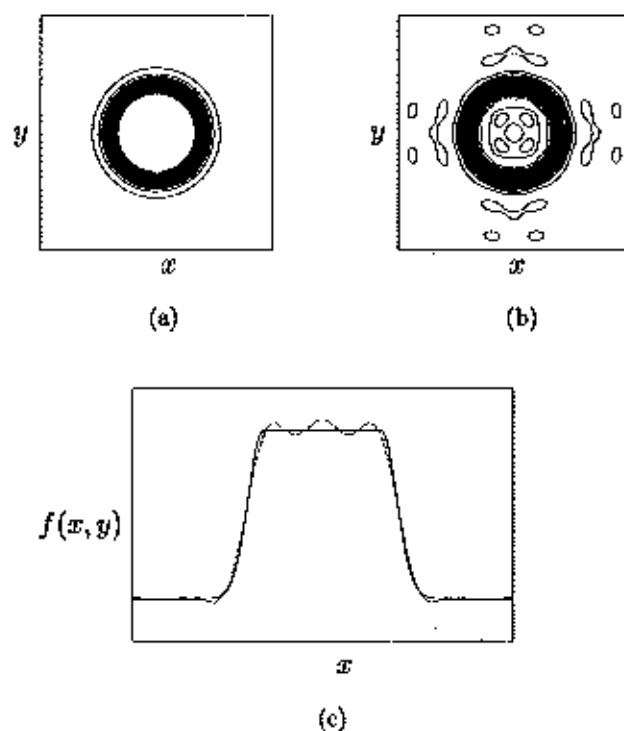
Figure 2.9: Comparison of a demonstration function represented with an infinite and truncated Fourier series. The test function is contour plotted in (a) with its 8×8 Fourier mode representation shown in (b). The two function values along a symmetry line are shown in (c), where the solid line indicates the original function (*i.e.* an infinite Fourier series) and the dashed line the eight-mode representation.
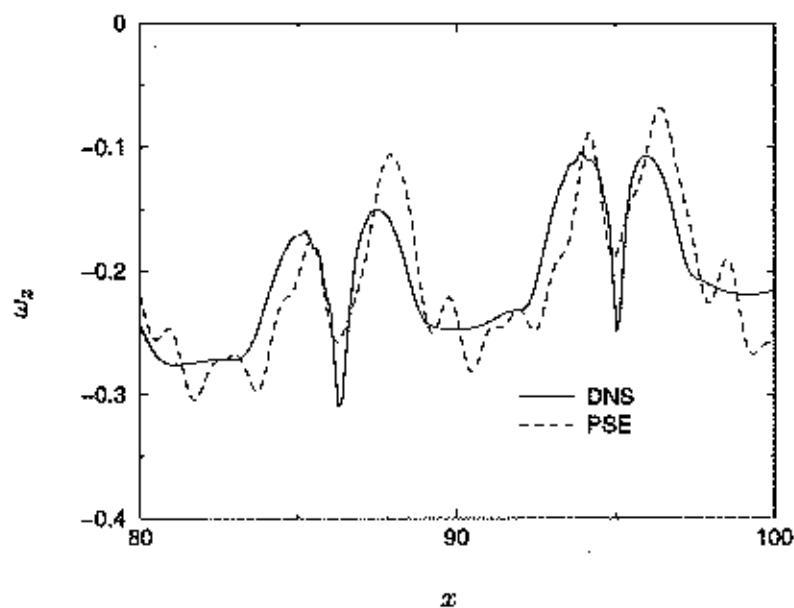
Figure 2.10: Comparison of PSE and DNS prediction for the centerline ($y=0$) spanwise vorticity ($M_c=0.5$, $r=0.6$, $s=1$, $\Theta = 0$, $M=8$).
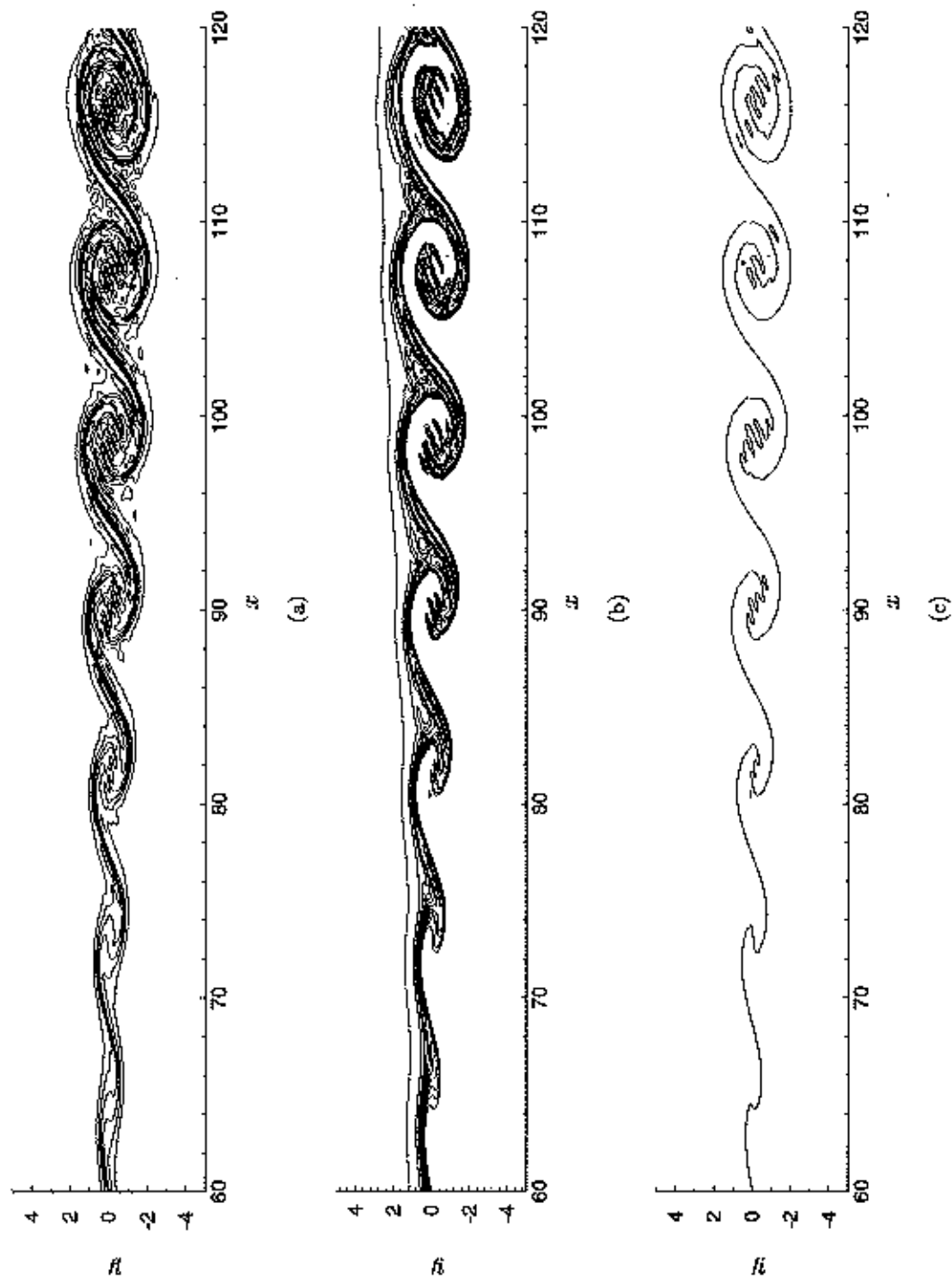
Figure 2.11: Mixture fraction, ξ, plots for the DNS test case ($M_c=0.5$, $r=0.6$, $s=1$, $\Theta = 0$, $M=8$) for (a) the full field, (b) oxidizer field, and (c) an isolated view of the flame sheet.
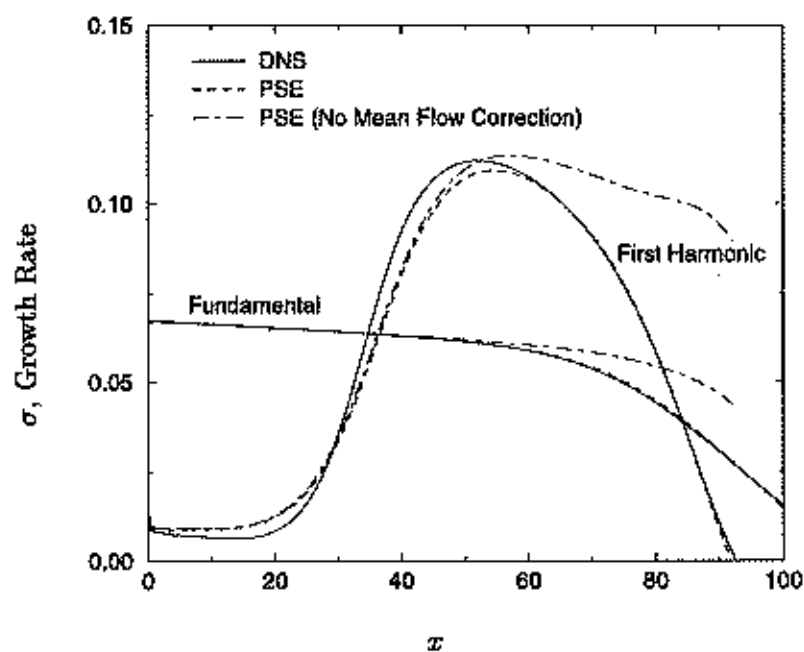
Figure 2.12: Comparison of PSE and DNS growth rates for the fundamental and first harmonic with no mean flow correction (M_c=0.5, r=0.6, s=1, Θ=0, M=8).
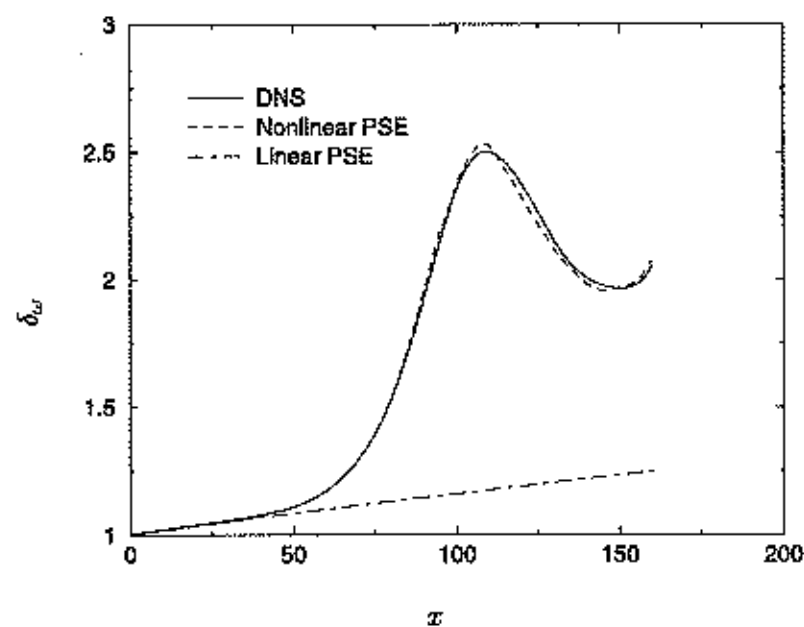
Figure 2.13: Comparison of linear and nonlinear PSE prediction to DNS results for the growth of the vorticity thickness in the test case (M_c=0.5, r=0.6, s=1, Θ = 0, M=8).

Chapter 3

Linear Stability Results

This chapter presents a detailed map of the compressible reacting mixing layer regimes in the five-dimensional parameter space of our investigation. Linear stability theory is used to provide an efficient but physically insightful analysis tool. The excellent comparison between linear theory and experimental results (see figures 1.5 and 1.6) allows the current work to explore a wide parameter space with confidence that its results will hold useful insight, provided the qualitative nature of linear stability results is acknowledged when extrapolating results to fully turbulent, reacting mixing layers.

The objective is to obtain a broad appreciation for how compressibility, heat release, and the flow-stream ratios of density, equivalence, and velocity affect the flow structure and what implications they have on mixing and combustion. To that end, the chapter begins in section 3.1 with a general introduction to the types of flow structure that exist in this parameter space, and an illustration of how the density-weighted vorticity profile can explain and predict this structure. A more thorough parametric study, where our interest is specifically focused on understanding how a given parameter can influence a change in the mixing layer structure, will follow in section 3.2.

The perspectives gained from this parametric study are then applied to help develop regime charts in section 3.3 that describe the change in the dominant flow structure across two-dimensional planes of the parameter space. Particular interest is placed on the locus of conditions where two instability modes are equally amplified, allowing the formation of 'colayer' structure. Combined with an understanding of how each parameter individually affects instabilities, these regime charts provide a complete picture of the structure expected to prevail in a compressible reacting mixing layer. They will also be used to guide the more detailed nonlinear stability investigations that will be the subject of the next chapter.

75

3.1 Overview of the Parameter Space

3.1.1 Density Weighted Vorticity

Before the parameter space of the mixing layer is investigated in detail, it is useful to present a general overview of the compressible reacting mixing layer. This begins with a discussion of the density-weighted vorticity, $\bar{\rho}\,d\bar{u}/dy$, the tool introduced in section 1.2 to explain the basic mechanism responsible for flow structure in the compressible reacting mixing layer. This profile will now be used in greater detail to both describe and predict the first-order behavior of the mixing layer.

A plot of how this profile changes under the influence of increasing compressibility and heat release is shown in figures 3.1 and 3.2. For situations of nonzero Θ, the position of the flame sheet is indicated by a kink in the profile caused by the infinitely-fast chemistry. The profile sequences in these two figures demonstrate that both combustion (through heat release) and compressibility (through the coupling of kinetic and thermal energy) act to increase the temperature and correspondingly decrease the density along the centerline. The twin-peaked $\bar{\rho}\,d\bar{u}/dy$ profile that results from this density deficit provides an explanation for the development of the fast and slow outer modes. It is also evident from the extrema locations of figures 3.1 and 3.2 that increasing M_c and Θ will move the outer modes away from the centerline. Note that a twin-peaked $\bar{\rho}\,d\bar{u}/dy$ profile is not a necessary condition for outer modes to be unstable. Instead, the instability condition of Lees and Lin (1946), $\bar{\rho}\,d\bar{u}/dy = 0$, is global in nature and is therefore only sufficient to predict that the flow will be unstable (Planché 1992). For example, the $\bar{\rho}\,d\bar{u}/dy$ profile development with compressibility in the absence of heat release (figure 3.1a) shows only a hint of two outer mode peaks for $M_c \leq 2$, although the results of section 3.2.1 will show their first appearance at $M_c \approx 1$. However, this does not diminish the utility of the density-weighted vorticity profile for providing basic insight into the flow physics.

The use of the density-weighted vorticity profile as a predictive tool also extends into forecasting the effects of density, equivalence, and velocity ratio variation on the flow structure. Situations of nonuniform density across the layer, shown in figure 3.3, demonstrate that the stream with higher density will have a larger $\bar{\rho}\,d\bar{u}/dy$ peak and hence the mode associated with that stream is expected to be the dominant instability. (Note that the density in these profiles has been normalized by the mean of the two free streams for visualization purposes; thus it is shown as ρ_m rather than ρ.) Figure 3.4 demonstrates that

the equivalence ratio affects the position of the flame sheet which, for example, will shift downward in position (*i.e.* towards the fuel in the slow stream) when the stoichiometry becomes lean. This shift results in a reduction of the $\bar{\rho}\, d\bar{u}/dy$ peak on the slow side coupled with a corresponding increase on the fast side, and it has a similar effect on the relative growth rates of the two modes. Finally, increasing the value of the velocity ratio r will reduce the shear and in turn the level of all $\bar{\rho}\, d\bar{u}/dy$ peaks, which results in the attenuation of all modal growth rates.

3.1.2 Eigenfunction Visualizations

Visualizations of flow structure derived from eigenfunction analysis provide a convenient way to validate qualitative predictions based on the $\bar{\rho}\, d\bar{u}/dy$ profile, and to develop a broad appreciation for the character of the compressible reacting mixing layer. The eigenfunction energy profile, $\hat{u}_i \hat{u}_i^\dagger(y) = \hat{u}\hat{u}^\dagger + \hat{v}\hat{v}^\dagger + \hat{w}\hat{w}^\dagger$, where $\dagger$ signifies a complex conjugate, provides an effective means to do this. To create a visualization that combines a view of both the distribution of vortical energy and the amplification rate, we define a new variable

$$\Psi = \frac{-\alpha_{i,\text{max}}}{-\alpha_{i,\text{max}_o}} \cdot \hat{u}_i \hat{u}_i^\dagger \tag{3.1}$$

where the energy term $\hat{u}_i \hat{u}_i^\dagger$ is calculated for the instability wave at the frequency and obliquity angle of the most amplified mode. The energy was normalized to have a maximum value of unity before being multiplied by the ratio of the amplification rate at the position of interest to a reference amplification. The reference chosen here is the canonical case of an incompressible, nonreacting, equal-density mixing layer with velocity ratio $r = 0$.

The Ψ profile that corresponds to this reference condition is shown in figure 3.5(a) as the first of three images that detail the influence of compressibility on the flow structure. There is only a single amplified mode at the reference condition. The peak of the energy profile is at the center of mixing layer ($y = 0$) and is therefore identified as the central mode. The broad distribution of energy in this case is the signature of the well understood large-scale structure that directly mixes fuel and oxidizer together. As compressibility increases to $M_c = 1$ in figure 3.5(b), the growth rate of the central mode drops to roughly 35% of the reference growth rate and the width of the energy distribution decreases. Also appearing at this compressibility, but at very low amplification rates, are the fast and slow outer modes. The outer modes are two dimensional at $M_c = 1$ but, in a result compatible with

both experimental and computational observations, the central mode has become three dimensional and our calculations predict it to be most unstable at $\theta = 56°$.

The difference in the obliquity of the modes results from the fact that the outer modes scale on the velocity difference between the flame position and the free stream of interest, rather than on the full velocity difference across the entire layer (Planché and Reynolds, 1991; Planché, 1992). (In the absence of heat release the flame position defaults to the mixing layer centerline.) Because the outer modes scale on only a fraction of the shear across the layer, it follows that they will be less susceptible to compressibility effects in comparison to the central mode, which scales on the full shear. This is reflected in the lower obliquity angles of the two outer modes—at $M_c = 1$ they are in fact two dimensional—relative to the central mode.

Consistent with the ideas presented in our discussion based on the $\bar{\rho}\, d\bar{u}/dy$ profile, the results at $M_c = 2$ in figure 3.5(c) indicate that the growth rates of the outer modes strengthen relative to the central mode with increasing compressibility. At this M_c level, all modes are three dimensional although the dominant outer modes are, predictably, found to exist at a shallower angle—56° and 52° for the fast and slow modes, respectively—than the 68° angle of the central mode. Figure 3.5(c) also demonstrates that the distribution of outer mode energy is more compact at high compressibility. Comparing these compact profiles to the broad distribution of the central mode suggests that outer-mode-dominated flows will be less efficient at mixing reactants from the two streams.

The outer modes will dominate the flow structure when heat release effects become significant. This situation is documented in figure 3.6, which shows the effect of increasing heat release relative to the nonreacting case at $M_c = 2$. A comparison between the eigenfunction energy profiles at $M_c = 2$, $\Theta = 0$ in figure 3.6(a) and $M_c = 2$, $\Theta = 1$ in 3.6(b) demonstrates that the introduction of heat release at this Mach number entirely stabilizes the central mode but destabilizes the outer modes. Increasing heat release to $\Theta = 2$ in figure 3.6(c) indicates that the outer mode destabilization continues with increasing heat release — the slow mode now dominates the flow structure. It should be noted that the discrepancy between the fast and slow outer mode amplification rates even for this stoichiometric and uniform density case results from the slight asymmetry of the self-similar input profiles. The nature of the inefficient two-step mixing process that was detailed in the DNS studies of Planché (1992) is evident in the compact and separate energy distributions shown in figure 3.6(c). Further, the dominance of the slow mode growth rate for these conditions is expected to have an

additional negative impact on combustion by entraining significantly more fuel from the slow stream than oxidizer from the fast. This situation motivates particular interest in the 'colayer' case where these two modes are equally amplified.

The influence of the density ratio on the flow structure is seen in figure 3.7. This sequence of energy profiles details the effect of biasing the density toward the fast (figure 3.7a) and slow (3.7c) side relative to the equal density $M_c = 2$, $\Theta = 0$ case shown in figure 3.7(b). The predictions made from considering the $\bar{\rho}\,d\bar{u}/dy$ profile are again clear in the results. Doubling the density on the fast side causes the fast and central modes to be near-equally amplified, forming one variety of colayer structure in the flow, while the same change is observed to stabilize the slow mode. The increase in density on the fast side has also moved the position of all three vortical modes upwards in the layer. High density on the slow side (figure 3.7c) shows the opposite result, with this change causing the formation of a central/slow mode colayer and a general shift towards the slow side. A comparison of the relative amplification rates for $s = 0.5$ and $s = 2$ reflects the experimentally-observed result that the layer is more unstable when the slow free stream has greater density (Brown and Roshko, 1974).

More detailed insight into the flow structure can be obtained by using the eigenfunction results to calculate streakline images for each mode from a flow field generated using equations (2.38) and (2.41). Following the method of Hama (1962), two-dimensional streakline profiles emerge from a locus of particle positions that are released at an initial location, (x_o, y_o), at a number of different times, t_o, and integrated to a common end time according to

$$\frac{dx}{dt} = \bar{u}(y) + \epsilon_o\,\hat{u}(y)\,e^{i(\alpha x + \beta z - \omega t)}, \tag{3.2a}$$

$$\frac{dy}{dt} = \epsilon_o\,\hat{v}(y)\,e^{i(\alpha x + \beta z - \omega t)}, \tag{3.2b}$$

where the initial magnitude, ϵ_o, was set to 0.001.

The use of streakline visualizations allows some insight into the development of the scalar field, which is of particular interest to our investigation. The streaklines for $M_c = 2, \Theta = 0$ shown in figure 3.8 very effectively contrast the compact nature of the outer mode structure relative to the central mode. Although these visualizations are qualitative in nature, the conclusion that the outer modes will inhibit the mixing of fuel and oxidizer follows clearly from the comparison; this subject will be explored more quantitatively in chapter 4. Figure 3.8 is also useful for providing an indication of the spacing between the large-scale

structures. In proportion with their compact distribution, the outer modes have significantly shorter wavelengths than the central mode, with the fast mode being approximately half that of the slow. These relative wavelength observations hold reasonably well across the entire parameter space that was investigated. The one exception to this concerns the velocity ratio, which tends to reduce the dominant wavelength difference between modes as it increases.

3.2 Parametric Investigations

With a general appreciation for the connection between structure and mixing now developed, the individual effect of the five parameters is investigated in more detail. This study was done to determine each parameter's ability to influence change in mixing layer's flow structure. This information will be particularly useful in the development and comprehension of the regime charts that map the change in structure of the mixing layer (to be discussed in section 3.3).

3.2.1 Compressibility

The amplification-rate response of all three instability modes to compressibility is shown in figure 3.9 for heat release values starting from zero with increments of $\Delta\Theta = 0.5$. The commonly-reported curve representing the stabilization of the central mode with rising compressibility appears in figure 3.9(a). As discussed in section 1.3.2, the most promising explanation for this stabilization appears in the work of Vreman *et al.* (1996), who used a relation between the growth rate and the production of turbulent kinetic energy, and data from DNS results to show that reduced pressure fluctuations stabilize the mixing layer by affecting production through the pressure-strain-rate redistribution term. This theme will also be explored in section 4.4 to explain the observed delay of vortex pairing with compressibility. Results for the central mode in figure 3.9(a) are shown at only three Θ values due to a transition in the flow structure at higher heat release values that excludes the amplification of this mode (see section 3.2.2 for details). The • symbols in these plots identify the end points of the locus of conditions where a *local maximum* in the amplification rate for the specified mode has been found in the search in the (ω, θ) plane, via the method outlined in section 2.2.3.

The results for the outer modes are shown in figures 3.9(b) and 3.9(c). Considering

both the fast and slow mode results together, we see that the growth rate of the outer modes is also suppressed, although the effect on the outer modes is, in general, less severe. Some insight into the reason for this can be found by returning to the density-weighted vorticity ideas presented in section 3.1.1. As M_c increases, the peaks of the $\bar{\rho}\, d\bar{u}/dy$ profile begin to develop and therefore suggest that the formation mechanism for the outer modes strengthens with compressibility. However, this strengthening is more than balanced by the attenuating influence of compressibility that operates on all instability modes; presumably the pressure-strain mechanism detailed by Vreman *et al.* (1996) in their study of the central mode can be extended to predict the effects on the outer mode growth rates. Another factor that affects the growth rate is the shearing velocity. As mentioned in the previous section, Planché and Reynolds (1991) introduced the idea that the outer modes scale on the velocity difference between the flame position and the free stream of interest, rather than on the full velocity difference across the layer. Again, the intuition behind this concept comes from the double-peaked nature of the density-weighted vorticity profile that has a minima at the flame position. This scaling implies that, in comparison to the central mode, the outer modes have a lower sensitivity to compressibility and its attenuating effect because they scale on a fraction of the velocity difference rather than on the complete shear across the layer.

In describing these competing factors, the first-order effect is evidenced in the results of figure 3.9: the amplification of the outer modes is suppressed with increasing M_c, although not to the same degree as the central mode, which receives no benefit from the change in the $\bar{\rho}\, d\bar{u}/dy$ profile. Increasing compressibility was also found to increase the wavelength of the dominant central mode instability (α_r decreases in a shape similar to figure 3.9a), in agreement with experimental observations. The slow mode demonstrated the same evolution but to a lesser extent, and the fast mode showed relative independence in its dominant structure spacing to increasing M_c. Finally, the effect of compressibility on the phase speeds of the three modes or, equivalently, on their position in the layer is shown in figure 3.10. Increasing compressibility is seen to cause a progression in the position of the outer modes toward their respective free streams while the central mode location remains unchanged; these observations directly reflect changes observed in the $\bar{\rho}\, d\bar{u}/dy$ profiles of section 3.1.1.

It should be re-emphasized that the amplification rate plots in figure 3.9 represent only local maximums found according to the procedure outlined in section 2.2.3. This presentation can produce what appear to be anomalies in the results. For example, the

outer mode termination points, marked by • symbols, are not meant to suggest that a given mode is no longer amplified at M_c values beyond this point, but rather that there is no longer a recognizable maximum for that mode. According to the linear stability model of exponential growth rates without saturation, only a local maximum value will be distinguishable from modes of adjacent frequencies in the developed flow structure.

The shortcomings of this procedure are demonstrated in figure 3.11(a) which plots amplification against frequency at $\theta = 0°$ for three M_c values that bridge the fast and slow mode introduction points at $\Theta = 0$. The corresponding phase speeds are shown directly below it in figure 3.11(b) to provide identification—based on phase speed—of the different modes. At $M_c = 0.95$, the one peak in the profile is identified as the central mode from its 0.55 phase speed. (It should be noted that its maximum amplification rate occurs at much higher obliquity, $\theta = 56°$.) At $M_c = 1.0$ the slow mode (dotted line) has appeared and the fast mode is nearly defined as a local maximum. By $M_c = 1.05$ the transition is complete, and peaks for each of the fast ($c_r = 0.60$), slow ($c_r = 0.44$) and central ($c_r = 0.54$) modes are distinct. In this way, the fast mode is able to first appear with increasing M_c in figure 3.9(b) at a nonzero amplification rate.

3.2.2 Heat Release

Some of the effects of heat release on growth rates of the three instability modes are shown in the plots of figure 3.9. But to gain more direct insight into the effect of this parameter, it is instructive to plot the amplification factor of each mode as a function of Θ at compressibility levels starting at zero and increasing at increments of $M_c = 0.5$. Results for the central mode are presented in figure 3.12(a) and show the attenuating influence of heat release on the amplification of the central mode. The similar nature of this effect at all compressibilities can be seen if the profiles are normalized by $-\alpha_{i,max}$ at $\Theta = 0$ for each value of M_c — this procedure provides an excellent collapse of the data. Each of the plotted lines ends with a symbol: ○ denotes a transition point from the central to the slow mode (to be discussed below) while • again marks the last point where the given mode was found to be amplified with a local maxima in the (ω, θ) plane.

For the incompressible case, our central mode growth rate calculations were shown in section 1.3.1 to compare well with the experimental results of Hermanson and Dimotakis (1989), who related the central mode stabilization to a generally observed reduction in turbulent shear stresses as heat is added to the flow. In contrast to this, the amplification

rates of both outer modes increase with heat release (see figures 3.12b and 3.12c), an observation that follows from the development of the $\bar{\rho}\, d\bar{u}/dy$ profile. Unfortunately, the experiments of Hermanson and Dimotakis were limited to the range $\Theta < 0.8$, a point shortly before our calculations predict that the dominant instability will change to a slow mode at $\Theta \approx 0.95$. While the stability calculations predict that the fast mode will first appear at $\Theta \approx 0.6$, its growth rate is less than half that of the central mode, so it is not inconsistent that its influence was not observed in the experimental results.

Figure 3.12(b) shows that heat release promotes the fast mode amplification rate when the influence of compressibility is significant (*i.e.* when $M_c \geq 0.5$) and has little effect below that level. However, the slow mode results of figure 3.12(c) demonstrate the opposite behavior — the greatest absolute gains in amplification rate with rising Θ appear in the domain of low compressibility. The low-compressibility coupling between the central and slow modes is explained in greater detail in figure 3.13. Plots of the amplification rate and corresponding phase speed are shown for heat release values that span the transition point at $M_c = 0.4$. Tracing the frequency of the $-\alpha_i$ peak to the phase speed plot below it identifies the $\Theta = 0.8$ and 0.9 peaks as central modes, while the distinct drop in c_r for peaks at $\Theta \geq 1.0$ are related to slow modes. It is clear from the profiles of figure 3.13(a) that the transition from central to slow mode is specified when $-\alpha_{i,\max}$ reaches a local minima with increasing heat release; this measure was used in the plots of figure 3.12.

The change in phase speed for all modes with heat release is shown in figure 3.14. Similar to the effects of compressibility seen in the previous section, increasing heat release moves both outer modes towards their associated free streams. The central mode is largely unaffected by increasing heat release, with a notable exception at $M_c = 2.0$ where another type of central to slow mode transition appears to be underway. The results for the change in wavenumber were found to increase the wavelength of all instability modes. This effect was strongest in the outer modes, while the central mode wavelength increased in a milder manner. At first look, this outcome appears contrary to the experimental results of Hermanson and Dimotakis (1989) that showed a slight decrease in structure spacing with increasing heat release (they also noted that this change will cause a decrease in entrainment ratio). They hypothesized that this decrease is caused by a suppression of vortex amalgamation (pairing). In a turbulent flow where multiple pairings occur, this could have the net effect of decreasing the structure spacing despite a slight increase in the length scale of the fundamental disturbance. The close correlation between instability growth rates and

pairing rate, which supports Hermanson and Dimotakis' theory, will be demonstrated in section 4.4. Thus, it seems likely that our linear stability conclusions are consistent with the experimental observations; we just happen to be looking at different parts of the flow development.

3.2.3 Density Ratio

The effect of density ratio variation on the amplification rate of the three stability modes are shown in figure 3.15 at three different compressibility values, all in the absence of heat release. Results are plotted across the range of $s = 1/4$ to $s = 4$, with $\diamond$ symbols used here to denote the end limits of this range in the results and, as in the previous sections, $\bullet$ details the point where a given mode is no longer maximally amplified. Starting at the incompressible state in figure 3.15(a), we see that the growth rate of the central mode scales quite strongly with the density ratio parameter in our calculations. The linearity of this response is striking considering that, from a physical perspective, the values of $s = 1/2$ and $s = 2$ are equivalent perturbations with respect to a uniform density flow.

These results are consistent with the trend, but not the scale of Brown and Roshko's (1974) experimental results: they reported that a change in the density ratio from $s = 7$ to $s = 1/7$ resulted in a decrease of the spreading angle by a factor of two for $r = 0$. The discrepancy can partly be explained by the fact that Brown and Roshko scaled their $s = 7$ growth rate results linearly with a velocity parameter $\lambda = \Delta U/(U_1 + U_2)$. However, stability results of Sandham and Reynolds (1990) predicted that the scaling is quadratic. Their stability calculations matched Brown and Roshko's data at $\lambda = 0.45$ and $\lambda = 0.75$ for $s = 7$, although with only these two data points, the extrapolation to $\lambda = 1$ ($r = 0$) is certainly not conclusive, and it should be noted that such conclusions are heavily dependent on the mean flow used in the stability analysis.

Frieler (1992) performed the most thorough study to date on density ratio effects. These experiments looked at the variations from $s = 1/8$ to $s = 8$ and found a 25% change in growth across this range at $r = 0.386$. In the range from $s = 1/4$ to $s = 4$, the growth rate changed only 15%, compared to the 70% prediction for linear stability at this r value. The significant discrepancy suggests that the computed velocity and density profiles differ from those of the experiment. This is indeed the case: Frieler's flow had constant temperature boundary conditions while our profile, which assumes constant molecular weight, varies considerably in temperature during density changes. The combined effect of density *and*

temperature changes in our results causes a considerably more dramatic effect. In discussing his results, Frieler also acknowledged the importance of coupling between velocity and density ratios. He makes the suggestion—seconded here—that a detailed experimental investigation of the density ratio effect at different velocity ratios should be undertaken to correctly resolve and isolate these different effects.

As compressibility is increased to $M_c = 1$ in figure 3.15(b), the central mode maintains its near-linear scaling across the entire range of s values. At this compressibility value the outer modes are also present, but note that their appearance is biased toward conditions where the stream opposite to their associated side has the greater density. For example, at $M_c = 1$, the fast mode exists as an amplified instability across the range $s = 1.7$ to $s = 4$ where the slow side is more dense. As the density ratio is reduced below $s = 1.7$, only the central and slow modes are present as peaks in the $-\alpha_i$ surface in the (ω, θ) stability plane. However, as compressibility is increased to $M_c = 2$ in figure 3.15(c), both outer modes become strong enough to exist across the full range of s values considered, and now it is the weakened central mode that exists for only a restricted range of values centered around $s = 1$.

The results at this high compressibility are consistent with what was predicted from the density-weighted vorticity profiles of section 3.1.1: outer modes associated with the heavier stream will dominate the flow structure with significantly larger growth rates than the other modes. An interesting aspect of the amplification rate plots in figure 3.15 is the similar response of the central and slow modes to changing density ratio for $M_c \geq 1.0$. The amplification rate of the slow mode increases with s and follows what we would predict, but the similar response of the central mode, although it is seen in experimental results, is interesting since the $\bar{\rho}\, d\bar{u}/dy$ profile offers no *a priori* knowledge of this. Rather, this mode is dominated by changes in the baroclinic vorticity generation term (Soteriou and Ghoniem, 1995).

It should be noted that our results, which indicate that the destabilization of the central mode with increasing s is present at all compressibility levels, are in contrast to the calculations of Ragab and Wu (1989), who suggested that the same change in s would become attenuating at high compressibility values. The discrepancy is likely due to their consideration of only two-dimensional modes, although it is now understood that the mixing layer is entirely three dimensional under those conditions.

The modal phase speed results of figure 3.16 offer further insight into the influence of

the density ratio on flow structure. Plots are shown at three different compressibility levels along with the prediction from an incompressible vortex sheet model (Drazin and Reed, 1981)

$$c_r = \frac{\rho_1 U_1 + \rho_2 U_2}{\rho_1 + \rho_2}. \tag{3.3}$$

True comparison of the model and stability predictions is only available at $M_c = 0$, and the results of figure 3.16(a) indicate general agreement. The major cause of the discrepancy, particularly evident in large s values, is the nonsymmetric self-similar profile of the stability calculations. Figure 3.16(c) plots results at $M_c = 2$, where all three modes are well defined, and the density ratio is found to nearly equally affect the location in y of each mode across the range of considered conditions. This figure also demonstrates that the central mode is entirely distinct from the outer modes at the termination points, a fact that was not clear in figure 3.15(c).

The phase speed results shown in figure 3.16 reflect the prediction from the density-weighted vorticity profile that phase speeds of all modes move in the direction of the density bias. Dimotakis (1986) offered an explanation for this behavior based on pressure-matching at the stagnation points between the vortical structures. An alternative rational was introduced by Soteriou and Ghoniem (1995), who developed a model for the movement based on baroclinic vorticity production. Both explanations can be extended to the outer modes and this is seen in practice in the results of figure 3.16.

For situations where the outer modes dominate the flow structure, the results of this section suggest that a nonuniform density will adversely impact the mixing performance through two means: first, it will heavily bias the amplification of the mode associated with the heavier stream, causing a one-step, off-center mixing process to develop and second, it will push the dominant mode further away from the other reactant stream. Through the influence of these two mechanisms it is clear that the density ratio is a very important parameter in determining both the structure and mixing performance of compressible reacting shear layers.

3.2.4 Equivalence Ratio

The basis for our investigation into the effect of stoichiometry on the mixing layer structure evolves from the concept of Planché and Reynolds (1991, 1992) to fully parameterize the equivalence ratio effect on growth rates through the use of a flame convective Mach

number. The idea behind this new compressibility parameter is simply to modify the definition of M_c (see equation 1.1) to reflect the fact that the correct convective reference frame for each of the outer modes is the average of the flame sheet and the relevant free-stream velocity. This approach yields two new parameters,

$$M_{f1} = \frac{U_1^* - U_f^*}{a_1^* + a_f^*} \quad \text{and} \quad M_{f2} = \frac{U_f^* - U_2^*}{a_f^* + a_2^*},$$

where f denotes quantities that are evaluated at the flame sheet position. In the case of a nonreacting flow, the flame sheet velocity simply defaults to the mean of the two free-stream speeds. Using the definition of M_c and $M_{f1,2}$ where appropriate, Planché and Reynolds were able to provide an improved collapse of two-dimensional amplification rate data compared to what had been possible when M_c alone was used to parameterize the effect of compressibility on all three stability modes.

The ability of these new definitions to parameterize compressibility results provides confidence in the notion that the growth rate of the outer modes scales on the shear between the flame sheet and the relevant free stream. This has direct implications when considering the effect of changing stoichiometry on the mixing layer structure. In a conventional situation where the fuel is present in the slow side of the mixing layer, a reduction in the equivalence ratio will reduce the flame sheet velocity and will therefore cause a drop in the shear driving the instability of the slow mode and, correspondingly, an increase for the fast mode. Further, for the same example, the emphasis as a whole towards the slower side of the mixing layer will be reflected in the phase speeds of the most amplified disturbances.

Changes in the shear are directly correlated to changes in the growth rate, but they logically also have an effect on the compressibility that is felt by the outer modes. An outer mode that has had its driving shear reduced (*e.g.* the slow mode in a situation of lean stoichiometry) will also be less susceptible to the attenuating effects of compressibility as the Mach number increases. One measure of the compressibility influence is the M_c value where a mode becomes three dimensional — plots of this appear in figure 3.17. The mode transition boundary corresponds to the locus of points where the maximum amplification rate at $\theta = 0°$ and $10°$ are equal. In contrast to the lack of influence on the central mode, the slow mode exhibits a large extension of the two-dimensional region with decreasing equivalence ratio. The fast mode, which observes an increase in both shear and therefore compressibility, has a progressively earlier transition.

A more detailed view of the equivalence ratio effect can be seen in the plots of amplification rate against compressibility at a fixed heat release that are shown in figure 3.18. Each of the three modes appears at a representative heat release value: the central mode at $\Theta = 0.5$ and the outer modes at $\Theta = 1.0$. The central mode of figure 3.18(a) appears to stabilize slightly with reducing equivalence ratio, although this effect is only noticeable at low compressibilities and for most of the domain the amplification rate difference is negligible. The more interesting case occurs for the outer modes. Starting first with the fast mode results of figure 3.18(b), the equivalence ratio reduction and the corresponding drop in the flame sheet position increases the driving shear and this understandably destabilizes this mode at low M_c values. However, as the Mach number increases, the same high shear that previously augmented the amplification rate now makes the mode more susceptible to the effects of compressibility. By $M_c = 1.0$ any enhancement provided by a lean stoichiometry is essentially lost. Indeed, at $M_c = 1.5$ the situation actually reverses itself and the lean stoichiometry appears as an attenuating influence on the growth of this mode relative to the $\phi = 1$ case.

Exactly the opposite behavior occurs for the slow mode amplification rates shown in figure 3.18(c). Comparing the equivalence ratio effect of the two outer modes at low compressibility, we see that the amplification rate of the slow mode is more susceptible to changes in stoichiometry. However, the slow mode shows the same general collapse of the growth rate predictions for $M_c > 1.0$. It should be noted that the kinks in the growth rate profiles of figure 3.18(c) are caused by the transition of the slow mode from a case where it is subsonic with respect to both free streams to a situation where it is supersonic and subsonic with respect to the fast and slow streams, respectively (see Jackson and Grosch, 1989 for details).

These results suggest that the influence of the equivalence ratio is essentially restricted to low compressibility situations. Since our primarily interest is focused on conditions of significant compressibility and heat release, this result renders the parameter ϕ as an interesting but less important factor in determining the dominant mixing layer structure when compared to the effect of M_c, Θ, and s variations. This perspective will be used to simplify the development of the regime charts presented in section 3.3.

3.2.5 Velocity Ratio

Most analyses of the velocity ratio effect on the growth rate of either experimental or computational results are done by considering the scaling performance of the parameter $\lambda = \Delta U/(U_1 + U_2)$. The extension of this parameter to compressible reacting conditions with outer mode structure will be the subject of section 3.4. For the moment, however, our interest is in evaluating the influence of the velocity ratio on the dominant mixing layer structure.

This issue is best investigated by plotting the change in amplification rate of a given mode as r increases from zero. Four of these plots are presented in figure 3.19 to test the amplification rate response in conditions of high compressibility, high heat release, and two cases where compressibility and heat release appear together at low and high values, respectively. The specific values of M_c, Θ, and s for each case were selected to represent colayer conditions (*i.e.* where two or three modes have similar amplification rates). Beyond providing insight into how changes in r affect the dominant structure, these choices allow the sensitivity of colayer conditions to r variation to be tested, a point of particular interest to the regime chart development of the following section. All calculations were proceeded until r reached a nondimensional value of 0.8, and this arbitrary termination point is denoted with a o symbol. It should be noted that maintaining a constant, nonzero M_c value requires the fast stream Mach number to increase as r is increased via equation 1.1.

The colayer condition formed at high compressibility between the slow and central mode at $M_c = 2.75$, $\Theta = 0$, and $s = 1$ is pictured in figure 3.19(a). The central and slow modes decrease in amplification rate with near-identical behavior. The less sensitive response of the fast mode suggests that these conditions will generate three modes of equal amplification as r increases. These characteristics generally hold true across the wide range of conditions that are presented in figures 3.19(b) through 3.19(d); the slow and central modes share a similar amplification rate attenuation with increasing r while the fast mode follows the same behavior but with slightly less sensitivity. It follows that the effect of the velocity ratio parameter on the structure manifests itself as a slight bias to the fast mode as r increases. However, this bias is small in comparison to the effect that compressibility, heat release, and the density ratio parameters have on determining the dominant instability mode. This suggests that variations of r are not a primary factor in determining the flow structure. Similar to the outcome of our equivalence ratio discussion, this result can be used to help simplify the regime charts that are the next subject to be addressed.

3.3 Regime Charts

Summarizing the results from the previous section, our parametric study suggested that compressibility, heat release, and density ratio effects were the most important parameters in determining the dominant flow structure; the effect of the equivalence and velocity ratios were, in general, found to be less critical. This conclusion allows the formulation of regime charts of the mixing layer structure to be restricted to M_c, Θ, and s parameters, provided certain caveats discussed in the previous section are acknowledged. In particular, the important effect of stoichiometry at low compressibility levels and a slight bias towards the fast mode with increasing velocity ratio should be kept in mind while viewing these results, all of which are for $\phi = 1$ and $r = 0$.

With this simplified perspective the parameter space is reduced to a three-dimensional problem and the task of presenting regime charts becomes manageable and the results more meaningful. A good appreciation for the interaction of the three dominant parameters can be developed by taking two-dimensional cuts through the parameter space to investigate regions where specific modes will dominate. The important aspects of the three different plane views are presented below to help improve our understanding of the mixing layer's structure.

3.3.1 Regime Charts in the (s, Θ) Plane

As a first step in the regime chart description, the effect of rising compressibility on flow structure in the (s, Θ) plane is shown in figure 3.20. Note that the density ratio axes have been stretched to maintain symmetry about $s = 1$. For example, $s = 1/2$ and $s = 2$ are positioned at equivalent displacements from the uniform-density case. Boundaries separating various modes were established by finding the locus of conditions where $\alpha_{i,\max}$ for the two modes agreed within 0.5%. Considering first the shape of the colayer boundaries for low M_c values in figure 3.20(a), we can again appeal to the density-weighted vorticity profile to help explain some of the prominent features of this chart. The evolution of the $\bar{\rho}\, d\bar{u}/dy$ profile toward two outer peaks with higher heat release is reflected in the progression of the regime chart from a central to outer mode structure with increasing Θ. Also, the correlation of regions where an outer mode (fast or slow) dominates with regions where their companion streams have greater density follows from predictions based on the $\bar{\rho}\, d\bar{u}/dy$ profile.

The wedge shape of the central mode region in figure 3.20(a) can be explained by the observations of sections 3.2.2 and 3.2.3 that addressed the influence of the heat release and density ratio parameters on modal growth rates. The effect of increasing heat release to stabilize the central and destabilize the outer modes is reflected in the diminishing density ratio range where the central mode dominates as heat release is increased; the outer modes require less bias in the density ratio value to match the central mode amplification as the Θ value rises. This situation continues until $\Theta \approx 1.5$ ($T_{\mathrm{ad}} \approx 2.5$) for the incompressible case, at which point the central mode is overwhelmed by the two outer modes and no longer dominates at any density ratio value. The conditions of particular interest in this regime chart are the locus of points that form the boundaries between modes. For these conditions, the flow will develop two vortical modes that contribute to the mixing of the fast and slow streams and therefore hold promise for enhanced mixing performance. Unfortunately, due to the difficulties associated with obtaining sufficient combination of heat release and compressibility for colayer conditions in a laboratory facility, no direct experimental evidence of this mixing enhancement currently exists. However, qualitative evidence has been observed in diffusion flames (see section 5.2.2) and a new shock-tube facility discussed by Rossmann *et al.* (1999) holds promise for obtaining quantitative measurements in the near future.

In figure 3.20(a), the colayer lines between the central and outer modes extend to larger density ratio values until a point (identified by a • symbol) where two equally amplified peaks in the (ω, θ) plane no longer exist. To explain what this means to the fully developed mixing layer structure, it is useful to consider an analogy to the critical point on a chart of thermodynamic properties. In that situation, on either side of the critical point we are clearly able to identify the state of the substance, liquid or vapor, but the region above the critical point the mixture defies strict categorization. Applying this analogy to our regime chart, we describe the flow structure past the termination point of the colayer boundary as containing a single vortical mode with characteristics that share aspects of the two previously-identifiable modes.

Shifting focus now to the results at $M_c = 0.5$ that also appear in figure 3.20(a), we see that the dominant features of the previous chart remain unchanged but here the outer modes occupy a larger region of the chart. This follows directly from the fact that both compressibility and heat release generate conditions where outer modes dominate the structure. The other observation of note in this figure is the relatively vertical orientation of colayer boundary formed between the fast- and slow-outer-mode-dominated regions at high

Θ values. This demonstrates that the relative amplification of these two modes depends principally on which stream is heavier and thus the boundary location is only weakly affected by compressibility. This boundary rests slightly below the density ratio value of unity due to the slight asymmetry of the self-similar input profiles for $\bar{u}$ and $\bar{T}$.

As compressibility is further increased to $M_c = 1$ in figure 3.20(b), the area of central mode influence is reduced further and its dominant structure will be entirely three dimensional. At this M_c level, the outer modes can appear in either a two- or three-dimensional orientation. The generally horizontal orientation of the dimensionality boundary demonstrates the effect of increasing heat release to force the outer modes toward a two-dimensional structure. The final frame in the progression of increasing compressibility is shown in figure 3.20(c), where colayer boundaries are plotted for M_c values of 1.5 and 2. The downward progression in the central/outer mode boundaries has continued and at $M_c = 2$ it becomes possible to maintain a colayer structure in nonreacting flow, provided the density ratio is carefully chosen. All modes will appear most amplified in a three-dimensional orientation at these high compressibility values.

Several 'triple points' are evident at discrete values in the regime charts of figure 3.20 where all three instability modes are equally amplified. The specific nature of these modes at a moderate compressibility and heat release triple point (M_c=1.0, Θ=0.90, s=0.94) are shown in figure 3.21 in the form of amplification rate contours in polar (ω, θ) coordinates. Indications of the θ angle are shown around the periphery of these plots, and frequency radii extend out from the origin to the boundary, where the latter signifies the locus of zero-amplified neutral modes. This figure shows that three distinct and equally-amplified instability modes are indeed present under these conditions. The central and fast mode peaks appear in the same stability map of figure 3.21(a), but at significantly different frequency and obliquity values. The focus on the central mode in figure 3.21(b) indicates that its peak occurs at an obliquity of $\theta = 56°$, in contrast to the outer modes which are just on the verge of becoming three dimensional at this compressibility. The behavior of the central mode also contrasts with the outer modes in its well-defined position; the peak contours ($-\alpha_i = 0.08$) of the outer modes (the fast mode in particular) encompass a significantly larger area than that of the central mode. This suggests that the outer modes may be difficult to view in experimental conditions because many different combinations of frequency and obliquity waves are near-equally amplified.

3.3.2 Regime Charts in the (s, M_c) Plane

While the initial cuts into the regime space along a density ratio and heat release plane are useful, a full appreciation for the flow structure requires investigation from other perspectives. A study of the structure in the (s, M_c) plane was also carried out and the results are shown in figure 3.22. A comparison of the low M_c regime charts of figure 3.20(a) and the low Θ charts of figure 3.22(a) demonstrates the strong similarity that exists between the effects of heat release and compressibility. Increasing both parameters forces a transition from central to outer mode structure, which was predicted from their similar effect of developing a bi-modal $\bar{\rho}\, d\bar{u}/dy$ profile.

The similarity between the effects of heat release and compressibility allows us to restrict discussion of the (s, M_c) regime chart to only its unique features. One such observation concerns the central mode's boundary between two- and three-dimensionality. The boundaries at $\Theta = 0$ and 0.5 in figure 3.22(a) are both nearly horizontal and almost overlay one another, suggesting that its position is only a function of compressibility and is almost invariant to heat release and density ratio effects. Figure 3.22(c) is also notable in its demonstration that a fast/slow colayer exists at incompressible conditions for this and greater heat release values. This observation has significant implications for near-field mixing in diffusion flames and will be the subject of further discussion in section 5.2.2.

3.3.3 Regime Charts in the (M_c, Θ) Plane

Figure 3.23 completes the set of regime charts by offering a perspective of the (M_c, Θ) plane for a variety of density ratios. These planar cuts allow discussion of the mixing layer development from the reference condition of an incompressible, nonreacting case (located in the lower left corner) to a fully compressible reacting flow over a range of fixed density ratios. It is useful to start the discussion with the reference case of $s = 1$ that is shown in figure 3.23(b). Under the conditions of $M_c = 0$ and $\Theta = 0$ the familiar, centrally-located, two-dimensional, large-scale structure will be present and dominant. With increasing compressibility there is first a transition to three dimensionality and then, for $M_c > 2.5$, the central mode gives way to the slow three-dimensional mode as the dominant flow structure. With increasing heat release the progression from central to slow mode structure is again observed. At this unity density ratio value, the slow mode will out-pace the fast and it dominates the regions of both high compressibility and heat release. Figure 3.23(b) also provides

a convenient view to contrast the dimensionality boundaries (*i.e.* the compressibility effect) of the central and outer modes that was explained in section 3.2.4.

For the case of a fast side density bias of $s = 2/3$ pictured in figure 3.23(a), the central/outer mode colayer boundary maintains the same characteristics as in the $s = 1$ case, but here the fast mode replaces the slow as the dominant outer structure. However, even with this fast side density bias, a high heat release and low compressibility combination can still promote a region where the slow mode will dominate. The $s = 1/2$ case also shown in figure 3.23(a) demonstrates that colayer regions are almost entirely eliminated at this level of density bias; only a small region where the central and fast three-dimensional modes are equally amplified remains present. Therefore, there will be only one discernible mixing mode in the flow for the vast majority of this parameter plane. When the density bias is moved to the slow side of the layer in figure 3.23(b), the location of the central/slow colayer is at lower M_c and Θ values and is shorter compared to the equivalent density case of figure 3.23(a). When the density ratio is increased further to $s = 2$, the colayer boundary is all but eliminated. This result is similar to what was found in the equivalent but opposite density bias of the $s = 1/2$ case.

3.4 Parametrizing the Velocity Ratio Effect

The ability of the velocity ratio parameter $\lambda = (U_1 - U_2)/(U_1 + U_2)$, the difference over the sum of the fast and slow free-stream velocities, to parameterize the growth rate of incompressible, nonreacting, and uniform-density mixing layers has been well demonstrated in both experimental (Brown and Roshko 1974) and computational (Monkewitz and Huerre 1982) studies. However, the use of this parameter to collapse growth rate data in compressible, reacting, and variable-density conditions has not been thoroughly explored.

Additional questions regarding the validity of this parameter arise in regions, documented in the previous section, where outer modes dominate. Since the conventional λ parameter has no means to account for this change in flow structure, its utility under these conditions needs to be investigated. The results of this section will evaluate the ability of the λ parameter to collapse growth rates across a range of compressible, reacting, and variable-density conditions and will consider simple additions to extend its relevance to all possible types of shear layer structure.

3.4.1 Evaluation Methodology

Previous studies have shown that the growth rate, σ, is linearly related to λ in incompressible, nonreacting, equal-density flows. Hence, the ratio σ/λ (the slope) should remain constant as U_2 $[\lambda = \lambda(U_2)]$ is varied, and we wish to test this hypothesis for a variety of conditions. This ratio takes on the value of $\sigma(U_2 = 0)$ because $\lambda(U_2 = 0)$ is unity. We can therefore determine the accuracy of the growth rate collapse by comparing the value of σ/λ at some nonzero U_2 to the value of $\sigma(U_2 = 0)$. To efficiently present information from a four-parameter study (M_c, Θ, s, and λ), we fixed $U_2 = 0.5$ as the value for the comparison. Results are plotted as contours of Υ, which represents a normalized accuracy for the scaling parameter (here, λ) defined as

$$\Upsilon = \frac{\sigma(U_2 = 0.5) / \lambda(U_2 = 0.5)}{\sigma(U_2 = 0)}, \tag{3.4}$$

where a unity value implies a perfect collapse. The choice of $U_2 = 0.5$ as the evaluation point is an arbitrary but reasonable selection; the specific choice is not important because the scaling error is approximately proportional to the magnitude of U_2 and hence these results can be extrapolated to other values.

3.4.2 Central Mode Scaling

The ability of λ to collapse the growth rate of the central mode in the regime of compressible reacting flow is evaluated in figure 3.24. The contours in this plot were spline interpolated from information at $\Delta M_c = \Delta\Theta = 0.1$ and they extend throughout the region of $M_c \le 2$ where the central mode exists as a local maximum amplification rate.

The excellent scaling performance of the λ parameter in incompressible nonreacting conditions is evident in the near intersection of the unity-valued Υ contour with the origin of figure 3.24. These results also indicate that the scaling accuracy begins to degrade, but not too severely, as compressibility and heat release are added to the flow. Specifically, this plot demonstrates that the scaling error is largest for reacting conditions in the absence of compressibility, and when the compressibility approaches levels as high as $M_c = 2$. Both of these conditions correspond to a significant modification of the mean density profile (or equally, the temperature profile); this points to the likely source of the scaling problems. But the complex nature of the density profile evolution with increasing M_c and Θ prevents the use of any density-based parameters in a modified λ definition to achieve a global

improvement in the scaling accuracy. A similar conclusion was reached by Ragab and Wu (1989) in their study of two-dimensional compressible nonreacting mixing layers, although our results demonstrate that this holds even when the more dominant three-dimensional effects are taken into account (in compressible conditions) and also extend the observation to include reacting flows. However, it should be noted that figure 3.24 validates the use of λ for very accurate growth rate scaling (within 5% for this calculation) for the range $M_c < 1.25$ and $\Theta < 0.5$ that encompasses the large majority of experimental results.

The errors that can result from using λ to scale growth rate information in variable-density, incompressible flows are evident, but not directly discussed in the results of Sandham and Reynolds (1990) and Lu and Lele (1994). A direct measure of this inaccuracy is shown in figure 3.25, where Υ is plotted for the central mode in a region of variable-density, compressible conditions: $0.2 \leq s \leq 5$ and $M_c \leq 2$. Note that the density ratio axis has been stretched to maintain symmetry about $s = 1$, which is shown here as a dotted line. The predominantly horizontal nature of the contours in figure 3.25 indicates that the density ratio has a far stronger effect than compressibility on the scaling performance. Indeed, a density difference of 50% is enough to cause significant scaling errors at most compressibility values.

3.4.3 Outer Mode Scaling

It seems sensible to propose new velocity ratio parameters that are based on the fact that outer mode growth rates depend on the shear formed by the velocity difference between the flame sheet and the respective free stream (Planché and Reynolds, 1991; see section 3.2.4 for further discussion). This result can be easily incorporated into the definition of λ by changing the appropriate velocity terms to generate two new mode-specific parameters

$$\lambda_F = \frac{U_1 - U_f}{U_1 + U_f} \qquad \text{and} \qquad \lambda_S = \frac{U_f - U_2}{U_f + U_2}, \tag{3.5}$$

where λ_F and λ_S are the fast and slow mode flame-based scaling parameters, and U_f is the velocity at the flame sheet position. To maintain a zero to unity range in all λ definitions, a normalized version of λ_F was defined as $\lambda_{F^*} = \lambda_F / \lambda_{F,\text{max}}$, where $\lambda_{F,\text{max}}$ occurs when $U_2 = 0$.

Scaling results for the fast mode regime in uniform-density conditions are shown in figures 3.26(a) and (b) for the λ and λ_{F^*} parameters, respectively. This outer mode is

understandably absent in the region surrounding the origin, where there is insufficient development in the density-weighted vorticity profile to form this instability. In the low heat release regime ($\Theta < 1$), figure 3.26 demonstrates that growth rate collapse with the conventional λ parameter is more precise, while the fast mode parameter λ_{F^*} is superior in high-heat-release regimes. The extent of these two scaling regimes roughly corresponds to the regions where the central and outer modes are dominant (see section 3.3.3). The colayer line where these modes are equal in growth rate has been used in figure 3.26 to delineate shaded regions where the λ and λ_{F^*} parameters should each be applied. Experimentally, this boundary should be easily observable since it corresponds to a change in flow structure. In summary, the λ_{F^*} parameter provides good accuracy for scaling the fast mode growth rate in regions where it will be a significant part of the flow structure.

Results for scaling the slow mode growth rate are shown in figure 3.27. It should be noted that there is a region roughly defined by $\Theta < 0.4$ and $M_c > 1$ where results are not presented because the slow mode is weakly amplified for $U_2 = 0$ and in fact disappears when $U_2 = 0.5$. Comparing the results in figures 3.27(a) and (b) suggests a conclusion similar to that of the fast mode: the conventional definition of λ performs best in regions of low heat release while the slow mode λ_S parameter should be used when there is significant heat addition to the flow. Unfortunately, the colayer boundary (shown as a dashed line in this plot) does not perform as well here as it did for the fast mode (see figure 3.26) to separate the two scaling regimes. Further, the close spacing of contours in the low compressibility ($M_c < 0.5$) region of both plots implies that neither scaling parameter is reliable there — the dominance of the heat release over the driving shear in this region seems to be the cause. However, in higher compressibility regimes ($M_c > 0.5$), the following rule can be applied with acceptable accuracy: λ should be used for $\Theta < 1.6$ while λ_S provides better accuracy when $\Theta > 1.6$.

3.5 Chapter Summary

This chapter has presented a detailed investigation into the effects of compressibility, heat release, and the flow-stream ratios of density, equivalence, and velocity on the structure of the compressible reacting mixing layer. The density-weighted vorticity profile was employed as a first step to develop an understanding for the effect of each parameter. Eigenfunction visualizations based on linear stability theory were then used to illustrate

the general behavior of the three different instability modes.

An extensive parametric study—also using linear stability—evaluated the influence of each parameter on the flow structure. Compressibility and heat release were found to exert very similar effects: both cause the flow to transition from central to outer mode dominance. The density ratio was identified as a third important parameter, exerting considerable influence on all modal growth rates, and selecting which outer mode dominates in high-heat-release and compressibility situations. Variation in the equivalence ratio was shown to have only a slight effect on the central mode. However, its influence on the outer modes was heavily dependent on compressibility, producing a large effect at low M_c values by adjusting the effective shear on each mode, but negligible influence at higher M_c due to balancing compressibility effects. Changes in the velocity ratio reduced the growth rates of all modes nearly equally. Based on these results, compressibility, heat release, and the density ratio were identified as the critical parameters for determining flow structure and regime charts were developed to document their combined effect.

The ability of scaling parameters to account for the growth-rate influence of the velocity ratio was investigated. The conventional λ parameter, developed in incompressible nonreacting flows, was shown to perform well for all three stability modes in moderate compressibility and heat release regimes of equal-density flow. However, the accuracy deteriorates rapidly with increasing density ratio. Two new flame-based parameters were introduced and shown to provide better parameterizing of the outer mode growth rates in conditions of significant heat release.
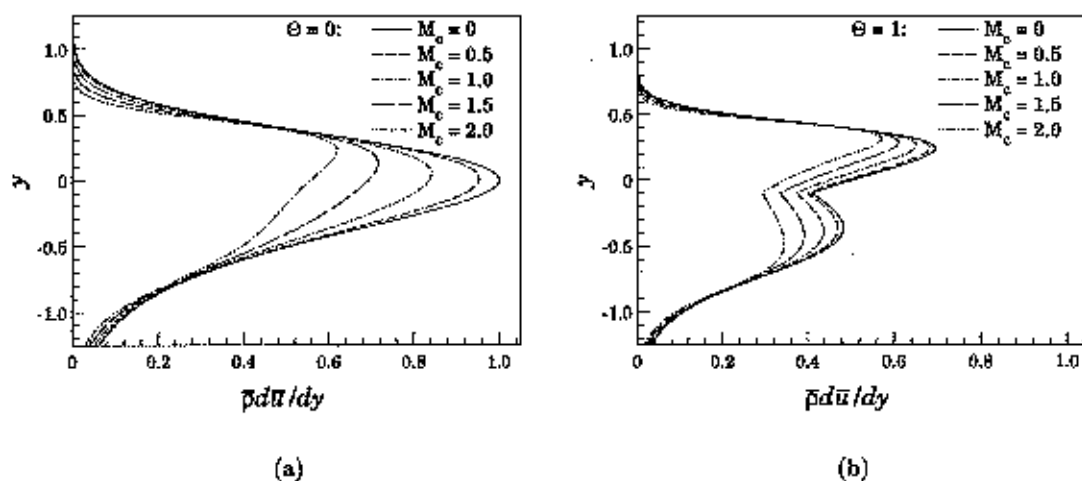
Figure 3.1: Development of the density-weighted vorticity profile with increasing compressibility at heat release values of (a) $\Theta = 0$ and (b) $\Theta = 1.0$ ($r = 0, s = 1, \phi = 1$).
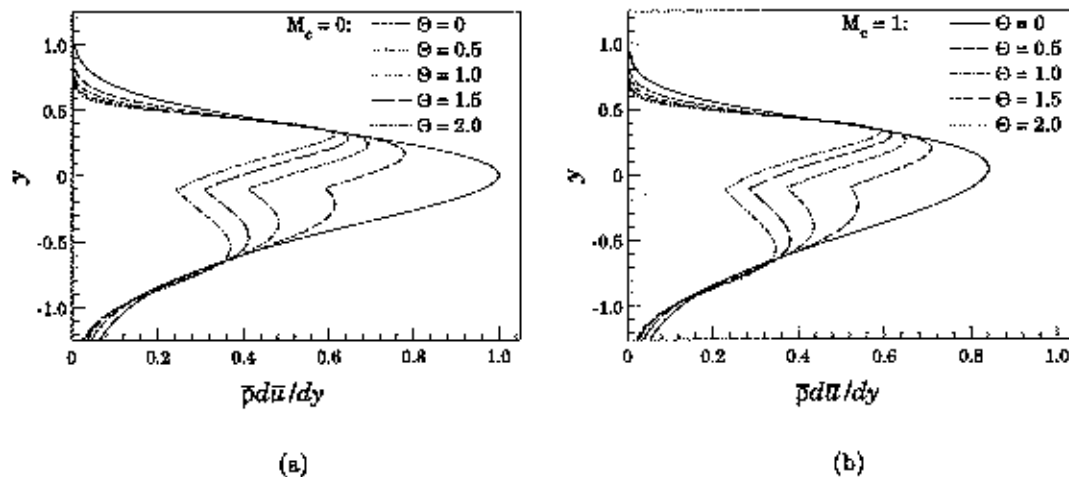
Figure 3.2: Development of the density-weighted vorticity profile with increasing heat release at compressibility values of (a) $M_c = 0$ and (b) $M_c = 1.0$ ($r = 0, s = 1, \phi = 1$).
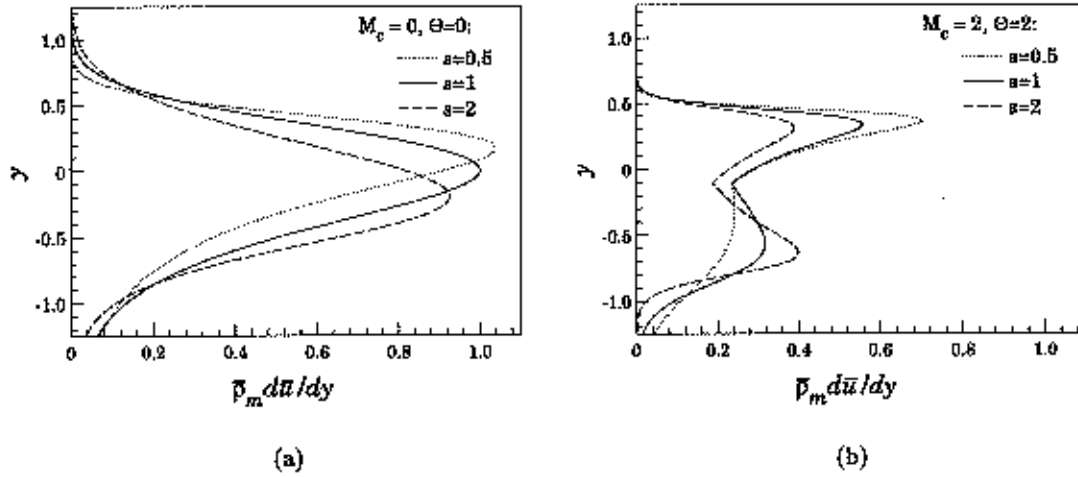
Figure 3.3: Effect of halving and doubling the density ratio on the density-weighted vorticity profile in both (a) incompressible, non-reacting and (b) fully compressible, reacting conditions ($r = 0, \phi = 1$).
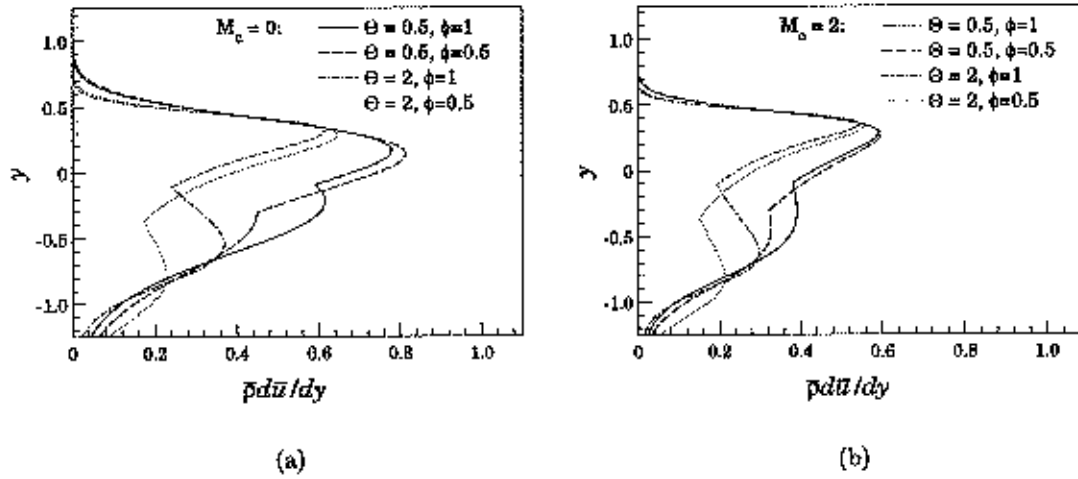
Figure 3.4: Effect of halving the equivalence ratio (*i.e.* reducing the slow side fuel mass fraction by half) on the density-weighted vorticity profile in low- and high-heat-release conditions at (a) $M_c = 0$ and (b) $M_c = 2.0$ ($r = 0, s = 1$).
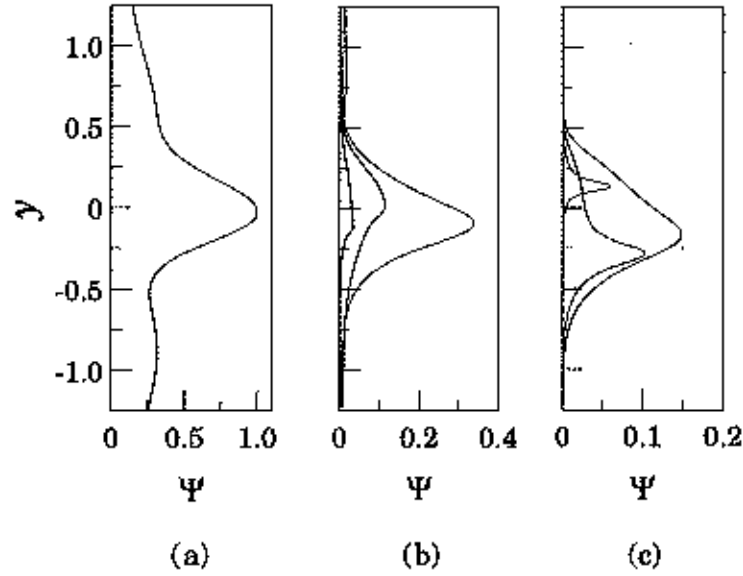
Figure 3.5: Effect of compressibility on the amplification-rate-normalized eigenfunction energy profiles for each mode at (a) $M_c = 0$, (b) $M_c = 1$ and (c) $M_c = 2$ ($\Theta = 0, r = 0, s = 1$).
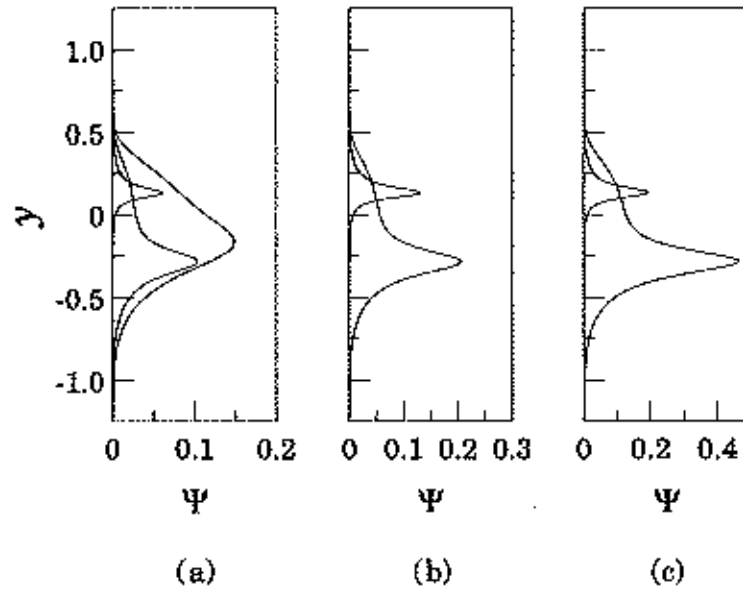
Figure 3.6: Effect of heat release on the amplification-rate-normalized eigenfunction energy profiles at high compressibility ($M_c = 2$): (a) $\Theta = 0$, (b) $\Theta = 1$ and (c) $\Theta = 2$ ($\phi = 1, r = 0, s = 1$).
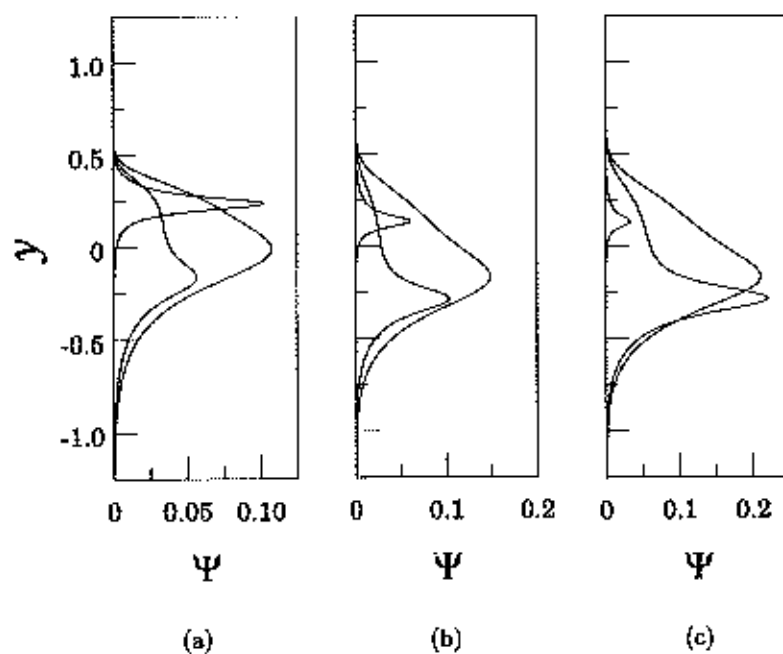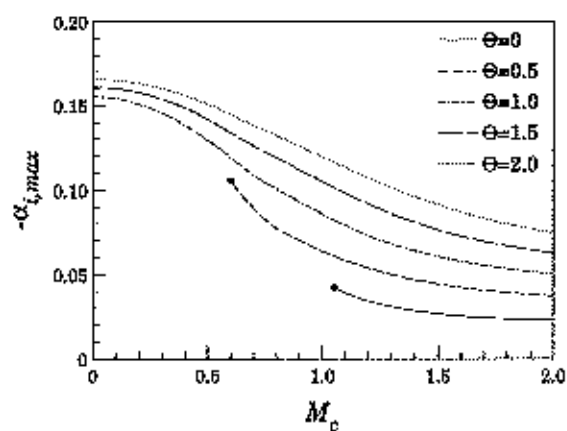
Figure 3.7: Effect of density ratio variation on the the amplification-rate-normalized eigenfunction energy profiles at high compressibility ($M_c = 2$): (a) $s = 0$, (b) $s = 1$ and (c) $s = 2$ ($\Theta = 0, U_2 = 0$).
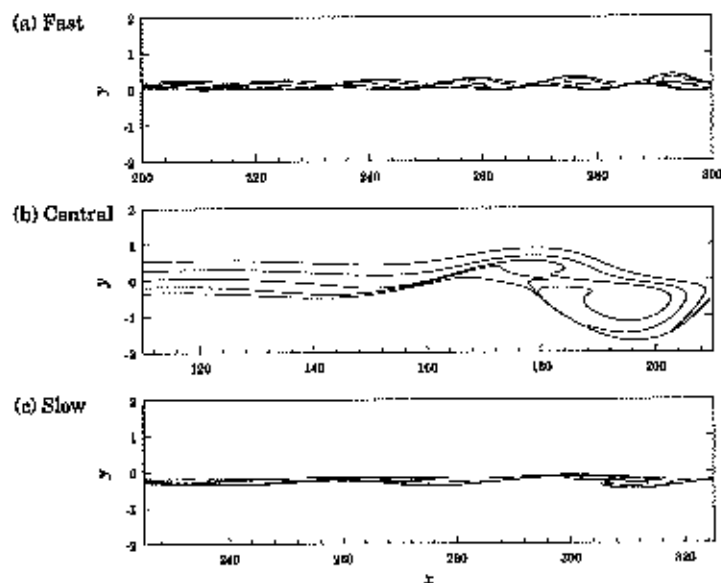
Figure 3.8: Eigenfunction streakline plots for all three modes at flow conditions of $M_c = 2$, $\Theta = 0$, $r = 0$ and $s = 1$.
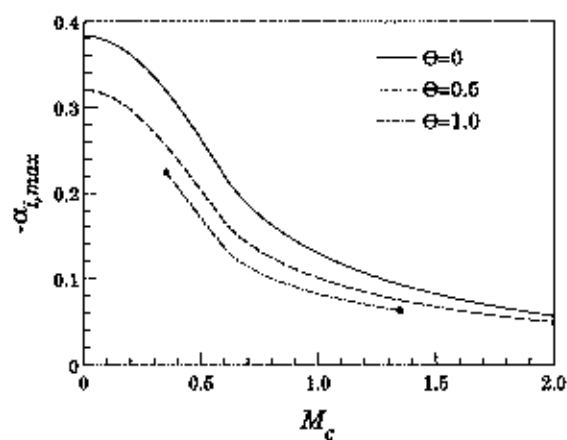
(a) Central

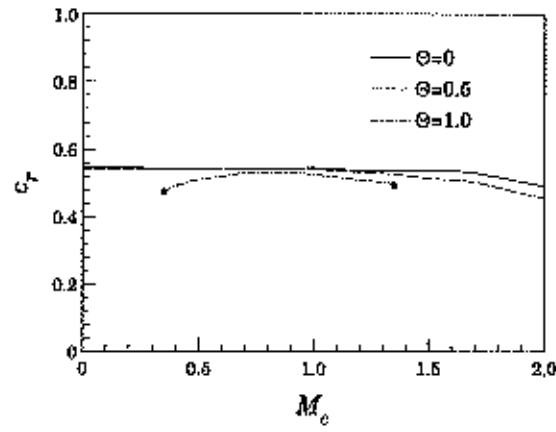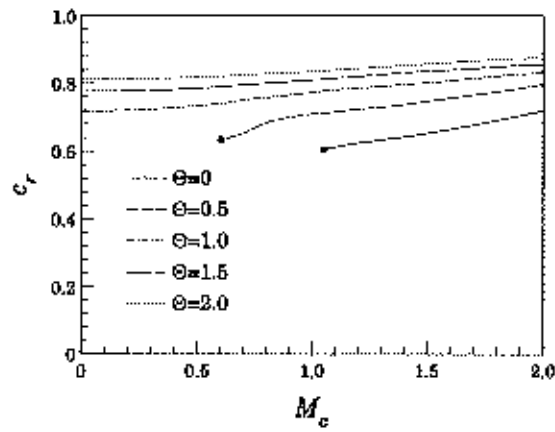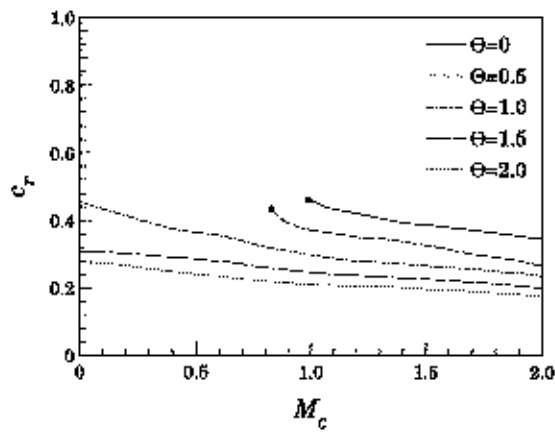
(b) Fast
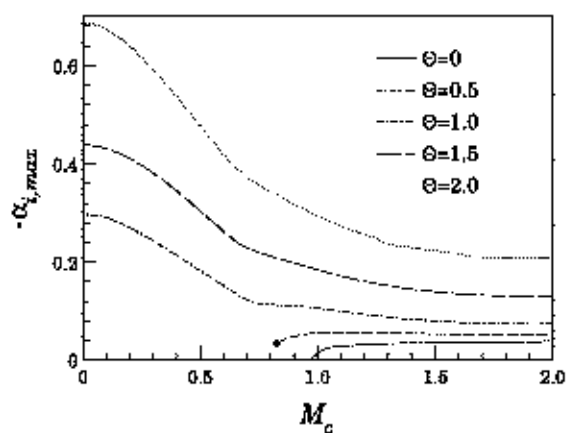
(c) Slow

Figure 3.9: Effect of compressibility on the (a) central, (b) fast, and (c) slow mode amplification rates across a range of heat release values ($r = 0, s = 1, \phi = 1$).
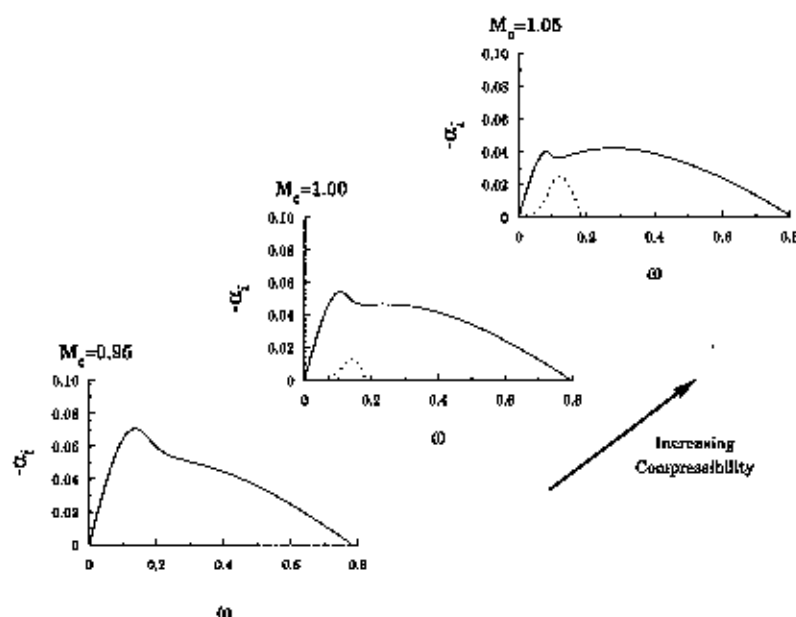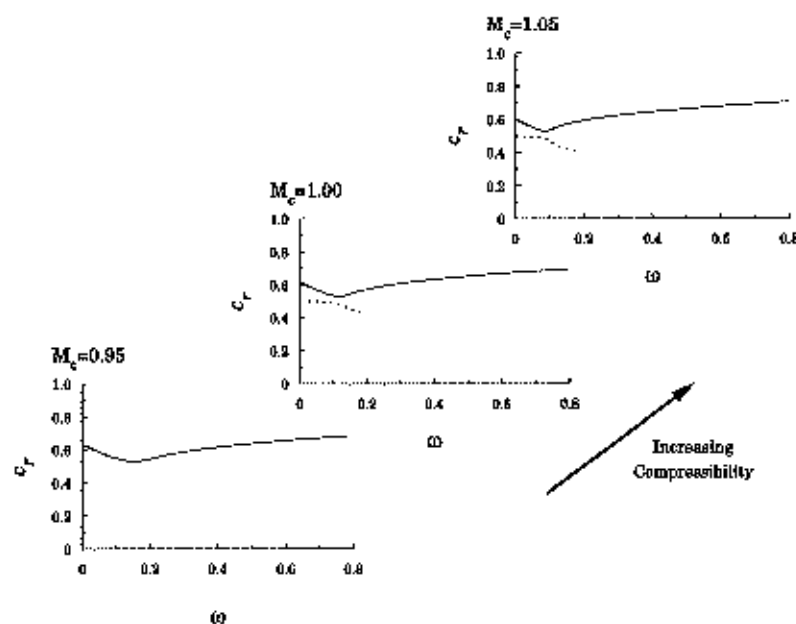
(a) Central

(b) Fast

(c) Slow

Figure 3.10: Effect of compressibility on the (a) central, (b) fast, and (c) slow mode phase speeds across a range of heat release values ($r = 0, s = 1, \phi = 1$).
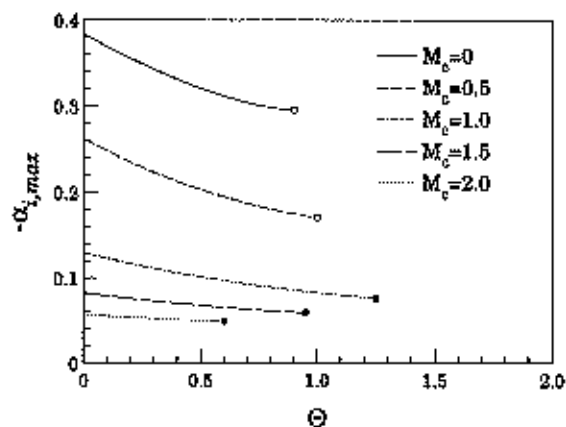
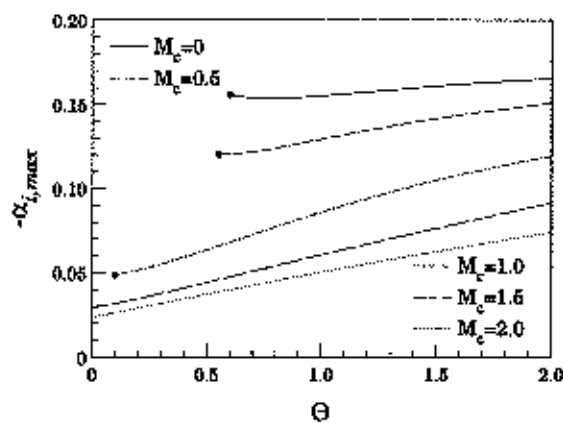(a) Amplification Rate Transition for 2D Modes

(b) Phase Speed Transition for 2D Modes

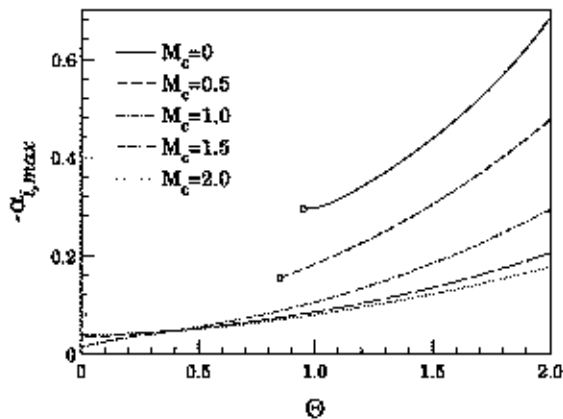Figure 3.11: Development of the fast and slow outer modes in the 2D frequency domain with increasing compressibility ($\theta = 0°, \Theta = 0, r = 0, s = 1, \phi = 1$). Amplification rates (a) and phase speeds (b) are plotted for the central/fast (———) and slow modes (...).
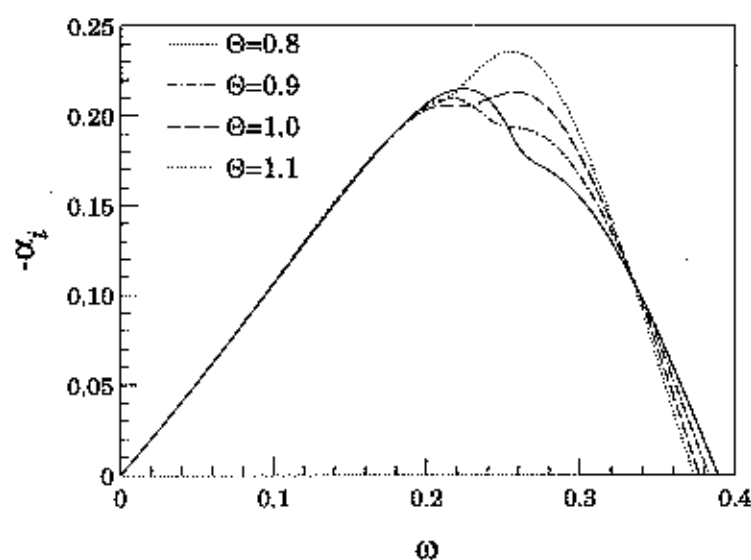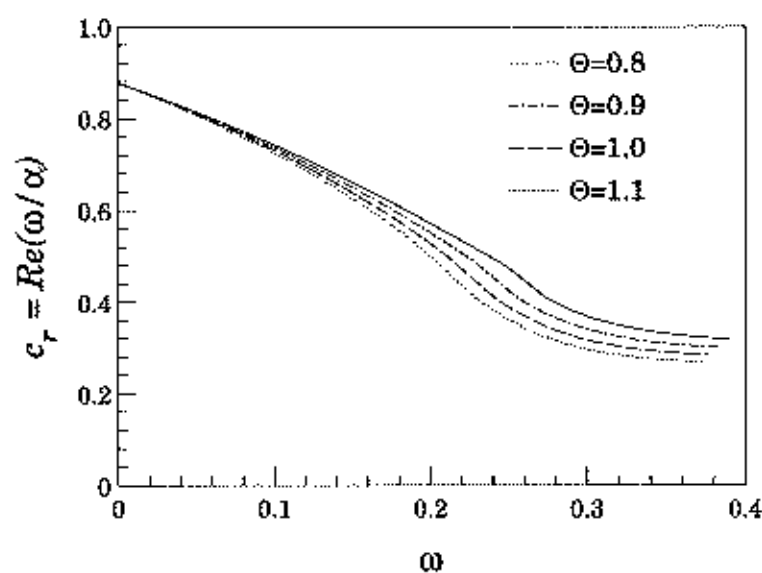
(a) Central

(b) Fast

(c) Slow

Figure 3.12: Effect of heat release on the (a) central, (b) fast, and (c) slow mode amplification rates across a range of compressibilities ($r = 0, s = 1, \phi = 1$). The ∘ symbol denotes a transition point between modes and the • symbol identifies modal termination points.

(a)

(b)

Figure 3.13: Coupling of the the central and slow mode instabilities at low compressibility ($M_c = 0.4$). Transition in (a) amplification rate and (b) phase speed profiles for two-dimensional disturbances with increasing heat release ($\theta = 0°, r = 0, s = 1, \phi = 1$).

(a) Central

(b) Fast

(c) Slow

Figure 3.14: Effect of heat release on the (a) central, (b) fast, and (c) slow mode phase speeds across a range of compressibilities ($r = 0, s = 1, \phi = 1$). The $\circ$ symbol denotes a transition point between modes and the $\bullet$ symbol identifies modal termination points.
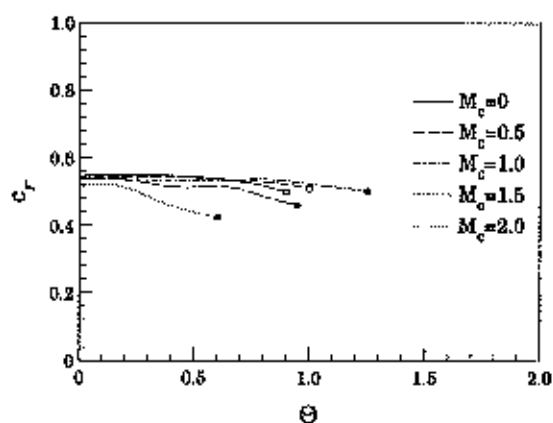
(c) $M_c = 2.0$

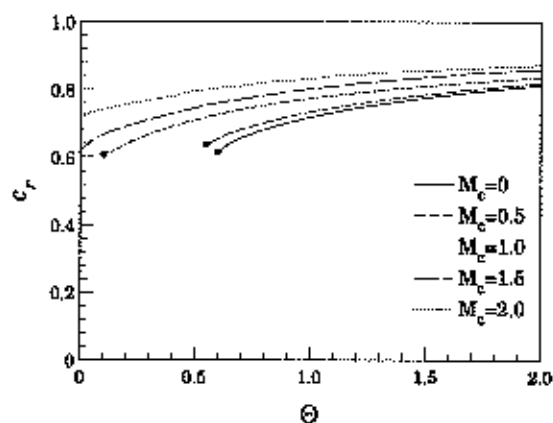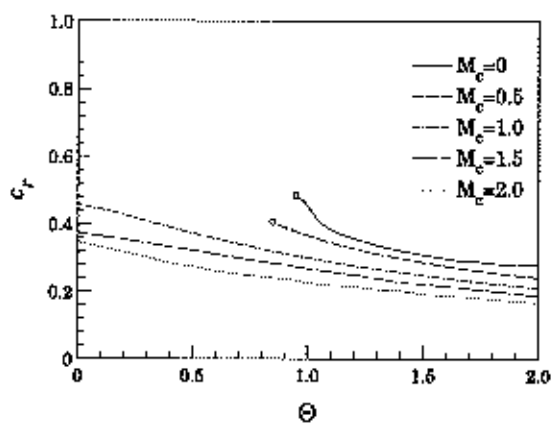
(b) $M_c = 1.0$

(a) $M_c = 0$

Increasing
Compressibility
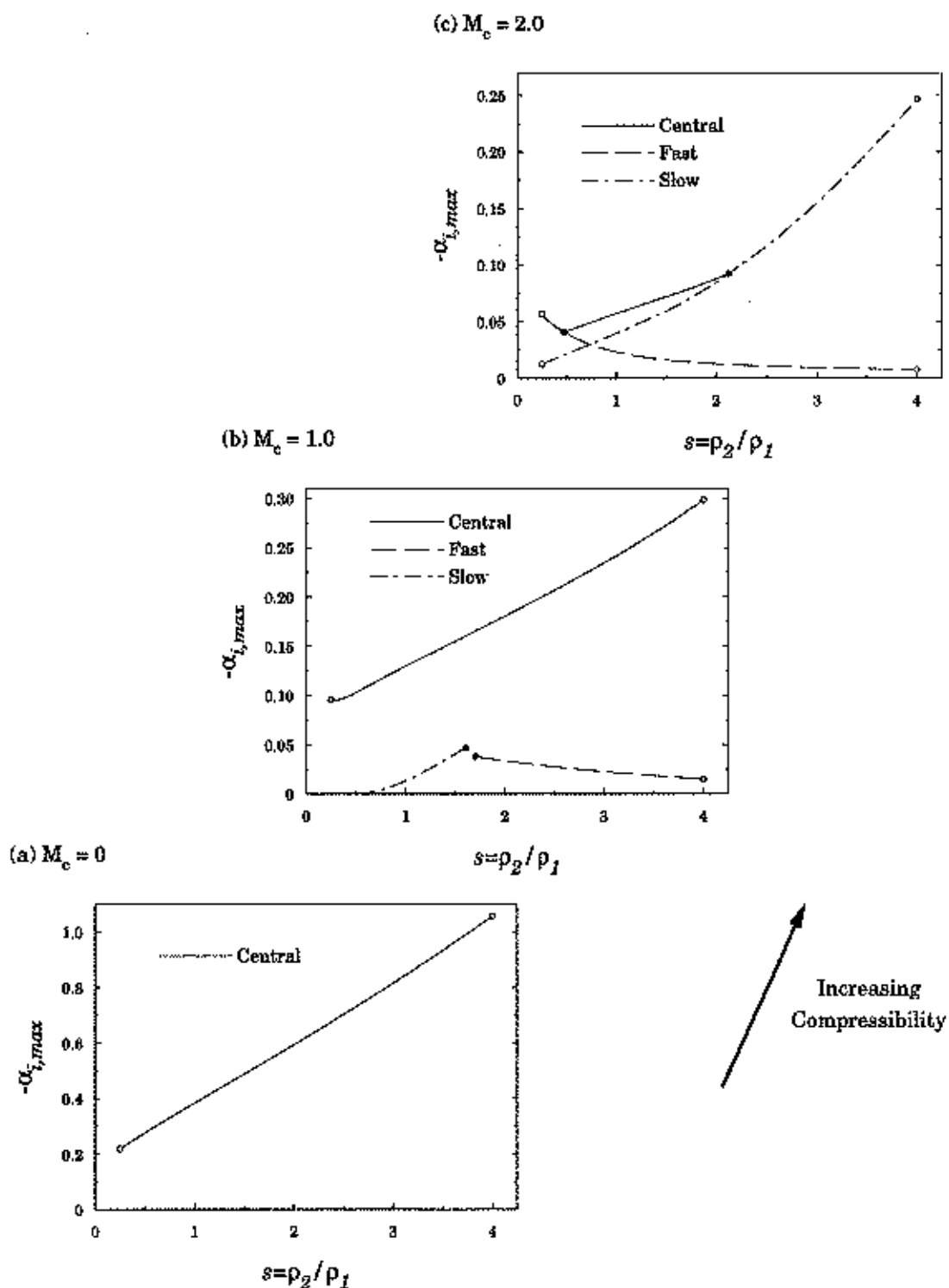
Figure 3.15: Effect of the density ratio on the amplification rate of the three instability modes at compressibility levels ranging from $M_c = 0$ to $M_c = 2$ ($\Theta = 0, r = 0$).

(c) $M_c = 2.0$

(b) $M_c = 1.0$

(a) $M_c = 0$

Increasing
Compressibility
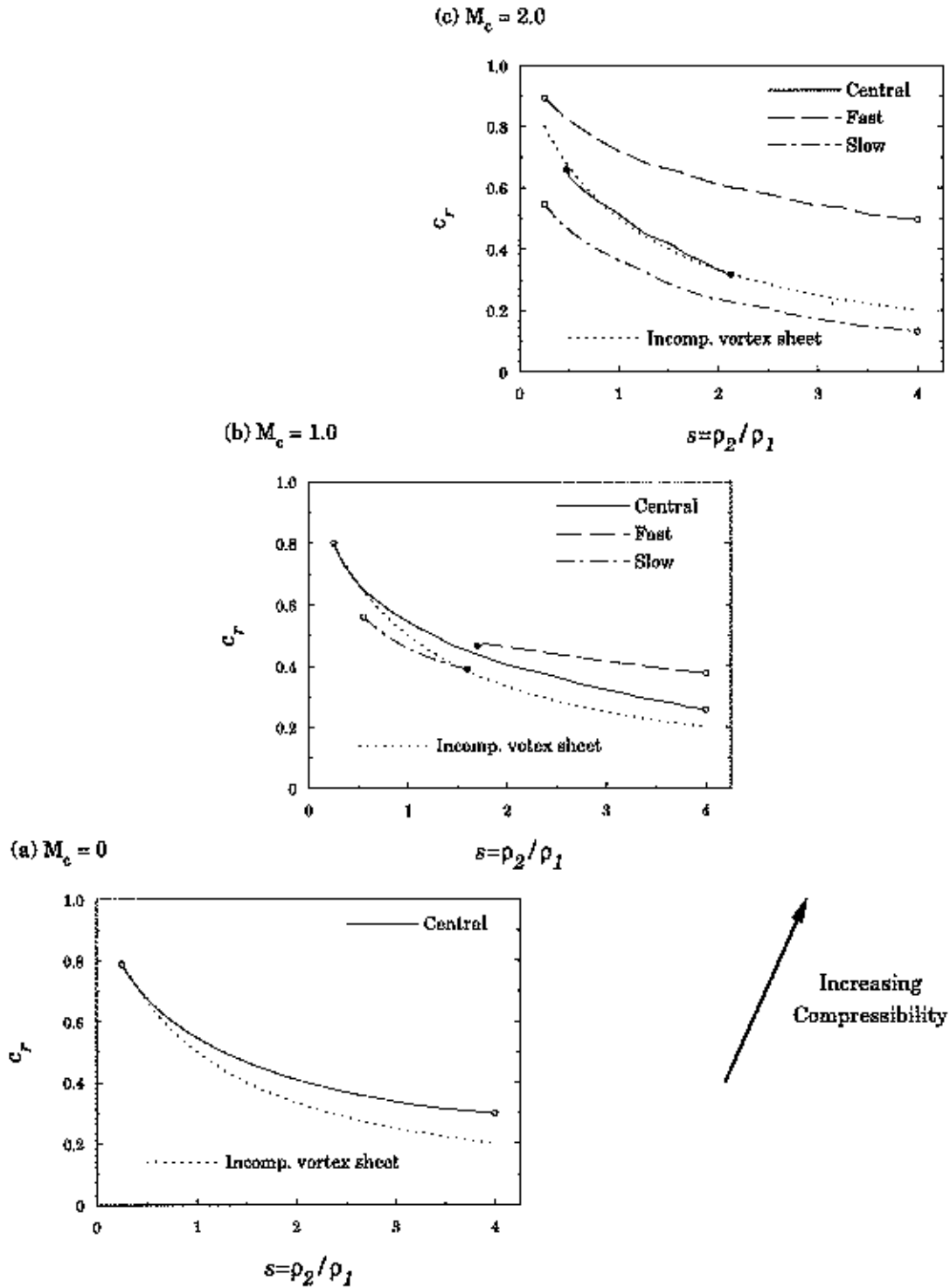
Figure 3.16: Effect of the density ratio on the phase speeds of the three instability modes at compressibility levels ranging from $M_c = 0$ to $M_c = 2$ ($\Theta = 0, r = 0, \phi = 1$). The phase speed for an incompressible vortex sheet solution is also shown.
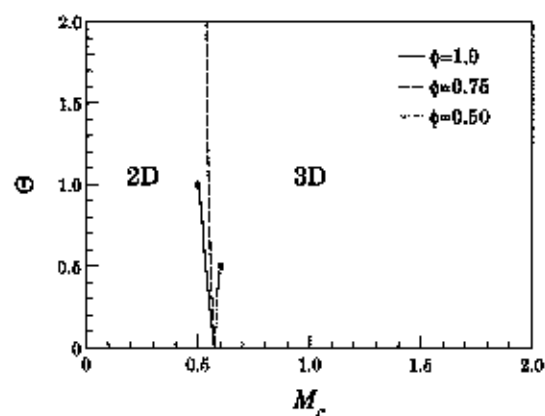
(a) Central
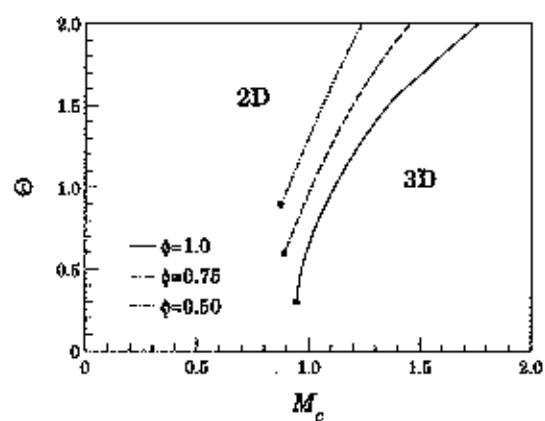
(b) Fast
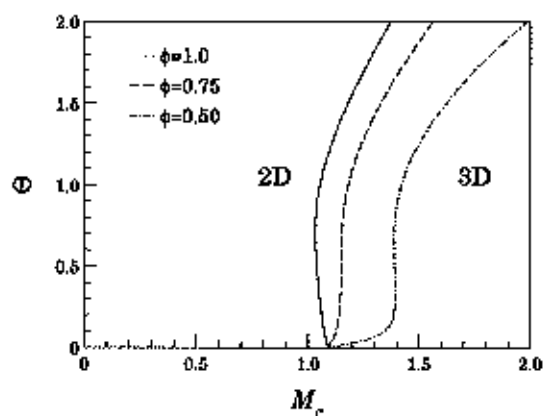
(c) Slow

Figure 3.17: Effect of stoichiometry on the boundary between two- and three-dimensional structure for each instability mode ($r = 0, s = 1$). Results are shown for three equivalence ratios ranging from stoichiometric ($\phi = 1$) to lean ($\phi = 0.5$) conditions.
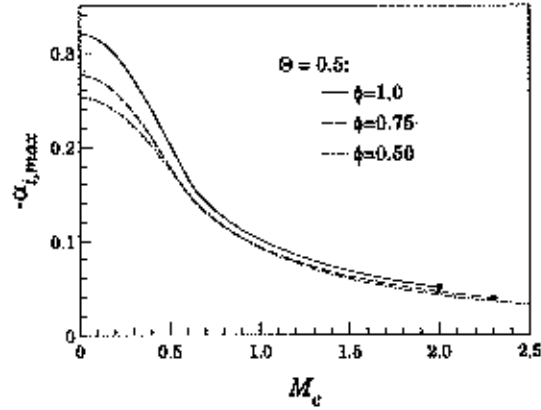
(a) Central
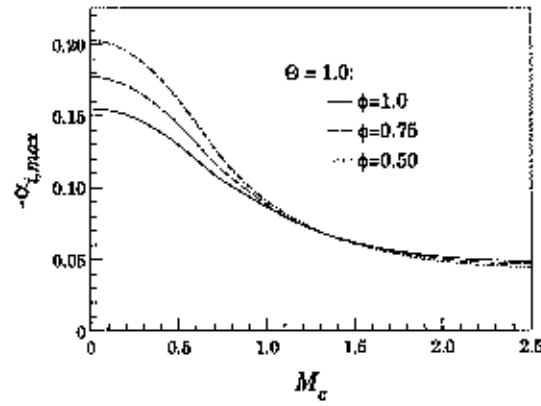
(b) Fast
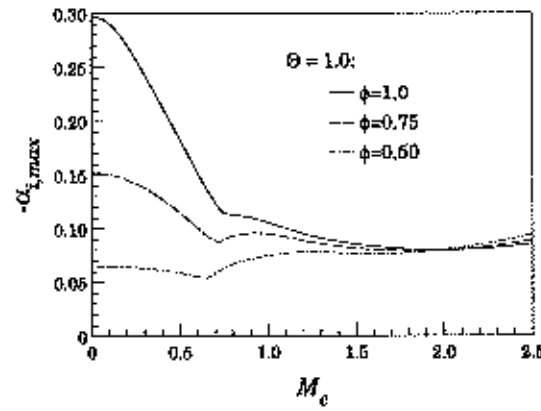
(c) Slow

Figure 3.18: Effect of stoichiometry on the amplification rates of the three instability modes at a constant heat release of $\Theta = 0.5$ for the central mode in figure (a) and $\Theta = 1.0$ for the outer modes in (b) and (c). Results are shown for three equivalence ratios ranging from stoichiometric ($\phi = 1$) to lean ($\phi = 0.5$) conditions ($r = 0, s = 1$).
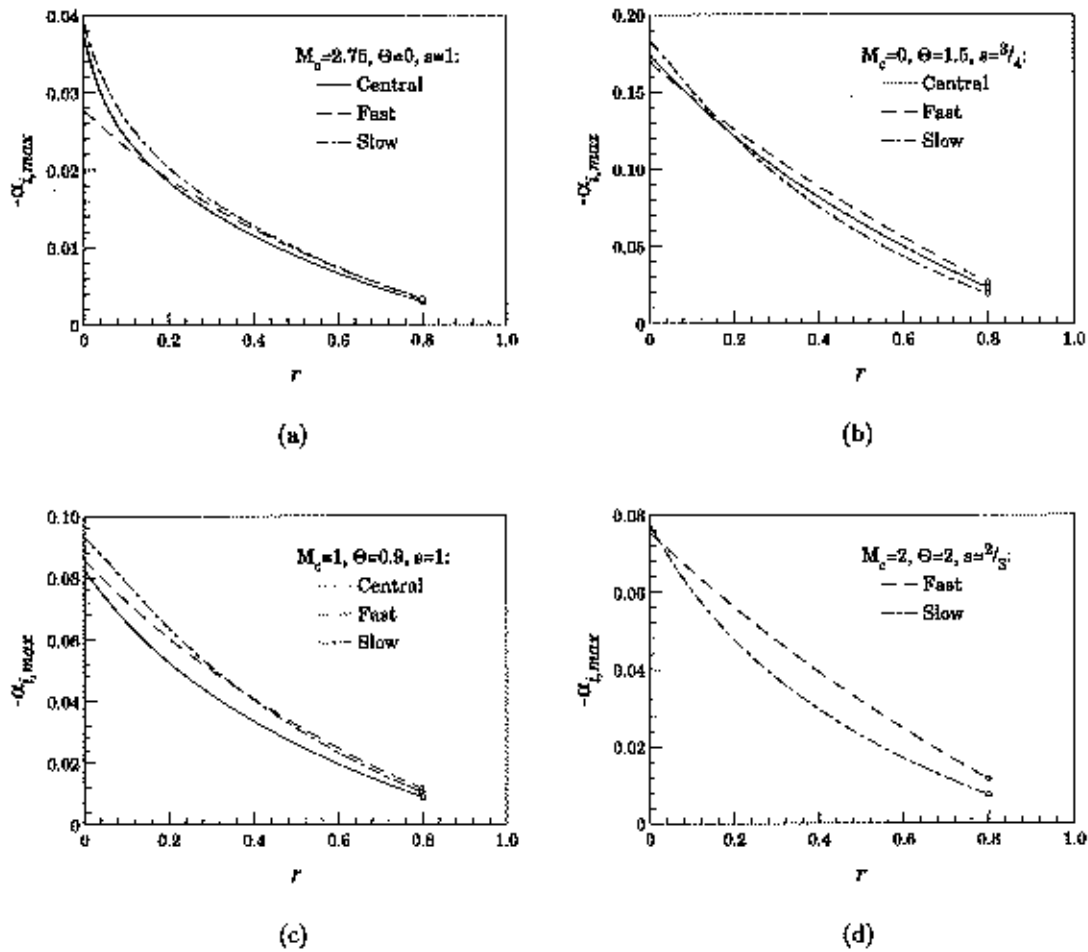
Figure 3.19: Relative effect of varying the slow stream velocity (U_2) on the amplification of all stability modes present at the given conditions: (a) $M_c = 2.75, \Theta = 0, s = 1$; (b) $M_c = 0, \Theta = 2, s = 3/4$; (c) $M_c = 1, \Theta = 0.9, s = 1$; and (d) $M_c = 2, \Theta = 2, s = 2/3$ ($\phi = 1$).

(c) High M_c Cases

(b) Transitional M_c Case

$s=\rho_2/\rho_1$

(a) Low M_c Cases

$s=\rho_2/\rho_1$

Increasing
Compressibility
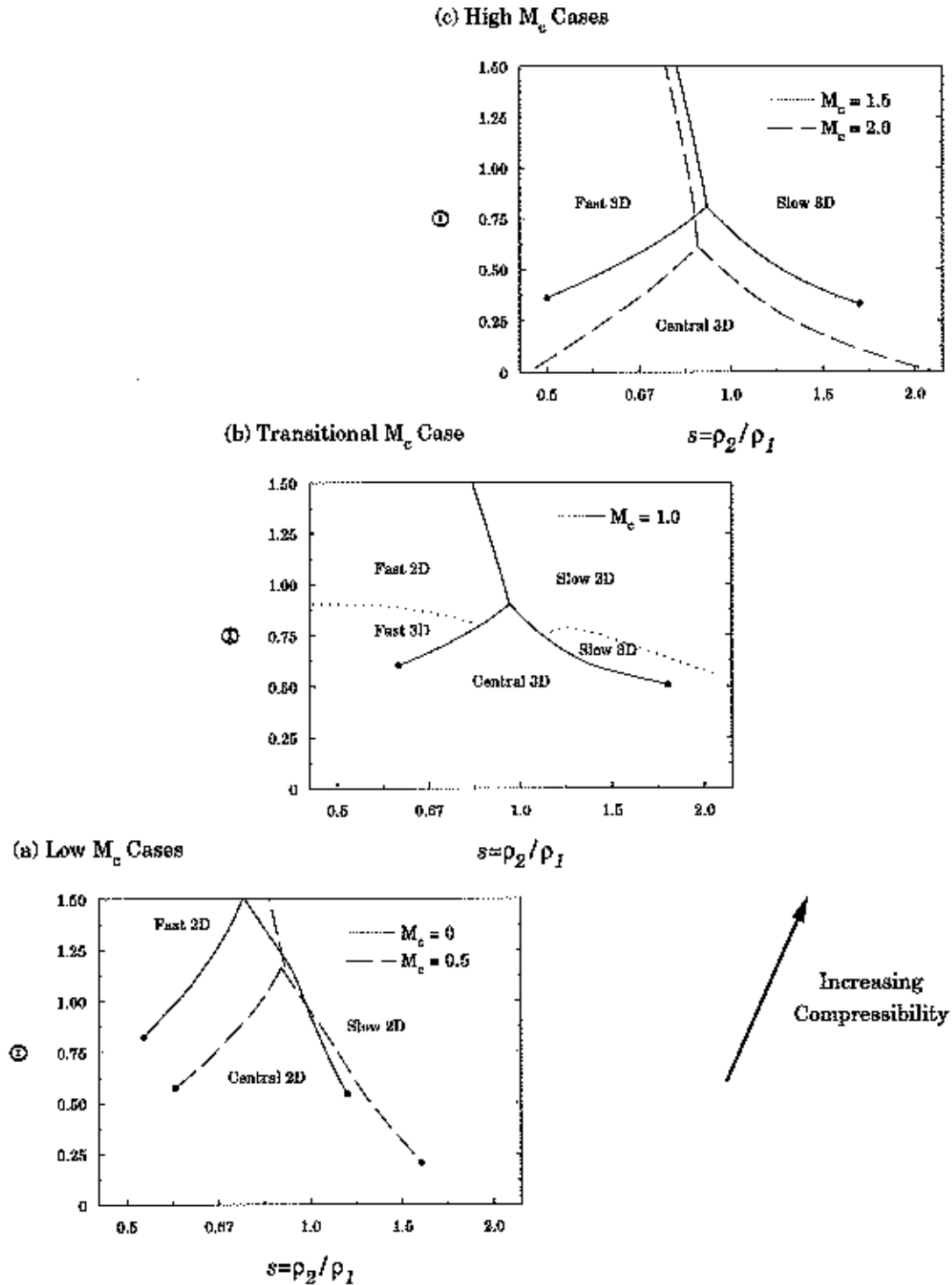
Figure 3.20: Evolution of a modal structure regime chart in the (s, Θ) plane with increasing compressibility. Structural regimes are shown for cases of low, transitional, and high compressibility values: (a) $M_c=0, 0.5$; (b) $M_c=1.0$; and (c) $M_c=1.5, 2.0$ ($\phi = 1, r = 0$).
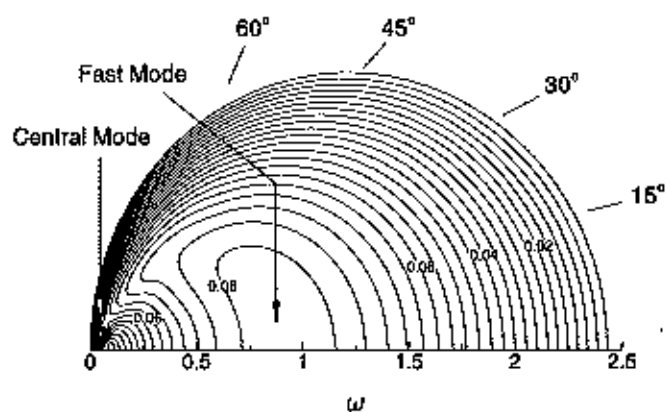
(a) Central/Fast Modes
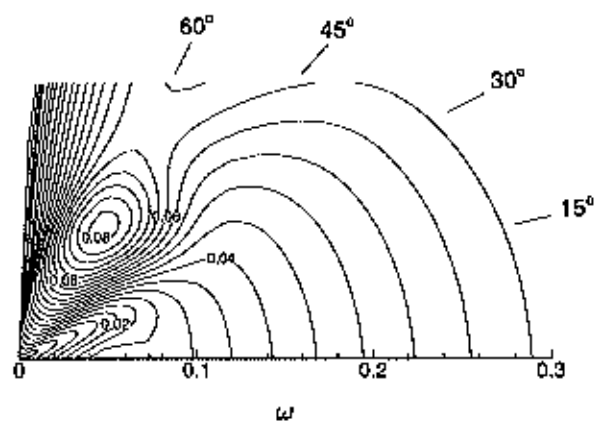
(b) Central Mode
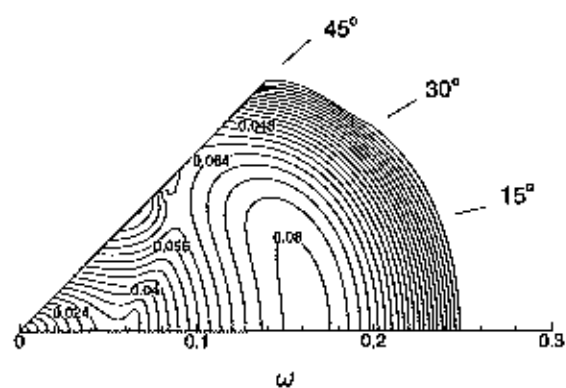
(c) Slow Mode

Figure 3.21: Polar contour plots of the amplification rate in (ω, θ) coordinates for (a) central and fast modes, (b) focus on central mode, and (c) slow mode at a triple point ($M_c = 1$, $\Theta = 0.9$, $s = 0.94$, $\phi = 1$). Contour min at 0, max at 0.08, and $\Delta \alpha_i = 0.004$.
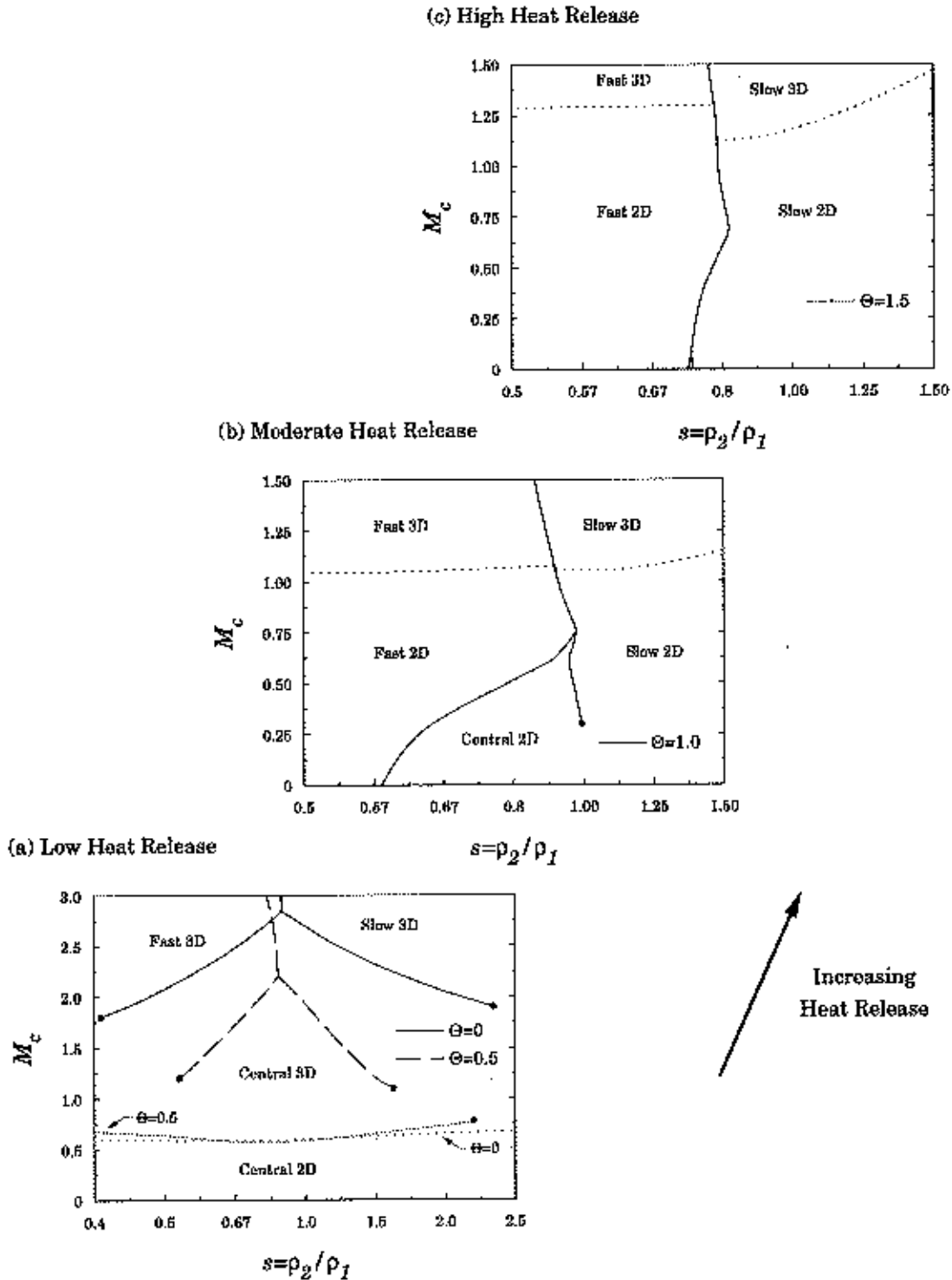
Figure 3.22: Evolution of a modal structure regime chart in the (s, M_c) plane with increasing heat release. Flow structure is shown for conditions of (a) $\Theta=0$, 0.5; (b) $\Theta=1.0$; and (c) $\Theta=1.5$ ($\phi = 1, r = 0$).

(c) Slow Side Bias: s=1.5

(b) Equivalent Density Ratio: s=1

(a) Fast Side Bias: s=0.667

Increasing
Density Ratio
$(s=\rho_2/\rho_1)$
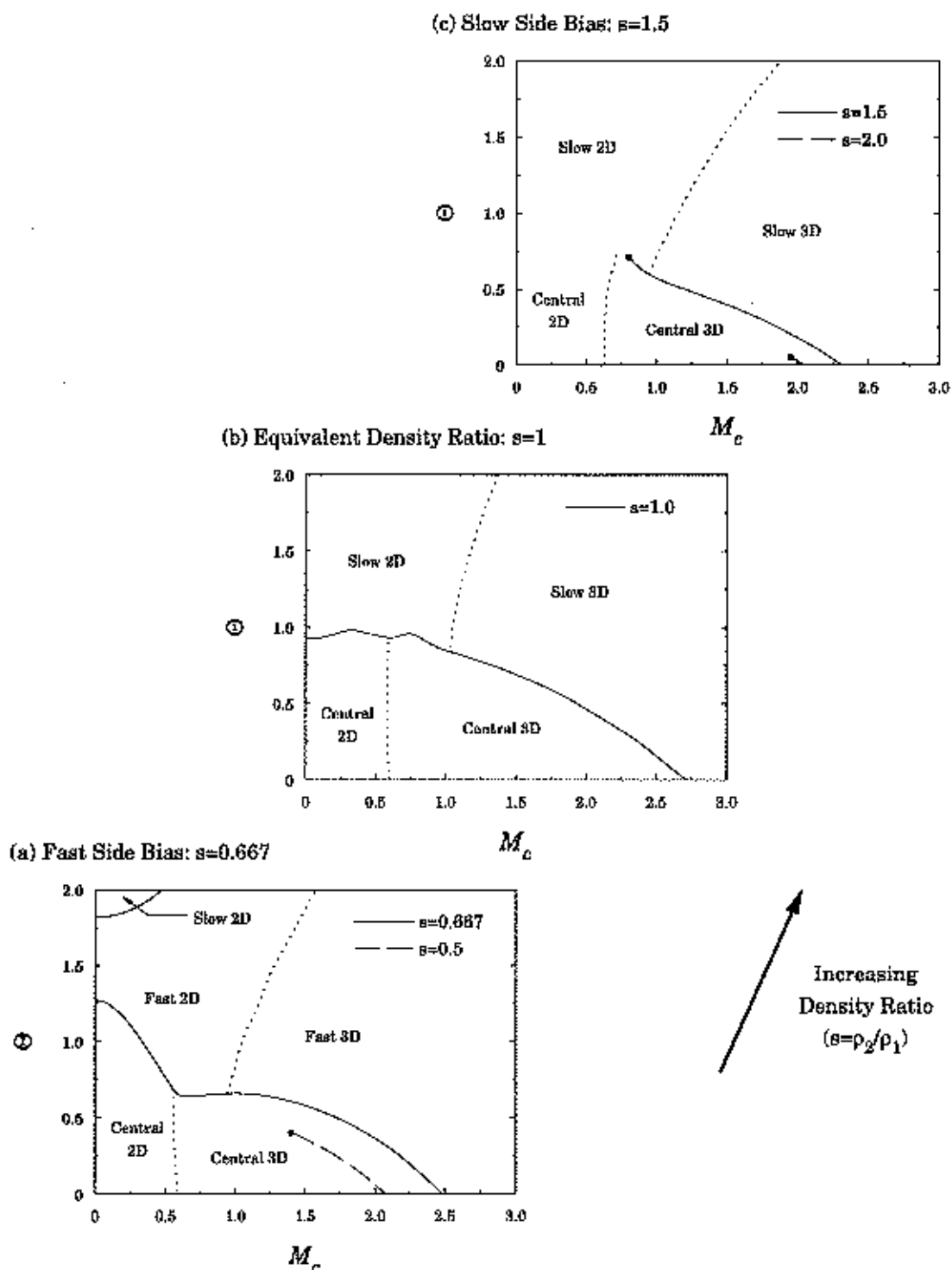
Figure 3.23: Evolution of a modal structure regime chart in the (M_c, Θ) plane with increasing density ratio. Flow structure is shown for conditions of (a) fast side bias, $s=1/2, 2/3$; (b) uniform condition, $s=1.0$; and (c) slow side bias, $s=3/2, 2$ ($\phi = 1, r = 0$).
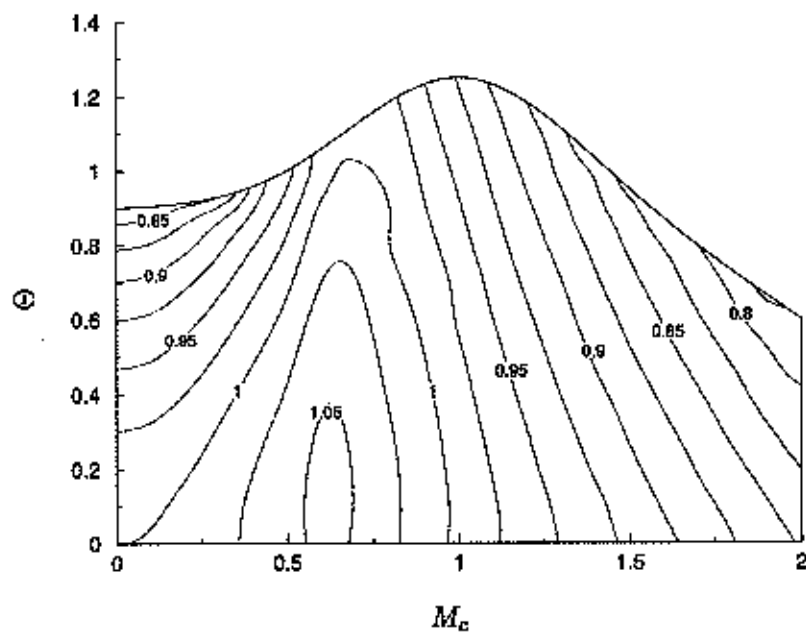
Figure 3.24: Υ contours for scaling the central mode growth rate with λ in the M_c/Θ regime ($s = 1$, $\phi = 1$).
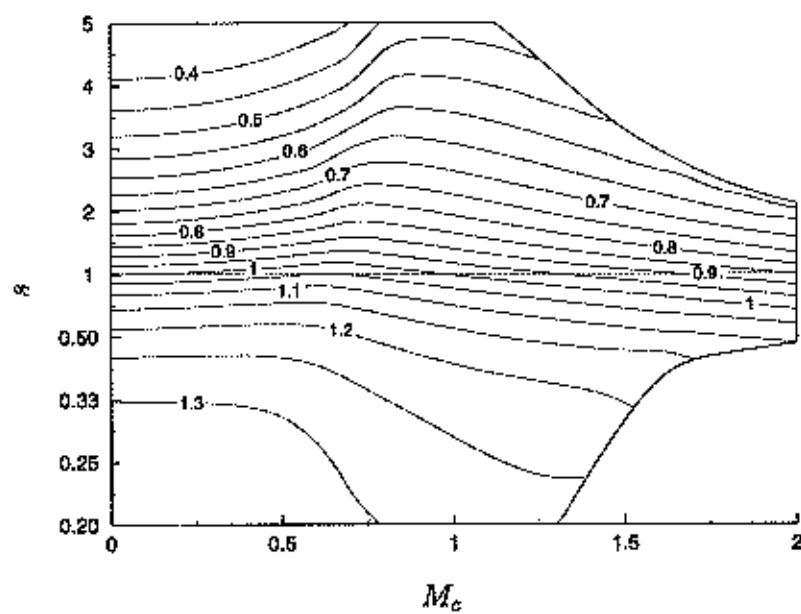
Figure 3.25: Υ contours for scaling the central mode growth rate with λ in the M_c/s regime ($\Theta = 0$).

(a)

(b)
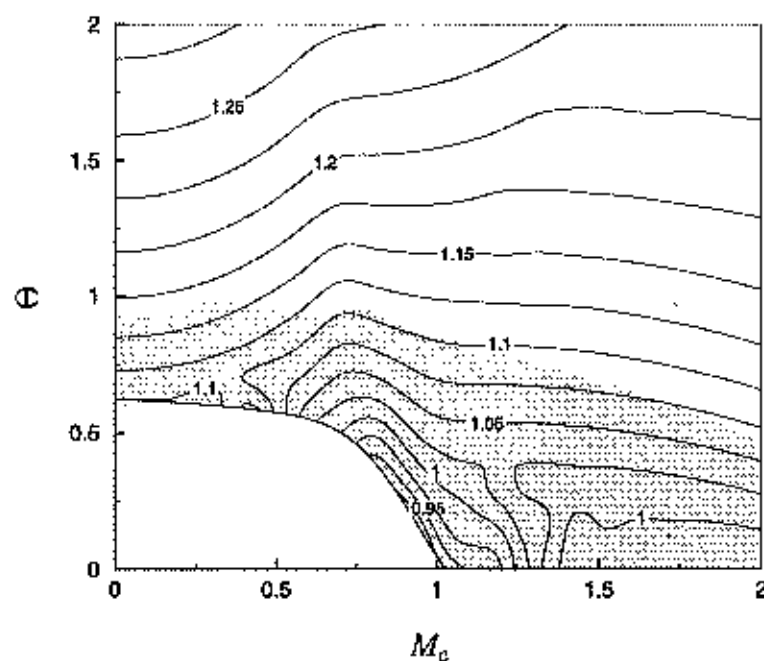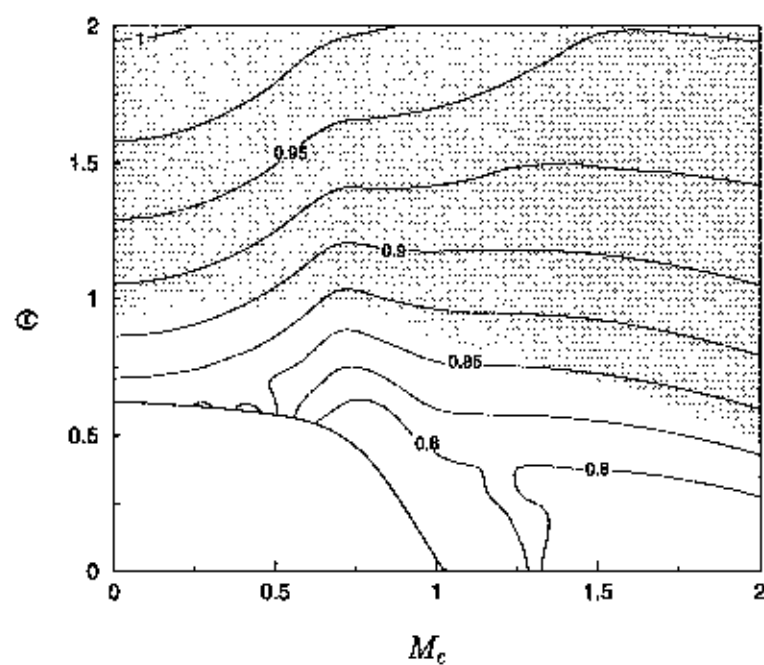
Figure 3.26: Υ contours using (a) λ and (b) λ_{F^*} parameters for scaling the fast mode growth rate in compressible reacting conditions ($s=1$, $\phi = 1$).

(a)

(b)
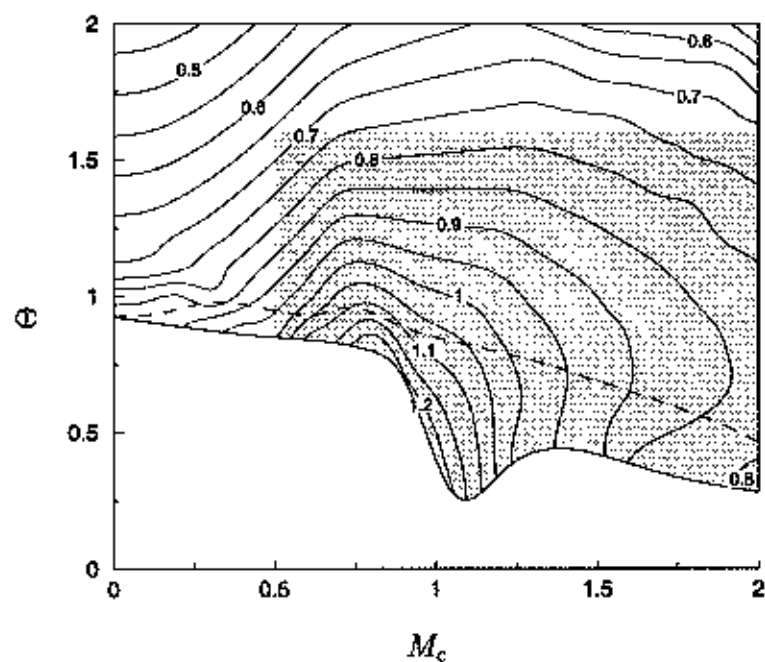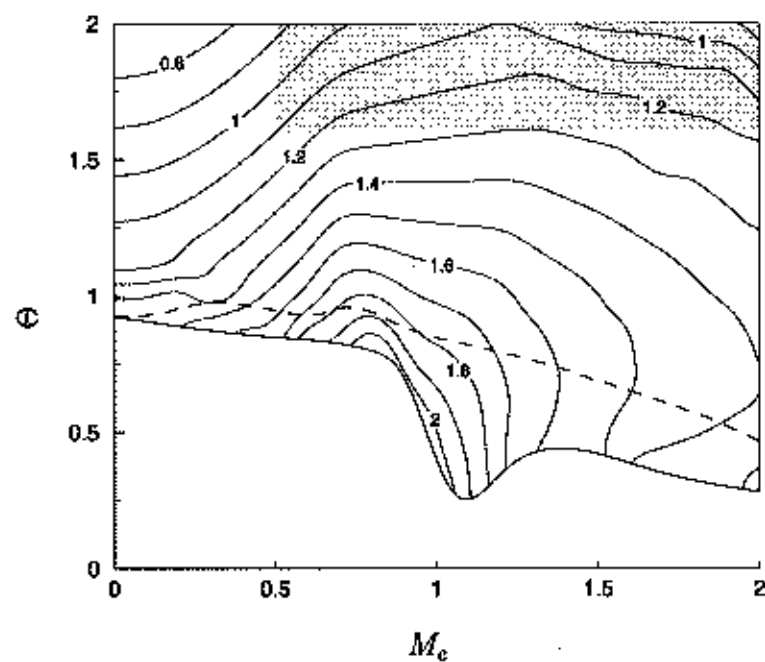
Figure 3.27: Υ contours using (a) λ and (b) λ_S parameters for scaling the slow mode growth rate in compressible reacting conditions ($s=1$, $\phi = 1$). The dashed line represents the colayer boundary.

Chapter 4

Nonlinear Stability Results

The different regimes of the compressible reacting mixing layer were established in the previous chapter. The detailed analysis of both single and multiple mode (colayer) flow structure is now addressed. The nature of these investigations, with their focus on the downstream evolution and mixing characteristics of different modes, requires a computational technique that can accurately simulate development in the nonlinear regime. Further, the broad, regime-based perspectives developed in the last chapter demand an analysis method that can be applied to a large number of flow conditions. These requirements have motivated our development of the parabolized stability equations, which provide accurate nonlinear modeling at reduced computational cost.

Our nonlinear investigations begin in section 4.1 with a discussion of the different cases and a detailed look at how one of these cases evolves. Results from single mode flow structure simulations are discussed in section 4.2. The nonlinear development of the different modes and their related mixing properties will be addressed. In section 4.3, the understanding developed from single mode flows will be applied to interpret results from colayer simulations. The final section of this chapter will demonstrate the ability of the PSE to simulate vortex pairing and will investigate the effect of compressibility on the pairing process.

4.1 Overview of the Nonlinear Calculations

To obtain reasonable conclusions regarding mixing from simulation results, it is desirable to calculate the flow beyond the saturation point of the fundamental mode. However, the relatively-rapid growth rate change at saturation can cause difficulty for the PSE calculation, which is based on the assumption of a slowly-varying flow. In the present study, this was addressed by taking advantage of observations from section 3.2.5 that increasing the velocity ratio provides near-equal reduction in growth rate for all instability modes. By setting the velocity ratio at $r = 0.5$, the growth rates were reduced to a third of their $r = 0$ values, allowing PSE calculations to run through saturation in most cases. Because this growth rate change occurs for all modes, our observations from the last chapter with $r = 0$ remain

valid here. Confirmation of this appears in figure 4.1, a regime chart in (s, Θ) coordinates at $M_c = 1.0$ and $r = 0.5$. The equivalent chart at $r = 0$ appears in figure 3.20(b), and their comparison reveals only a slight change in the boundaries between various regimes.

Figure 4.1 also shows the six flow conditions that form the basis of the nonlinear investigations described in this chapter. For single mode studies, two cases where the central mode is dominant were investigated with and without heat release in uniform-density conditions. At the same $\Theta = 0.75$ value of the former case, the density ratio was changed to $s = 2/3$ and $3/2$ to bias the flow structure towards either a fast or slow mode. Two colayer conditions were also evaluated: a fast/slow case at $(s = 0.94, \Theta = 1)$, and a central/slow case at $(s = 3/2, \Theta = 0.45)$.

4.1.1 Modal Interactions

Before presenting nonlinear stability results in section 4.2, it is instructive to first explain how instability modes interact in nonlinear PSE simulations. An example of this is shown in figure 4.2 for a two-dimensional colayer flow simulated with eighteen frequency modes. A typical initial condition is shown in figure 4.2(a) where energy is specified at $m = 1$ and $m = 6$ for the fast and slow modes, respectively. The energy distribution at an early point of the flow development is shown in figure 4.2(b), where energy from the initialized modes (black dots) has interacted to form modes at other frequencies (grey dots).

The nonlinear interactions shown in figure 4.2(b) work on a simple addition principle according their discrete Fourier representation (eq. 2.77). For example, the interaction between energy in frequency modes $m = 2$ and $m = 4$ makes a contribution to $m = 6$ through

$$
\begin{aligned}
u'u' &= \hat{u}_2 \, e^{-2i\omega_o t} \, \hat{u}_4 \, e^{-4i\omega_o t} + \ldots \\
&= \hat{u}_2 \, \hat{u}_4 \, e^{-6i\omega_o t} + \ldots
\end{aligned}
$$

where $(\ldots)$ represents additional terms from the interaction of modes with themselves and their conjugates. In this manner, energy can transfer from low to high frequencies. The reverse communication path, for example, involves the interaction of energy at $m = 7$ and a conjugate mode, $m = -6$, to make a contribution to $m = 1$. Section 4.3.1 will further address the computational issues of colayer simulations.

Energy development in a three-dimensional PSE simulation of the central mode at $M_c = 1, \Theta = 0.75$ is shown in figure 4.3. Modes that are present at a given streamwise location

are indicated by a circle, which is shaded according to logarithm of integrated energy in that mode. The flow has been initialized with energy in the fundamental mode (1,1) and the two-dimensional mode (1,0). The maximum initial fluctuation magnitude of these modes was set to 0.001 and 0.0002, respectively. (Full documentation of the input conditions is provided in Appendix C.)

Interactions with a second Fourier dimension work in the same manner as described above. The fundamental mode at (1,1) interacts with its conjugate (-1,-1) to contribute to the mean-flow correction (0,0), and with itself to produce energy at (2,2). The mean-flow correction contains significantly more energy than the instability modes because its magnitude scales on the energy of the mean flow. With increasing downstream distance, other modal interactions cause the Fourier map to fill according to the addition criteria discussed in section 2.4.1. A considerable amount of this development occurs between $x = 150$ and 250 when nonlinearities in the flow become significant.

It should be pointed out again that PSE simulations offer resolution of only the large-scale motion in the mixing layer by simulating the flow with (in effect) a severely truncated Fourier domain. This is quite clear in figure 4.3(f) where, at $x = 250$, there is a significant amount of energy at the finest scales of the simulation, although we note that this map only shows the resolved modes. The domain with dealiasing actually extends out to $M = 8$ and $N = 7$ to provide an energy sink for the PSE.

4.2 Single Mode Flow Structure

This section presents results from nonlinear simulations of flows with a single, dominant instability mode. Our focus is specifically placed on understanding the mixing mechanisms of the different flow structures. The central mode will be addressed first because it provides a reference point for the discussion of outer mode structure that follows in section 4.2.2.

4.2.1 Central Mode Mixing

There has been a considerable amount of investigation into the effect of compressibility on the mixing properties of the central mode. Experimental observations (reviewed completely in section 1.3.2) by Hall (1991), Dimotakis and Leonard (1994), Clemens and Paul (1995), and Island (1997) suggest that compressibility has negligible effect on the mixing efficiency of the central mode, and possibly even causes a slight increase. It should be clarified

that this conclusion does not imply an increase in the *amount* of mixed fluid; the reduced growth rate of the layer will certainly cause this to drop. Instead, this result states that the *fraction* of molecularly-mixed fluid inside the layer remains approximately the same as compressibility rises.

There have been no studies, however, into the effect of heat release in the presence of compressibility. This section will present results from two simulations done with the PSE at M_c=1.0 in both cold ($\Theta = 0$) and hot ($\Theta = 0.75$) conditions. We mention from the outset that the PSE can only be used as a first-order model of the mixing process. The PSE inherently limit simulation to only the first step in the formation of product: the entrainment of fluid that is governed by large-scale structure. However, the two subsequent steps of molecular mixing and chemical reaction are either ignored, in the case of molecular mixing, or simplified, in the case of the fast-chemistry assumption for chemical reaction. That notwithstanding, there is value in making general comments on the change in PDF shape between different flow conditions, particularly for regimes that have not been previously addressed by either experiment or computation. These calculations will also serve as a useful basis of comparison to the outer mode PDFs to be discussed in the following section.

Energy Development

Energy development in the reacting central mode case at $M_c = 1.0$, $\Theta = 0.75$, and $s = 1$ was discussed generally in section 4.1 in relation to modal interactions. A more detailed picture of the development is shown in figure 4.4(a) for a selection of prominent stability modes throughout the entire simulation. The importance of the streamwise vorticity mode (0,2) is noted in this plot. The calculation ends when the large energy content in multiple three-dimensional modes (*i.e.* the transition to turbulence) prohibits convergence of the PSE iteration at $x = 345$. Simulations of the three-dimensional central mode were the only calculations that were unable to run to saturation for this reason.

It should be noted that no phase shift was applied between the (1,1) and (1,0) modes. In lower compressibility simulations, the phase difference can produce appreciable changes in the flow structure: zero shift produces a 'bulging' mode while a $\pi/2$ shift results in a 'translative' mode, as described in Pierrehumbert and Widnall's (1982) secondary stability studies. At high compressibility levels, however, the oblique modes grow more quickly and quite independently of the two-dimensional wave. Therefore, the effect of this phase shift on flow structure becomes progressively weaker (Sandham 1989). At $M_c = 1.0$ this effect is

negligible, as demonstrated by the significant energy difference between the (1,1) and (1,0) modes in figure 4.4(a).

A similar set of energy profiles (not plotted here) are observed for the nonreacting case at the same compressibility, although their development occurs more quickly because heat release attenuates the central mode growth rate (see section 3.2.2). A summary of this effect is clearly seen in figure 4.4(b), which plots the energy development of the fundamental modes for both reacting and nonreacting simulations. A point of equal energy in the two fundamentals, marked on this figure at $x = 166$ and $x = 310$ for the nonreacting and reacting cases, was chosen for comparison of the mixture fraction PDFs that will be discussed below. It should be noted that the slight discrepancy in energy at the input condition is caused by the different eigenfunction shape in the two conditions — both simulations were initialized with the same magnitude.

Effect of Heat Release on the Scalar Field

Mixture fraction contours of the scalar field in the $y = 0$ spanwise plane are shown in figure 4.5 for the hot and cold cases. Both contour plots exhibit the type of three-dimensional structure that is associated with this compressibility level. Comparison of the two figures reveals the effect of heat release to lengthen the scale of large structures in both the streamwise and spanwise directions. The orientation angle between disturbance structures in figure 4.5 is unchanged between the two cases; the effect of heat release to orient the flow towards two dimensionality is only seen in the outer modes (see figure 3.17 and the related discussion in section 3.2.4).

A comparison of streamwise structure in the $z = 0$ plane of the scalar field appears in figure 4.6. The range of x values in this figure were chosen to represent regions of approximately equal fundamental-mode energy and scalar thickness in the two simulations. The larger-scale structure of the reacting case (figure 4.6a) is equally apparent in this view, with a fundamental mode streamwise wavelength of $31\delta_{\omega_o}$ versus $18\delta_{\omega_o}$ for the nonreacting case.

Mixture Fraction PDFs

Probability density functions provide a compact description of the time- and spanwise-averaged scalar field. It indicates the probability of finding fluid of mixture fraction $\xi \pm \Delta\xi/2$ at a given streamwise and cross-stream position in the flow and is subject to the

normalization

$$\int_0^1 P(\xi, x, y)\, d\xi = 1. \tag{4.1}$$

PDFs for the reacting and nonreacting cases are shown in figure 4.7. The streamwise locations were chosen at equal energy levels (see figure 4.4b), and this corresponds to 99% scalar thicknesses of $\delta_{\text{vis}} = 2.4$ and 2.2 for the hot and cold cases, respectively. Seven PDF's are shown at positions of equal spacing, $\Delta y = 1/8\delta_{\text{vis}}$, between $y/\delta_{\text{vis}} = -3/8$ and $+3/8$. The probability distributions were constructed by sampling 400 times across the period of the fundamental mode and, at each time, 400 samples were taken across the largest spanwise wavelength. The results were distributed into 50 bins to yield $\Delta\xi = 0.02$. The bin corresponding to $\bar{\xi}$ at each position is shaded in on the figure to provide a reference point. Both PDF's show a tilted behavior, which is consistent with the observations of Freund (1997) in well-resolved direct numerical simulations of a compressible jet. Based on the results of Rogers and Moser (1994), we do not expect to obtain the marching PDFs viewed in compressible experiments because of our highly-forced input condition (see section 1.3.2 for further discussion).

Again, we reiterate that these PDFs provide only a general understanding of the real shape because they lack molecular-mixing effects. However, there are some useful comparisons to make between the two distributions of figure 4.7. The first observation of note is the tendency of the reacting case to have a larger range of representation and a higher probability across that range in the PDFs at the two edges ($y = \pm 3/8\delta_{\text{vis}}$). This trend continues toward the central part of the layer, where the reacting PDFs have significantly higher concentrations of pure fluid (pure oxidizer at $\xi = 0$ and pure fuel at $\xi = 1$) than the reacting case. The contrast is particularly noticeable at the centerline, where the pure fluid concentration in the cold flow is negligible in comparison. As a result, the nonreacting case suggests better mixing, in the sense of having a larger integrated probability of mixed fluid, P_m, inside the layer where

$$P_m(x, y) = \int_{\Delta\xi}^{1-\Delta\xi} P(\xi, x, y)\, d\xi. \tag{4.2}$$

The reacting case, however, with its larger length scales, offers better stirring of the free-stream fluid into the reaction zone. The presence of molecular mixing would moderate some of this behavior by enhancing the diffusion of pure fluid (indeed, this is the reason why P_m was not directly evaluated), but the observed trends are still expected to dominate when this effect is included.

Finally, it should be pointed out that these comparisons are made at equivalent points of streamwise development. If they had been made instead at the same streamwise position, the larger growth rate in the nonreacting case would clearly result in better mixing and entrainment into the flow. This effect was seen in the incompressible experiments of Hermanson and Dimotakis (1989).

4.2.2 Outer Mode Mixing

The regime chart of figure 4.1 demonstrates that a 50% density bias in either free stream can result in an outer-mode-dominant flow structure at $M_c = 1.0$ and $\Theta = 0.75$. The scalar fields and associated PDFs for these two cases are addressed below. Both simulations are done with five frequency modes and four spanwise modes even though the dominant fast and slow instabilities at this compressibility level are still two dimensional.

Fast Mode

Mixture fraction contours for the fast mode case ($M_c = 1.0$, $\Theta = 0.75$, $\phi = 1$, and $s = 2/3$) are shown for spanwise and streamwise cross-sections in figure 4.8. Contours in the spanwise plane demonstrate the largely two-dimensional nature of the flow structure. The streamwise view details the position bias of the vortical structure entirely to one side of the layer, which results in little direct mixing in the reacting zone and almost no convolution of the flame sheet (shown as the dotted contour).

This one-sided isolation is clearly seen in the PDF profiles plotted in figure 4.9 at $x = 230$, a streamwise position just past the saturation of the fast mode fundamental instability. The lack of mixing on the slow side of the layer is evident in the near delta-function behavior of the PDF for $y < 0$ positions. Even at the centerline position there is only a modest range of mixture fraction values in comparison to what was seen with the central mode. The majority of the mixing influence is, understandably, concentrated on the fast side, although these PDFs also demonstrate a fairly limited range of populated mixture fraction values. Each of these three fast side PDF locations also feature a dominant probability of pure fluid. These distributions suggest a combustion process that is well supplied with oxidizer from mixing action on the fast side but is limited by the delivery of fuel through diffusion from the slow stream.

Slow Mode

A similar set of plane views and PDF plots for the slow mode case are shown in figures 4.10 and 4.11. The larger growth rate of the slow mode results in fundamental-mode saturation at $x = 125$. Similar to the fast mode, the flow structure is largely two dimensional, and exists entirely on one side of the flame sheet. A comparison of these PDFs to the fast mode case indicates an even greater polarization to one side. The delta-function behavior extends all the way to the center of the layer, implying that no appreciable mixing action extends down to the flame sheet position. Instead, the mixing influence from the slow mode is only present in the three positions on the slow side of the layer. Each of these positions demonstrates a similar probability distribution, having a strong bias towards pure fuel concentrations and a range of populated bins that extend out to $\xi \approx 0.5$.

4.2.3 Equivalence Ratio Effect on Outer Mode Mixing

The poor distribution of mixed fluid that was found in both outer mode cases provides motivation to investigate mixing enhancement techniques. One proposed approach, requiring no physical intervention to the flow, is simply to adjust the equivalence ratio to move the flame sheet towards the stream with the dominant flow structure. Presumably, placing the reaction zone closer to the area of vortical mixing would provide direct enhancement to the combustion process.

The slow mode case was chosen for this investigation and two lean equivalence ratios, $\phi = 0.25$ and 0.25, were compared to the base case at $\phi = 1$. Contours of the mixture fraction are shown in figure 4.12 for the three cases at similar regions of streamwise development. A comparison between plots indicates that the flame sheet does indeed move closer to the flow structure, although both elements are seen to shift towards the slow side as the equivalence ratio drops. An understanding of this behavior was developed in section 3.2.4, where the slow mode position, growth rate, and compressibility effect were shown to scale on the shear between the flame sheet and the slow stream. At $M_c = 1.0$, a relatively low value for the outer modes, the reduction in shear outweighs the benefit from the reduced compressibility effect and a net reduction in growth rate results when ϕ is lowered. This effect is seen in the longer streamwise distance it takes to develop observable flow structure in the progression from figure 4.12(a) through (c) — note the shift in the x coordinate.

However, this observation does not directly address the question of combustion enhancement. For this task, a measure based on the amount of product formation was developed to offer direct comparison between the mixing performance of different cases. This is constructed by integrating the density-weighted product mass fraction (see equation 2.128) over the period of the fundamental mode, T_λ, and across the span of the simulation in the cross-stream direction to yield

$$\mathcal{W}'(x) = \int_0^{T_\lambda} \int_{-\infty}^{\infty} \rho Y_p \, dy \, dt. \tag{4.3}$$

This constructed quantity must be normalized in a consistent manner before comparisons can be made. The factor T_λ to remove the time basis is obvious, but the choices for density and length scales only become clear by looking at the inlet profiles of $\bar{\rho}$, $\bar{Y}_p$, and their product, which are plotted in figure 4.13. The profiles in figures 4.13(a) and (b) show that the minimum (flame) density and product thickness both increase as ϕ drops, resulting in a larger integral of the ρY_p profile. These effects can be removed by adding the inlet values of flame density, ρ_{f_o}, and visual thickness to the normalization of equation (4.3) to give

$$\mathcal{W}(x) = \frac{1}{T_\lambda \, \delta_{vis_o} \, \rho_{f_o}} \int_0^{T_\lambda} \int_{-\infty}^{\infty} \rho Y_p \, dy \, dt. \tag{4.4}$$

Plots of the integrated product for the three equivalence ratio cases are shown in figure 4.14 in addition to profiles of the fundamental-mode energy development. The good collapse of base-line $\mathcal{W}$ values that is evident in figure 4.14 allows for direct comparison between the different cases. These profiles start to grow measurably when nonlinear effects become significant, and this point is closely correlated to the energy development shown in figure 4.14(b). The effect of ϕ on the growth rate is also clearly seen in the energy development.

For an analysis of combustion enhancement, our interest lies in the peak values of $\mathcal{W}$, which are seen to rise for $\phi = 0.5$ relative to $\phi = 1$ but fall for $\phi = 0.25$. This implies that moving the flame closer to the flow structure provides some initial benefit to product creation, but continued movement of the flame sheet eventually pushes the flow structure so far to the slow side that this benefit is lost. With the coupled effect of reducing the growth rate also taken into account, the evaluation of combustion enhancement from equivalence ratio variation is not encouraging: moderate ϕ reduction can, at best, provide a slight net benefit but further changes will have a negative effect on product formation.

It should be noted that at the end of the $\mathcal{W}$ growth period (corresponding to the saturation of the fundamental mode) some nonphysical behavior occurs in figure 4.14(a) when a reduction in total product is predicted despite the irreversible nature of fast chemistry. This is another limitation of the model, and is a direct consequence of evolving the mixture fraction field in Fourier space (see the mode detailed discussion to follow in section 5.2.3) but it does not affect the nature of our conclusions.

4.3 Colayer Investigations

The previous section provided a detailed understanding of the single mode flow structures that dominate most regimes of the compressible reacting mixing layer. In this section, however, we focus our attention on the special case of colayers where two modes are equally amplified. The development of this flow structure and its potential for mixing and combustion enhancement will be addressed. Nonlinear PSE calculations will also explore the practical extent of colayer conditions in the parameter space.

4.3.1 Colayer Modeling with the PSE

There are several complications involved with the PSE simulation of colayer flow and these will be addressed before results are presented in section 4.3.2. The challenge with multi-modal flows occurs when two or more stability modes of different phase speed, $c = \omega/\alpha$, are dominant in the same (ω_m, β_n) position of Fourier space. In this case, the traditional PSE representation of a disturbance,

$$\tilde{\phi}(x,y,z,t) = \sum_{m,n} \hat{\Phi}_{mn}(x,y) \, e^{i(\beta_n z - \omega_m t)}, \tag{4.5}$$

$$= \sum_{m,n} \hat{\phi}(x,y) \, A(x) \, e^{i(n\beta_1 z - m\omega_1 t)}, \tag{4.6}$$

where $A(x)$ is given by equation (2.74), lacks the ability to describe more than one magnitude and phase of $\hat{\Phi}$ (i.e. one stability mode) for each (ω_m, β_n) value. This overlap would require the introduction of a third Fourier dimension for the streamwise wavenumber, α, to resolve this ambiguity. This Fourier representation would take the form

$$\tilde{\phi}(x,y,z,t) = \sum_{k,m,n} \epsilon_o \, \hat{\phi}_{kmn}(x,y) \, e^{i(k\alpha_1 x + n\beta_1 z - m\omega_1 t)}, \tag{4.7}$$

although it is unclear how the reference alpha, α_1, would be chosen because α is a calculated quantity, unlike ω and β. Herbert (1994) briefly outlined an explicit-accounting approach for this three-dimensional formulation, but it is preferable to avoid the considerable complexity and computational cost of this method, if possible.

Fortunately, the colayer physics of mixing layer flows allow for a simpler approach because the different modes do not significantly overlap in Fourier space. The case of a triple point where all three—fast, slow, and central—modes have equal growth rates is particularly well suited for a demonstration of this fact. The polar contour plots of the triple point in figure 3.21 can be re-plotted in Cartesian Fourier coordinates (via equation 2.42) with the result plotted in figure 4.15. The general observations from figures 4.15(a) and (b) hold true across all flow conditions: the fast mode peak occurs at a frequency that is significantly greater than the slow mode, the slow mode is amplified at slightly higher frequencies than the central mode, and the central mode occurs at at higher spanwise wavenumber than either of the fast or slow modes in compressible flows. The most telling plot appears in figure 4.15(c), where the contours of the near-peak amplification rates of all three modes are shown to exist in distinctly separate regions. The lack of overlap suggests that an additional dimension in Fourier space is not required to resolve the different instabilities; this assumption was made in our calculations.

A final note on colayer calculations involves the method of introducing additional modes to the PSE simulation. As discussed in section 2.4.1, the initial phase of these modes was specified in relation to the fundamental mode, e.g. $\mathcal{R}\{\alpha_{mn}\} = m\mathcal{R}\{\alpha_{10}\}$. However, in colayer flows there are two fundamentals to consider. Modes that were input at frequencies higher than the fast mode where input in phase with the fast mode, while lower frequency wavenumbers were phase-specified by the slow mode. Variation in this procedure did not seem to affect the simulation results.

4.3.2 Fast/Slow Colayers

The flow physics of the colayer formed between fast and slow modes was explored extensively in the DNS simulations of Planché (1992), and it forms the basis of the two-step mixing process outlined in section 1.2. It is also the only variety of colayer that will exist in conditions of high heat release and compressibility. PSE simulations of this colayer structure were performed to allow direct comparison between the mixing of both outer modes in identical conditions. The computed PDF distributions can also be compared to Planché's

three-dimensional DNS results to confirm that our PSE calculations capture the important trends of better-resolved computations before we set out to answer new questions.

Flow Development

A fast/slow colayer case was simulated for the conditions $M_c = 1$, $\Theta = 1$, $s = 0.94$, a point that lies directly on the regime boundary of figure 4.1. This chart also shows the two-dimensionally dominance of the outer modes in these conditions and, correspondingly, a two-dimensional PSE simulation was run. To investigate the long-term development of this flow structure, subharmonics of the fundamental modes were also forced at the inlet. More specifically, the fundamental fast and slow modes were forced at the frequencies $m = 6$ and $m = 4$, a ratio that was chosen to correspond to the most unstable frequencies determined by linear stability. The subharmonics were forced at $m = 2$ (slow) and $m = 3$ (fast) with half the magnitude of the fundamental and a phase shift of $\phi_s = \pi/2$ to optimize their interaction with the fundamental modes (Planché 1992). The second subharmonic of the slow mode was also introduced with negligible forcing at $m = 1$. Full details of this input condition are given in Appendix C (case 6).

Energy development of the principle modes is shown in figure 4.16 with circles marking the points where energy in a subharmonic overtakes the fundamental mode. The colayer nature of the flow is evident in the similar (exponential) growth rates of the two fundamental modes; the slight difference results from forcing these instabilities at discrete frequencies prescribed by the PSE. Interestingly, the slow mode reaches saturation first at 50% of the fast mode energy level. Both fundamentals decay in energy with further streamwise development and are eventually overtaken by their subharmonics at $x = 330$ for the slow mode and $x = 395$ for the fast. The second subharmonic of the slow mode grows rapidly throughout the simulation and eventually overtakes the first subharmonic at $x = 420$.

Three views of the corresponding development in the mixture fraction field are shown in figure 4.17. The earliest view in figure 4.17(a) corresponds to the first saturation point and the dominance of energy in the two fundamental modes results in clearly observable flow structure on both sides of the layer. This mixing field appears to be a superposition of two single mode simulations: the vortical mixing is completely isolated to either side and the convolution of the flame sheet is negligible, implying little mixing in the reaction zone. This is exactly the nature of the independent, two-step mixing process that was described earlier in section 1.2.

With longer streamwise development, the flow structure becomes convoluted by the competing influence of the fundamental and subharmonic modes, which are now at equal energy levels. Compared to the slow modes, the fast fundamental and subharmonic contain the larger amount of energy and their combined presence has increased the thickness of the layer and, in the final view of figure 4.17, has pushed the flame sheet towards the slow side. However, this increase in thickness has occurred without the vortex-pairing mechanism that marks the interaction between the central mode fundamental and subharmonic (see section 4.4). DNS studies by Planché and Reynolds (1992) (and Planché 1992 in greater detail) showed the same phenomenon and gave it the term 'gulping'. Analysis of vorticity generation terms in the DNS revealed the presence of a large baroclinic torque that acts to prevent outer mode structures from pairing. They also identified the elongated shape and absence of roll-up in the outer mode vortices as factors in producing the gulping behavior.

Mixture Fraction PDFs

The mixing characteristics of this flow were investigated with a three-dimensional PSE simulation of the same case, but without resolving the subharmonics. Three-dimensional simulations are required for PDF construction because they provide a second statistical dimension to the flow, which results in a far better realization of the PDF than sampling over the time period alone. Plots of the mixture fraction contours through the $z = 0$ plane are shown at three different times to detail the structure evolution in figure 4.18. The plots are separated by $\Delta t = \pi$ where, for the special case of this simulation, the periods of the fast and slow modes are 2π and 4π. Dotted lines are drawn between plots to indicate the displacement in time of a specific fast and slow mode structure. The difference in slope between these lines is proportional to the phase speed difference of the modes: 0.64 and 0.88 for the slow and fast fundamentals, respectively. The difference would be more significant if the velocity ratio was reduced, but $r = 0.5$ was set constant in all simulations.

The mixture fraction PDF of this flow structure at x=230 is shown in figure 4.19 using the same plotting convention as the previous section. Similar to the mixture fraction field, the colayer PDF has the appearance of being constructed from half of each single mode PDF sequence of figures 4.9 and 4.11. Again, this implies very little communication between the different sides. However, the presence of mixing on both sides of the layer, even without direct interaction, represents significant enhancement relative to the single mode PDFs of section 4.2.2. It is also noted that figure 4.19 is very similar to the PDFs from Planché's

(1992) three-dimensional DNS simulations. Our PSE-based PDF at the centerline even replicates the probability bias towards the slow stream that was observed in Planché's DNS results. This was attributed to the better performance of the slow mode in entraining pure fluid to the reacting zone.

4.3.3 Central/Outer Colayers

Beyond documenting the shape of the fast/slow colayer boundary in the parameter space, the regime charts of section 3.3 also identified a new type of colayer structure created between the central and either of the fast or slow modes. A central/slow mode colayer was chosen for investigation. The specific flow conditions were obtained by reducing Θ from the slow mode case ($M_c = 1$, $\Theta = 0.75$, and $s = 3/2$) until its growth rate was equal to the central mode, which occurred at $\Theta = 0.45$ (see figure 4.1). The energy development for a selection of modes in the three-dimensional PSE simulation of this case are shown in figure 4.20. The initial condition consisted of equal-magnitude forcing of the three-dimensional central mode (1,1) and the two-dimensional slow mode (3,0). However, the integrated energy of the central mode is still significantly larger than the slow mode at the inlet because of its broader scale (see section 3.1.2).

The downstream development of central and slow mode energy is approximately equal until the slow mode saturates at $x = 175$. The mixture fraction contours of figure 4.21(a) detail the flow structure in this region and the presence of slow side mixing is observable. Figure 4.21(b) presents a view further downstream, just before the calculation was forced to terminate. At this point the energy of the central mode completely dominates the flow structure with some additional mixing present on the slow side of the layer. The PDF distributions for this flow are shown in figure 4.22 at two streamwise positions. The earlier position ($x = 180$), has a PDF that features a strong bias towards mixing slow-side fluid ($\xi > 0.5$) but is more widely distributed than the PDF from the slow mode alone (shown in figure 4.11). At $x = 215$ the PDFs now more closely resemble the central mode probability distributions of figure 4.7(a), with a broad population of bins and pure fluid from both sides present at most positions. Evidence of the slow mode is seen in the slightly higher probability of mixed fluid ($0 < \xi < 1$) on the slow side of layer. Thus, the slow mode presence offers some benefit to mixing but it is largely overwhelmed by the higher energy level of the central mode in this class of colayer. The same conclusion is expected to result in central/fast colayer conditions.

4.3.4 Colayer Regimes

With the mixing enhancement of colayers now established, there is a need to determine how difficult these conditions are to reproduce in a real flow. Specifically, the question concerns the effective 'thickness' of the colayer lines that were plotted in the regime charts of section 3.3: how close to those boundaries do the flow conditions need to be to observe colayers? Linear stability results suggest that the boundaries are very thin; a slight difference in exponential growth rates will eventually lead to the dominance of one mode over another. In reality, however, there is a saturation mechanism in place that limits this exponential growth. If saturation occurs before the difference in growth rates can effectively separate the modes, then colayer conditions will be observed in the resulting flow structure.

Several PSE simulations of a fast/slow colayer were conducted to determine the sensitivity of this dual-mode flow to changing conditions. Starting at a fast/slow colayer point, the density ratio was increased to move in a direction normal to the colayer boundary; the progression of these points on the (s,Θ) regime chart is shown in figure 4.23(a). The corresponding linear stability growth rates of the fast and slow modes appear in figure 4.23(b), which provides a further view of the strong effect the density ratio has on the relative amplification of the outer modes (see section 3.2.3). The energy development of the fundamental fast and slow modes are plotted in figure 4.24 for the four different density ratio cases. At the true colayer condition ($s = 0.94$), the similar growth rates of the modes lead to saturation of the fast and slow modes at the same general streamwise position. But as s is increased, the energy profiles of the fast and slow modes become increasingly disparate. At $s = 1.125$, for example, the fast mode energy is two orders of magnitude lower than the slow mode when it saturates.

A qualitative view of what this does to the flow structure is seen in the mixture fraction contours of figure 4.25. The 30% change in density ratio between the first and last case is enough to apparently erase the fast mode flow structure. The fast mode will eventually appear with further streamwise development, although probably only after the point that the slow mode has interacted with its subharmonics and grown appreciably in both size and energy. Our conclusion is that the range of fast/slow colayer conditions—and hence the mixing enhancement they provide—will be relatively limited in the parameter space.

A final note concerns the presence of conditions for colayers between the central and outer modes. The calculations of the previous section suggest that the central mode influence will extend into the outer mode regimes, with the outer mode structure becoming a

more dominant part and appearing earlier in the flow development as either M_c or Θ is increased to favor their growth rate over the central mode. In practice, this will manifest itself as an early concentration of mixing energy on one side of the layer that persists even as the broadly-distributed central mode becomes appearent. This change in downstream structure will be the identifying mark of this colayer condition, rather than the co-development of outer modes seen in a fast/slow colayer case.

4.4 Simulation of Central Mode Vortex Pairing

The pairing of vortices is the dominant growth mechanism for the central mode (Winant and Browand 1974; Pierrehumbert and Widnall 1982; Monkewitz 1988) and it is therefore essential that simulation techniques—regardless of their approximation—are able to capture the flow physics of this process. This presents a significant challenge to the parabolized stability equations. By construction, parabolic methods exclude upstream propagation of information, allowing the computation to proceed in a streamwise advancing procedure. This would seem at odds with one explanation for the mechanism of vortex pairing which is based on the interaction between vortices—their coupling and induced co-rotation—that implies an elliptic effect. Comparison of PSE results to DNS computation are provided for both subsonic and supersonic conditions to demonstrate how the PSE approach can, in fact, accurately simulate vortex merging. This observation brings further support to the viewpoint (Monkewitz 1988) that pairing is simply dominated by the growth of instability modes rather than governed by the Biot-Savart (elliptic) interaction between vortices. With its fidelity confirmed, PSE simulations can also be used to investigate an outstanding question concerning the delay in vortex pairing with compressibility.

4.4.1 Subsonic Vortex Pairing

The direct numerical simulation of Colonius *et al.* (1997) at $Re = 5000$, $M_c = 0.125$, $s = 1$, and $r=0.5$ is an excellent comparison case for the PSE. Their spatial simulation, which was conducted to evaluate the accuracy of acoustic analogies, used an input velocity profile from the boundary-layer equations coupled with the most-amplified (fundamental) linear instability disturbance and its first three subharmonics at the initial conditions, all with a normalized inlet magnitude of 0.001. A PSE simulation was constructed in a nearly identical manner. For simulations with a fixed number of harmonics of the fundamental—three in

this case—the inclusion of each subharmonic requires doubling the number of modes. For this reason, only the first two subharmonics were included in the PSE calculation to yield a total of 16 frequency modes. In this configuration, the fundamental mode corresponds to $m = 4$ and the first and second subharmonics to $m = 2$ and $m = 1$, respectively.

A phase shift was applied to the first subharmonic to minimize the distance between pairings. This was done by ensuring that v' at the centerline for the $m = 2$ mode was exactly out of phase with both $m = 1$ and $m = 4$. With the phase of each input mode set to be purely real at the centerline by default (see section 2.4.1), this shift simply amounted to multiplying the $m = 2$ mode by $e^{i\pi}$ at the initial condition. Colonius *et al.* applied small shifts to each input mode because of their different phase normalization procedure.

A direct, visual comparison between DNS and PSE calculations can be made in the spanwise vorticity contour plots of figure 4.26. The qualitative agreement is excellent considering that the PSE is done using only sixteen frequency modes. The large-scale features are nearly identical, with the location of the two vortex pairing events occurring at the same streamwise position. (A precise comparison of the pairing location should be done by comparing the vorticity thickness evolution, but this data is unfortunately not available for the DNS.) Similar to the DNS comparisons made during the validation of section 2.5, the PSE results indicate ω_z fluctuations inside the vortices of the fundamental (between $x=40$ and 90) which are caused by insufficient resolution in the frequency domain. The wavelength of the $m = 16$ mode in this simulation is approximately two nondimensional lengths; features on and below this size in the streamwise direction are not being accurately modeled.

A quantitative comparison of the two simulations is shown in figure 4.27, where integrated energy in $\hat{u}$ for the three input modes are plotted. The PSE results for the subharmonic modes ($m=1$ and 2) are nearly indistinguishable from the DNS solution. (There is some early disagreement in the $m = 1$ mode due to flow adjustment in the DNS but this disappears when the energy in the mode becomes significant.) The agreement in the fundamental mode ($m = 4$) is also impressive but with some discrepancy in the later stages which, again, is most likely due to insufficient frequency resolution.

4.4.2 PSE Insight into the Nature of Vortex Pairing

The excellent agreement between PSE and DNS calculations in the accurately-modeled, large-scale flow features demonstrates that the PSE approximations have not eliminated

the important physics of the problem. Returning to the discussion of ellipticity given in section 2.3.5, we recall that the rapid part of the streamwise pressure derivative is retained even with our approximation of $\Omega = 0$ in equation (2.91). A testament to the importance of this term appears in figure 4.28, which plots the energy comparison for the PSE simulation with the streamwise pressure derivative completely removed, rendering the technique completely ineffective.

A further simulation with the PSE was done to investigate the degree of interaction between the modes by removing forcing of the fundamental. The energy development for this case is shown in figure 4.29. Comparison to the DNS results and to the PSE results for the full simulation in figure 4.27 reveals little difference in the energy development of the two remaining modes. The only observable change is a slightly earlier saturation in the first subharmonic ($m = 2$), most likely caused by the absence of the effect from the fundamental mode on the mean flow to grow the layer thickness. An understanding of what this does to the flow structure is seen in figure 4.30, where we compare spanwise vorticity contours between the complete PSE solution and the PSE solution initialized without the fundamental mode. The only missing feature in figure 4.30(b) are the vortices of the fundamental modes; all of the other large-scale features—even early in the flow development—are nearly identical.

The close agreement between these plots suggests that the growth of the stability modes is the controlling mechanism and that mutual pairing interactions play only a secondary role. However, the relative importance of mutual induction (Biot-Savart) between vortices cannot be established without a detailed analysis that lies beyond the scope of this investigation. Regardless of the exact mechanism, however, these observations show that the overall development of the layer through vortex pairing is closely connected to the growth rate of the instability modes. This result extends the similar conclusion of Monkewitz (1988) that was limited to studying weakly nonlinear interactions. Indeed, as Monkewitz points out, this observation may provide a physical explanation for the accuracy of linear stability calculations. Winant and Browand (1974) demonstrated that the rate of pairing interactions determines the spreading rate of mixing layers and thus linear stability analysis, which accurately models the appropriate physics of the pairing process (the growth rate of instability waves), should also closely predict experimentally-observed spreading rates. Some agreement with this hypothesis can be found in the suggestion of Hermanson and Dimotakis (1989) that the mechanisms for vortex amalgamation (*e.g.* pairing) are inhibited

by heat release. This same effect was noted in the linear stability growth rate predictions of section 3.2.2. This connection will be explored further in section 4.4.4.

4.4.3 Supersonic Pairing Case

A second vortex pairing comparison to direct simulation results was conducted for the $M_c = 0.5$, $s = 1$, and $r = 0.6$ flow that served to validate the PSE implementation in section 2.5. In this case, however, the subharmonic was forced at a phase shift of $\phi_s = \pi/2$ to promote pairing. The PSE simulation for these conditions was done with sixteen frequency modes. Figure 4.31 compares PSE and DNS results for both modal energy and vorticity thickness. The noticeable feature of the energy development shown in figure 4.31(a) is the early divergence of the subharmonic mode ($m = 1$) solutions. The PSE solution grows more rapidly and predicts saturation at an earlier streamwise position than the DNS.

The larger energy in the subharmonic mode causes a similar divergence between the vorticity thickness results shown in figure 4.31(b). However, the PSE solution retains the same overall shape characteristics, predicting the first plateau that corresponds to the saturation of the fundamental, the sharp change that occurs when two inflection points develop in the mean velocity profile, and the point of maximum thickness when the vortices have rotated $90°$ around each other (Sandham 1994). The point of maximum thickness will be used to identify the pairing distance in the next section; the PSE solution differs only slightly from the DNS on this measure, predicting pairing at $x = 152\delta_{\omega_o}$ verses $x = 159\delta_{\omega_o}$ from the DNS result.

Some insight into the disagreement between the PSE and DNS solutions can be found in comparing the growth rates of the fundamental and subharmonic modes in figure 4.32. The agreement for the fundamental mode in figure 4.32(a) is quite good until the growth rate undergoes a steep change at $x = 125$. This rate of change is contrary to the slowly-varying approximation of the PSE formulation, and this may explain some of the discrepancy. The behavior of the subharmonic growth rate is more difficult to explain. The PSE solution predicts an increase in growth rate starting very early in the streamwise development and well before nonlinear interaction becomes important. This appears to be due to some type of resonance that is present in the PSE but not the DNS simulation. The reason for this resonance, which is the source of disagreement in the energy development of figure 4.31(a), is not currently understood.

4.4.4 The Effect of Compressibility on Vortex Pairing

With the ability of the PSE to simulate vortex pairing now demonstrated, the technique can be used to address an outstanding question concerning the delay in vortex pairing caused by compressibility. In an investigation of this effect, Sandham (1994) identified three alternate explanations:

- The observed elongation in vortex shape caused by compressibility was affecting their ability to co-rotate;

- the rate of rotation of vortices was affected by compressibility;

- or, the well-know suppression of instability growth rates related to compressibility was responsible for the delay.

Sandham used a vortex sheet model in comparison to DNS results to first show that the model was an accurate representation of pairing and, second, that changing the effective size of the vortices in this model did not account for the observed delay in pairing. He also conducted direct simulations of simple co-rotating vortices to demonstrated that Mach number changes resulted in only a secondary effect on their rotation rate. Thus, by discounting the first two explanations, Sandham (1994) concluded that the 'most likely explanation is that compressibility effects .... continue to play a role in the vortex pairing process.'

The observations of the previous sections tend to support this hypothesis. The demonstrated independence of the different instability modes in the pairing process supports the conclusion that their growth-rate suppression will directly delay the onset of pairing. The parabolized stability equations were used to further investigate this conclusion. Six simulations, equally spaced between $M_c = 0$ and $M_c = 0.625$, were conducted with the two-dimensional PSE using eight frequency modes for otherwise identical input conditions ($r=0.5$, $s = 1$, $Re = 5000$). The vorticity thickness evolution for these simulations is shown in figure 4.33. The delay in pairing, as measured by the location of maximum vorticity thickness, is clearly seen with increasing compressibility. A direct comparison of this delay to the growth rate suppression of the most-amplified (*i.e.* fundamental) mode from linear stability calculations is shown in figure 4.34. Both the linear stability growth rate and pairing distance, the latter for both PSE and DNS results, have been normalized by their values at $M_c = 0$. Plotted in this manner, the direct relationship between the two effects becomes clear. Thus, the attenuation of instability waves with compressibility, which impacts both

linear and nonlinear processes equally (Luo *et al.* 1996; see also section 1.3.2), can be seen to directly account for the delay in vortex pairing.

4.5 Chapter Summary

The parabolized stability equations were applied to study the nonlinear evolution of the compressible reacting mixing layer. In single mode studies, three-dimensional PSE calculations demonstrated the effect of heat release to reduce the growth rate of the central mode but increase the scale of the flow structure. Comparison of mixture fraction PDFs between the hot and cold conditions at positions of equivalent streamwise development suggested better mixing in the nonreacting case, while the larger scales of the reacting case resulted in better stirring. Probability distributions from simulations of single outer mode flows documented the poorly-distributed, one-sided mixing that accompanies this flow structure.

Colayers formed between the fast and slow modes produced a flow with little interaction between mixing zones on either side of the flame sheet. This situation persists well into the nonlinear regime, and even after the subharmonic modes have become dominant. The fast/slow colayer was shown to be sensitive to changing density ratio and, therefore, the mixing enhancement offered by this flow structure will only appear in limited regions of the parameter space. Colayers between the central and outer modes, however, will have a larger presence and will appear as an outer mode flow structure that becomes overwhelmed by the central mode with increasing streamwise evolution.

Finally, it was shown that the PSE can accurately simulate vortex pairing of the central mode. This result extends the conclusion of Monkewitz (1988) into the fully nonlinear, non-parallel domain: vortex pairing appears to be determined simply by the independent growth of instability waves. While our demonstrations cannot definitively exclude the mutual induction mechanism (Biot-Savart), they do suggest that induction is of secondary importance to the growth of stability modes in controlling vortex pairing. This observation received further support in the demonstration that the delay in pairing caused by compressibility was very closely correlated to the attenuation of instability growth rates.
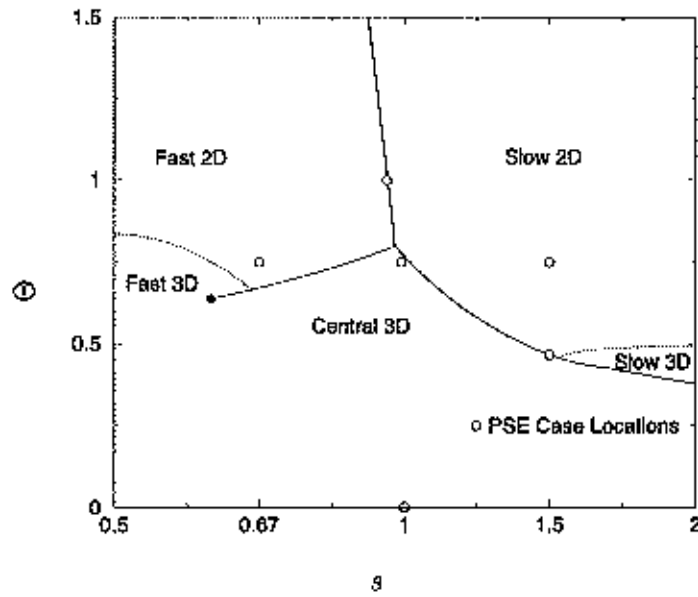
Figure 4.1: Plot of PSE Cases on the mid-compressibility (s,Θ) regime chart with $r = 0.5$ ($M_c=1$, $\phi = 1.0$).
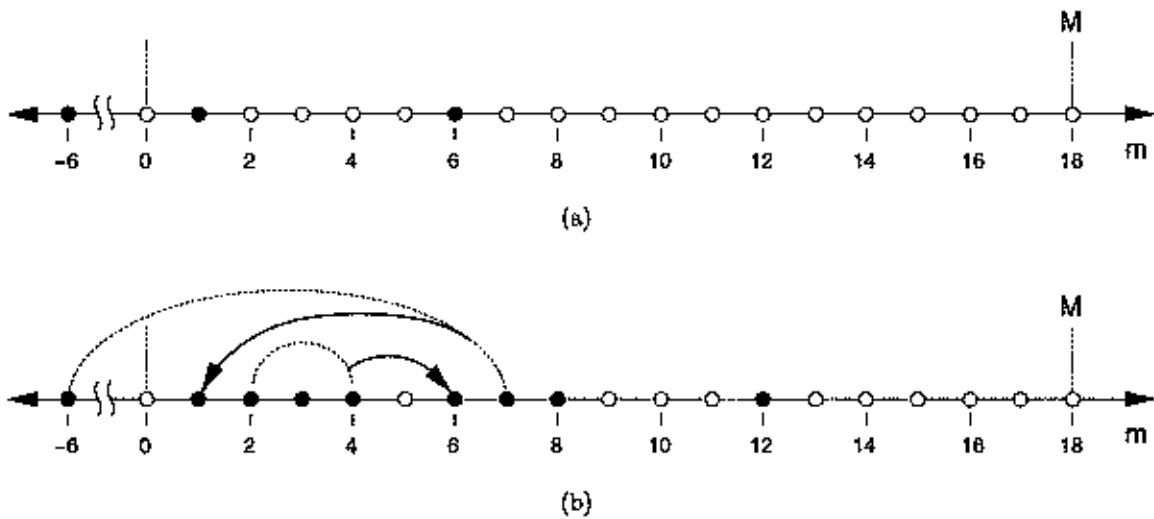

Figure 4.2: Map of energy locations at (a) the initial condition and (b) a point of early development in a typical colayer simulation where examples of interaction from low to high frequency and vice versa are shown.
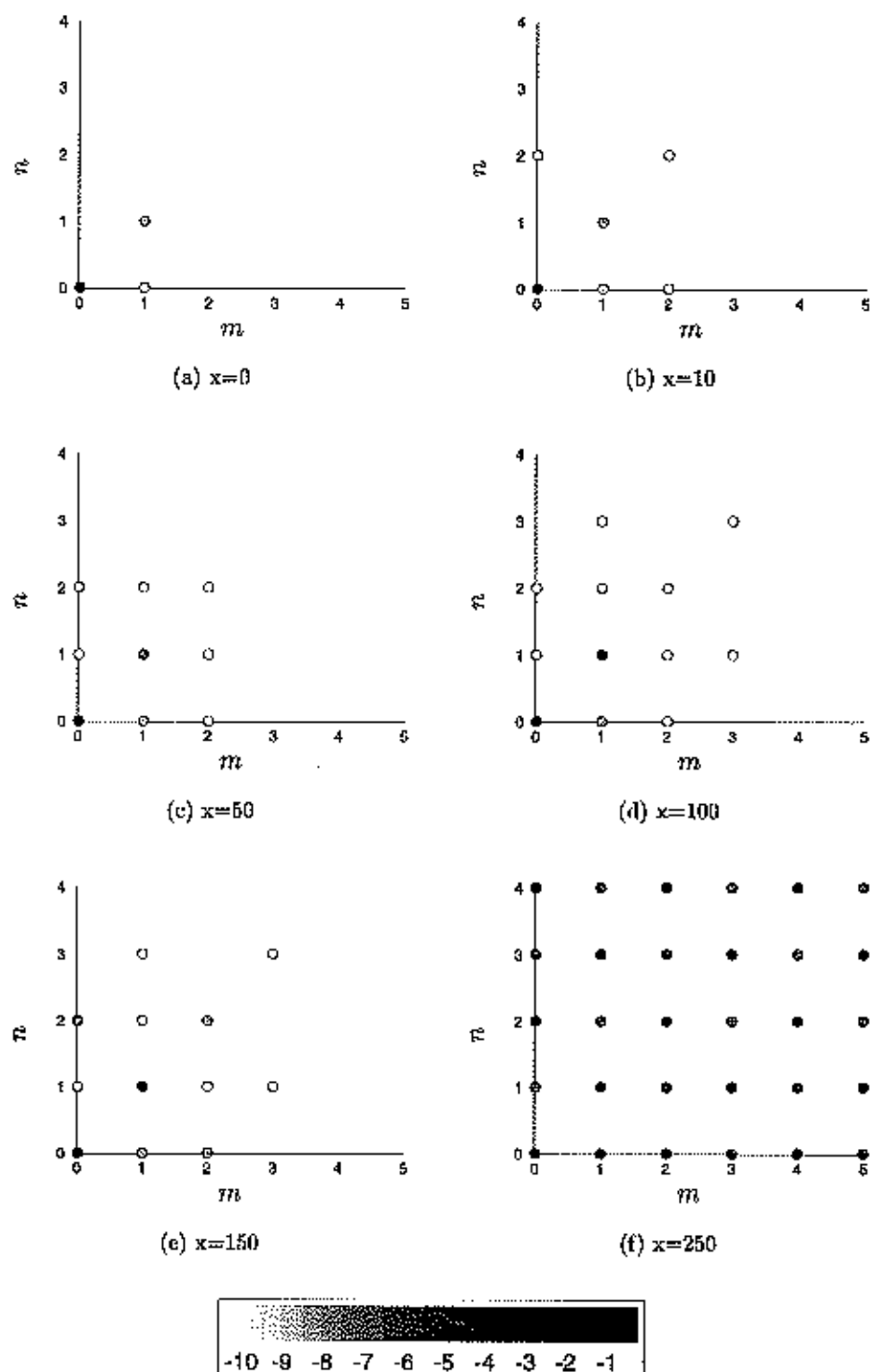
Figure 4.3: Development of the $\text{Log}(E^t_{mn})$ map in Fourier space for a central mode in compressible reacting conditions $M_c = 1.0$, $\Theta = 0.75$, $\phi = 1$, $s = 1.0$, $r = 0.5$.
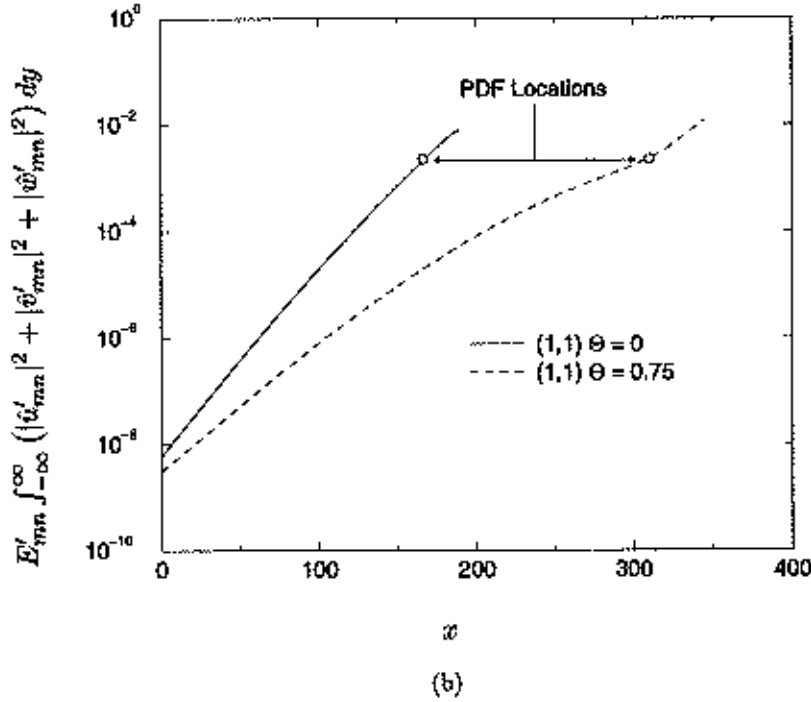
(a)
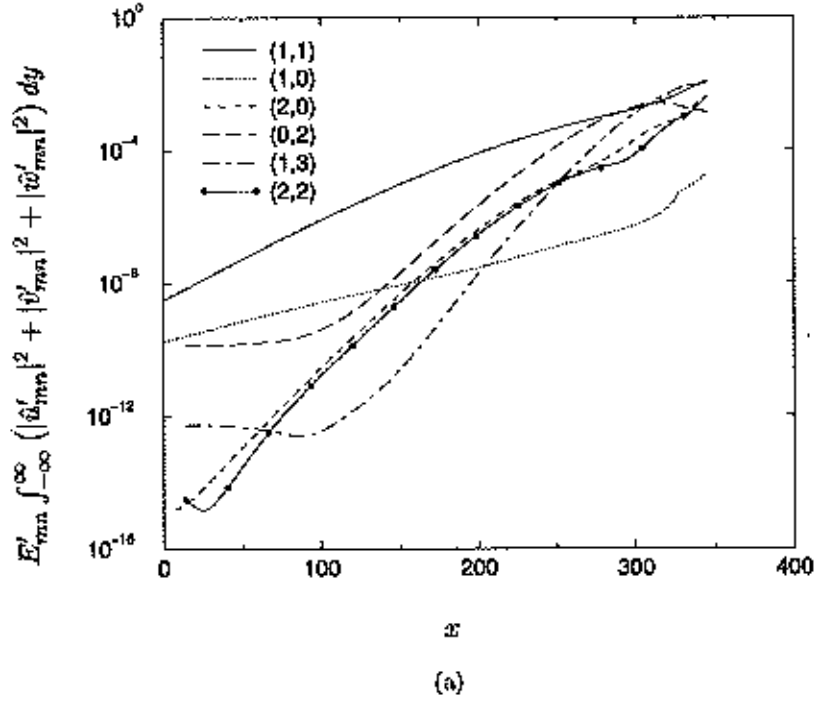

(b)

Figure 4.4: (a) Energy development for selected modes of the central mode compressible reacting case (M_c=1, $\Theta = 0.75$, ϕ=1, s=1.0, r=0.5, M=5, N=4), and (b) a comparison of energy in the fundamental mode (1,1) with and without heat release for the same case; locations corresponding mixture fraction PDFs are also marked.
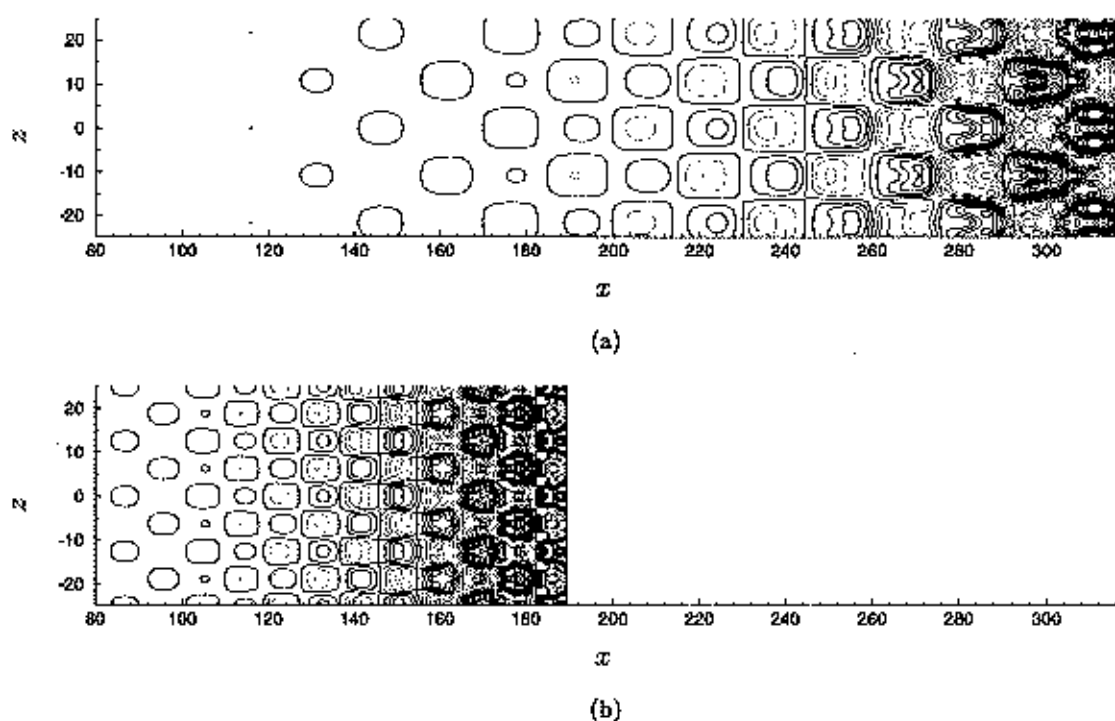
(a)

(b)

Figure 4.5: Comparison of the spanwise mixture fraction field at $y = 0$ for the central mode in (a) reacting ($\Theta = 0.75$) and (b) nonreacting ($\Theta = 0$) compressible conditions ($M_c=1$, $\phi=1$, $s=1.0$, $r=0.5$, $M=5$, $N=4$). Mixture fraction contours with $\Delta\xi = 0.08$, $\xi_{\max} = 0.98$, and $\xi_{\min} = 0.02$; contours for $\xi < 0.5$ are dashed.
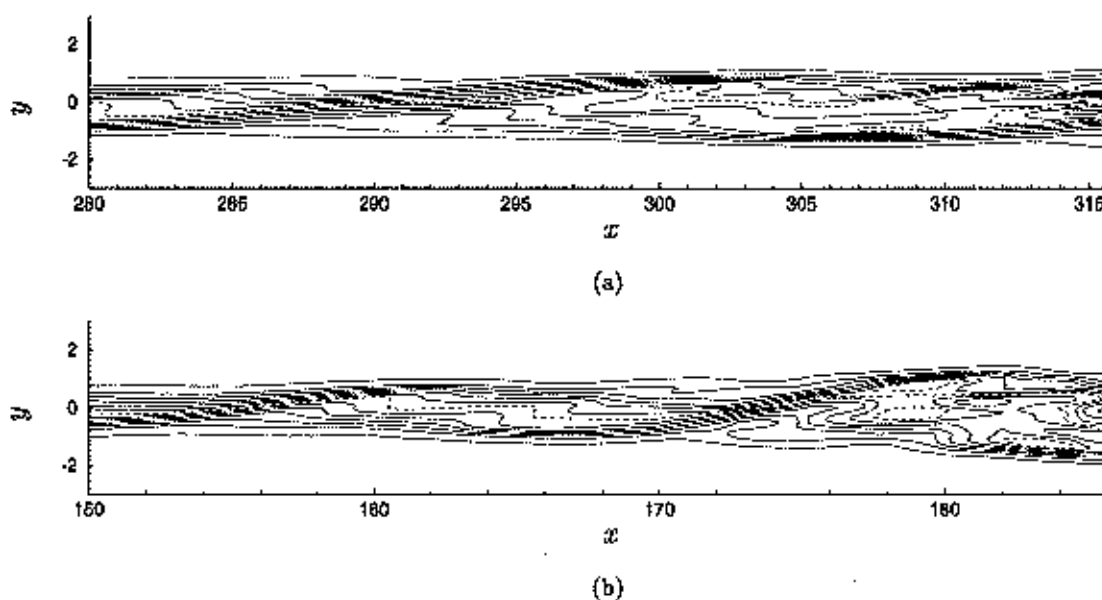

(a)

(b)

Figure 4.6: Comparison of the streamwise mixture fraction field at $z = 0$ for the central mode in (a) reacting and (b) nonreacting conditions (see caption for figure 4.5). Flame sheet at $\xi=0.5$ marked as a dotted line.
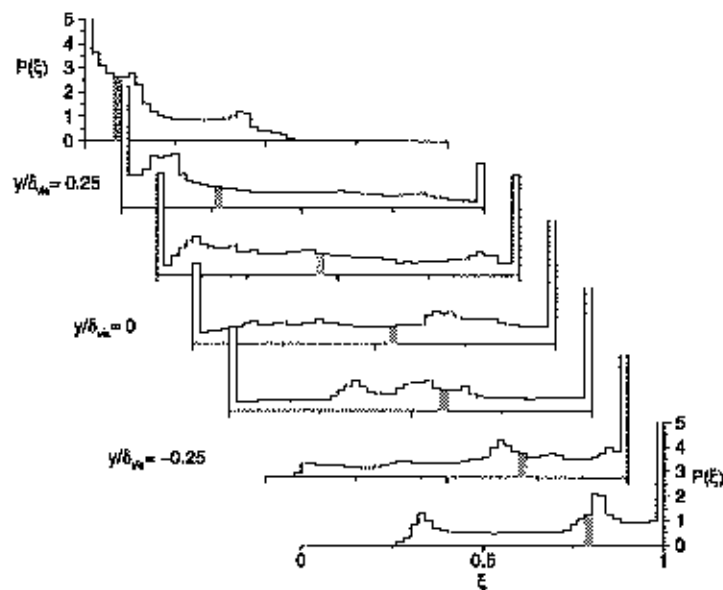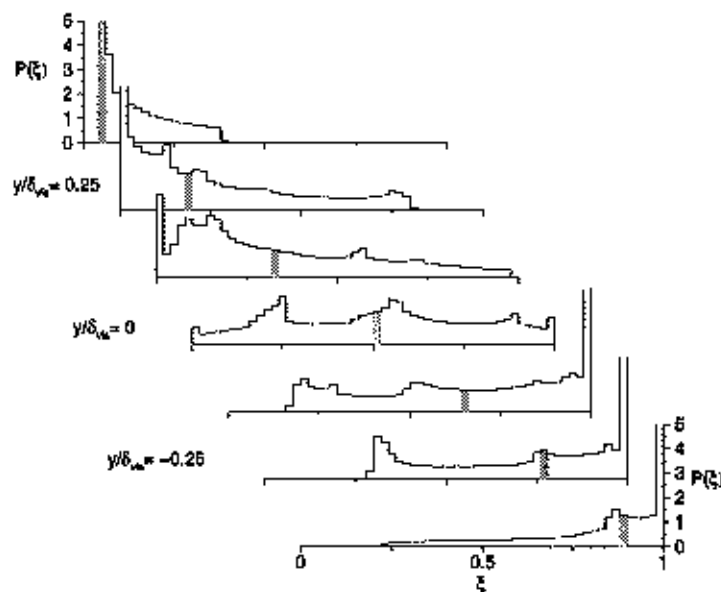
(a) $\Theta=0.75$, $x=310$

(b) $\Theta=0$, $x=166$

Figure 4.7: Mixture fraction PDFs of the central mode at $z = 0$ in (a) compressible reacting flow ($\Theta = 0.75$, $x = 310$) and (b) compressible nonreacting flow ($\Theta = 0$, $x = 166$) at the conditions of figure 4.5. Seven symmetric y positions are represented with $\Delta y = 0.125\delta_{vis}$. The probability axis has been truncated for visualization purposes and the bin corresponding to $\bar{\xi}$ has been shaded in. The x locations were selected to have equal energy in the fundamental modes (see figure 4.4).
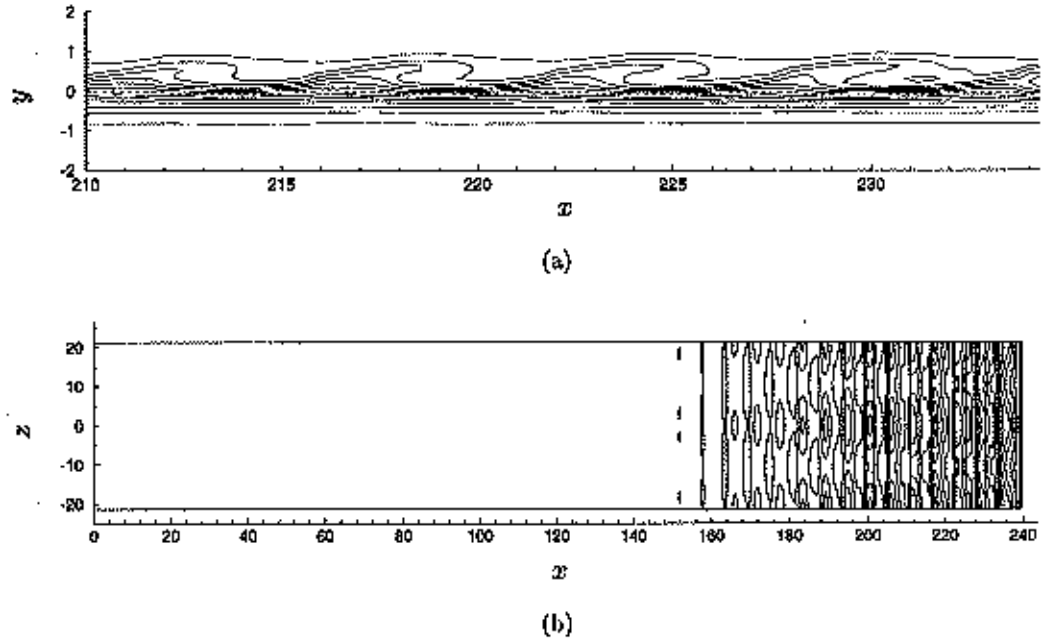
(a)

(b)

Figure 4.8: Mixture fraction field for a fast mode in compressible reacting conditions across (a) streamwise ($z = 0$) and (b) spanwise ($y = 0.5$) planes ($M_c=1$, $\Theta=0.75$, $\phi=1$, $s=1.5$, $r=0.5$, $M=5$, $N=4$). Mixture fraction contours with $\Delta\xi = 0.08$, $\xi_{max} = 0.98$, and $\xi_{min} = 0.02$ and the flame sheet at $\xi=0.5$ marked as a dotted line.
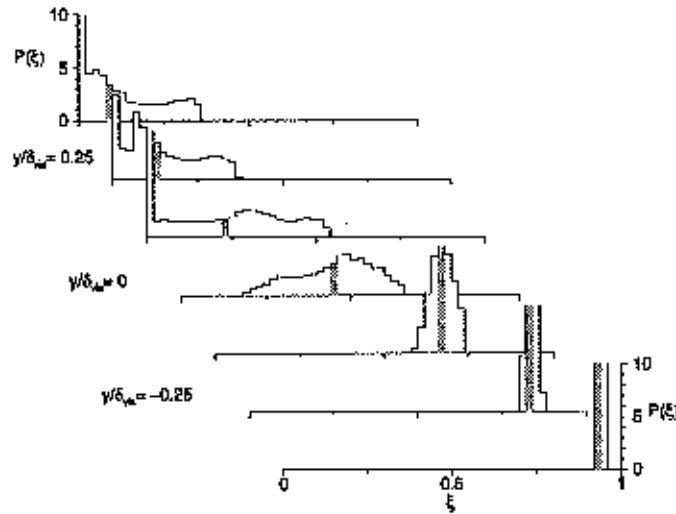

Figure 4.9: Mixture fraction PDF at $x=230$ for the fast mode of figure 4.8. Seven symmetric y positions are represented with $\Delta y = 0.125\delta_{vis}$. The probability axis has been truncated for visualization purposes and the bin corresponding to $\bar{\xi}$ has been shaded in.

(a)

(b)
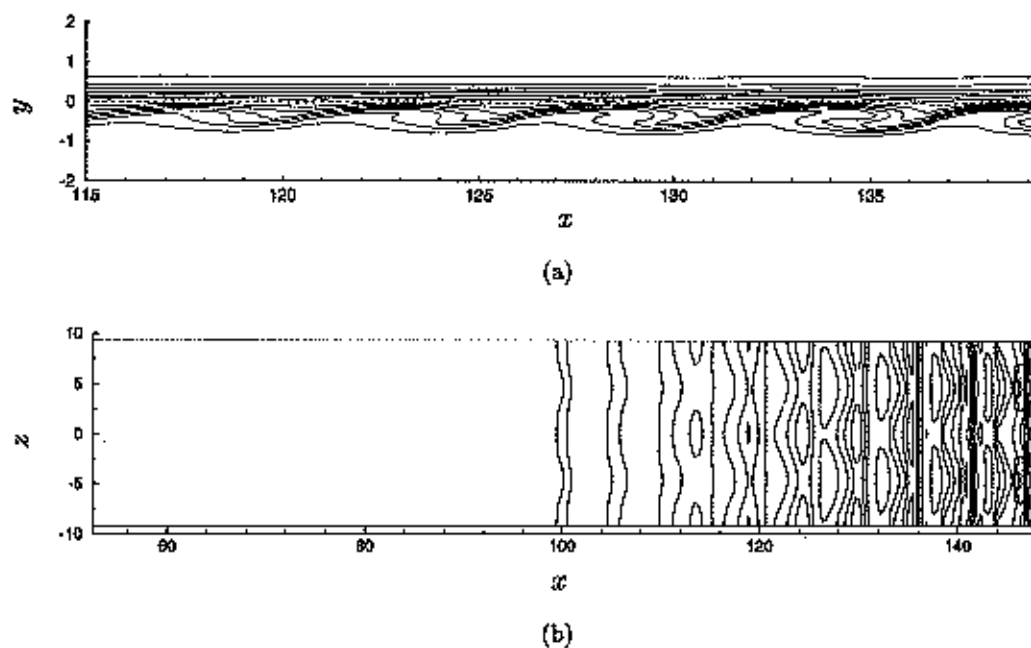
Figure 4.10: Mixture fraction field for a slow mode in compressible reacting conditions across (a) streamwise ($z = 0$) and (b) spanwise ($y = -0.58$) planes ($M_c=1$, $\Theta=0.75$, $\phi=1$, $s=2/3$, $r=0.5$, $M=5$, $N=4$). Mixture fraction contours with $\Delta\xi = 0.08$, $\xi_{max} = 0.98$, and $\xi_{min} = 0.02$ and the flame sheet at $\xi=0.5$ marked as a dotted line.

Figure 4.11: Mixture fraction PDF at $x=140$ for the slow mode of figure 4.10. Seven symmetric y positions are represented with $\Delta y = 0.125\delta_{vis}$. The probability axis has been truncated for visualization purposes and the bin corresponding to $\bar{\xi}$ has been shaded in.

(a)

(b)

(c)
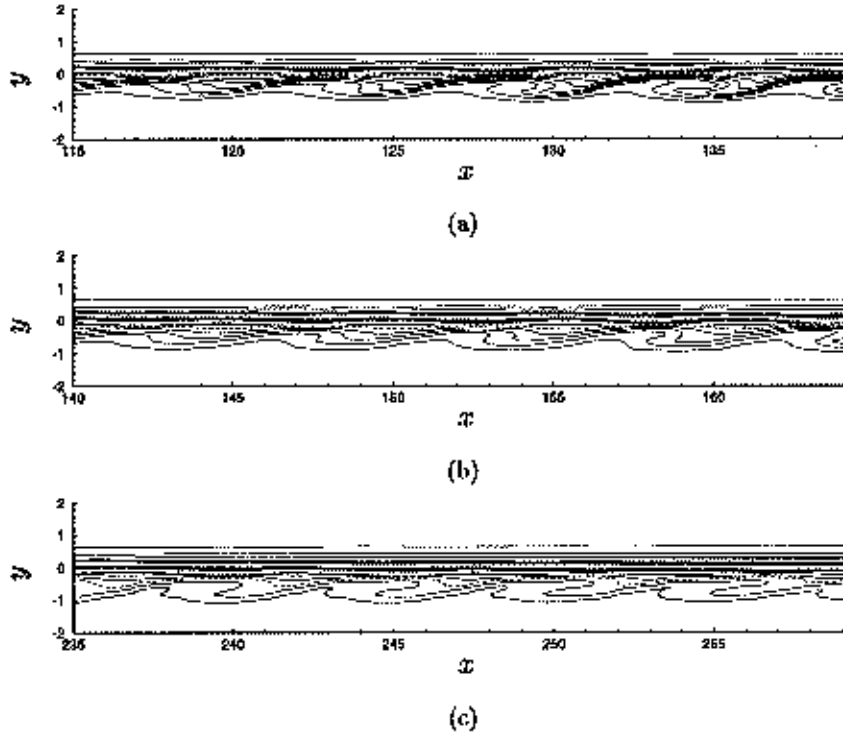
Figure 4.12: Effect of equivalence ratio on the slow mode mixture fraction contours for (a) $\phi = 1.0$, (b) $\phi = 0.5$, and (c) $\phi = 0.25$ with the flame sheet contour shown as a dashed line at $\xi = 0.5$, 0.66, and 0.8, respectively ($M_c = 1.0$, $\Theta = 0.75$, $s = 1.5$, $r = 0.5$, $M = 6$, $N = 0$).

$\bar{\rho}$

(a)

$\tilde{Y}_p$

(b)

$\bar{\rho}\tilde{Y}_p$

(c)
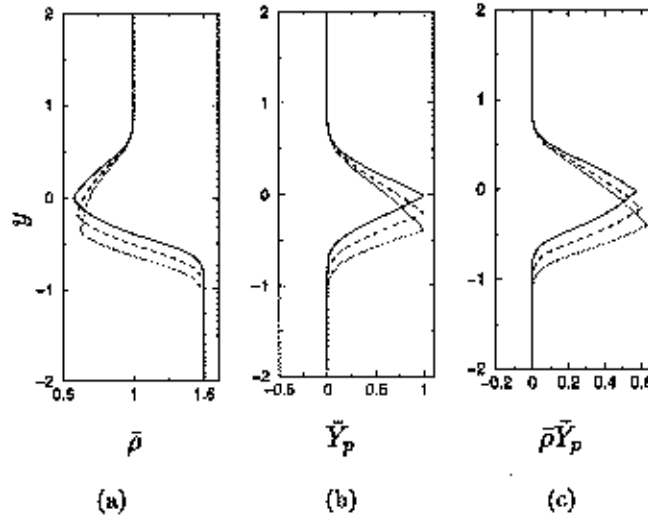
Figure 4.13: Effect of equivalence ratio on initial conditions profiles for (a) mean density, (b) mean product mass fraction, and (c) the product of profiles (a) and (b) ($M_c = 1.0$, $\Theta = 0.75$, $s = 1.5$, $r = 0.5$).
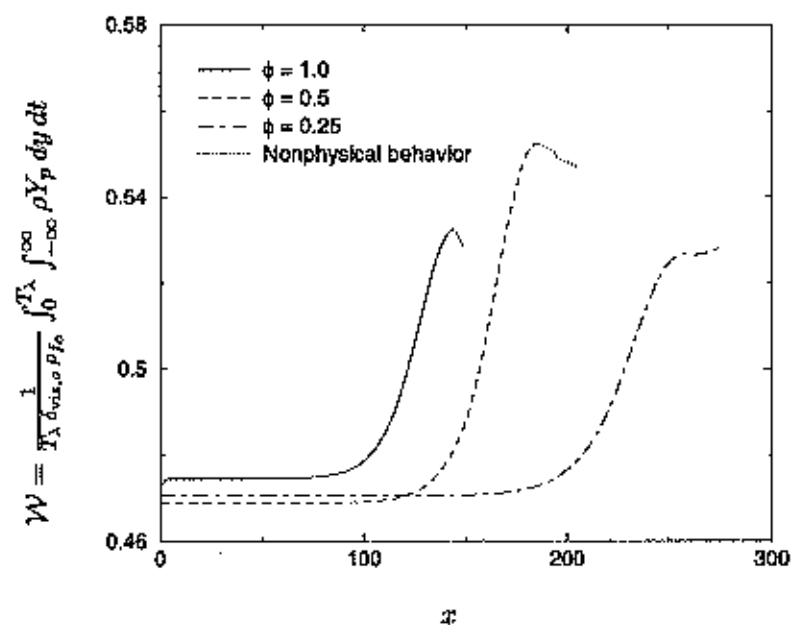
(a)
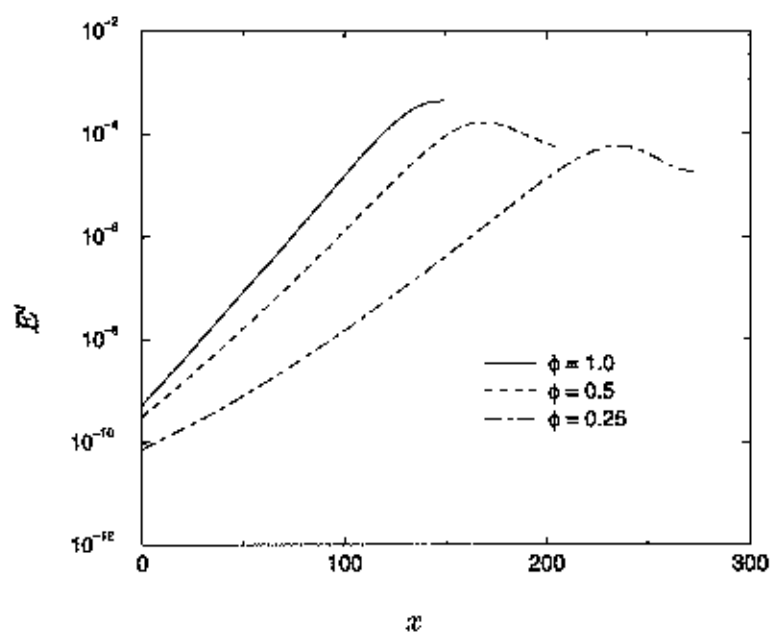
(b)

Figure 4.14: Effect of equivalence ratio on the slow mode (a) integrated product and (b) fundamental mode energy profiles (M_c=1.0, Θ=0.75, s=1.5, r=0.5). Nonphysical behavior is noted in (a) when the total product decreases despite the irreversibility of the reaction -- this is a limitation of the PSE implementation.
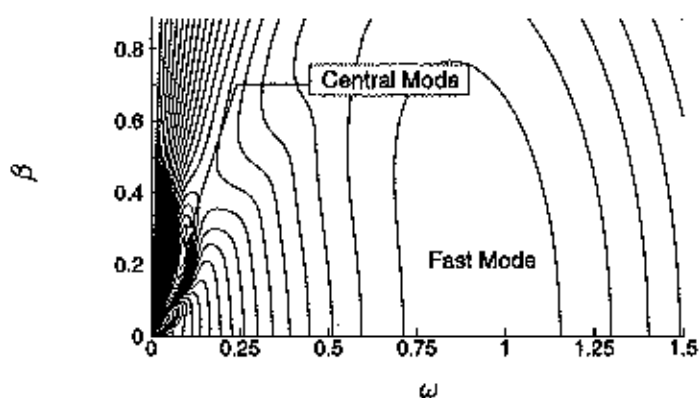
(a) Central/Fast Modes
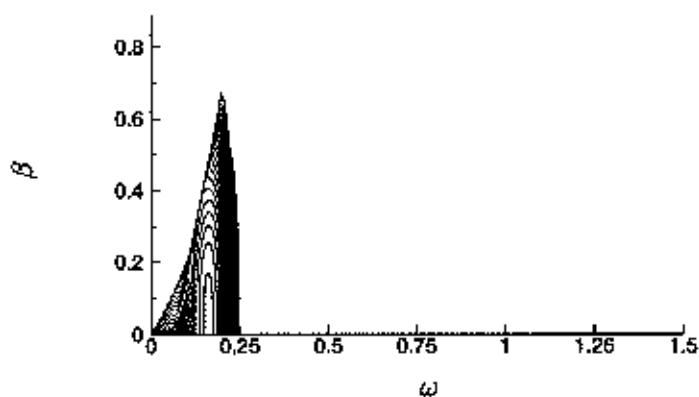
(b) Slow Mode
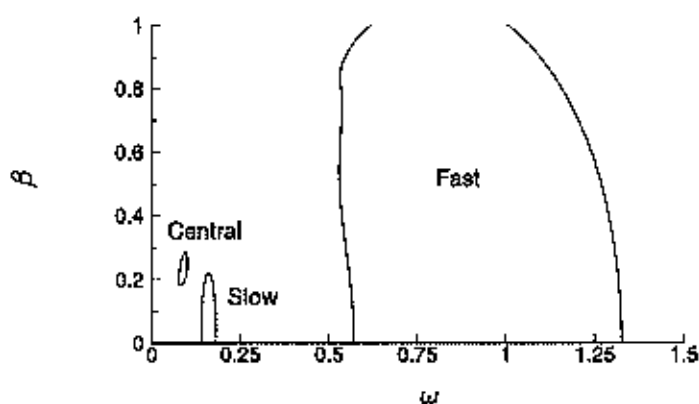
(c) Modal Peak Contour Distribution

Figure 4.15: Contour plots of the LST growth rate in (ω, β) coordinates for (a) central and fast modes and (b) slow mode at the triple point ($M_c = 1$, $\Theta = 0.9$, $s = 0.94$, $\phi = 1$). Contour min at 0, max at 0.08, and $\Delta\alpha_i = 0.004$. The location of the 0.075 contour for all three modes is show in (c).
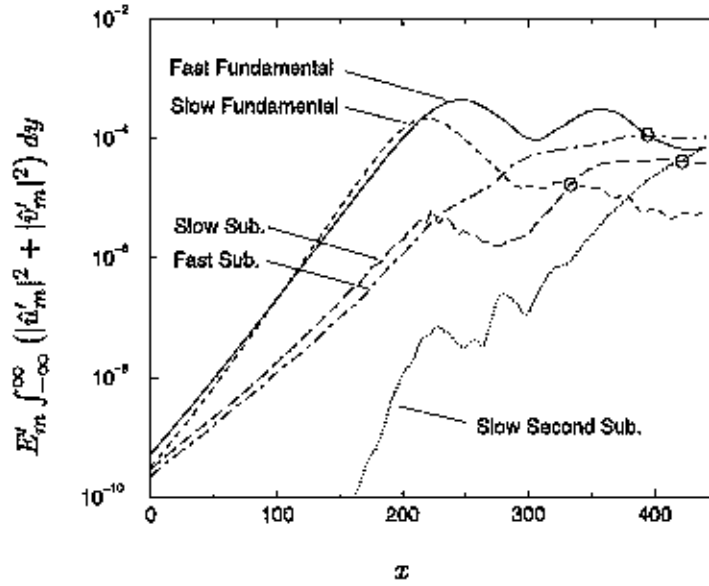
Figure 4.16: Energy evolution in a fast/slow mode colayer case with subharmonics of both the fast and slow modes initialized with $\phi_s = \pi/2$. (M_c=1, Θ=1, ϕ=1, s=0.94, r=0.5, M=24, N=0. The $\circ$ symbols denote a change in dominance from a higher to lower harmonic.)

(a)

(b)

(c)
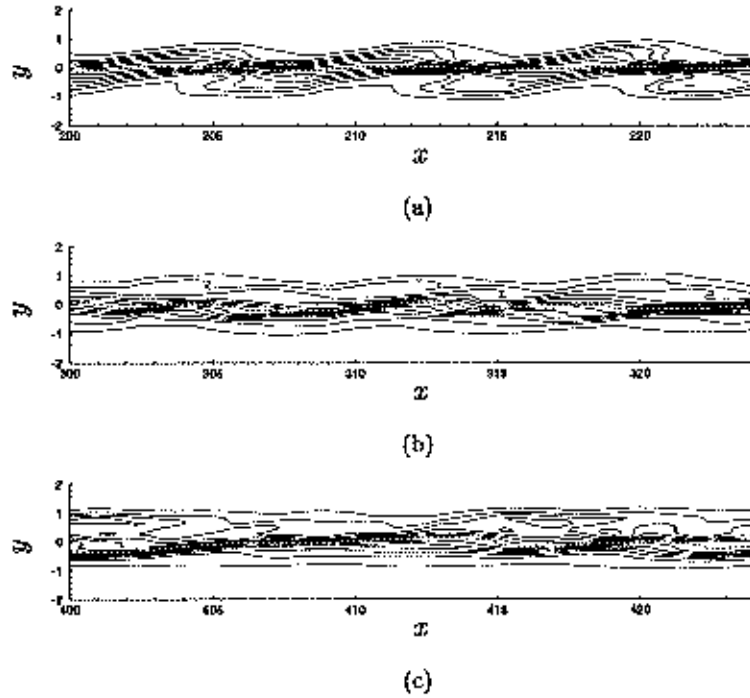
Figure 4.17: Evolution of the mixture fraction field for the fast/slow colayer of figure 4.16. Two visualizations are shown at x locations where (a) the fundamental modes dominate ($x = 200$) and where a mode transition is taking place at (b) x=300 and (c) x=400. Mixture fraction contours with $\Delta\xi = 0.08$, $\xi_{max} = 0.98$, and $\xi_{min} = 0.02$ and the flame sheet at ξ=0.5 marked as a dotted line.
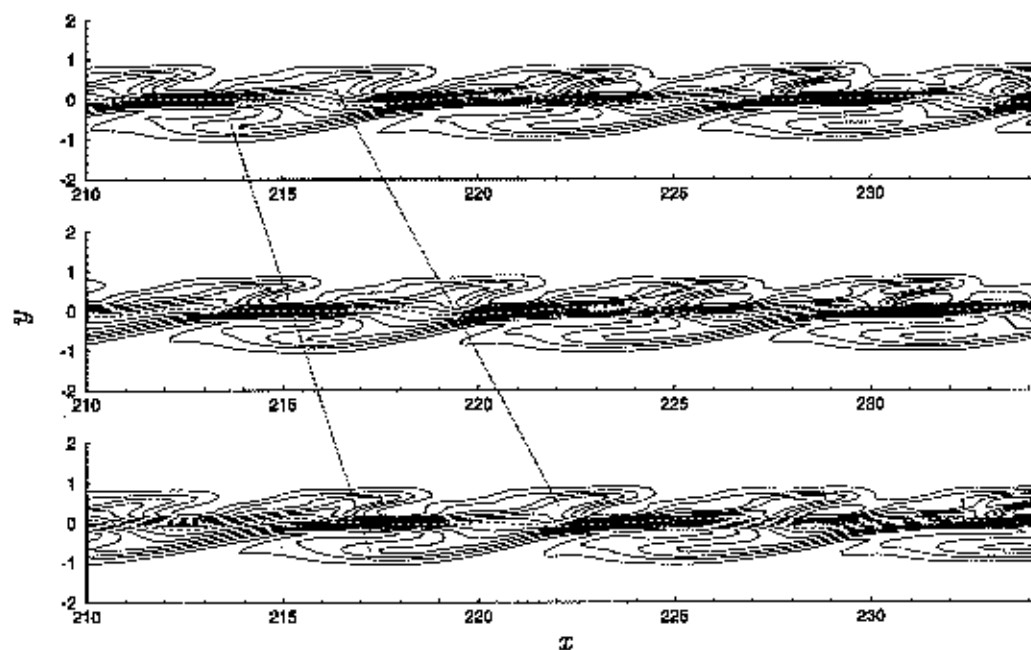
Figure 4.18: Mixture fraction field for a fast/slow colayer in compressible reacting conditions visualized at $t = 0$, $t = \pi$, and $t = 2\pi$ ($M_c=1$, $\Theta=1$, $\phi=1$, $s=0.94$, $r=0.5$, $M=4$, $N=4$). Mixture fraction contours with $\Delta\xi = 0.08$, $\xi_{max} = 0.98$, and $\xi_{min} = 0.02$ and the flame sheet at $\xi=0.5$ marked as a dotted line. Lines joining plots indicate the streamwise movement of a fast and slow structure.
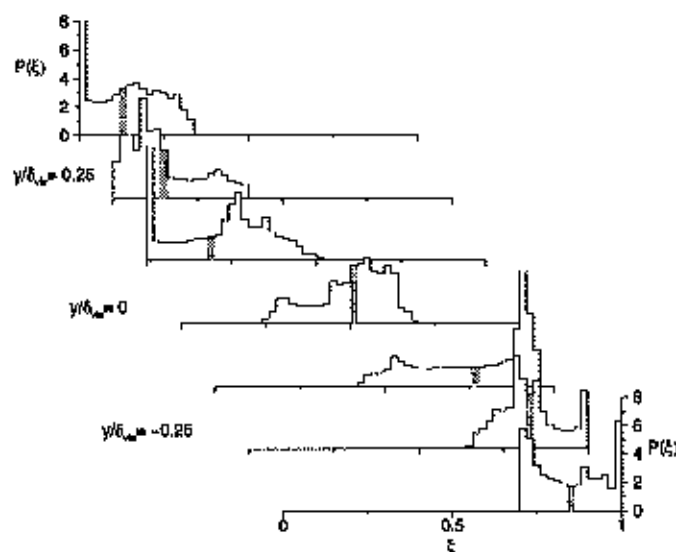
Figure 4.19: Mixture fraction PDF at $x=230$ for the fast/slow colayer of figure 4.18. Seven symmetric y positions are represented with $\Delta y = 0.125\ \delta_{vis}$. The probability axis has been truncated for visualization purposes and the bin corresponding to $\tilde{\xi}$ has been shaded in.
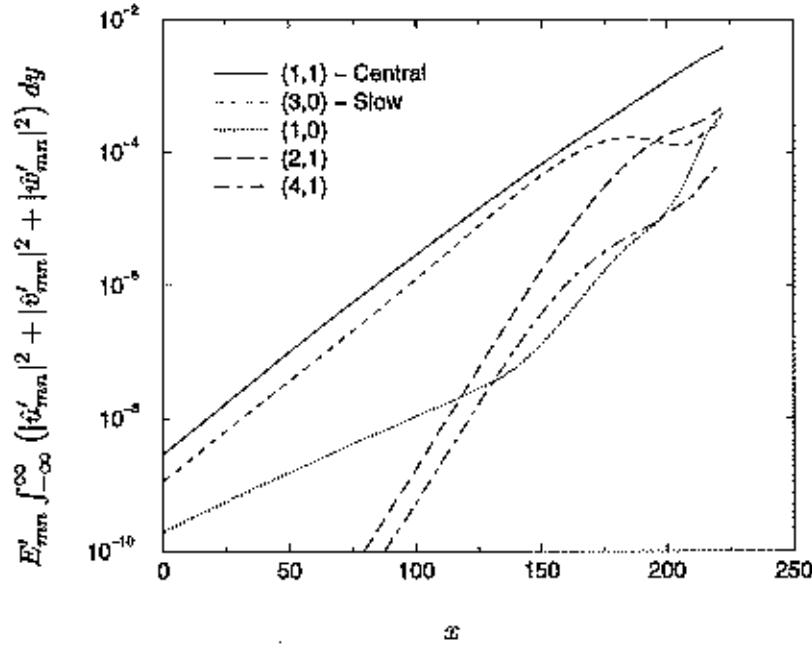
Figure 4.20: Energy evolution in a central/slow mode colayer case with initial condition forcing of the central (1,1) and slow (3,0) modes (M_c=1, Θ=0.45, ϕ=1, s=1.5, r=0.5, M=9, N=3).

(a)

(b)
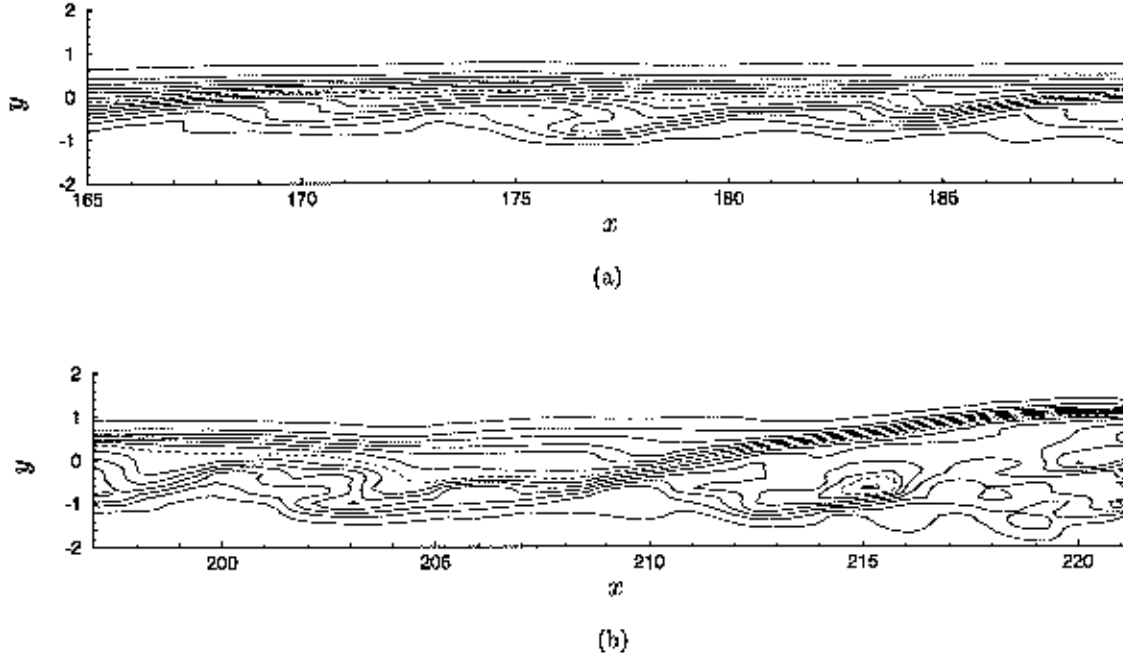
Figure 4.21: Mixture fraction field for a central/slow mode colayer in (a) early (slow mode dominant) and (b) late (central mode dominant) downstream positions (M_c=1, Θ=0.45, ϕ=1, s=1.5, r=0.5, M=9, N=3). Mixture fraction contours with $\Delta\xi = 0.08$, $\xi_{max} = 0.98$, and $\xi_{min} = 0.02$ and the flame sheet at ξ=0.5 marked as a dotted line.
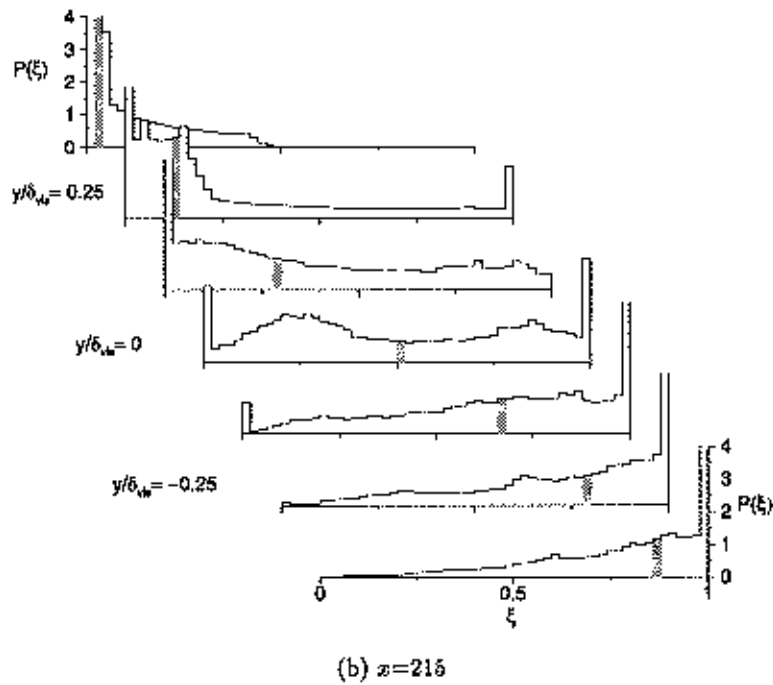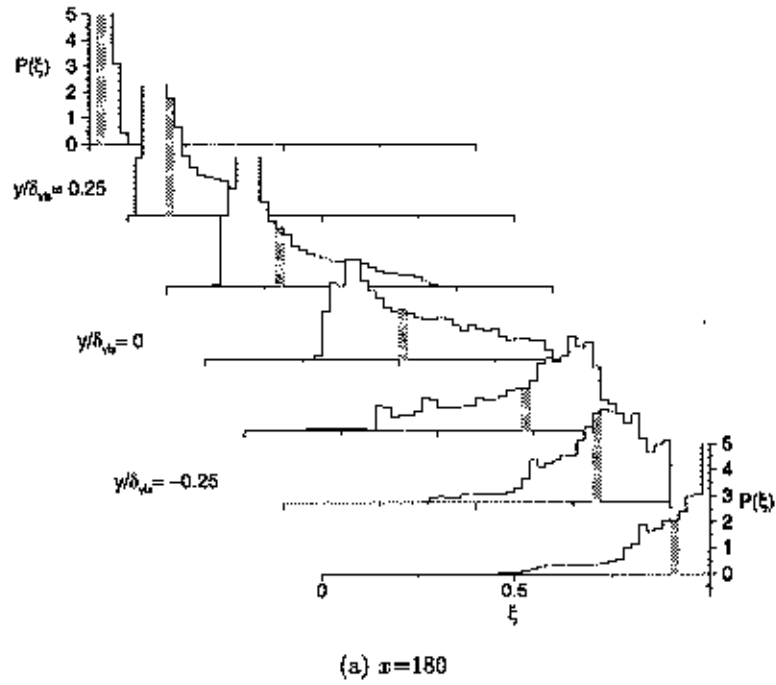
(a) x=180

(b) x=215

Figure 4.22: Mixture fraction PDF of a central/slow mode colayer at (a) $x = 180$ (slow mode dominant position) and (b) $x = 215$ (central mode dominant position) for the flow conditions of figure 4.21. Seven symmetric y positions are represented with $\Delta y = 0.125\ \delta_{vls}$. The probability axis has been truncated for visualization purposes.
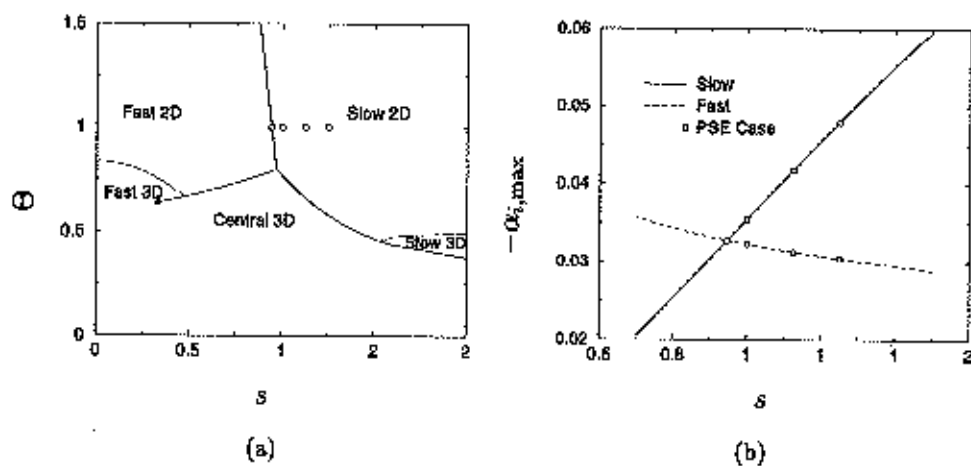
Figure 4.23: Location of colayer width test cases on (a) the (s,Θ) regime chart and (b) LST growth rate plot with density.

(a) $s=0.94$
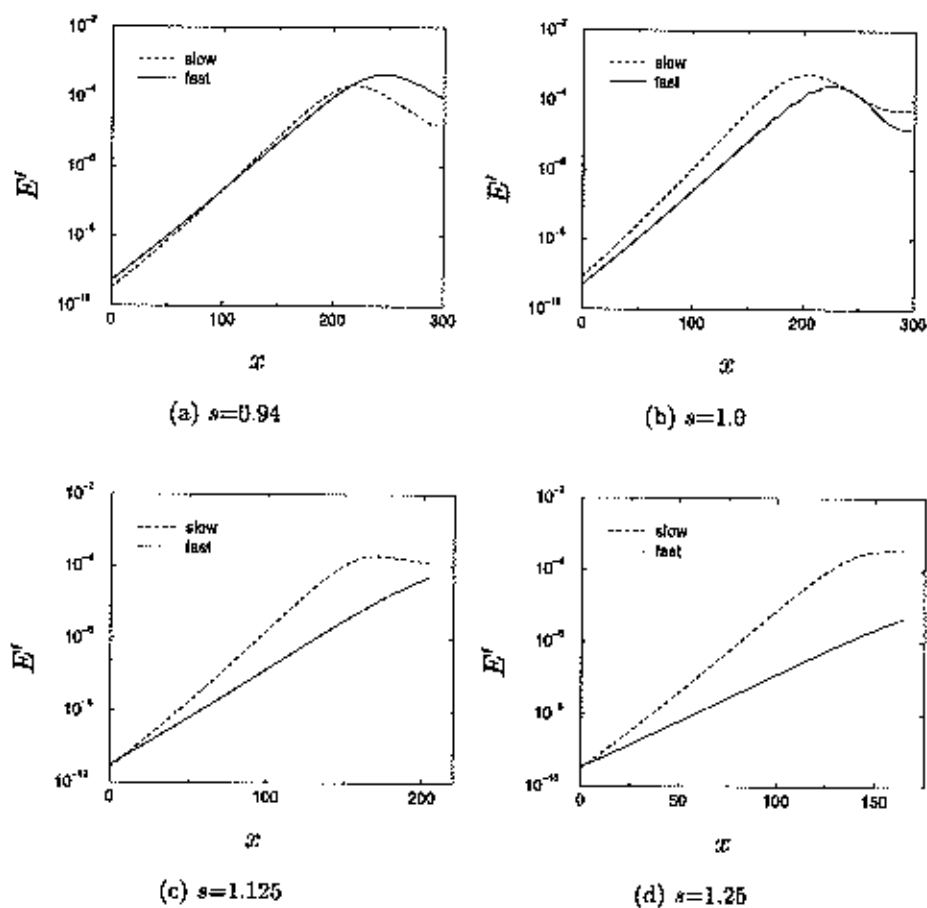
(b) $s=1.0$

(c) $s=1.125$

(d) $s=1.25$

Figure 4.24: Evolution of fast and slow mode energy growth with increasing slow side density bias starting from a colayer case: (a) $s=0.94$ (colayer), (b) $s=1.0$, (c) $s=1.125$, and (d) $s=1.25$ ($M_c=1$, $\Theta=1$, $r=0.5$, $\phi=1.0$, $M=8$).

(a) s=0.94
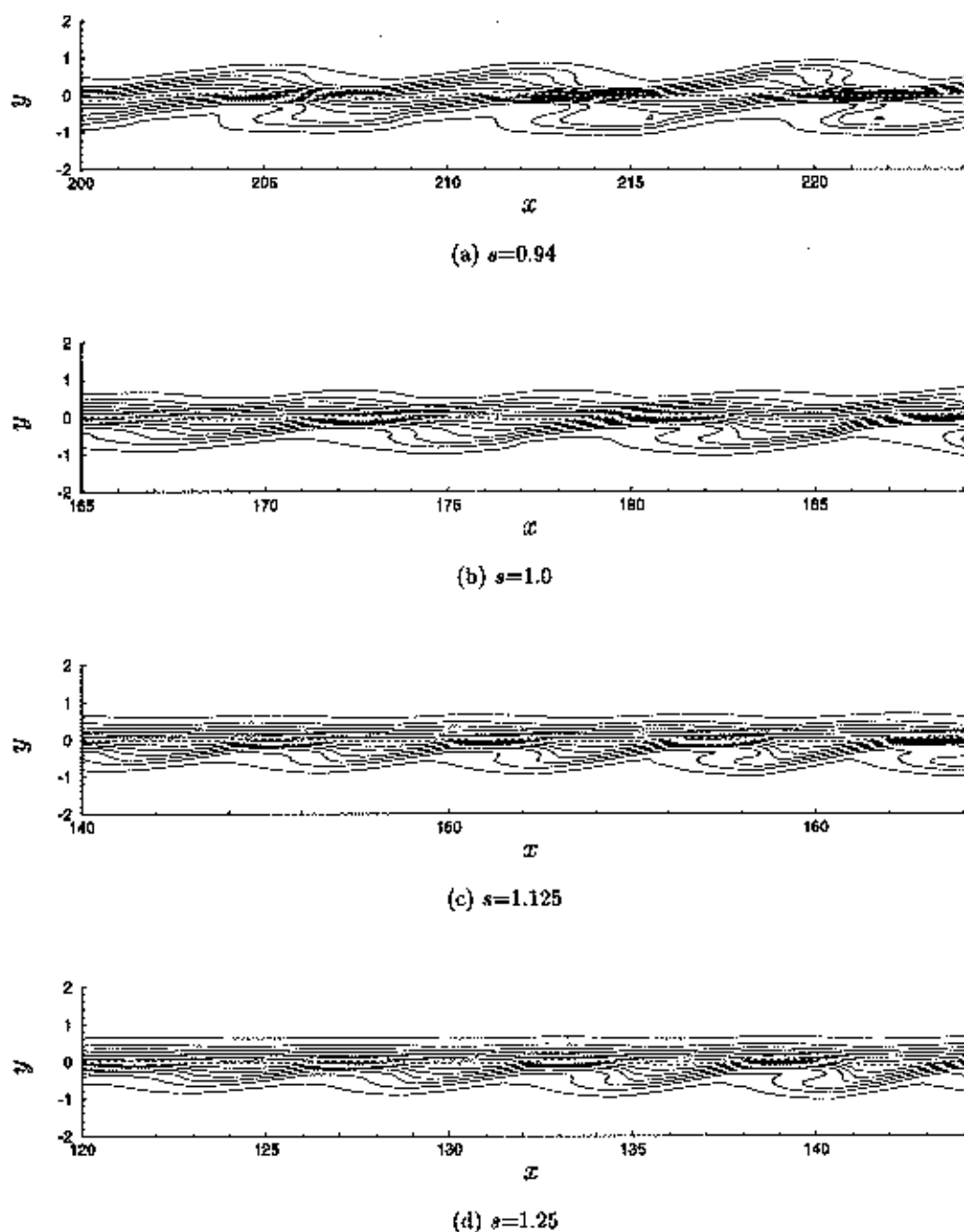
(b) s=1.0

(c) s=1.125

(d) s=1.25

Figure 4.25: Evolution of the mixture fraction field for a colayer case with increasing slow side density bias: (a) s=0.94 (colayer), (b) s=1.0, (c) s=1.125, and (d) s=1.25 (M_c=1, Θ=1, r=0.5, ϕ=1.0, M=8). Mixture fraction contours with $\Delta\xi = 0.08$, $\xi_{max} = 0.98$, and $\xi_{min} = 0.02$ and the flame sheet at ξ=0.5 marked as a dotted line.

(a)

(b)
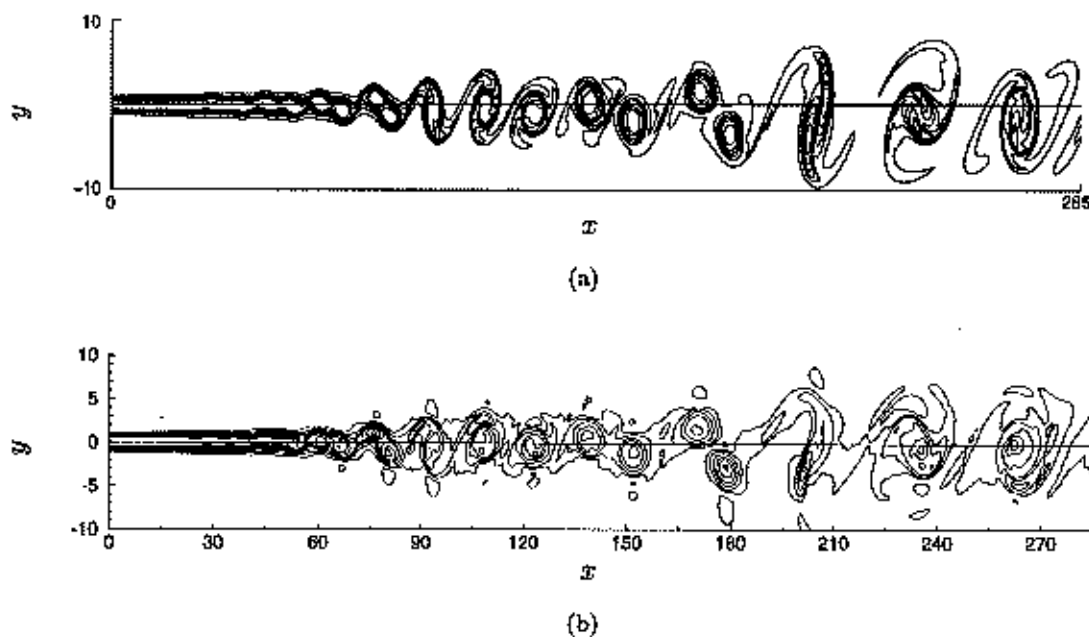
Figure 4.26: Comparison of spanwise vorticity contours for (a) DNS results of Colonius *et al.* (1997), and (b) PSE simulation with $M = 16$ for a low compressibility pairing case (M_c=0.125, r=0.5, s=1, Θ=0). The contour levels are set with $\Delta\omega_z = 0.04$, $\omega_{z_{min}} = -0.26$, and $\omega_{z_{max}} = 0.02$. The normal axis is expanded by a factor of 2.5; both images are plotted to the same scale.
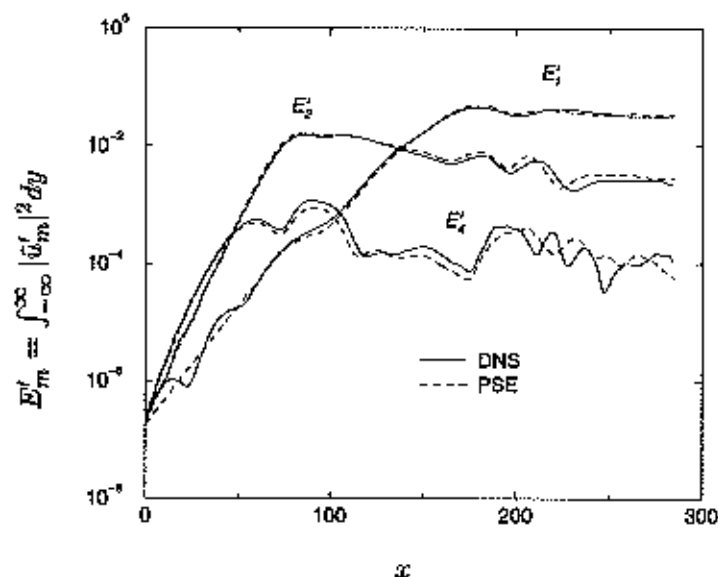
Figure 4.27: Comparison of $\hat{u}$ energy between the DNS of Colonius *et al.* (1997) and PSE simulation results for the fundamental ($m = 4$), first subharmonic ($m = 2$), and second subharmonic ($m = 1$) modes (M_c=0.125, r=0.5, s=1, Θ=0).
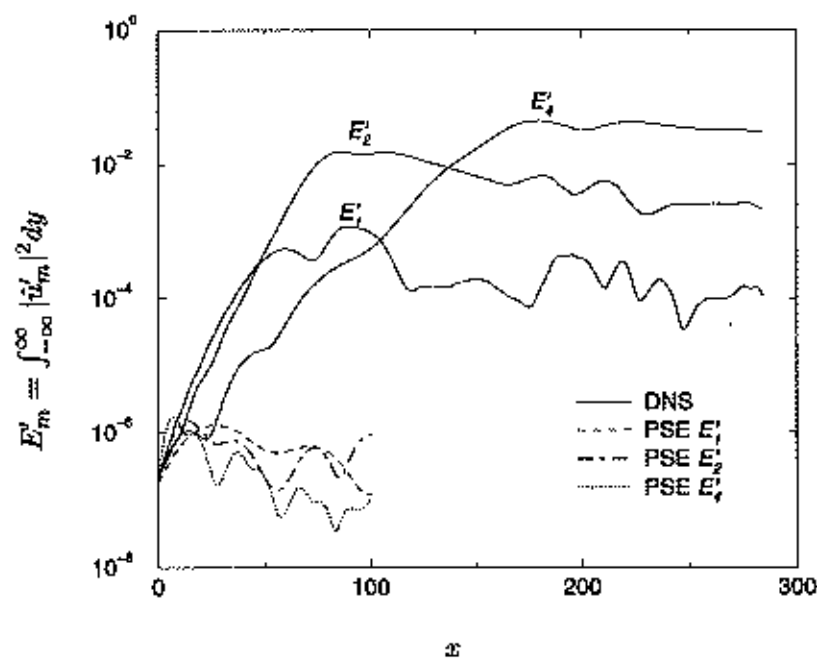
Figure 4.28: Effect of removing the rapidly-varying portion of the streamwise pressure derivative on $\hat{u}$ energy.
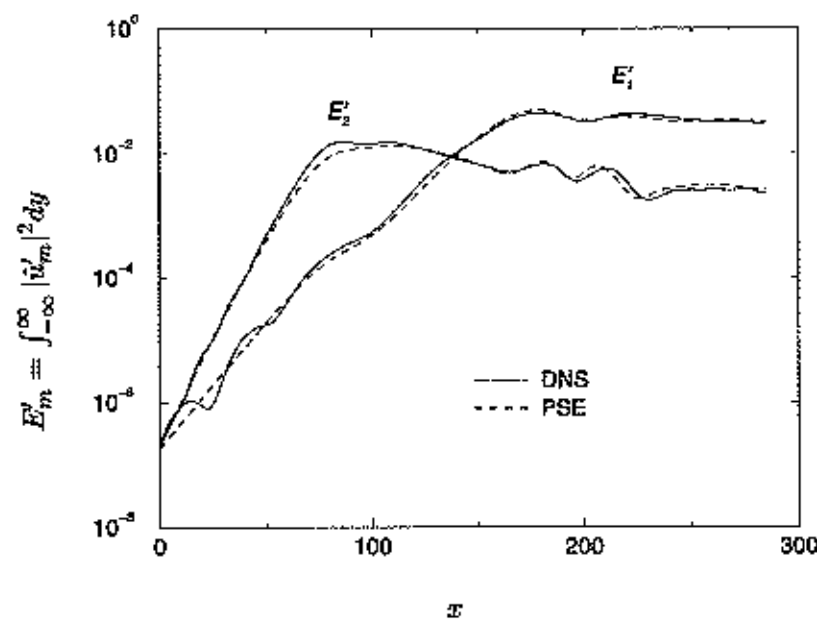
Figure 4.29: Comparison of $\hat{u}$ energy to the DNS solution for the low M_c pairing case with only the two subharmonics initialized in the simulation.
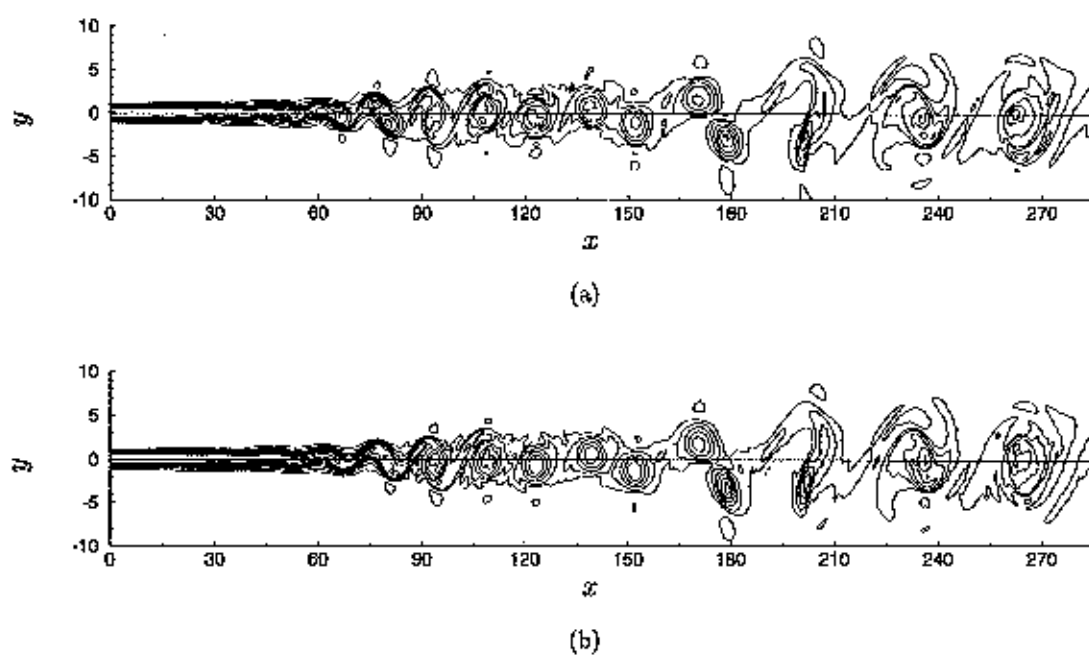
Figure 4.30: Comparison of spanwise vorticity contours for (a) the completely-specified PSE, and (b) PSE simulation initialized without the fundamental mode for the low M_c pairing case. Refer to figure 4.26 caption for case details.
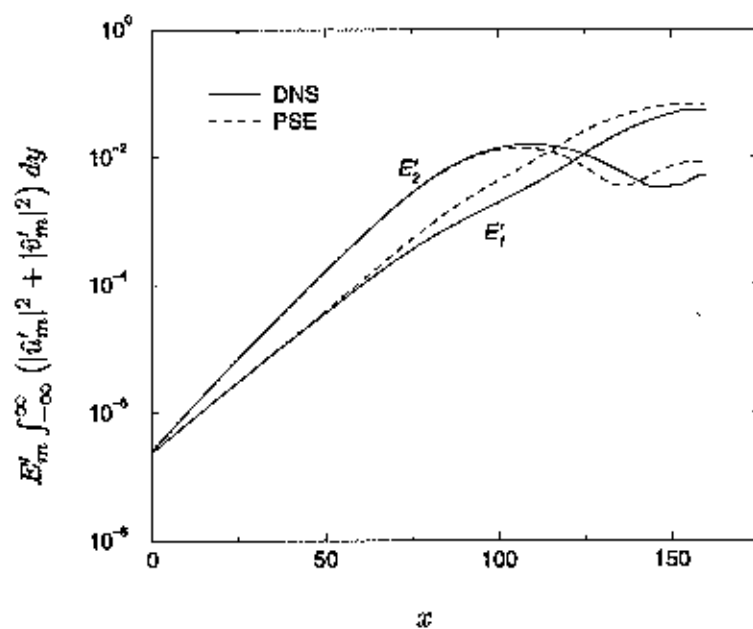
(a)
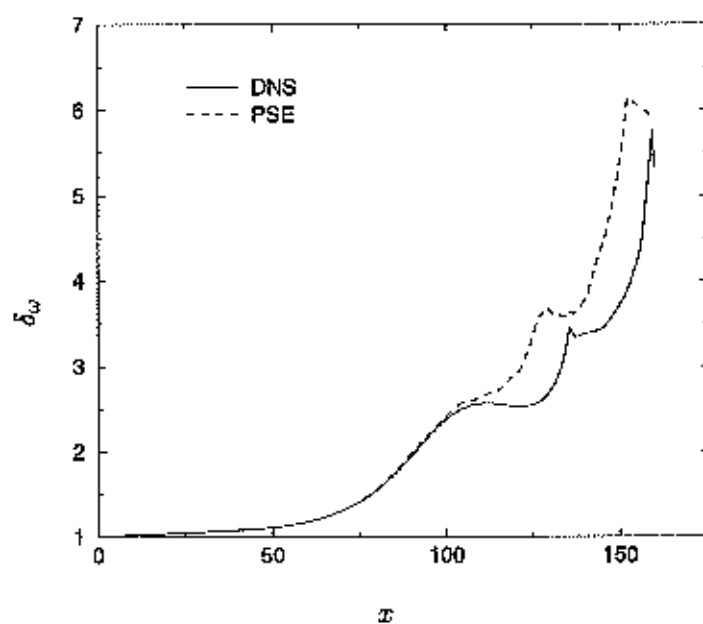
(b)

Figure 4.31: Comparison of DNS and PSE results for a high compressibility pairing case shown for (a) modal energy and (b) vorticity thickness ($M_c = 0.5$, $r = 0.6$, $s = 1$, $M=16$).

(a)

(b)
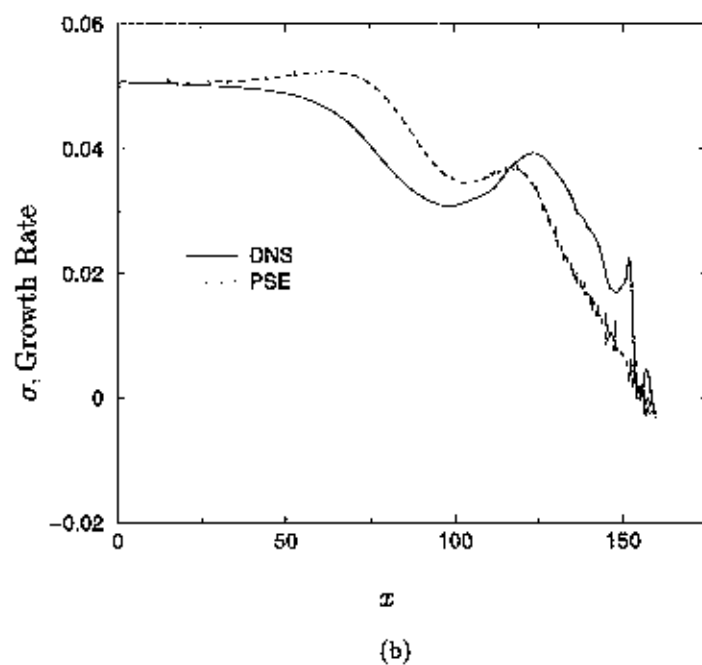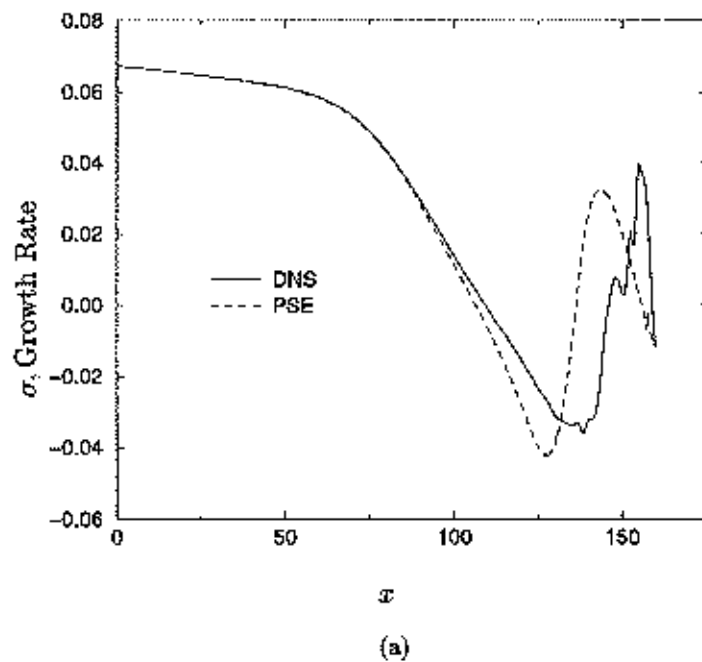
Figure 4.32: Comparison of DNS and PSE results for the modal growth rates in a high compressibility pairing case shown for the (a) fundamental and (b) subharmonic frequencies ($M_c = 0.5$, $r = 0.6$, $s = 1$, $M=16$).
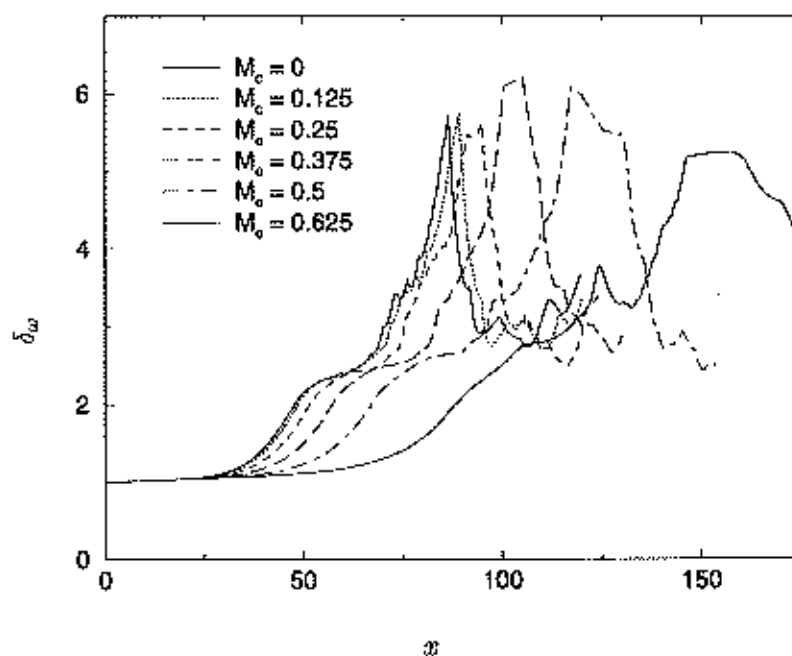
Figure 4.33: Effect of compressibility on the onset of pairing as visualized in the development of the vorticity thickness profile for 2D PSE simulations (r=0.5, s=1, $\Theta = 0$, $Re = 5000$, M=8).
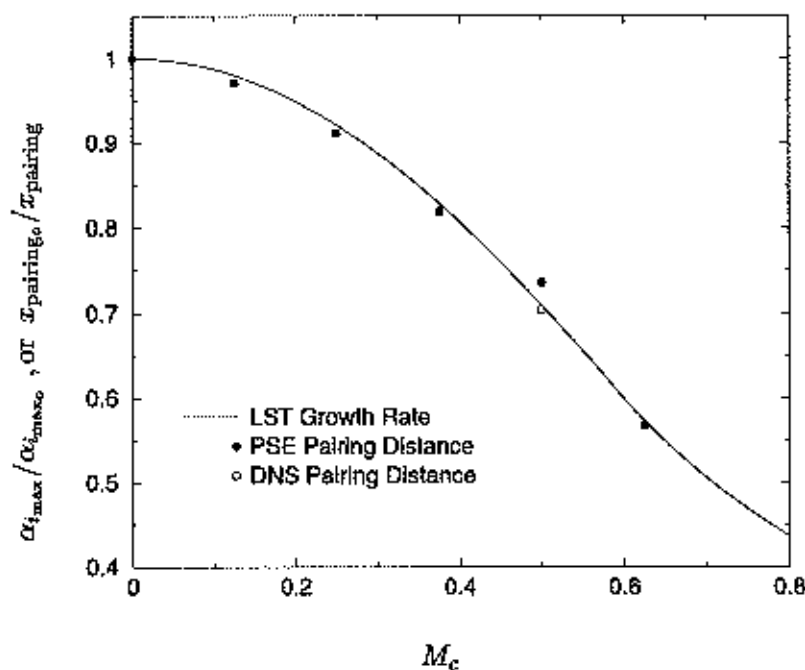
Figure 4.34: Comparison of the compressibility effect on the extension of pairing length and the suppression of the LST growth rate, both of which are normalized on the incompressible result (r=0.5, s=1, $\Theta = 0$, $Re = 5000$, M=8).

Chapter 5

Conclusions and Recommendations

This dissertation has presented a study on the development of flow structure in compressible reacting mixing layers throughout a five-dimensional parameter space specified by compressibility, heat release, and the flow-stream ratios of density, equivalence, and velocity. The density-weighted mean vorticity profile was used to develop a basic understanding for the flow structure and to predict the influence of each parameter. Linear stability methods were then employed to conduct a complete parametric study, and these results guided the development of flow-structure regime charts. Finally, a nonlinear stability method—based on the parabolized stability equations—was applied to further detail the flow physics of each structure and to lend insight into fluid mixing. The principle conclusions from this investigation are listed below and a discussion of topics for future research is presented in section 5.2.

5.1 Conclusions

5.1.1 Diagnostic Development

The parabolized stability equations were applied to the study of both reacting flows and mixing layers for the first time. A comprehensive and very favorable comparison of the technique to DNS results was provided for sub- and super-sonic conditions, thereby validating the technique—and this implementation in particular—for the study of free-shear-layer flows. The ability of the PSE to accurately model vortex pairing was also demonstrated by detailed comparison between PSE and DNS results. In subsonic conditions, the PSE simulations revealed the critical importance of the rapid portion of the streamwise pressure derivative to the correctly capture vortex pairing. In contrast, the slowly-varying contribution was found to be insignificant and was ignored in our computations.

This investigation has demonstrated the ability of the PSE to be useful in *qualitative* mixing studies with fast chemistry. The limitations of this implementation were discussed, most notably the lack of molecular mixing in simulations that are constricted to modeling

only large-scale motions. Further thoughts on the simulation of reacting flows with the PSE are offered in section 5.2.3 in connection to future work recommendations.

Additional technical contributions of this investigation include the development of an implicit boundary condition for the simulation of supersonic flows with radiative instabilities, a critical element to this work in the study of outer modes. This boundary condition has application to PSE simulations of acoustic instabilities in boundary layers.

5.1.2 Parametric Study

The use of the density-weighted vorticity profiles to explain and predict the effect of each parameter on flow structure was demonstrated. Eigenfunction visualizations, provided by considering both energy profile and streakline results, were used to illustrate the general characteristics of the three instability modes and the nature of the vortical structure that will appear in the mixing layer. Energy profiles also served to explain how a transition in the flow from a broad central mode to a compact and off-center outer mode structure would negatively impact mixing.

Detailed parametric studies highlighted the similar role that compressibility and heat release play in the emergence and eventual dominance of the outer modes. In conditions of sufficiently high Θ and M_c to generate multiple modes, the density ratio was shown to be an important parameter in determining the *relative* amplification rates of the different instabilities. The parametric study also demonstrated that the equivalence and velocity ratio values were, in comparison, less important factors in determining the dominant flow structure. One important exception to this is the equivalence-ratio effect on the outer modes in regimes that combine low compressibility with high heat release.

Insights from the parametric study were used to create regime charts which demonstrate the coupled effect of M_c, Θ, and s on selecting the dominant instability mode. This allowed a complete appreciation to be developed for the structure of the compressible reacting mixing layer. These regime charts provide a clear view of the central to outer mode transition caused by both heat release and compressibility, and showed how the density bias selects the dominant outer mode.

The ability of the scaling factor $\lambda = (U_1 - U_2)/(U_1 + U_2)$ to collapse linear-stability growth rates in compressible reacting conditions was investigated. This factor was shown to perform well for the central mode throughout the majority of its uniform-density regime space. Two new scaling parameters—tailored specifically to the outer modes in reacting

conditions—were shown to provide accurate scaling of these modes when heat release was significant; the conventional λ definition worked acceptably well in most low-heat-release regimes. Finally, the utility of all parameters was shown to be limited to the case of near-uniform density.

5.1.3 Single Mode Flow Structure

Central Mode

Studies of the central mode flow structure demonstrated that vortex pairing occurs with very little interaction between the fundamental mode and its subharmonics. With rising compressibility, the delay in vortex pairing was shown to precisely correlate with the attenuation of instability growth rates, confirming that neither changes in shape nor the rate of rotation of the vortices were the responsible mechanism. Further, the accurate prediction of pairing—a mechanism that is responsible for the nonlinear growth of mixing layers—from linear growth rates offers insight into why linear stability theory is such an effective analysis technique.

The effect of heat release on the central mode in compressible conditions was evaluated. Beyond the growth rate reduction observed in the parametric study, nonlinear stability results demonstrated the effect of heat release to broaden the spanwise and streamwise scale of the flow structure. A comparison of the mixture fraction PDFs between these two cases at equal points of *energy* development indicated better stirring of the reactants in the presence of heat release although, more importantly, the cold case provided better mixing. This observation was attributed to the larger length scales of energetic motion in the reacting case. However, it was noted that a comparison at points of equal *streamwise* position would heavily favor the nonreacting cause in both mixing and stirring because of its significantly higher growth rate.

Outer Modes

Mixture fraction PDFs generated by outer mode flow structure demonstrated a marching set of profiles in the cross-stream direction. Their shape was relatively compact on the side associated with the mode, while the PDF approached the delta-function behavior of laminar flow on the opposite side. This is a clear indication that the impact of the outer modes on mixing is entirely localized to one side, and is separated from the other by the flame sheet.

The location of the flame sheet outside the region of prominent mixing motivated interest in adjusting the equivalence ratio to position the flame sheet closer to the vortical structure. It was found, however, that this movement also displaces the outer mode in the same direction, providing only marginal benefit to product formation. Further, moving the flame sheet was shown to reduce the instability growth rate, which scales on the shear between the flame sheet and the free stream; the net result was a decrease in mixing performance.

5.1.4 Colayer Structure

Two new types of colayer structure were identified that correspond to equivalent growth rates between the central and both the fast and slow modes. An investigation of the central/slow colayer in the nonlinear regime revealed that outer modes saturate at a far lower energy level than the central mode. This results in the early development of observable flow structure on the slow side of the layer, only to be later overwhelmed by the development of the central mode. Mixture fraction PDFs indicated similar evolution, with the shape of the distributions being dictated by the central mode with some additional mixing on the slow side. These observations suggest that colayers between the central and outer modes will be difficult to discern from regular central mode flows in experimental conditions.

The nonlinear development of the fast/slow colayer was also studied. Subharmonics of the outer modes were found to overtake the fundamental without pairing. This process occurred without any interaction between the different sides of the layer. Mixture fraction PDFs indicated a similar lack of communication across the flame sheet. They appeared to have been formed by the superposition of two PDFs from flows where the outer modes individually appeared. While this colayer flow presents a significant enhancement of mixing relative to a single-outer-mode configuration, it does not approach the degree of mixing provided by the central mode. Further, nonlinear stability studies indicated that the width of fast/slow colayer conditions on the regime charts was, in practice, quite limited: a 25% change in density ratio relative to a colayer case resulted in complete dominance of flow structure on the density-biased side.

5.2 Recommendations for Future Work

5.2.1 Compressible Reacting Mixing Layers

The linear stability studies of this investigation, in addition to the experiments conducted by Frieler (1992), indicate a strong interaction between the density and velocity ratio that remains to be fully understood. The effect of different types of mean flow, corresponding to boundary conditions of equal molecular weight or, alternatively, equal temperature, should also be investigated in connection with the density ratio effect.

With a full knowledge of the parameter space now developed, selective DNS investigations would be helpful to establish quantitative comparisons of the mixing efficiency between different flow structures. The question of which outer mode—fast or slow—offers better mixing remains partially unanswered. The presence of mixing isolated to one side of the layer also prompts questions concerning the 'effective stoichiometry' of chemical reactions: if one reactant is preferentially transported into the reaction zone this may have an interesting effect on combustion, similar to what is seen when the equivalence ratio is changed. However, it should be noted that the accurate simulation of these problems would require sufficient resolution to capture molecular-mixing effects (Freund, 1997).

Finally, the relatively poor mixing performance of the outer modes also motivates interest in using specific enhancement mechanisms, such as forcing the development of streamwise vortices. Significant mixing enhancement work has been done in compressible flows dominated by the central mode (*e.g.* see Island 1997; Gutmark *et al.* 1995). It is not clear if these techniques will work on outer mode flow structure.

5.2.2 Colayers

A productive area of continuing work for both computations and experiments concerns the creation of colayers in incompressible conditions. This colayer regime holds specific interest because it is the least difficult to replicate in laboratory experiments. Indeed, the visualizations of Chen *et al.* (1988) of a buoyant CH_4 diffusion flame shown in figure 5.1 indicate a similar type of colayer structure that we have discussed. The underlying physics of this case are identical to the mixing layer: velocity shear exits in the presence of a density deficit caused by chemical heat release. This, in turn, produces a bi-modal density-weighted vorticity profile that generates the fast and slow vortical modes that are clearly seen the visualization.

A mixing layer simulation of the same flow was attempted for comparison. Figures 5.2(a) and (b) plot the mean density and velocity profiles for the same conditions as in the experiment. A comparison of these figures shows that the extreme equivalence ratio of $\phi = 0.048$ in this diffusion flame results in a flame sheet position at $y \approx -1$, where the mean streamwise velocity is nearly at the slow stream boundary condition. As a result, there is little difference in shear between the flame position and the slow stream, causing the slow mode to become only slightly unstable while the fast mode dominates the flow structure. This unequal relationship is clearly seen in the normalized eigenfunction energy profiles in figure 5.2(c) (see equation 3.1 for a definition of Ψ).

The large growth rate difference between fast and slow modes does not match the experiment because the calculation of the input velocity profile in figure 5.2(b) lacks the correct physics. A profile that accounted for the effects of buoyancy and entrainment would extend $\bar{u}$ and $\bar{T}$ gradients far into the slow stream. That notwithstanding, qualitative comparison to the experiment can be made by selecting a moderately-lean equivalence ratio, $\phi = 0.3$. The mixture fraction contours for this PSE simulation are shown in figure 5.2(d). Similarities to the experiment include the early development of fast-side vortical structure, the larger wavelength of the slow mode, and the partial wrapping of the flame sheet into the slow mode. The latter flame sheet effect has been identified as the source of flame flicker (Chen *et al.* 1988).

While this initial evidence of the existence of colayers is encouraging, an experiment with PIV and some type of temperature measurement would provide the required data for proper comparison. The current PSE code could be extended to this type of axi-symmetric flow by incorporating buoyancy and a confining boundary condition on the fast side to simulate the jet centerline symmetry.

5.2.3 Relevant Extensions to the PSE

Further investigation into the modeling of the mean-flow correction in the PSE could improve both the accuracy and the duration of the simulation. A better understanding of how energy dissipates from the mean-flow correction is a suggested starting point for this analysis. There is also a general need to remove the ambiguity in the streamwise evolution norm by introducing a universally applicable and rigorously developed closure to the parabolized stability equations. Some initial thoughts on a procedure for doing this are developed in Appendix B.

The coupling of the PSE to an acoustic analogy such as Lilley's equation for sound field calculations is a notable area for future research. Understandably, this would be restricted to analyzing the sound generated by large-scale structures. A direct comparison to DNS results should be done to determine how well the PSE approximation works within the inherent sensitivity of acoustic calculations.

The PSE have significant potential for realizing a cost-effective design tool for combustion problems. Future work done with the parabolized equations in reacting flows requires improvements in modeling chemical reaction. A first step would be to develop an approach that allows both chemical and viscous heating effects to coexist in a stable PSE calculation. Fast chemistry does not allow this, strictly speaking, because the temperature field is completely specified by the mixture fraction field. Reformulating the problem with a total enthalpy equation might prove useful.

Finite-rate chemistry would be the second and more complex step. This implementation would be limited to some type of equilibrium approach because of the time-periodic nature of the Fourier-space calculation. A second complication of this extension is a careful consideration of the mass fraction constraints. Specifically, they are

$$\sum_k Y_k = 1 \quad \text{or} \quad \begin{cases} \sum_k \hat{Y}_k = 1 \\ \sum_k Y_k' = 0 \end{cases} \tag{5.1a}$$

for the system, and

$$0 \leq Y_k \leq 1 \tag{5.1b}$$

for individual species. The constraint (5.1b) poses the most serious problem for a stability method because it can only be evaluated in real space as the sum of the mean and fluctuating components at a given position. This requirement is entirely at odds with the PSE technique, which solves the mean and perturbation fields separately and, further, evolves the perturbation field in Fourier space. A precursor to the application of finite-rate chemistry methods to the PSE requires a rigorous method to apply these constraints in Fourier space.
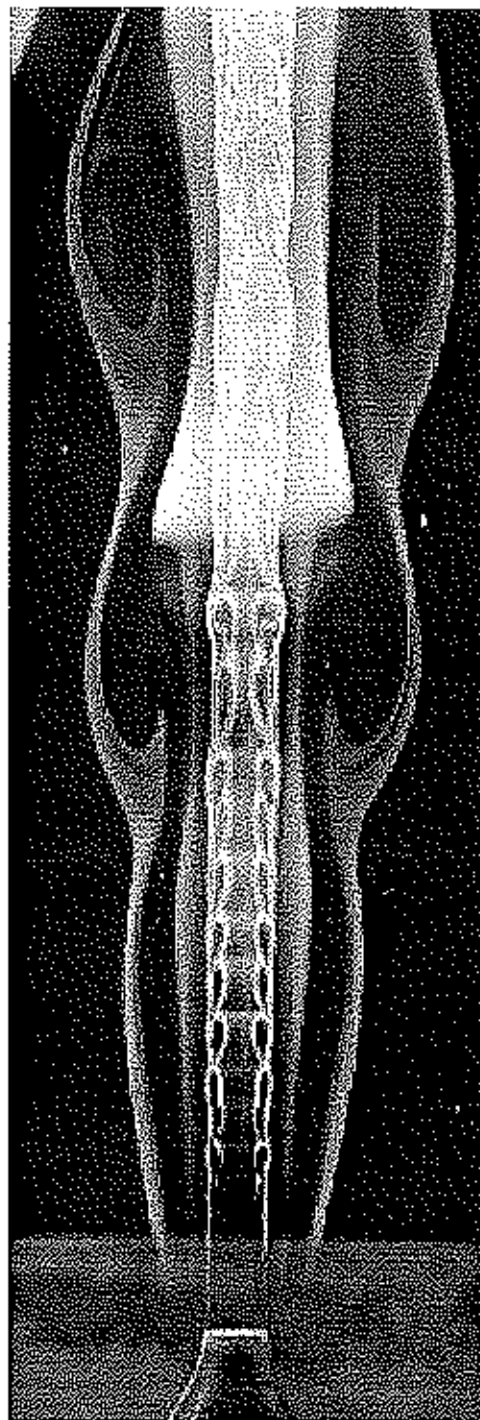
Figure 5.1: Evidence of colayer structure in a buoyant CH_4 jet diffusion flame from Chen *et al.* (1988) (R_e=1890, r=0.05, M_c=0., ϕ=0.048). Visualization done with a laser sheet and TiO_2 seeding.
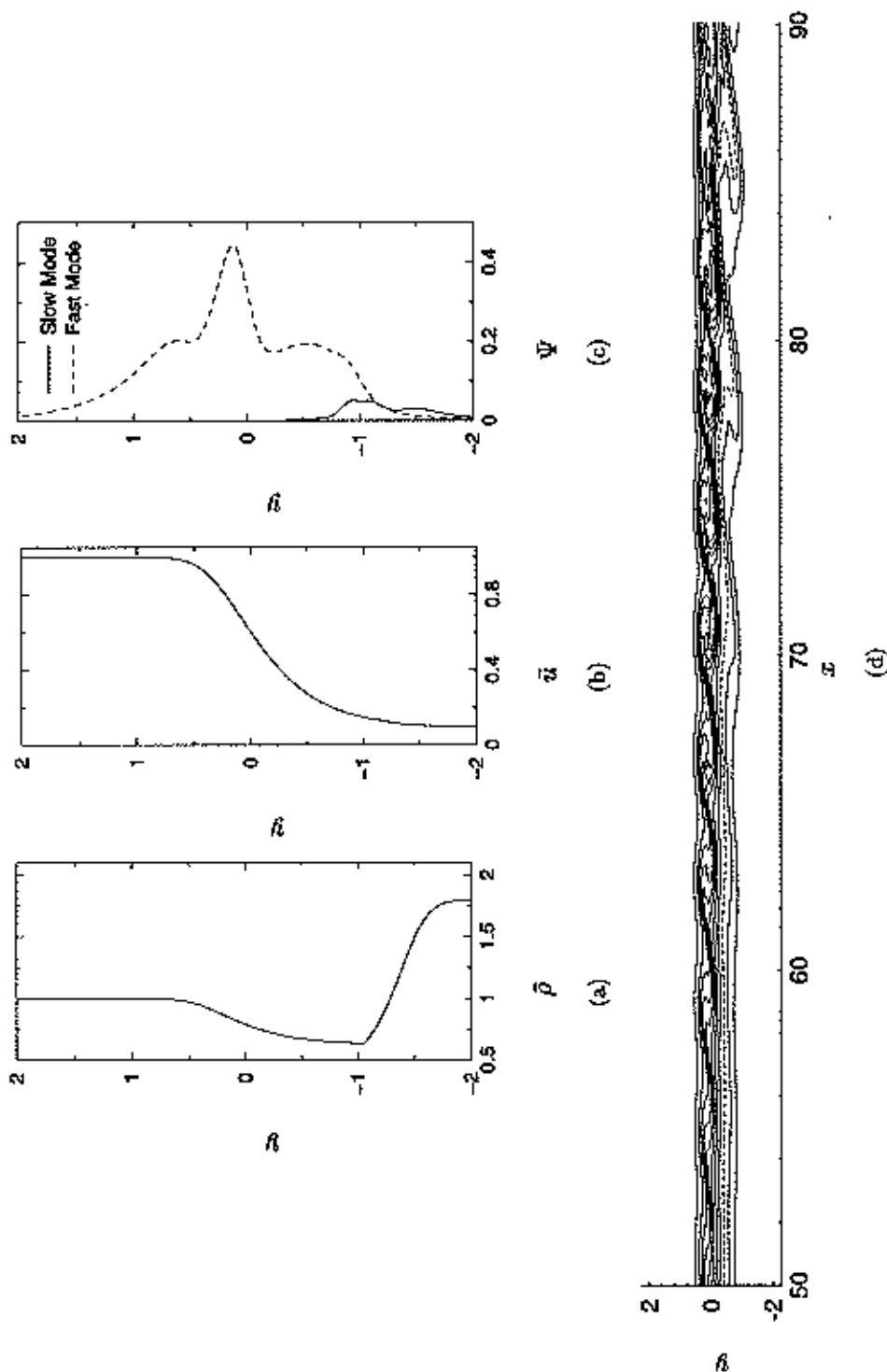
Figure 5.2: Plots of (a) mean density, (b) mean velocity, and (c) normalized eigenfunction energy (see equation 3.1) at the input condition of a mixing layer simulation for the same parameters as the experiment (R_δ=1890, r=0.25, M_c=0, Θ=1, ϕ=0.048). The mixture fraction contours of a PSE simulation ($M = 16$) are shown in (d) for an equivalence ratio of $\phi = 0.3$. Contour ξ_{max}=0.95, ξ_{min}=0.05, and $\Delta\xi = 0.09$ and the flame sheet (ξ_{st}=0.77) shown as a dashed line.

Appendix A

PSE Term Expansions

A.1 Nonlinear Contributions

In what follows, for completeness, the time derivatives of the mean flow components and the streamwise derivative of the mean pressure have been included although these are zero for the calculations in this work. The equations are presented in tensor notation for compactness; it should be noted that there is no mean flow in the z direction in $\bar{u}_i$ terms.

A.1.1 Thermodynamic Variables

For the ideal gas law in nondimensional form,

$$p = \rho R T, \tag{A.1}$$

a uniform molecular weight assumption gives the base and linear decompositions

$$\text{Base Flow} \quad : \bar{p} = \quad \bar{\rho}\bar{T} = 1 \tag{A.2a}$$

$$\text{Linear} \quad : \hat{p} = \quad \tilde{T}\bar{\rho} + \tilde{T} \tag{A.2b}$$

$$\text{Nonlinear} \quad : 0 = \quad \tilde{\rho}\tilde{T} \tag{A.2c}$$

The derivative of pressure that occurs in the momentum equations is decomposed as follows

$$\text{Base Flow} \quad : \frac{\partial \bar{p}}{\partial x_i} = \quad \bar{T}\frac{\partial \bar{\rho}}{\partial x_i} + \bar{\rho}\frac{\partial \bar{T}}{\partial x_i} \tag{A.3a}$$

$$\text{Linear} \quad : \frac{\partial \tilde{p}}{\partial x_i} = \quad \tilde{T}\frac{\partial \bar{\rho}}{\partial x_i} + \tilde{\rho}\frac{\partial \tilde{T}}{\partial x_i} \tag{A.3b}$$

Note that there is no nonlinear contribution to this term because it originally appears in a linear form. The inclusion of this incorrect forcing term can cause considerable problems in the stability of the technique.

A.1.2 Continuity Equation

Next consider the development of the nondimensional continuity equation in compressible form

$$\frac{\partial \rho}{\partial t} + \frac{\partial \rho u_i}{\partial x_i} = 0 \tag{A.4}$$

Decomposing the flow variables into mean and fluctuating components and grouping the terms into base flow, linear, and nonlinear categories yields

$$\text{Base Flow} \quad : \quad \frac{\partial \bar{\rho}}{\partial t} + \frac{\partial \bar{\rho} \bar{u}_i}{\partial x_i} = 0 \tag{A.5a}$$

$$\text{Linear} \quad : \quad \frac{\partial \tilde{\rho}}{\partial t} + \bar{\rho}\frac{\partial \tilde{u}_i}{\partial x_i} + \tilde{u}_i\frac{\partial \bar{\rho}}{\partial x_i} + \bar{\rho}\frac{\partial \bar{u}_i}{\partial x_i} + \bar{u}_i\frac{\partial \tilde{\rho}}{\partial x_i} = 0 \tag{A.5b}$$

$$\text{Nonlinear} \quad : \quad \tilde{\rho}\frac{\partial \tilde{u}_i}{\partial x_i} + \tilde{u}_i\frac{\partial \tilde{\rho}}{\partial x_i} = 0 \tag{A.5c}$$

A.1.3 Momentum Equation

The nondimensional inviscid momentum equations are

$$\rho\frac{\partial u_i}{\partial t} + \rho u_j\frac{\partial u_i}{\partial x_j} = -\frac{\partial p}{\partial x_i} + \frac{1}{Re_o}\frac{\partial \dot{\tau}_{ij}}{\partial x_j} \tag{A.6}$$

Decomposing and collecting into like-order groups yields

$$\text{Base Flow} \quad : \quad \bar{\rho}\frac{\partial \bar{u}_i}{\partial t} + \bar{\rho}\bar{u}_j\frac{\partial \bar{u}_i}{\partial x_j} = -\frac{\partial \bar{p}}{\partial x_i} + \frac{\sigma_\tau}{Re_o}\frac{\partial}{\partial x_2}\left(\bar{\mu}\frac{\partial \bar{u}_i}{\partial x_2}\right) \tag{A.7a}$$

$$\text{Linear} \quad : \quad \bar{\rho}\frac{\partial \tilde{u}_i}{\partial t} + \tilde{\rho}\frac{\partial \bar{u}_i}{\partial t} + (\tilde{\rho}\bar{u}_j + \bar{\rho}\tilde{u}_j)\frac{\partial \bar{u}_i}{\partial x_j} + \bar{\rho}\bar{u}_j\frac{\partial \tilde{u}_i}{\partial x_j}$$

$$= -\frac{\partial \tilde{p}}{\partial x_i} + \frac{\sigma_\tau}{Re_o}\left[\frac{\partial}{\partial x_2}\left(\tilde{\mu}\frac{\partial \bar{u}_i}{\partial x_2}\right) + \frac{\partial}{\partial x_2}\left(\bar{\mu}\frac{\partial \tilde{u}_i}{\partial x_2}\right)\right] \tag{A.7b}$$

$$\text{Nonlinear} \quad : \quad \tilde{\rho}\frac{\partial \tilde{u}_i}{\partial t} + \bar{\rho}\tilde{u}_j\frac{\partial \tilde{u}_i}{\partial x_j} + (\tilde{\rho}\bar{u}_j + \bar{\rho}\tilde{u}_j + \tilde{\rho}\tilde{u}_j)\frac{\partial \tilde{u}_i}{\partial x_j}$$

$$= \frac{\sigma_\tau}{Re_o}\frac{\partial}{\partial x_2}\left(\tilde{\mu}\frac{\partial \tilde{u}_i}{\partial x_2}\right) \tag{A.7c}$$

where σ_τ is $4/3$ for $i = 2$ and is 1 otherwise, according to the thin-shear-layer approximation.

A.1.4 Species Equation

Here we develop the formulation for the evolution of a conserved scalar, Z. Start with the inviscid form of the species conservation equation, retaining the cross-stream molecular diffusivity term as per the thin-shear-layer assumption

$$\rho\left(\frac{\partial Z}{\partial t} + u_i \frac{\partial Z}{\partial x_i}\right) = \frac{1}{Re_o Sc} \frac{\partial}{\partial x_i}\left(\mu \frac{\partial Z}{\partial x_i}\right) \tag{A.8}$$

Decomposing this equation into mean, linear, and nonlinear components yields

$$\text{Base Flow}: \bar{\rho}\frac{\partial \bar{Z}}{\partial t} + \bar{\rho}\bar{u}_i \frac{\partial \bar{Z}}{\partial x_i} = \frac{1}{Re_o Sc} \frac{\partial}{\partial x_2}\left(\bar{\mu} \frac{\partial \bar{Z}}{\partial x_2}\right) \tag{A.9a}$$

$$\text{Linear}: \bar{\rho}\frac{\partial \tilde{Z}}{\partial t} + \tilde{\rho}\frac{\partial \bar{Z}}{\partial t} + (\bar{\rho}\tilde{u}_i + \tilde{\rho}\bar{u}_i)\frac{\partial \bar{Z}}{\partial x_i} + \bar{\rho}\bar{u}_i \frac{\partial \tilde{Z}}{\partial x_i} =$$
$$\frac{1}{Re_o Sc}\left[\frac{\partial}{\partial x_2}\left(\tilde{\mu}\frac{\partial \bar{Z}}{\partial x_2}\right) + \frac{\partial}{\partial x_2}\left(\bar{\mu}\frac{\partial \tilde{Z}}{\partial x_2}\right)\right] \tag{A.9b}$$

$$\text{Nonlinear}: \bar{\rho}\frac{\partial \tilde{Z}}{\partial t} + \bar{\rho}\tilde{u}_i \frac{\partial \bar{Z}}{\partial x_i} + \left(\bar{\rho}\tilde{u}_i + \tilde{\rho}\bar{u}_i + \tilde{\rho}\tilde{u}_i\right)\frac{\partial \tilde{Z}}{\partial x_i} = \frac{1}{Re_o Sc}\frac{\partial}{\partial x_2}\left(\tilde{\mu}\frac{\partial \tilde{Z}}{\partial x_2}\right) \tag{A.9c}$$

A.1.5 Energy Equation

Finally, consider the inviscid form of the energy equation for fast chemistry. Note that this equation appears with the assumption of constant molecular weight across the layer, and hence the gas constant is also uniform.

$$\rho\left(\frac{\partial T}{\partial t} + u_i \frac{\partial T}{\partial x_i}\right) = -p(\gamma - 1)\frac{\partial u_i}{\partial x_i} + \frac{\gamma}{Re_o Pr} \frac{\partial}{\partial x_i}\left(\mu \frac{\partial T}{\partial x_i}\right) \tag{A.10}$$

This equation decomposes into the follow terms (recall that the mean pressure is unity in the following)

$$\text{Base Flow}: \bar{\rho}\frac{\partial \bar{T}}{\partial t} + \bar{\rho}\bar{u}_i \frac{\partial \bar{T}}{\partial x_i} = -\bar{p}(\gamma - 1)\frac{\partial \bar{u}_i}{\partial x_i} + \frac{\gamma}{Re_o Pr}\frac{\partial}{\partial x_2}\left(\bar{\mu}\frac{\partial \bar{T}}{\partial x_2}\right) \tag{A.11a}$$

$$\text{Linear}: \bar{\rho}\frac{\partial \tilde{T}}{\partial t} + \tilde{\rho}\frac{\partial \bar{T}}{\partial t} + (\bar{\rho}\tilde{u}_i + \tilde{\rho}\bar{u}_i)\frac{\partial \bar{T}}{\partial x_i} + \bar{\rho}\bar{u}_i \frac{\partial \tilde{T}}{\partial x_i} = -(\gamma - 1)\left(\tilde{p}\frac{\partial \bar{u}_i}{\partial x_i} + \bar{p}\frac{\partial \tilde{u}_i}{\partial x_i}\right)$$
$$+ \frac{1}{Re_o Pr}\left[\frac{\partial}{\partial x_2}\left(\tilde{\mu}\frac{\partial \bar{T}}{\partial x_2}\right) + \frac{\partial}{\partial x_2}\left(\bar{\mu}\frac{\partial \tilde{T}}{\partial x_2}\right)\right] \tag{A.11b}$$

$$\text{Nonlinear}: \bar{\rho}\frac{\partial \tilde{T}}{\partial t} + \bar{\rho}\tilde{u}_i \frac{\partial \bar{T}}{\partial x_i} + \left(\bar{\rho}\tilde{u}_i + \tilde{\rho}\bar{u}_i + \tilde{\rho}\tilde{u}_i\right)\frac{\partial \tilde{T}}{\partial x_i}$$
$$= -\tilde{p}(\gamma - 1)\frac{\partial \tilde{u}_i}{\partial x_i} + \frac{1}{Re_o Pr}\frac{\partial}{\partial x_2}\left(\tilde{\mu}\frac{\partial \tilde{T}}{\partial x_2}\right) \tag{A.11c}$$

A.2 Expanded System of PSE Equations

The linear system described in equation (2.75) is expanded below. Note that term collection is done for readability and not calculation efficiency; since the terms are evaluated separately in the matrix their collection is irrelevant.

$$\hat{\rho}\frac{\partial \bar{u}}{\partial x} + \bar{\rho}\frac{\partial \hat{u}}{\partial x} + \hat{u}\frac{\partial \bar{\rho}}{\partial x} + \bar{u}\frac{\partial \hat{\rho}}{\partial x} + \hat{\rho}\Big[i(\alpha\bar{u} - \omega) + \frac{\partial \bar{v}}{\partial y}\Big]$$
$$+ \hat{v}\frac{d\bar{\rho}}{dy} + \bar{v}\frac{\partial \hat{\rho}}{\partial y} + \bar{\rho}\Big[i(\alpha\hat{u} + \beta\hat{w}) + \frac{\partial \hat{v}}{\partial y}\Big] = 0 \quad \text{(A.12a)}$$

$$\bar{u}\Big[\hat{\rho}\frac{\partial \bar{u}}{\partial x} + \bar{\rho}\frac{\partial \hat{u}}{\partial x}\Big] + \bar{\rho}\Big[i(\alpha\bar{u} - \omega)\hat{v} + \hat{v}\frac{d\bar{u}}{dy} + \bar{v}\frac{\partial \hat{u}}{\partial y}\Big] + \hat{\rho}\bar{v}\frac{\partial \bar{u}}{\partial y}$$
$$+ \frac{i\alpha\hat{p}}{\gamma_1 M_1^2} + \frac{\Omega}{\gamma_1 M_1^2}\frac{\partial \hat{p}}{\partial x} - \frac{1}{Re_o}\Big[\frac{\partial \hat{\mu}}{\partial y}\frac{\partial \bar{u}}{\partial y} + \frac{\partial \bar{\mu}}{\partial y}\frac{\partial \hat{u}}{\partial y} + \hat{\mu}\frac{\partial^2 \bar{u}}{\partial y^2} + \bar{\mu}\frac{\partial^2 \hat{u}}{\partial y^2}\Big] = 0 \quad \text{(A.12b)}$$

$$\bar{u}\Big[\bar{\rho}\frac{\partial \hat{v}}{\partial x} + \hat{\rho}\frac{\partial \bar{v}}{\partial x}\Big] + \bar{\rho}\hat{u}\frac{\partial \bar{v}}{\partial x} + \bar{\rho}\Big[i(\alpha\bar{u} - \omega)\hat{v} + \bar{v}\frac{\partial \hat{v}}{\partial y} + \hat{v}\frac{\partial \bar{v}}{\partial y}\Big] + \hat{\rho}\bar{v}\frac{\partial \bar{v}}{\partial y}$$
$$+ \frac{1}{\gamma_1 M_1^2}\frac{\partial \hat{p}}{\partial y} - \frac{4}{3Re_o}\Big[\frac{\partial \hat{\mu}}{\partial y}\frac{\partial \bar{v}}{\partial y} + \frac{\partial \bar{\mu}}{\partial y}\frac{\partial \hat{v}}{\partial y} + \hat{\mu}\frac{\partial^2 \bar{v}}{\partial y^2} + \bar{\mu}\frac{\partial^2 \hat{v}}{\partial y^2}\Big] = 0 \quad \text{(A.12c)}$$

$$\bar{\rho}\bar{u}\frac{\partial \hat{w}}{\partial x} + \bar{\rho}\Big[i(\alpha\bar{u} - \omega)\hat{w} + \bar{v}\frac{\partial \hat{w}}{\partial y}\Big] + \frac{i\beta\hat{p}}{\gamma_1 M_1^2} - \frac{1}{Re_o}\Big[\frac{\partial \bar{\mu}}{\partial y}\frac{\partial \hat{w}}{\partial y} + \bar{\mu}\frac{\partial^2 \hat{w}}{\partial y^2}\Big] = 0 \quad \text{(A.12d)}$$

$$\bar{\rho}\bar{u}\frac{\partial \bar{Z}}{\partial x} + \bar{\rho}\Big[\bar{u}\frac{\partial \hat{Z}}{\partial x} + \hat{u}\frac{\partial \bar{Z}}{\partial x}\Big] + \bar{\rho}\Big[i(\alpha\bar{u} - \omega)\hat{Z} + \hat{v}\frac{\partial \bar{Z}}{\partial y} + \bar{v}\frac{\partial \hat{Z}}{\partial y}\Big] + \hat{\rho}\bar{v}\frac{\partial \bar{Z}}{\partial y}$$
$$- \frac{1}{Re_o Sc}\Big[\frac{\partial \bar{\mu}}{\partial y}\frac{\partial \hat{Z}}{\partial y} + \frac{\partial \bar{Z}}{\partial y}\frac{\partial \hat{\mu}}{\partial y} + \hat{\mu}\frac{\partial^2 \bar{Z}}{\partial y^2} + \bar{\mu}\frac{\partial^2 \hat{Z}}{\partial y^2}\Big] = 0 \quad \text{(A.12e)}$$

$$\bar{\rho}\bar{u}\frac{\partial \bar{T}}{\partial x} + \bar{\rho}\Big[\bar{u}\frac{\partial \hat{T}}{\partial x} + \hat{u}\frac{\partial \bar{T}}{\partial x}\Big] + \bar{\rho}\Big[i(\alpha\bar{u} - \omega)\hat{T} + \hat{v}\frac{d\bar{T}}{dy} + \bar{v}\frac{\partial \hat{T}}{\partial y}\Big] + \hat{\rho}\bar{v}\frac{\partial \hat{T}}{\partial y}$$
$$+ (\gamma - 1)\Big[\hat{p}\Big(\frac{\partial \bar{u}}{\partial x} + \frac{\partial \bar{v}}{\partial y}\Big) + \frac{\partial \hat{u}}{\partial x} + i(\alpha\hat{u} + \beta\hat{w}) + \frac{\partial \hat{v}}{\partial y}\Big]$$
$$- \frac{\gamma}{Re_o Pr}\Big[\frac{\partial \bar{\mu}}{\partial y}\frac{\partial \hat{T}}{\partial y} + \frac{\partial \bar{T}}{\partial y}\frac{\partial \hat{\mu}}{\partial y} + \hat{\mu}\frac{\partial^2 \bar{T}}{\partial y^2} + \bar{\mu}\frac{\partial^2 \hat{T}}{\partial y^2}\Big] = 0 \quad \text{(A.12f)}$$

$$\hat{p} - \bar{\rho}\hat{T} - \hat{\rho}\bar{T} = 0 \quad \text{(A.12g)}$$

where the derivative of equation (A.12g) can be taken to close the system of equations

$$\frac{\partial \hat{p}}{\partial x} = \bar{\rho}\frac{\partial \hat{T}}{\partial x} + \hat{T}\frac{\partial \bar{\rho}}{\partial x} + \bar{T}\frac{\partial \hat{\rho}}{\partial x} + \hat{\rho}\frac{\partial \bar{T}}{\partial x} \quad \text{(A.13)}$$

Appendix B

Adjoint Methods for PSE Evolution

This appendix outlines a more rigorous method for closing the system of PSE equations than the conventionally-applied norm of equation (2.88). This effort is not expected to provide improved accuracy, but rather to remove some of the subjectivity in selecting a closure method by introducing a standardized approach. While the adjoint-based closure developed here achieves this, it can only be applied in linear PSE calculations because of its basis in expansions of linear stability solutions. Its inclusion here is meant to provide ideas for further extension to nonlinear domains or, perhaps, for a completely different formulation.

B.1 Conventional Multiscale Approach

To provide a basis for understanding this adjoint-based approach, it is helpful to first outline the methodology behind conventional multiscale methods. These methods seek a local solution to the stability problem of the form

$$\hat{\mathbf{\Phi}}(x,y) = \hat{\mathbf{\Phi}}_0 + \varsigma\hat{\mathbf{\Phi}}_1, \quad \text{and} \quad \alpha(x) = \alpha_o + \varsigma\alpha_1, \tag{B.1}$$

where

$$\varsigma = x - x_0, \quad \hat{\mathbf{\Phi}}_0 = \hat{\mathbf{\Phi}}(x_0,y), \quad \hat{\mathbf{\Phi}}_1 = \frac{\partial\hat{\mathbf{\Phi}}(x_0,y)}{\partial x}, \quad \alpha_o = \alpha(x_0), \quad \alpha_1 = \frac{d\,\alpha(x_0)}{dx}.$$

Substituting equation (B.1) into equation (2.75) results in the system of equations

$$-i\omega\Gamma\hat{\mathbf{\Phi}}_0 + A(i\alpha_0\hat{\mathbf{\Phi}}_0 + \hat{\mathbf{\Phi}}_1) + B\frac{\partial\hat{\mathbf{\Phi}}_0}{\partial y} + i\beta C\hat{\mathbf{\Phi}}_0 + D\hat{\mathbf{\Phi}}_0 = 0, \tag{B.2}$$

$$-i\omega\Gamma\hat{\mathbf{\Phi}}_1 + Ai(\alpha_0\hat{\mathbf{\Phi}}_1 + \alpha_1\hat{\mathbf{\Phi}}_0) + B\frac{\partial\hat{\mathbf{\Phi}}_1}{\partial y} + i\beta C\hat{\mathbf{\Phi}}_1 + D\hat{\mathbf{\Phi}}_1 = 0. \tag{B.3}$$

The equations (B.2) and (B.3) define fourteen equations for sixteen unknowns; the two additional equations come from the normalization condition, applied here to $\hat{u}$ in the form

$$\frac{\partial\hat{u}_0(y_{\max})}{\partial y} = 0 \qquad \frac{\partial\hat{u}_1(y_{\max})}{\partial y} = 1. \tag{B.4}$$

where $y_{\max}$ is the location where the respective eigenfunction is a maximum.

B.2 Adjoint Method for Alpha Advancement

Following in the spirit of a multiscale approach to find a local solution, an approximation for mean flow quantities is made with

$$\bar{\Phi}(x,y) = \bar{\Phi}_0(y) + \epsilon\bar{\Phi}_1(y)\varsigma + \mathcal{O}(\varsigma^2), \tag{B.5}$$

where

$$\bar{\Phi}_0 = \bar{\Phi}(x_0,y), \quad \epsilon\bar{\Phi}_1 = \frac{\partial\bar{\Phi}(x_0,y)}{\partial x}, \quad \varsigma = x - x_0.$$

Following the method of Ling and Reynolds (1973), the eigenfunctions are expanded differently with the form

$$\hat{\Phi}(x,y) = \hat{\Phi}_0(y) + \epsilon\hat{\Phi}_1(y,\varsigma) + \mathcal{O}(\varsigma^2) \tag{B.6a}$$

$$\hat{\Phi}_1(y,\varsigma) = \hat{\Phi}_{10}(y) + \varsigma\hat{\Phi}_{11}(y) \tag{B.6b}$$

to allow differentiation between nonparallel ($\hat{\Phi}_{10}$) and streamwise evolution ($\hat{\Phi}_{11}$) corrections. Similarly, the wavenumber is expanded to account for these two separate influences

$$\alpha = \alpha_0 + \epsilon\alpha_{10} + \epsilon\alpha_{11}\varsigma + \mathcal{O}(\varsigma^2). \tag{B.7}$$

Because there is a physical basis to argue that the frequency will not change in the streamwise direction (further, expansion of this parameter would cause significant problems with the nonlinear formulation) we define

$$\omega = \omega_0. \tag{B.8}$$

Substituting these expansion expressions into the governing equations and collecting terms of $\mathcal{O}(\varsigma^0)$ yields the system

$$L(\hat{\Phi}_0) = 0, \tag{B.9}$$

where $\hat{\phi} = [\hat{\rho}, \hat{u}, \hat{v}, \hat{w}, \hat{Z}, \hat{T}, \hat{p}]^T$ and the operator and its adjoint are given by

$$
L = \begin{bmatrix}
L_{11} & L_{12} & L_{13} & L_{14} & 0 & 0 & 0 \\
0 & L_{22} & L_{23} & 0 & 0 & 0 & L_{27} \\
0 & 0 & L_{33} & 0 & 0 & 0 & L_{37} \\
0 & 0 & 0 & L_{44} & 0 & 0 & L_{47} \\
0 & 0 & L_{53} & 0 & L_{55} & 0 & 0 \\
0 & L_{62} & L_{63} & L_{64} & 0 & L_{66} & 0 \\
L_{71} & 0 & 0 & 0 & 0 & L_{76} & L_{77}
\end{bmatrix}
\qquad (B.10)
$$

$$
\mathcal{L} = \begin{bmatrix}
\mathcal{L}_{11} & 0 & 0 & 0 & 0 & 0 & \mathcal{L}_{17} \\
\mathcal{L}_{21} & \mathcal{L}_{22} & 0 & 0 & 0 & \mathcal{L}_{26} & 0 \\
\mathcal{L}_{31} & \mathcal{L}_{32} & \mathcal{L}_{33} & 0 & \mathcal{L}_{35} & \mathcal{L}_{36} & 0 \\
\mathcal{L}_{41} & 0 & 0 & \mathcal{L}_{44} & 0 & \mathcal{L}_{46} & 0 \\
0 & 0 & 0 & 0 & \mathcal{L}_{55} & 0 & 0 \\
0 & 0 & 0 & 0 & 0 & \mathcal{L}_{66} & \mathcal{L}_{67} \\
0 & \mathcal{L}_{72} & \mathcal{L}_{73} & \mathcal{L}_{74} & 0 & 0 & \mathcal{L}_{77}
\end{bmatrix}
\qquad (B.11)
$$

where

$$L_{11} = i(\alpha_0 \bar{u}_0 - \omega_0)$$

$$L_{12} = i\bar{\rho}_0 \alpha_0$$

$$L_{13} = \frac{\partial \bar{\rho}_0}{\partial y} + \bar{\rho}_0 \frac{\partial}{\partial y}$$

$$L_{14} = i\bar{\rho}_0 \beta$$

$$L_{22} = i\bar{\rho}_0(\alpha_0 \bar{u}_0 - \omega_0)$$

$$L_{23} = \bar{\rho}_0 \frac{\partial \bar{u}_0}{\partial y}$$

$$L_{27} = \frac{i\alpha_0}{\gamma_1 M_1^2}$$

$$L_{33} = i\bar{\rho}_0(\alpha_0 \bar{u}_0 - \omega_0)$$

$$L_{37} = \frac{1}{\gamma_1 M_1^2} \frac{\partial}{\partial y}$$

$$L_{44} = i\bar{\rho}_0(\alpha_0 \bar{u}_0 - \omega_0)$$

$$L_{47} = \frac{i\beta}{\gamma_1 M_1^2}$$

$$L_{53} = \bar{\rho}_0 \frac{\partial \bar{Z}_0}{\partial y}$$

$$L_{55} = i\bar{\rho}_0(\alpha_0 \bar{u}_0 - \omega_0)$$

$$L_{62} = i(\gamma - 1)\alpha_0$$

$$L_{63} = \bar{\rho}_0 \frac{\partial \bar{T}_0}{\partial y} + (\gamma - 1)\frac{\partial}{\partial y}$$

$$L_{64} = i(\gamma - 1)\beta$$

$$L_{66} = i\bar{\rho}_0(\alpha_0 \bar{u}_0 - \omega_0)$$

$$L_{71} = -\bar{T}$$

$$L_{76} = -\bar{\rho}_0$$

$$L_{77} = 1.$$

$$\mathcal{L}_{11} = L_{11}$$

$$\mathcal{L}_{17} = L_{71}$$

$$\mathcal{L}_{21} = L_{12}$$

$$\mathcal{L}_{22} = L_{22}$$

$$\mathcal{L}_{26} = L_{62}$$

$$\mathcal{L}_{31} = -\bar{\rho}_0 \frac{\partial}{\partial y}$$

$$\mathcal{L}_{32} = L_{23}$$

$$\mathcal{L}_{33} = L_{33}$$

$$\mathcal{L}_{35} = L_{53}$$

$$\mathcal{L}_{36} = \bar{\rho}_0 \frac{\partial \bar{T}_0}{\partial y} - (\gamma - 1)\frac{\partial}{\partial y}$$

$$\mathcal{L}_{41} = L_{14}$$

$$\mathcal{L}_{44} = L_{44}$$

$$\mathcal{L}_{46} = L_{64}$$

$$\mathcal{L}_{55} = L_{55}$$

$$\mathcal{L}_{66} = L_{66}$$

$$\mathcal{L}_{67} = L_{76}$$

$$\mathcal{L}_{72} = L_{27}$$

$$\mathcal{L}_{73} = -\frac{1}{\gamma_1 M_1^2} \frac{\partial}{\partial y}$$

$$\mathcal{L}_{74} = L_{47}$$

$$\mathcal{L}_{77} = L_{77}.$$

(B.12)

This system corresponds to the typical linear stability approach where, with homogeneous boundary conditions, equation (B.9) defines an eigenvalue problem for α_0. Collecting terms

of $\mathcal{O}(\epsilon^1 \varsigma^1)$ for the streamwise evolution corrections gives a system of the form

$$L(\hat{\Phi}_{11}) = -\alpha_{11}G + H, \tag{B.13}$$

and terms of $\mathcal{O}(\epsilon^1 \varsigma^0)$ for the nonparallel correction results in the system

$$L(\hat{\Phi}_{10}) = -\alpha_{10}P + Q, \tag{B.14}$$

where

$$G = \begin{bmatrix} i\left(\hat{\rho}_0\bar{u}_0 + \frac{\hat{p}_0}{\gamma_1 M_1^2}\right) \\ i\bar{\rho}_0\bar{u}_0\hat{u}_0 \\ i\bar{\rho}_0\bar{u}_0\hat{v}_0 \\ i\bar{\rho}_0\bar{u}_0\hat{w}_0 \\ i\bar{\rho}_0\bar{u}_0\hat{Z}_0 \\ i\left(\bar{\rho}_0\bar{u}_0\hat{T}_0 + (\gamma-1)\hat{u}_0\right) \\ 0 \end{bmatrix} \tag{B.15}$$

$$H = \begin{bmatrix} -i\bar{\rho}_0\alpha_0\bar{u}_1 + \hat{v}_0\frac{\partial\bar{\rho}_1}{\partial y} - \bar{\rho}_1\left(i\alpha_0\,\hat{u}_0 + i\beta\,\hat{w}_0 + \frac{\partial\hat{v}_0}{\partial y}\right) \\ -\bar{\rho}_0(i\alpha_0\bar{u}_1\hat{u}_0 + \hat{v}_0\frac{\partial\bar{u}_1}{\partial y}) - \bar{\rho}_1\left(i\left(-\omega_0 + \alpha_0\,\bar{u}_0\right)\hat{u}_0 + \hat{v}_0\frac{\partial\bar{u}_0}{\partial y}\right) \\ -i\bar{\rho}_0\alpha_0\bar{u}_1\hat{v}_0 - i\,\bar{\rho}_1\left(-\omega_0 + \alpha_0\,\bar{u}_0\right)\hat{v}_0 \\ -i\bar{\rho}_0\alpha_0\bar{u}_1\hat{w}_0 - i\,\bar{\rho}_1\left(-\omega_0 + \alpha_0\,\bar{u}_0\right)\hat{w}_0 \\ -\bar{\rho}_0(i\alpha_0\bar{u}_1\hat{Z}_0 + \hat{v}_0\frac{\partial\bar{Z}_1}{\partial y}) - \bar{\rho}_1\left(i\left(-\omega_0 + \alpha_0\,\bar{u}_0\right)\hat{Z}_0 + \hat{v}_0\frac{\partial\bar{Z}_0}{\partial y}\right) \\ -\bar{\rho}_0(i\alpha_0\bar{u}_1\hat{T}_0 + \hat{v}_0\frac{\partial\bar{T}_1}{\partial y}) - \bar{\rho}_1\left(i\left(-\omega_0 + \alpha_0\,\bar{u}_0\right)\hat{T}_0 + \hat{v}_0\frac{\partial\bar{T}_0}{\partial y}\right) \\ \hat{\rho}_0\hat{T}_1 + \bar{\rho}_1\hat{T}_0 \end{bmatrix} \tag{B.16}$$

$$P = \begin{bmatrix} i(\hat{\rho}_0 \bar{u}_0 + \hat{u}_0 \bar{\rho}_0) \\ i(\bar{\rho}_0 \bar{u}_0 \hat{u}_0 + \frac{\hat{p}_0}{\gamma_1 M_1^2}) \\ i\bar{\rho}_0 \bar{u}_0 \hat{v}_0 \\ i\bar{\rho}_0 \bar{u}_0 \hat{w}_0 \\ i\bar{\rho}_0 \bar{u}_0 \hat{Z}_0 \\ i\left(\bar{\rho}_0 \bar{u}_0 \hat{T}_0 + (\gamma - 1)\hat{u}_0\right) \\ 0 \end{bmatrix} \tag{B.17}$$

$$Q = \begin{bmatrix} -\left(\hat{\rho}_{11}\bar{u}_0 + \bar{\rho}_1 \hat{u}_0 + \bar{\rho}\hat{u}_{11}\right) \\ -\left(\hat{\rho}_0 \bar{u}_0 \bar{u}_1 + \bar{\rho}_0 \bar{u}_0 \hat{u}_{11} - \frac{\hat{p}_{11}}{\gamma_1 M_1^2}\right) \\ -\bar{\rho}_0 \bar{u}_0 \hat{v}_{11} \\ -\bar{\rho}_0 \bar{u}_0 \hat{w}_{11} \\ -\left(\hat{\rho}_0 \bar{u}_0 \bar{Z}_1 + \bar{\rho}_0 (\hat{u}_0 \bar{Z}_1 + \bar{u}_0 \hat{Z}_{11})\right) \\ -\left(\bar{u}_0 \hat{T}_{11}(\hat{\rho}_0 + \bar{\rho}_0) + \bar{\rho}_0 \hat{u}_0 \bar{T}_1\right) + (\gamma - 1)(\bar{u}_1 \hat{p}_0 + \hat{u}_{11})\right) \\ 0 \end{bmatrix} \tag{B.18}$$

The boundary conditions follow directly from those for $\hat{\Phi}$, yielding

$$\hat{\Phi}_0 \to 0, \quad \hat{\Phi}_{10} \to 0, \quad \text{and} \quad \hat{\Phi}_{11} \to 0 \quad \text{for} \quad y \to \pm\infty. \tag{B.19}$$

B.2.1 Solveability Condition

The use of the adjoint to the operator L provides a means to solve these systems of equations without having to incorporate a normalization condition. The adjoint system and corresponding eigenfunction take the form

$$\mathcal{L}\Lambda = 0, \tag{B.20}$$

with the boundary condition

$$\Lambda \to 0 \quad \text{for} \quad y \to \pm\infty. \tag{B.21}$$

For any two vector functions f and g that satisfy the boundary conditions of equation (B.19), an important property of the adjoint system is the relation

$$\int_{-\infty}^{\infty} f^T \left[L(g) \right] dy = \int_{-\infty}^{\infty} g^T \left[\mathcal{L}(f) \right] dy.$$

(B.22)

Thus, for an inhomogeneous problem (*e.g.* equation B.13 or B.14) of the form

$$L(h) = M,$$

(B.23)

it follows from equations (B.20), (B.22), and (B.23) that

$$\int_{-\infty}^{\infty} \Lambda^T M \, dy = 0.$$

(B.24)

B.2.2 Solution Procedure

The solution procedure begins with solving the linear stability problem of equation (B.9) (or, equivalently, the adjoint of this equation) to determine α_0 for given values of ω_0 and β_0. With this result the adjoint eigenfunction vector Λ can be calculated. The solveability condition of equation (B.24) can then be applied to the inhomogeneous equation (B.13) to determine the one unknown on the right hand side:

$$\alpha_{11} = \int_{-\infty}^{\infty} \Lambda^T H \, dy \left/ \int_{-\infty}^{\infty} \Lambda^T G \, dy. \right.$$

(B.25)

With α_1 known, equation (B.7) provides a rigorous basis for evaluating the downstream wavenumber evolution as

$$\frac{d\alpha}{dx} = \epsilon \, \alpha_{11}$$

(B.26)

B.2.3 Adjoint Eigenvalue Problem

The system of equations with $\mathcal{O}(\epsilon^0 \varsigma^0)$ has the form

$$\hat{\rho}_0 i(\alpha_0 \bar{u}_0 - \omega_0) + \hat{v}_0 \frac{\partial \bar{\rho}_0}{\partial y} + \bar{\rho}_0 \left[i(\alpha_0 \hat{u}_0 + \beta \hat{w}_0) + \frac{\partial \hat{v}_0}{\partial y} \right] = 0, \tag{B.27a}$$

$$\bar{\rho}_0 \left[i(\alpha_0 \bar{u}_0 - \omega_0) \hat{u}_0 + \hat{v}_0 \frac{\partial \bar{u}_0}{\partial y} \right] + \frac{i \alpha_0 \hat{p}_0}{\gamma_1 M_1^2} = 0, \tag{B.27b}$$

$$\bar{\rho}_0 i(\alpha_0 \bar{u}_0 - \omega_0) \hat{v}_0 + \frac{1}{\gamma_1 M_1^2} \frac{\partial \hat{p}_0}{\partial y} = 0, \tag{B.27c}$$

$$\bar{\rho}_0 i(\alpha_0 \bar{u}_0 - \omega_0) \hat{w}_0 + \frac{i\beta \hat{p}_0}{\gamma_1 M_1^2} = 0, \tag{B.27d}$$

$$\bar{\rho}_0 \left[i(\alpha_0 \bar{u}_0 - \omega_0) \hat{Z}_0 + \hat{v}_0 \frac{\partial \overline{Z}_0}{\partial y} \right] = 0, \tag{B.27e}$$

$$\bar{\rho}_0 \left[i(\alpha_0 \bar{u}_0 - \omega_0) \hat{T}_0 + \hat{v}_0 \frac{\partial \overline{T}_0}{\partial y} \right] + (\gamma - 1) \left[i(\alpha_0 \hat{u}_0 + \beta \hat{w}_0) + \frac{\partial \hat{v}_0}{\partial y} \right] = 0, \tag{B.27f}$$

$$\hat{p}_0 - \bar{\rho}_0 \hat{T}_0 - \hat{\rho}_0 \overline{T}_0 = 0, \tag{B.27g}$$

which can be reduced to the coupled system

$$(\bar{u}_0 - c_0) \hat{\psi}_0' - \bar{u}' \hat{\psi}_0 = g_0 \hat{\pi}_0, \tag{B.28}$$

$$\alpha_0^2 \bar{\rho}_0 (\bar{u}_0 - c_0) \hat{\psi}_0 = \hat{\pi}_0', \tag{B.29}$$

where

$$\hat{\psi}_0 = \frac{\hat{v}_0}{i\alpha}, \qquad \hat{\pi}_0 = \frac{\hat{p}_0}{\gamma_1 M_1^2}, \quad \text{and} \quad g_0 = \frac{1 + (\beta_0/\alpha_0)^2}{\bar{\rho}_0} - \frac{\gamma_1}{\gamma} M_1^2 (\bar{u} - c)^2. \tag{B.30}$$

The adjoint of this system is

$$i(\alpha_0 \, \bar{u}_0 - \omega_0)\hat{\rho}_0^* - \bar{T}_0 \hat{p}_0^* = 0, \tag{B.31a}$$

$$\alpha_0 \, \bar{\rho}_0 \, \hat{\rho}_0^* + \bar{\rho}_0(\alpha_0 \, \bar{u}_0 - \omega_0)\hat{u}_0^* + \alpha_0 \, (\gamma - 1) \, \hat{T}_0^* = 0, \tag{B.31b}$$

$$-\bar{\rho}_0 \, \frac{\partial \hat{\rho}_0^*}{\partial y} + \bar{\rho}_0 \, \frac{\partial \bar{u}_0}{\partial y} \, \hat{u}_0^* + i\bar{\rho}_0(\alpha_0 \, \bar{u}_0 - \omega_0)\hat{v}_0^*$$

$$+\bar{\rho}_0 \, \frac{\partial \bar{Z}_0}{\partial y} \, \hat{Z}_0^* + \left[\bar{\rho}_0 \, \frac{\partial \bar{T}_0}{\partial y} - (\gamma - 1) \, \frac{\partial}{\partial y} \right] \hat{T}_0^* = 0, \tag{B.31c}$$

$$\beta \, \bar{\rho}_0 \, \hat{\rho}_0^* + \bar{\rho}_0(\alpha_0 \, \bar{u}_0 - \omega_0)\hat{w}_0^* + \beta \, (\gamma - 1) \, \hat{T}_0^* = 0, \tag{B.31d}$$

$$\bar{\rho}_0(\alpha_0 \, \bar{u}_0 - \omega_0)\hat{Z}_0^* = 0, \tag{B.31e}$$

$$i\bar{\rho}_0 \left[(\alpha_0 \, \bar{u}_0 - \omega_0)\hat{T}_0^* - \hat{p}_0^* \right] = 0, \tag{B.31f}$$

$$\frac{1}{\gamma_1 M_1^2} \left[i(\alpha_0 \hat{u}_0^* + \beta \omega_0^*) - \frac{\partial \hat{v}_0^*}{\partial y} \right] + \hat{p}_0^* = 0, \tag{B.31g}$$

which can also be reduced to two coupled equations of similar form:

$$(\bar{u}_0 - c_0)^2 \, \hat{\psi}_0^{*\prime} = g_0 \hat{\pi}_0^*, \tag{B.32}$$

$$\alpha_0^2 \, \bar{\rho}_0 \, (\bar{u}_0 - c_0)^2 \, \hat{\psi}_0^* = \hat{\pi}_0^{*\prime}, \tag{B.33}$$

where

$$\hat{\psi}_0^* = \hat{v}_0^* \quad \text{and} \quad \hat{\pi}_0^* = -\gamma \hat{p}_0^*. \tag{B.34}$$

Shooting methods applied to both sets of coupled equations (regular or adjoint) will yield the same eigenvalue, α_0, for specified ω_0 and B values.

Appendix C

Code and Data Archive

This appendix is intended to give some guidance to researchers who are interested in employing the PSE. This appendix evolved partly out of a desire for completeness, and partly as a response to the lack of publicly available information on the technique; Herbert (1997) points out that the commercial potential of the technique has resulted in sparse communication about PSE details in the literature. In what follows, the basic structure of the archived code, suggested changes to it, and a detailed list of input conditions that were used in the current study are outlined. Researchers interested in obtaining this code should direct requests to day@stanfordalumni.org.

C.1 PSE Code Archive

To begin with, a general disclaimer: despite extensive validation (documented herein), errors most certainly remain in a code of this size and complexity and thus its accuracy is not guaranteed. However, at the very least, the current version should provide insight into some details of the technique that took considerable time and effort to sort out. The program elements are described below. As the file name extensions suggest, the code is written in Fortran 90 and makes use of FFT routines from the SGI/Cray Math Library and several spline and integration routines from Numerical Recipes (Press *et al.* 1992). These routines are specified in the supplied makefile.

pse_main.f90	Contains the module declarations, main program subroutines, and the program units for memory allocation, mode addition, grid initialization, and output file writing.
pse_calc.f90	Subroutines for calculating statistical quantities, both for diagnostic and operational tasks (*e.g.* energy integrals).
pse_evolution.f90	Controls the streamwise stepping of the shape functions, which involves setting up equation (2.112) and applying the iteration procedure of equation (2.116).

189

`pse_ders.f90`	Streamwise and cross-stream derivative routines.
`pse_ic.f90`	Routines for developing the initial condition, including the subroutines for calculating LST solutions.
`pse_nonlinear.f90`	Manages the calculation of the nonlinear forcing vector, F, of equation (2.112).
`pse_profiles.f90`	Subroutines for evaluating the mean-flow similarity solutions.

The PSE code outputs a data file of information from the simulation. A post-processing code was developed to process this file and output useful quantities and statistics. It contains the following parts:

`pse_postpro.f90`	Manages the file input, memory allocation, data interpolation to a fine grid, and the calculations of some basic quantities like vorticity.
`pse_statistics.f90`	Subroutines for calculating secondary statistical quantities like the energy, PDF, and integrated reaction rates.
`pse_postders.f90`	Post-processing derivative routines.

C.2   Code Changes

The PSE code has evolved considerably from its earliest incarnation as a linear code to its present status as a fully nonlinear simulation tool. Naturally, this development history has resulted in a number of legacy issues in the code, *e.g.* constructs that have changed so many times that their present form is less than optimal. As such, the archived code should be thought of as a reference point for the development of entirely new PSE implementations. It should be well suited to this task because, within limits, a concerted effort was made to document and organize the code in a sensible fashion.

Future versions should also be developed from inception to incorporate the ability for parallel computations. Parallelization would be very successful in a PSE code because its mode-specific nature allows for simple decomposition of computational tasks and the low memory requirements would render message-passing costs insignificant.

C.2.1 PSE Case Conditions

The following tables outline the details of several representative PSE cases.

Parameter	Le	Pr	Sc	γ	$\mathcal{M}$
Value	1	1	1	1.4	Constant

Table C.1: Thermodynamic properties common to all PSE simulations.

Case	Description	M_c	Θ	ϕ	s	r	Re
1	DNS Central Mode Validation	0.5	0	N/A	1.0	0.6	5,000
2	Nonreacting Central Mode	1.0	0	N/A	1.0	0.5	10,000
3	Reacting Central Mode	1.0	0.75	1.0	1.0	0.5	10,000
4	Fast Mode Mixing	1.0	0.75	1.0	2/3	0.5	10,000
5	Slow Mode Mixing	1.0	0.75	1.0	3/2	0.5	10,000
6	Fast/Slow Colayer w/ Subharmonics	1.0	1.0	1.0	0.94	0.5	10,000
7	Central/Slow Colayer	1.0	0.45	1.0	3/2	0.5	10,000
8	Subsonic Pairing	0.125	0	N/A	1.0	0.5	500
9	Supersonic Pairing	0.5	0	N/A	1.0	0.5	5,000

Table C.2: Flow Parameters for selected PSE cases.

Case	M	N	δx	n_y	L_y	b_y
1	8	0	0.4	150	30	2.0
2	5	4	0.75	150	30	2.5
3	5	4	0.4	150	30	2.5
4	5	3	0.4	200	50	2.5
5	5	3	0.3	250	50	2.5
6	18	0	0.3	300	50	2.0
7	9	3	0.5	250	50	2.0
8	16	0	0.2	400	200	3.0
9	8	0	0.2	300	50	2.0

Table C.3: Simulation-specific parameters for the selected PSE cases of table C.2.

Case	Mode	ϵ_o	α	ω	β	ϕ_s
1	(1,0)	0.0005	(0.7197, -0.06806)	(0.5781,0)	(0,0)	0
	(2,0)	0.0001	(1.429, -0.009097)	(1.156,0)	(0,0)	0
2	(1,0)	0.0001	(0.3355, -0.01392)	(0.261,0)	(0,0)	0
	(1,1)	0.0005	(0.3456, -0.04300)	(0.261,0)	(0.5,0)	0
3	(1,0)	0.0001	(0.2166, -0.01444)	(0.154,0)	(0,0)	0
	(1,1)	0.0005	(0.2039, -0.02914)	(0.154,0)	(0.29,0)	0
4	(1,0)	0.0005	(1.0978, -0.03170)	(0.970,0)	(0.0,0)	0
	(1,1)	0.0002	(1.0977, -0.03169)	(0.970,0)	(0.295,0)	0
5	(1,0)	0.0005	(1.1672, -0.04877)	(0.711,0)	(0,0)	0
	(1,1)	0.0002	(1.1711, -0.04652)	(0.711,0)	(0.676,0)	0
6	(1,0)	0.000001	(0.1729, -0.01204)	(0.125,0)	(0,0)	0
	(2,0)	0.00025	(0.3682, -0.02260)	(0.25,0)	(0,0)	$\pi/2$
	(3,0)	0.00025	(0.4515, -0.02262)	(0.375,0)	(0,0)	$\pi/2$
	(4,0)	0.0005	(0.7792, -0.03231)	(0.50,0)	(0,0)	0
	(6,0)	0.0005	(0.8526, -0.03115)	(0.75,0)	(0,0)	0
7	(1,0)	0.0005	(0.1970, -0.05526)	(0.1575,0)	(0,0)	0
	(2,0)	0.0005	(0.4050, -0.09473)	(0.315,0)	(0,0)	$\pi/2$
	(4,0)	0.0005	(0.8336, -0.1253)	(0.63, 0)	(0,0)	0
8	(1,0)	0.0005	(0.3550, -0.05166)	(0.28905, 0)	(0,0)	$\pi/2$
	(2,0)	0.0005	(0.7197, -0.06806)	(0.57810,0)	(0,0)	0

Table C.4: Input modes and their initial eigenvalue guesses for the cases of table C.2. Note that initial amplitudes, ϵ_o, are effectively doubled when the complex conjugate is taken into account (see equation 2.73).

References

ANDERSSON, P., HENNINGSON, D. S., & HANIFI, A. 1998 On a stabilization procedure for the parabolic stability equations. *J. Eng. Math.* **33**, 311–332.

BARRE, S., QUINE, C., & DUSSAUGE, J. P. 1994 Compressibility effects on the structure of mixing layers: Experimental results. *J. Fluid Mech.* **259**, 47–78.

BERNAL, L. P., & ROSHKO, A. 1986 Streamwise vortex structure in plane mixing layers. *J. Fluid Mech.* **170**, 499–525.

BERTOLOTTI, F. P., & HERBERT, T. 1991 Analysis of the Linear Stability of Compressible Boundary Layers Using the PSE. *Theoret. Comput. Fluid Dynamics* **3**, 117–124.

BERTOLOTTI, F. P., HERBERT, T., & SPALART, P. R. 1992 Linear and Nonlinear Stability of the Blasius Boundary Layer. *J. Fluid Mech.* **242**, 441–474.

BLAISDELL, G. A., MANSOUR, N. N., & REYNOLDS, W. C. 1993 Compressibility effects on the growth and structure of homogeneous turbulent shear flow. *J. Fluid Mech.* **256**, 443–485.

BOGDANOFF, D. W. 1983 Compressibility Effects in Turbulent Shear Layers. *AIAA J.* **21**, 926–927.

BREIDENTHAL, R. E. 1981 Structure in turbulent mixing layers and wakes using a chemical reaction. *J. Fluid Mech.* **109**, 1–24.

BRIGGS, R. J. 1964 *Electron-stream interaction with Plasmas.* MIT Press.

BROADWELL, J. E., & BREIDENTHAL, R. E. 1982 A simple model of mixing and chemical reaction in a turbulent shear layer. *J. Fluid Mech.* **125**, 397–410.

BROWN, G. L., & ROSHKO, A. 1974 On density effects and large structure in turbulent mixing layers. *J. Fluid Mech.* **64**, 775–816.

CHANG, C.-L., & MALIK, M. R. 1994 Oblique-mode breakdown and secondary instability in supersonic boundary layers. *J. Fluid Mech.* **273**, 323–60.

CHANG, C.-L., MALIK, M. R., ERLEBACHER, G., & HUSSAINI, M. Y. 1993 Linear and Nonlinear PSE For Compressible Boundary Layers. *ICASE Rep.* 93-70.

CHEN, L. D., SEABA, J. P., ROQUEMORE, W. M., & GOSS, L. P. Buoyant Diffusion Flames. In *Twenty-Second Symposium (International) on Combustion, The Combustion Institute, Pittsburgh, USA* (1988), pp. 677–684.

CHINZEI, N. G., MASUYA, T., KOMURO, T., MURAKAMI, A., & KUDOU, K. 1986 Spreading of two-stream supersonic turbulent mixing layers. *Phys. Fluids* **29**, 1345–1347.

CLEMENS, N. T., & MUNGAL, M. G. 1995 Large–scale structure and entrainment in the supersonic mixing layer. *J. Fluid Mech.* **284**, 171–216.

CLEMENS, N. T., & PAUL, P. H. 1995 Scalar measurements in compressible axisymmetric mixing layers. *Phys. Fluids A*, 1071–1081.

COLONIUS, T., LELE, S. K., & MOIN, P. 1997 Sound generation in a mixing layer. *J. Fluid Mech.* **330**, 375–409.

DAY, M. J., MANSOUR, N. N., & REYNOLDS, W. C. 1998 The structure of the compressible reacting mixing layer: Insights from linear stability analysis. *Phys. Fluids* **10**, 993–1007.

DIMOTAKIS, P. 1991 Turbulent mixing and combustion. In S.N.B. Murthy and E.T. Curran (Eds.). *High-Speed Flight Propulsion Systems* **137**, 265–340.

DIMOTAKIS, P. E. 1986 Two-Dimensional Shear-Layer Entrainment. *AIAA J.* **24**, 1791–1796.

DIMOTAKIS, P. E., & BROWN, G. L. 1976 The mixing layer at high Reynolds number. *J. Fluid Mech.* **78**, 535–560.

DIMOTAKIS, P. E., & LEONARD, A. 1994 Chemical reactions in turbulent mixing flows. *California Institute of Technology Rep.* 94-3.

DRAZIN, P. G., & REID, W. H. 1981 *Hydrodynamic Stability.* Cambridge Univ. Press.

DUNN, D. W., & LIN, C. C. 1955 On the stability of the laminar boundary in a compressible fluid. *J. Aero. Sci.* **22**, 455–477.

DUTTON, J. C., BURR, R. F., GOEBEL, S. G., & MESSERSMITH, N. L. Compressibility and mixing in turbulent free shear layers. In *12th Symposium on Turbulence, Rolla, MO* (1990).

DUTTON, J. C., MIKKELSEN, C. D., & ADDY, A. L. 1982 A theoretical and experimental investigation of the constant area, supersonic-supersonic ejector. *AIAA J.* **20**, 1392–1400.

ELLIOT, G. S., SAMIMY, M., & ARNETTE, S. A. 1993 The characteristics and evolution of large-scale structures in compressible mixing layers. *Phys. Fluids* **7**, 864–876.

ERDOS, J., TAMAGNO, J., BAKOS, R., & TRUCCO, R. 1992 Experiments on Shear layer Mixing at Hypervelocity Conditions. *AIAA-92-0628*.

FOURGUETTE, D. C., MUNGAL, M. G., & DIBBLE, R. W. 1991 Time evolution of the shear layer of a supersonic axisymmetric jet. *AIAA J.* **29**, 1123–1130.

FREUND, J. B. *Compressibility Effects in a Turbulent Annular Mixing Layer*. PhD thesis, Stanford University, Stanford, CA 94305, Sep 1997. Also available as Freund, J.B., Moin, P., and Lele, S.K., Report No. TF-72, Mechanical Engineering Department, Stanford University.

FREUND, J. B. 1997b A proposed inflow/outflow boundary condition for direct computation of aerodynamic sound. *AIAA J.* **35**, 740–742.

FREYMUTH, P. 1966 On transition in a separated laminar boundary layer. *J. Fluid Mech.* **25**, 683–704.

FRIELER, C. E. *Mixing and reacting in the subsonic 2–D turbulent free shear layer*. PhD thesis, California Institute of Technology, Pasadena, CA 91125, 1992.

GOEBEL, S. G., & DUTTON, J. C. 1991 Experimental Study of Compressible Turbulent Mixing Layers. *AIAA J.* **29**, 538–546.

GROPENGIESSER, H. 1970 Study on the stability of boundary layers and compressible fluids. *NASA Rep.* TT F-12786.

GUTMARK, E. J., SCHADOW, K. C., & WILSON, K. J. 1995 Mixing enhancement in supersonic free shear layer flows. *Annual Review of Fluid Mechanics* **27**, 375–417.

HAJ-HARIRI, H. 1994 Characteristics analysis of the parabolized stability equations. *Stud. Appl. Math.* **92**, 41–53.

HALL, J. L. *An experimental investigation of structure, mixing and combustion in compressible turbulent shear layers*. PhD thesis, California Institute of Technology, 1991.

HALL, J. L., DIMOTAKIS, P. E., & ROSEMANN, H. 1993 Experiments in Nonreacting Compressible Shear Layers. *AIAA J.* **31**, 2247–2254.

HAMA, F. R. 1962 Streaklines in a perturbed shear flow. *Phys. Fluids* **5**, 644–650.

HERBERT, T. 1994 Parabolized Stability Equations. *Von Kármán Inst., Rhode-Saint-Genese, Belgium Rep.* AGARD-FDP-VK1 Special Course on Progress in Transition Modeling, AGARD-R-793.

HERBERT, T. 1997 Parabolized Stability Equations. *Ann. Rev. Fluid Mech.* **29**, 245–283.

HERBERT, T., & BERTOLOTTI, F. P. 1987 Stability Analysis of Nonparallel Boundary Layers. *Bulletin of the American Physical Society* **32**, 2079.

HERMANSON, J. C., & DIMOTAKIS, P. E. 1989 Effects of heat release in a turbulent, reacting shear layer. *J. Fluid Mech.* **199**, 333–375.

HO, C.-M., & HUERRE, P. 1984 Perturbed Free Shear Layers. *Ann. Rev. Fluid Mech.* **16**, 365–424.

HUERRE, P., & MONKEWITZ, P. A. 1985 Absolute and convective instabilities in free shear layers. *J. Fluid Mech.* **159**, 151–168.

IKAWA, H., & KUBOTA, T. 1975 Investigation of a supersonic turbulent mixing layer with zero pressure gradient. *AIAA J.* **13**, 566–572.

ISLAND, T. *Quantitative Scalar Measurements and Mixing Enhancement in Compressible Shear Layers.* PhD thesis, Stanford University, Stanford, CA 94305, April 1997. Also available as Island, T. C. Report No. TSD-104, Mechanical Engineering Department, Stanford University.

JACKSON, T. L., & GROSCH, C. E. 1989 Inviscid spatial stability of a compressible mixing layer. *J. Fluid Mech.* **208**, 609–637.

JACKSON, T. L., & GROSCH, C. E. 1991 Inviscid spatial stability of a compressible mixing layer. Part 3. Effect of thermodynamics. *J. Fluid Mech.* **224**, 159–175.

KARASSO, P. S., & MUNGAL, M. G. 1996 Scalar mixing and reaction in plane liquid shear layers. *J. Fluid Mech.* **323**, 23–63.

KELLY, R. E. 1967 On the stability of an inviscid shear layer which is periodic in space and time. *J. Fluid Mech.* **27**, 657–689.

KONRAD, J. H. *An experimental investigation of mixing in two-dimensional turbulent shear flows with applications to diffusion-limited chemical reactions*. PhD thesis, California Institute of Technology, 1976.

KOOCHESFAHANI, M. M., & DIMOTAKIS, P. E. 1986 Mixing and chemical reactions in a turbulent liquid mixing layer. *J. Fluid Mech.* **170**, 83–112.

KUO, K. 1986 *Principles of Combustion*. John Wiley & Sons.

LEES, L., & LIN, C. C. 1946 Investigation of the Stability of the Laminar Boundary Layer in a Compressible Fluid. *NACA Tech. Note* No. 1115.

LESSEN, M., FOX, J. A., & ZIEN, H. M. 1965 On the Inviscid Instability of the Laminar Mixing of Two Parallel Streams of a Compressible Fluid. *J. Fluid Mech.* **23**, 355–367.

LESSEN, M., FOX, J. A., & ZIEN, H. M. 1966 Stability of the laminar mixing of two parallel streams with respect to supersonic disturbances. *J. Fluid Mech.* **25**, 737–742.

LI, F., & MALIK, M. R. 1996 On the Nature of the PSE Approximation. *Theoret. Comput. Fluid Dynamics* **8**, 253–273.

LING, C., & REYNOLDS, W. C. 1973 Non-parallel flow corrections for the stability of shear flows. *J. Fluid Mech.* **59**, 571–591.

LU, G., & LELE, S. K. 1994 On the density ratio effect on the growth rate of a compressible mixing layer. *Phys. Fluids* **6**, 1073–1075.

MALIK, M. R., & CHANG, C.-L. 1997 PSE Applied to Supersonic Jet Instability. *AIAA-97-0758*.

MALLIER, R., & MASLOWE, S. A. 1994 Fully coupled resonant-triad interactions in a free shear layer. *J. Fluid Mech.* **278**, 101–21.

MASUTANI, S. M., & BOWMAN, C. T. 1986 The structure of a chemically reacting plane mixing layer. *J. Fluid Mech.* **172**, 93–126.

MCMURTRY, P. A., RILEY, J. J., & METCALFE, R. W. 1989 Effects of heat release on the large-scale structures in turbulent mixing layers. *J. Fluid Mech.* **199**, 297–332.

MESSERSMITH, N. L., & DUTTON, J. C. 1992 An experimental investigation of organized structure and mixing in compressible turbulent free shear layers. *University of Illinois Rep.* UILU-ENG 92-4002.

MESSERSMITH, N. L., & DUTTON, J. C. 1996 Characteristic features of large structures in compressibile mixing layers. *AIAA J.* **34**, 1814–1821.

MICHALKE, A. 1965 On spatially growing disturbances in an inviscid shear layer. *J. Fluid Mech.* **23**, 521–544.

MILLER, M. F., BOWMAN, C., & MUNGAL, M. 1998 An experimental investigation of the effects of compressibility on a turbulent reacting mixing layer. *J. Fluid Mech.* **356**, 25–64.

MILLER, R. S., MADNIA, K., & GIVI, P. 1994 Structure of a turbulent reacting mixing layer. *Combut. Sci. and Tech.* **99**, 1–36.

MONKEWITZ, P. A. 1988 Subharmonic resonance, pairing and shredding in the mixing layer. *J. Fluid Mech.* **188**, 223–52.

MONKEWITZ, P. A., & HUERRE, P. 1982 Influence of the velocity ratio on the spatial instability of mixing layers. *Phys. Fluids* **25**, 1137–1143.

PAPAMOSCHOU, D. 1989 Structure of the Compressible Turbulent Shear Layer. *AIAA-89-0126*.

PAPAMOSCHOU, D., & BUNYAJITRADULYA, A. 1997 Evolution of large eddies in compressible shear layers. *Phys. Fluids* **9**, 756–765.

PAPAMOSCHOU, D., & LELE, S. K. 1993 Vortex-induced disturbance field in a compressible shear layer. *Phys. Fluids A* **5**, 1412–1419.

PAPAMOSCHOU, D., & ROSHKO, A. 1988 The compressible turbulent shear layer: an experimental study. *J. Fluid Mech.* **197**, 453–477.

PIERREHUMBERT, R. T., & WIDNALL, S. E. 1982 The two- and three-dimensional instabilities of a spatially periodic shear layer. *J. Fluid Mech.* **114**, 59–82.

PLANCHÉ, O. H. *A numerical investigation of the compressible reacting mixing layer.* PhD thesis, Stanford University, Stanford, CA 94305, Oct 1992. Also available as Planché, O.H. & Reynolds, W.C. Report No. TF-56, Mechanical Engineering Department, Stanford University.

PLANCHÉ, O. H., & REYNOLDS, W. C. 1991 Compressibility Effect on the Supersonic Reacting Mixing Layer. *AIAA-91-0739.*

PLANCHÉ, O. H., & REYNOLDS, W. C. 1992 Heat release effects on mixing in supersonic reacting free shear-layers. *AIAA-92-0092.*

PRESS, W. H., TEUKOLSKY, S. A., VETTERLING, W. T., & FLANNERY, B. P. 1992 *Numerical Recipes.* Cambridge Univ. Press.

PRUETT, C. D., & CHANG, C.-L. 1995 Spatial Direct Numerical Simulation of High-Speed Boundary-Layer Flows Part II: Transition on a Cone in Mach 8 Flow. *Theoret. Comput. Fluid Dynamics* **7**, 397–424.

RAGAB, S. A., & WU, J. L. 1989 Linear Instabilities in Two-Dimensional Compressible Mixing Layers. *Phys. Fluids* A **1**, 957–966.

ROGERS, M., & MOSER, R. D. 1994 Direct simulation of a self-similar turbulent mixing layer. *Phys. Fluids* **6**, 903–923.

ROSSMANN, T., & MUNGAL, M. G. 1999 A New Shock Tunnel Facility for High Compressibility Mixing Layer Studies. *AIAA 99-0415.*

SAMIMY, M., & ELLIOT, G. S. 1990 Effects of Compressibility on the Characteristics of Free Shear Layers. *AIAA J.* **28**, 439–445.

SANDHAM, N. D. *A Numerical Investigation of the Compressible Mixing Layer: Linear Theory and Direct Simulation.* PhD thesis, Stanford University, Stanford, CA 94305, Sept. 1989. Also available as Sandham, N.D. & Reynolds, W.C. Report No. TF-45, Mechanical Engineering Department, Stanford University.

SANDHAM, N. D. 1994 The effect of compressibility on vortex pairing. *Phys. Fluids* **6**, 1063–1072.

SANDHAM, N. D., & REYNOLDS, W. C. 1990 Compressible Mixing Layer: Linear Theory and Direct Simulation. *AIAA J.* **28**, 618–624.

SANDHAM, N. D., & REYNOLDS, W. C. 1991 Three-dimensional simulations of large eddies in the compressible mixing layer. *J. Fluid Mech.* **224**, 133–158.

SARIC, W. S., & H., N. A. 1975 Non-parallel Stability of Boundary-Layer Flows. *Phys. Fluids* **18**, 945–950.

SARKAR, S., ERLEBACHER, G., HUSSAINI, M. Y., & KREISS, H. O. 1991 The analysis and modelling of dilatational terms in compressible turbulence. *J. Fluid Mech.* **227**, 473–493.

SCHLICHTING, H. 1979 *Boundary-Layer Theory.* 7th edition, McGraw Hill.

SHIN, D. S., & FERZIGER, J. H. 1991 Linear Stability of the Reacting Mixing Layer. *AIAA J.* **29**, 1634–1642.

SHIN, D. S., & FERZIGER, J. H. 1993 Linear Stability of the Compressible Reacting Mixing Layer. *AIAA J.* **31**, 677 685.

SIEGMAN, A. E. 1986 *Lasers.* University Science Books.

SIRIEIX, M., & SOLIGNAC, J. L. Contribution a l'etude experimentale de la couche de melange turbulent isobare d'un ecoulment supersonique. In *AGARD Conference Proceedings No. 4, Separated Flows* (1966).

SLESSOR, M. D. *Aspects of turbulent-shear-layer dynamics and mixing.* PhD thesis, California Institute of Technology, 1998.

SLESSOR, M. D., ZHUANG, M., & DIMOTAKIS, P. E. 1998b Turbulent shear-layer mixing: growth-rate compressibility scaling. *California Institute of Technology Rep.* FM98-9.

SOTERIOU, M. C., & GHONIEM, A. F. 1995 Effects of the free-stream density ratio on free and forced spatially developing shear layers. *Phys. Fluids* **7**, 2036–2051.

STUART, J. T. 1967 On finite amplitude oscillations in laminar mixing layers. *J. Fluid Mech.* **29**, 417–440.

TAM, C. K. W., & BURTON, D. E. 1984 Sound generated by instability waves of supersonic flows. Part 1. Two-dimensional mixing layers. *J. Fluid Mech.* **138**, 249–271.

URBAN, W. D. *Planar Velocity Measurements in Compressible Mixing Layers.* PhD thesis, Stanford University, Stanford, CA 94305, March 1999. Also available as Urban, W. Report No. TSD-119, Mechanical Engineering Department, Stanford University.

VREMAN, A. W., SANDHAM, N. D., & LUO, K. H. 1996 Compressible mixing layer growth rate and turbulence characteristics. *J. Fluid Mech.* **320**, 235–258.

VREMAN, B., KUERTEN, H., & GEURTS, B. 1995 Shocks in direct numerical simulation of the confined three-dimensional mixing layer. *Phys. Fluids* **7**, 2105–2107.

WALLACE, A. K. *Experimental investigation of the effects of chemical heat release in the reacting turbulent plane shear layer.* PhD thesis, The University of Adelaide, 1981. Also available as AFSOR Rep. TR-84-0650.

WILLE, R. 1963 Beiträge zur Phänomenologie der Freistrahlen. *Z. Flugwiss* **11**, 222–33.

WILLIAMS, F. A. 1985 *Combustion Theory.* Benjamin/Cummings Pub. Co.

WINANT, C. D., & BROWAND, F. K. 1974 Vortex Pairing. *J. Fluid Mech.* **63**, 237–255.

YEN, C. C., & MESSERSMITH, N. L. 1998 Application of Parabolized Stability Equations to the prediction of Jet Instabilities. *AIAA J.* **36**, 1541–1544.